Variability of cloud optical depth and cloud droplet effective radius in layer clouds: satellite based analysis

by

Malgorzata Szczodrak

M.Sc., Jagiellonian University, 1984

A DISSERTATION SUBMITTED IN PARTIAL FULFILLMENT OF
THE REQUIREMENTS FOR THE DEGREE OF

Doctor of Philosophy

in

THE FACULTY OF GRADUATE STUDIES

(Department of Geography)

We accept this dissertation as conforming
to the required standard

THE UNIVERSITY OF BRITISH COLUMBIA

January 1998

In presenting this thesis in partial fulfilment of the requirements for an advanced degree at the University of British Columbia, I agree that the Library shall make it freely available for reference and study. I further agree that permission for extensive copying of this thesis for scholarly purposes may be granted by the head of my department or by his or her representatives. It is understood that copying or publication of this thesis for financial gain shall not be allowed without my written permission.

Department of Geography

The University of British Columbia
Vancouver, Canada

Date 19.03.1998

DE-6 (2/88)

Abstract

Measurements made by the AVHRR (Advanced Very High Resolution Radiometer) on board of five NOAA polar orbiting satellites were used to retrieve cloud optical depth (τ) and cloud droplet effective radius (r_{eff}) for marine boundary layer clouds over the Pacific Ocean west of California and over the Southern Ocean near Tasmania. Retrievals were obtained for 21 days of data acquired between 1987 and 1995 from which over 300 subscenes $\sim 256\ km \times 256\ km$ in size were extracted. On this spatial scale cloud fields were found to have mean τ between 8 and 32 and mean r_{eff} between 6 and 17 μm. The frequency distribution of τ is well approximated by a two parameter gamma distribution. The gamma distribution also provides a good fit to the observed r_{eff} distribution if the distribution is symmetric or positively skewed but fails for negatively skewed or bi-modal distributions of r_{eff} which were also observed.

The retrievals show a relationship between τ and r_{eff} which is consistent with a simple "reference" cloud model with $r_{eff} \sim \tau^{1/5}$. The proportionality constant depends on cloud droplet number concentration N and cloud subadiabaticity β through the parameter $N_{sat} = N/\sqrt{\beta}$. Departures from the reference behaviour occur in scenes with spatially coherent N_{sat} regimes, separated by a sharp boundary. AVHRR imagery is able to separate two N_{sat} regimes if they differ by at least 30% in most cases.

Satellite retrievals of τ and r_{eff} were compared with in situ aircraft measurement near Tasmania. The retrievals overestimated r_{eff} by 0.7 to 3.6 μm on different flights, in agreement with results from earlier comparison studies. The r_{eff} overestimation was found to be an offset independent of τ. The reference cloud model and the N_{sat} retrieval were tested on aircraft data and yield results consistent with direct in situ measurements of N and β.

Spectral and multifractal analyses of the spatial structure of cloud visible radiance, τ and r_{eff} fields in 34 satellite scenes revealed scale breaks at 3 to 20

km in all analysed scenes in agreement with some earlier observations (Davis *et al.* (1996a)) but in contrast with other work (Lovejoy *et al.* (1993)). The nonstationarity $H(1)$ and intermittency $C(1)$ parameters were computed for the 34 scenes, stratified using the reference cloud model and according to mean τ and r_{eff} . Similar values of $H(1)$ and $C(1)$ were found in all these categories.

These measurements of the frequency distribution and spatial variability of τ, r_{eff}, liquid water path (lwp), and N_{sat} can be used to place constraints on mesoscale models of layer clouds.

Contents

List of Tables

List of Figures

List of Symbols

a	intercept in the linear least squares regression
a_0	constant in eq. 3.2 and 3.2
A_c	cloud fraction
A_g	ground albedo
b	exponent in the general power law
$B(Temp)$	Planck function
$B(x)$	ordinary Brownian motion
c, c_{adiab}	rate of increase of cloud liquid water content with height
$ch1$	visible wavelength cloud reflected radiance
$C(q)$	hierarchy function of exponents $K(q)$
CCN	cloud condensation nuclei
D_g	Hölder dimension of graph g
D_q	generalised dimension
D_H	Hausdorf dimension
$E(k)$	power spectrum
E	Euclidean dimension
F_0	solar flux
$g_q(r)$	structure function of order q
$G(r,x)$	autocorrelation function
$H, H(q)$	scaling exponent (eq. 6.1), hierarchy function of exponents $\zeta(q)$
k	wavenumber
$K(q)$	exponent function for scaling of singular measures
lwc	cloud liquid water content
lwp	cloud liquid water path
L	domain of the stochastic process in chapter 6

L, L_{obs}	cloud reflected radiance and satellite received radiance, chapter 2
$n(r)$	distribution of cloud droplets size in eq. 1.1, 1.2 and 2.1
N	cloud droplet number concentration
N_{sat}	$N/\sqrt{\beta}$
N_-, N_+	lower and upper limits of cloud droplet number concentration uncertainty interval
q	moment order of structure functions and singular measures in chapter 6
q, q_{adiab}	cloud liquid water content and adiabatic cloud liquid water content in Appendix A
Q_{ext}	extinction efficiency factor for a water droplets
p, p_*	pressure, saturation level pressure
$p(\tau)$	frequency distribution of τ in GCM pixel
r	cloud droplet radius in eq. 1.1, 1.2 and 2.1 plane albedo of the cloud layer in eq. 2.3 and 8.1, $\log(r_{eff})$, distance lag for structure functions and degradation scale for singular measures in chapter 6
r_β	percentage of variability of N_{sat} explained by variability of cloud subadiabaticity β
r_{eff}	cloud droplet effective radius
$\bar{r}_{eff}, < r_{eff} >$	mean r_{eff}
r_{eff}'	r_{eff} in equation 4.11
r_{pp}, r_s	plane albedo in PPH approximation in eq. 8.1, and spherical albedo of the cloud layer in eq. 2.3
r_N	percentage of variability of N_{sat} explained by variability of cloud droplet number concentration N
r_0	mode radius of droplet size distribution in eq. 2.1

rr	Pearson's linear correlation coefficient
rr_s	Spearman's rank order correlation coefficient
R	bidirectional reflection in chapter 2,
	upper limit of scaling range in chapter 6
t	transmissivity of the cloud layer in eq. 2.3, $\log(\tau)$
t_c	transmissivity of cloud layer in AVHRR channel 4
T	bidirectional transmission
T_c	cloud top temperature
T_g	ground temperature
(v_i, v_j)	values of measured field at locations i and j
$z, \Delta z$	height in the atmosphere, cloud geometrical thickness
α, α_0	constant in the general power law, constant defined in eq. A.7
	Hölder order of singularity in section 6.4.2
β	cloud subadiabaticity defined in eq. A.2,
	scaling exponent in the power spectrum eq. 6.11
β_B	Betts' mixing parameter
$\gamma, \gamma(\mathbf{h})$	atmospheric lapse rate, semivariogram
Γ	the gamma function
$\epsilon(r, x)$	singular measure
$\zeta(q)$	exponent function in structure function scaling
η	lower limit of scaling range in chapter 6
θ	cosine of satellite viewing angle
θ_0	cosine solar zenith angle
λ	wavelength, change of scale ratio in chapter 6
μ	cosine of satellite viewing angle
μ_0	cosine solar zenith angle
ν	parameter of gamma distribution in eq. 4.6,
	number of degree of freedom in chapter 4

$\nu_\tau, \nu_{r_{eff}}$	parameters of gamma distribution fitting histograms of τ and r_{eff}
ρ	density of water
σ	log standard deviation of droplet size distribution in eq. 2.1
σa	uncertainty of intercept from the least squares regression
σb	uncertainty of slope from the least squares regression
σ_e	standard deviation of regression residuals (log), eq. 4.3
$\sigma_{r_{eff}}$	standard deviation of r_{eff}
σ_β	uncertainty of intercept of cloud subadiabaticity β estimated in chapter 5
$\sigma\tau$	standard deviation of τ
τ	cloud optical depth, total optical depth of the atmosphere in eq. 2.2 and 2.3
$\tau\prime$	τ in equation 4.11
$\bar{\tau}, <\tau>$	mean $<\tau>$
τ_c, τ_u	cloud optical depth, optical depth of the atmosphere above the cloud layer in eq. 2.2 and 2.3
ϕ	sun-satellite azimuth angle
φ_n	AVHRR response function in channel n
$\varphi(x), \Delta\varphi(x,r)$	a generic stochastic process and its increment over a distance r at point x

List of Acronyms

AVHRR	Advanced Very High Resolution Radiometer
ASTEX	Atlantic Stratus Transition Experiment
CSIRO	The Commonwealth Scientific and Industrial Research Organisation
ERBE	Earth Radiation Budget Experiment
FIRE	First ISCCP Regional Experiment
*F*87	FIRE 1987 data set
GCM	Global Circulation Model
IPA	Independent Pixel Approximation
ISCCP	International Satellite Cloud Climatology Project
MCR	Multi-spectral Cloud Radiometer
MODIS	Moderate Resolution Imaging Spectroradiometer
NASA	National Aeronautics and Space Administration
NOAA	National Oceanic and Atmospheric Administration
NCAR	National Center for Atmospheric Research
PPH	Plane Parallel Homogeneous
*P*94, *P*95	Pacific Ocean 1994 and 1995 data sets
SOCEX	Southern Ocean Cloud Experiment
SSMI	Special Sensor Microwave Imager
*S*95	SOCEX 1995 data set
TOA	Top of Atmosphere
TM	Thematic Mapper
VAS	Vertical Atmospheric Sounder

Acknowledgements

I am enormously grateful to my supervisor, Phil Austin, for introducing me to the fascinating world of clouds and satellites, and the inner workings of cloud remote sensing. I greatly appreciate Phil's guidance and assistance through this project, especially the countless hours he spend reviewing my manuscript, and the many intriguing questions which would stimulate my research. This thesis, is in one way my attempt to answer some of Phil's questions.

I wish to thank my supervisory committee Douw Steyn and William Hsieh for their guidance and advice provided during my years in the graduate programme and a thorough review of the thesis draft. Douw Steyn first welcomed me to the department while I was still working as a particle physicist at the neighbourhood TRIUMF, and it was his enthusiasm about the atmosphere and atmospheric research that led me away from smashing nuclei in accelerators to the UBC Department of Geography to study more "gentle" atmospheric processes.

This thesis would not exist in its current form without the assistance of many people.

Teruyuki Nakajima and Takashi Nakajima of the University of Tokyo kindly provided their cloud optical depth and cloud droplet effective radius retrieval code and assisted with my initial tests of the model. Steven Platnick of NASA Goddard provided assistance with further tests by checking a sample of my retrievals using his code.

Robert Pincus of NASA Goddard provided AVHRR and NMC data for the FIRE period and answered my numerous email inquiries of various nature, ranging from satellite navigation to, C programming to, Lagrangian cloud trajectories. Paul Krummel of CSIRO Victoria provided the SOCEX data, satellite and aircraft. Through discussions with Paul I gained a better understanding of the conditions during the experiment which help my interpretation of the results of the satellite and in situ comparisons in SOCEX.

Denis Laplante from the Department of Oceanography supervised the collection of the AVHRR data at the UBC Satellite Lab. He also graciously shared with me his computer expertise and knowledge of satellite data formats and helped on numerous occasions with decoding data in the many "standard" formats of HRPT.

Thanks also to Jim Mintha and Vincent Kujala for the practically round the clock computer assistance.

Chapter 1

Introduction

1.1 Role of boundary layer clouds in Earth's radiation budget

Boundary layer clouds, through their wide extent, persistent occurrence and radiative properties are of fundamental importance to the global energy budget and Earth's climate.

Warren *et al.* (1988) estimate the global area coverage of low level stratiform clouds at 29% (34% over the Earth's oceans). Low layer clouds affect the climate system through the net exchange of radiant energy at the top of the boundary layer. Over the ocean, clouds that are highly reflective in visible wavelengths (reflectivity $\sim$ 60%) obscure the dark ocean (reflectivity $\sim$ 5%) contributing significantly to the planetary albedo, while the warm temperatures of these clouds continue to cool the atmosphere by emission of outgoing long wave radiation. On annual average, boundary layer stratiform clouds contribute 15 Wm^{-2} net cooling to the radiation balance at the top of the atmosphere (TOA) (Hartmann *et al.* (1992)).

Arking (1991) distinguishes three classes of processes which determine the radiative effect of clouds on climate: 1) the macrophysical structure of clouds - their horizontal extent, cloud fraction, optical thickness, horizontal and vertical inhomogeneities; 2) the microphysical structure - the size distribution of cloud droplets

within the macroscale volume; 3) the cloud ambient environment - temperature and humidity structure of the atmosphere, atmospheric stability, and distribution of the atmospheric aerosols.

These three groups of processes are tightly coupled. For example, changes in the aerosol population may affect cloud liquid water content by suppressing or promoting precipitation, while aqueous phase chemistry within the cloud droplets modifies the aerosol size distribution. The number of possible interactions between the three process categories makes estimating the sensitivity of the planetary radiation budget to various changes in cloud properties problematic.

There have been a large number of modelling studies identifying potentially important feedbacks between aerosols, cloud microphysics, and cloud reflectivity. I review several of these in section 1.2.2 below. In section 1.2.3 I review satellite and in-situ observations showing the impact of cloud microphysics on reflectivity and cloud spatial structure. These observations show that layer clouds are horizontally inhomogeneous. In section 1.3 I review modelling work that suggests that the inhomogeneous spatial distribution of cloud water may by itself have an important effect on cloud reflectivity. In section 1.4 I discuss several approaches to quantifying spatial inhomogeneity that are applicable to satellite measurements. Finally, in section 1.5 I review work in which two cloud properties, the cloud optical depth and cloud droplet effective radius (defined below in section 1.2.1) are measured using aircraft and satellite radiometers.

In this thesis I focus on processes identified by Arking (1991) in points 1) and 2). In particular, I use satellite data to infer and quantify the variability of cloud optical thickness as a measure of cloud macro-structure, and cloud droplet size as a measure of cloud micro-structure. Furthermore, I quantify the relationship between these two parameters, which establishes a new observational link between cloud macro and microphysics.

1.2 Cloud optical depth and cloud droplet effective radius

1.2.1 Basic definitions

This thesis examines couplings between macro- and microphysical cloud properties and deals extensively with two cloud parameters. These parameters are: cloud visible wavelength optical depth (τ), which characterises cloud extinction at visible wavelengths, and cloud droplet effective radius (r_{eff}) which is a cloud microphysical parameter and represents a measure of the distribution of cloud droplet sizes. Another cloud parameter frequently appearing in this thesis is cloud liquid water path (lwp), which measures the water content in column of cloudy air. Below, I define these cloud parameters explicitly:

Cloud optical depth

Cloud optical depth determines cloud reflectivity at visible wavelengths and is defined as

$$\tau = \int_0^{\Delta z} [\int_0^{\infty} n(r,z) Q_{ext}(2\pi r/\lambda) \pi r^2 dr] dz \tag{1.1}$$

where the integration is over the cloud droplet radius r and height within the cloud z. Δz is the cloud geometrical thickness, $n(r)$ is the cloud droplet size distribution, and $Q_{ext}(2\pi r/\lambda)$ is the efficiency factor for extinction for a water droplet of radius r at a wavelength λ. For large size parameters ($2\pi r/\lambda$), Q_{ext} asymptotically approaches 2 (Stephens (1978)). For cloud droplets $r \approx 10\mu m$, and for visible radiation $\lambda \approx 0.7\mu m$, thus the size parameter $\gg 1$ and the approximation Q_{ext}=2 is justified.

Cloud droplet effective radius

The cloud droplet effective radius is the mean radius of the cloud droplet size distribution $n(r)$ $[cm^{-3}\mu m^{-1}]$ weighted by the droplet surface area

$$r_{eff} = \frac{\int_0^\infty n(r)r^3dr}{\int_0^\infty n(r)r^2dr}. \tag{1.2}$$

Cloud liquid water path

The cloud liquid water path is defined as

$$lwp = \int_0^{\Delta z} lwc(z)dz \tag{1.3}$$

where $lwc = \int_0^\infty \frac{4}{3}\pi\rho n(r)r^3dr$ is cloud liquid water content , z is height within the cloud layer, and Δz is cloud geometrical thickness, ρ is the density of water.

From (1.1), (1.2) and (1.3) one obtains

$$\tau = \int_0^{\Delta z} \frac{3}{2\rho}\frac{lwc}{r_{eff}}dz. \tag{1.4}$$

I will also define cloud droplet number concentration $N = \int_0^\infty n(r)dr$ where r is the radius of cloud droplet and $n(r)$ the size distribution of cloud droplets.

The parameters τ and r_{eff} control the cloud reflectivity on spatial scales greater than 200-500 m, the photon mean free path (Cahalan and Joseph (1989)). They are also directly related to the physical properties of the cloud, the cloud liquid water path defined above in (1.3) and the drop size distribution $n(r)$.

1.2.2 Review of sensitivity studies

The interaction between cloud microphysics and atmospheric aerosol has a potentially significant impact on cloud radiative properties and may considerably affect

the earth's radiation budget and hydrological cycle. Twomey (1977) and Twomey *et al.* (1984) modelled the effect of an increased concentration of CCN on cloud optical thickness and found that assuming an increase in the total aerosol concentration increases concentration of cloud condensation nuclei (CCN) which in turn activate more droplets at cloud base. The resulting reduction in cloud droplet size could potentially increase cloud reflectivity and thus enhance the planetary albedo. Charlson *et al.* (1987) estimated that a doubling of CCN concentration could offset the warming induced by doubling of the atmospheric CO_2 concentration. This increase in TOA planetary albedo due to the increase of cloud reflectivity in response to increased aerosol concentration at fixed *lwp* is termed "the indirect effect" to distinguish it from the "direct effect" of aerosol scattering of solar radiation in a cloud free environment.

A modelling study of Jones *et al.* (1994) concluded that modification of cloud droplet number distribution and concentration by anthropogenic aerosol results in an indirect aerosol radiative forcing (i.e. top of the atmosphere flux difference) whose global annual average of -1.3 Wm^{-2} exceeds the direct cooling effect of aerosol scattering of solar radiation (-0.3 to -0.9 Wm^{-2}).

In related studies, Global Circulation Model (GCM) simulations indicate large sensitivity of climate to changes in cloud cover and cloud microphysical parameters such as cloud optical depth, cloud droplet size and cloud liquid water path. Several authors have shown that even small perturbations to low cloud fraction or cloud droplet effective radius in cloud schemes within GCMs can greatly affect the simulated impact of greenhouse gases on climate. For example, a 15% reduction in global cloud droplet size at constant *lwp* offsets the predicted CO_2 doubling induced climate warming of 4 $W\ m^{-2}$. The same effect is achieved by increasing the cloud fraction by 20% while keeping droplet size and *lwp* constant (Slingo (1990)) .

Not only the droplet size but also the cloud liquid water path may be indirectly affected by aerosols. Albrecht (1989) proposed that a reduction of the mean

cloud droplet size in response to increased aerosol concentration can act to inhibit precipitation and contribute to a prolonged cloud lifetime and increased cloud fraction. Baker (1993) suggested that variation in cloud droplet number concentration may play a role in determining cloud lifetimes, cloud cover and large scale cloud albedo, and precipitation rates. She postulated the existence of two steady states in the well-mixed marine cloud-topped boundary layer which represent precipitating and non-precipitating clouds. These steady states are determined by distinctly different CCN (or cloud droplet number concentration) concentrations. The low cloud droplet number concentration N state corresponds to approximately 10 cm^{-3}, the high N state corresponds to $\sim$ 1000 cm^{-3}. The cloud droplet number concentration is regulated by production of droplets and removal due to droplet growth and precipitation. N also plays a role in controlling the heating profile the cloudy boundary layer. Net positive heating occurs in thin clouds with low cloud droplet number concentration which makes these clouds particularly prone to break-up (Baker (1993)).

The modelling study of Ackerman *et al.* (1993) showed that if the CCN concentration in the cloud-topped boundary layer is depleted to very low values (about 10 cm^{-3}), (due for example to droplet growth by collisions), the cloud layer can become so optically thin that cloud top radiative cooling will become too weak to drive the vertical mixing in the boundary layer and the layer collapses to a shallower one. Through this mechanism the marine layer clouds can limit their own lifetimes.

In another modelling study Pincus and Baker (1994) investigated changes in cloud thickness and cloud albedo resulting from changes in precipitation rates and solar absorption due to varying cloud droplet number concentration. They found that the sensitivity of cloud albedo to cloud droplet number concentration is increased by a factor ranging from 1.5 to 2 if cloud thickness is allowed to vary in response to varying cloud droplet number concentration and argued that the relationship between cloud thickness and cloud droplet number concentration needs to be accounted for in predictions of global albedo by climate models. Their model

results showed that, in the case of thin clouds with low cloud droplet number concentration, injection of aerosol into the boundary layer increases cloud liquid water and cloud albedo by suppressing precipitation. In thick clouds with high albedos adding new aerosols changes droplet radius but has only a small effect on albedo. These results are in qualitative agreement with the observation of ship tracks (Radke *et al.* (1989), Coakley *et al.* (1987)) discussed below in section 1.2.3.

Boers and Mitchell (1994) proposed a feedback mechanism which modified the enhancement of cloud top albedo expected from an increase in the CCN concentration (Twomey (1977)). The feedback was based on the effect that the change in droplet size and concentration has on the absorption of solar radiation within the cloud, which in turn modifies the mixing process between cloud and the overlaying dry air, and hence affects the microphysics of cloud droplets. In the limit of thin clouds ($\tau < 10$) this feedback mechanism partly offsets the reflectance increase due to the increase of droplet concentration. In optically thick clouds the reflectance is further enhanced due the feedback.

Feingold *et al.* (1997) recognised that the onset of rain drop growth through collisions transforms the unimodal droplet size spectrum created in the process of condensation into a bimodal spectrum with a secondary mode corresponding to drizzle-size droplets. This transition from uni- to bimodal spectrum reduces cloud optical depth through 1) decrease of cloud droplet number concentration, and 2) increase of mean droplet size, even if cloud liquid water path is held constant. Using a simple box model of stochastic collection (Tzivion *et al.* (1987)) and an eddy resolving model (Stevens *et al.* (1996)) Feingold *et al.* (1997) found that the relation between cloud droplet number concentration and cloud optical depth differs between uni- and bi-modal clouds. As a result the susceptibility of cloud albedo to changes in cloud droplet number concentration (i.e. change in cloud albedo in response to changes in N, at constant cloud liquid water content , $S = dA/dN$) can be up to 2.5 times larger in clouds with active collection than in the uni-modal

(non precipitating) clouds.

The uncertainties surrounding the aerosol, cloud droplet and cloud reflectivity interactions have stimulated much research in this field in recent years. The challenge is twofold: 1) to better understand cloud microphysical and radiative properties and their interactions, and 2) to develop more accurate cloud parametrisations for use in GCMs that capture the important interactions between cloud microphysical and macrophysical processes.

1.2.3 Observations

Modelling studies postulate numerous feedbacks between cloud properties and climate. Observations which could confirm the modelling results are fewer and often contradictory.

Martin *et al.* (1994) observed an increase in cloud droplet number concentration with increasing aerosol concentration in warm stratocumulus clouds confirming the predictions of Twomey (1977). Kim and Cess (1993) reported satellite based observations of increased albedos in low level marine clouds near coastal boundaries where aerosol concentrations were large.

The ship track phenomena, where cloud reflectivity is increased in trails of ship effluents which act as CCN and lead to an increase in cloud droplet number concentration, provides observational evidence of the modification of cloud properties by atmospheric aerosol (Radke *et al.* (1989), Coakley *et al.* (1987), Platnick *et al.* (1997)).

Suggestions that precipitation may be an important modulator of cloud thickness and cloud albedo are particularly difficult to verify observationally. Austin *et al.* (1995) observed complex spatial variations in precipitation rates and optical depth of marine boundary layer clouds. The observed clouds exhibited localised regions of intense precipitation large enough to cause cloud water depletion. These precipitation events did not seem to have an impact on hourly satellite retrieved cloud

fraction or cloud optical depth in the region, where both remained high throughout the day.

Additional satellite observations of Pincus *et al.* (1997) also do not indicate that precipitation greatly affects cloud fraction or cloud optical depth variability. Pincus *et al.* (1997) used cloud optical depth retrievals from geostationary satellites to study the Lagrangian evolution of cloud fraction and cloud optical depth in North Pacific clouds in response to varying environmental parameters (sea surface temperature, lower troposphere stratification and others). They found that in the principal component decomposition the environmental components explain only a fraction of the variability in cloud fraction and cloud optical depth. The cloud optical depth at sunrise turned out to be the best predictor of the diurnal cycle of cloud fraction and cloud optical depth (a threshold value seems to exists for the sunrise cloud optical depth which determines whether or not the cloud breaks-up in the afternoon). Pincus *et al.* (1997) conjectured that cloud droplet number concentration can be another major factor in determining cloud properties, as large concentrations increase cloud optical depth even in the absence of changes in the cloud liquid water, but had no observations of either cloud droplet number concentration or cloud droplet effective radius to examine this question in detail.

Drizzle depletion of cloud water was also observed in situ by Boers *et al.* (1996), who reported aircraft observations of marine clouds over the Southern Ocean where horizontal variability in cloud liquid water content appeared to be driven primarily by variations in cloud droplet number concentration. Their calculations showed that on days with intense drizzle, cloud optical depth was possibly reduced (at the same lwp) by as much as 50% due to a shift to larger values of cloud droplet effective radius associated with precipitation.

In another study Boers *et al.* (1997) sampled a layer of stratocumulus clouds embedded with linear convective elements. They found a factor of two difference in cloud droplet number concentration between the convective line and the surrounding

stratocumulus deck. This contrast between convective and quiescent regions was also apparent in cloud liquid water content.

In other in situ studies, aircraft observations (Paluch and Lenschow (1991), Austin *et al.* (1995)) revealed large variability in cloud base height in marine stratocumulus and relatively less variable cloud top height in precipitating layer clouds.

Collectively, all of these postulated feedbacks and interactions raise questions about the links between cloud fraction, liquid water path, cloud droplet effective radius , cloud optical depth and cloud reflectivity.

1.2.4 Summary

Both observational evidence and modelling results point to potentially complex interactions between cloud processes on scales ranging from microscale (size of cloud droplets [μm]) to macroscale (geometrical cloud thickness $\sim 100\ m$, cloud horizontal extent $\sim 100\ km$). These interactions can affect cloud spatial structure and cloud radiative properties, and thus can help to determine the role of clouds in global energy budget and their effect on Earth's climate.

We need to understand the couplings between cloud fraction, liquid water path, cloud droplet effective radius, cloud optical depth and cloud reflectivity, and the spatial distribution of these cloud parameters to resolve the uncertainties surrounding postulated cloud-climate feedbacks, and improve cloud parametrisations in global circulation models.

As I discuss next in section 1.3, the inhomogeneous distribution of liquid water even in fully cloudy layers has a particularly important impact on cloud reflectivity, and is the current focus of significant observational and theoretical work.

1.3 Implications of cloud inhomogeneity for radiative transfer calculations on GCM grid size scale

Satellite and aircraft observations provide evidence of structural complexity and spatial inhomogeneity of cloud fields on scales ranging from a few centimetres (Baker (1992)) to 1000 *km* (Cahalan *et al.* (1982), Davies (1994) for example). This range of scales encompasses those of the GCM gird cell size (approximately 200 $km \times$ 200 *km*). This contrasts with the assumptions made in GCMs, which treat clouds as plane parallel and homogeneous (PPH). Numerous studies (Welch and Wielicki (1984), Davis *et al.* (1990) Barker (1992)) have shown that there is a significant difference between radiative transfer within plane parallel homogeneous clouds and in inhomogeneous clouds with the same mean optical properties. In view of this research the PPH assumption of GCMs is clearly unsatisfactory, even for marine stratocumulus, which of all cloud types best fit the description of plane parallel and homogeneous. For typical marine stratocumulus cloud optical depths ($\sim$ 10) the PPH assumption can generate an albedo bias (difference between the observed and model values of albedo) of 10-30% (Barker (1996), Cahalan *et al.* (1993)) when compared to albedos calculated by models which take into consideration the spatial variability of cloud optical depth .

There are several methods for computing radiative transfer in horizontally inhomogeneous clouds (Stephens (1988), Evans (1993) for example) but these are too computationally demanding to be of use in GCMs. The alternative is to develop methods of accounting for the sub-grid scale variability of GCM pixels. Barker (1996) proposed a parametrisation for computing GCM grid averaged solar fluxes for inhomogeneous boundary layer clouds based on the independent pixel approximation (IPA) (Cahalan *et al.* (1993), Cahalan *et al.* (1994), Chambers *et al.* (1997b)) and an assumed distribution of cloud optical depth in a GCM cell.

Motivated in part by Barker's work, Abdella and McFarlane (1997) proposed

a stochastic cloud scheme for use in GCM based on a statistical approach in the formulation of the sub-grid scale condensation process. In this approach, first used by Sommeria and Deardorff (1977) and Bougeault (1981) in simulations of the trade wind boundary layer, the liquid water content is modelled as a sum of the large scale mean and local fluctuations induced by sub-grid scale condensation. These fluctuations are expressed as a departure of the actual thermodynamic state from the saturation curve of the mean state and are distributed according to a prescribed probability density function. For a given probability distribution function the cloud fraction and the liquid water content are functions of the mean state departure from saturation and the variance of the fluctuations. The cloud fraction and the cloud liquid water path are then used to compute the radiative fluxes in a cloudy boundary layer.

Both the methods of Abdella and McFarlane (1997) and Sommeria and Deardorff (1977) require knowledge of the distribution of cloud liquid water path, and in future versions of the model, could benefit from the knowledge of correlations between cloud liquid water path, cloud optical depth and cloud droplet effective radius on scales below the GCM cell size. Satellite imagery provided by the Advanced Very High Resolution Radiometer (AVHRR), which has a nadir resolution of 1.1 $km \times$ 1.1 km, can provide distributions of cloud optical depth and cloud droplet size within GCM cells for use with these schemes. The measurement and parametrisation of these distributions is the topic of section 4.2 of this thesis.

1.4 Quantifying spatial inhomogeneity in cloud optical depth and cloud droplet effective radius

AVHRR imagery provides information about the spatial distribution (spatial structure) of cloud parameters on scales from 1-1000 km , and thus provides ways of quantifying the inhomogeneity of the fields of cloud parameters within a typical

GCM grid cell.

Given the variety of potentially important links between aerosols, cloud droplet size and cloud liquid water discussed above, new observations of cloud micro and macrophysical characteristics may provide constraints on some of the proposed sensitivities reported in section 1.2.

In this thesis I report the distribution of τ and r_{eff} on the scale of GCM cell. I also use various forms of texture analysis to address the following questions:

- what is the minimum sample size for meaningful spatial averages of cloud parameters?
- what is the scale distribution of variance (the power spectrum) of the τ and r_{eff} fields?

Texture analysis methods can be applied to images of cloud parameters in order to quantify the spatial structure of cloud fields. In a broad sense, texture is defined as a set of statistical measures on the spatial distribution of gray levels in an image. There are a number of statistical approaches to image analysis (see Welch *et al.* (1988)). In this thesis I consider two of them: 1) spectral analysis and 2) fractal (or multifractal) analysis.

Spectral analysis (the decomposition of the total signal variance into contributions from various scales) is the standard procedure for characterising spatial correlation in data sets, but this approach has serious limitations for extracting information which would aid cloud modelling. For example, signal intermittency (the occurrence of sudden bursts of intense variability), characteristic of many geophysical signals such as the spatial distribution of cloud reflectivity, cannot be determined by this type of analysis.

For processes that are scale invariant (at least over some range of scales), spectral analysis can identify scales of stationary and nonstationary regimes. I will use this approach in this thesis to establish the scale invariant regime in fields of

cloud optical depth , cloud droplet effective radius and cloud radiance, and find the minimum averaging scale required to insure statistical stationarity of the inferred statistics.

In random field theory stationarity refers to statistical invariance under translation in time and homogeneity to statistical invariance under translation in space. In cloud analysis and modelling literature it is conventional to use the term "stationary" to denote either space or time invariance while "(in)homogeneity" is reserved to designate (non-)constant ("(non-)trivial") fields.

The issue of nonstationarity is particularly important, yet rarely address directly. Most atmospheric fields are nonstationary, at least over some range of scales. When parametrisations or generalisations are based on statistical inference from observations it is important to establish that the observations come from the stationary regime otherwise the results could be artifacts of the details of the averaging procedure. Therefore, it is important that distributions of τ and r_{eff} which I measure in later chapters of this thesis come from stationary regimes. In the case of cloud liquid water fluctuations Marshak *et al.* (1997) showed that using datasets shorter than 20-40 km to infer statistical properties (means and variances) of clouds yields questionable results since the data are nonstationary on these scales.

The concept of a "scaling fractal" (Mandelbrot (1977)) has proven useful in application to analysis of the structure of inhomogeneous cloud fields (Davis *et al.* (1994), Cahalan and Joseph (1989), Cahalan *et al.* (1993) for example). A scaling fractal is defined as an object or set which is very irregular on all scales, yet at the same time statistically invariant under certain transformations of scale. The fractal dimension determines the scaling properties of the fractal object. The simplest fractals are geometrical objects. The geometrical fractals are self-similar i.e. their magnified subsets look like or are identical to each other and to the whole object (Barnsley *et al.* (1989)). Non-geometrical fractals objects may scale differently in different coordinates. Such objects are called self-affine. The most

general scaling fractals are the multifractals, which exhibit a spectrum of fractal dimensions. Multifractals were introduced by Hentschel and Procaccia (1983) and Parisi and Frisch (1985) and today constitute a general framework for statistical analysis and stochastic modelling of natural phenomena.

In the atmospheric sciences multifractals have been used in several areas. The better known applications involve rainfall analysis and modelling (Gupta and Waymire (1990) and Gupta and Waymire (1993)), analysis of the spatial variability of the earth's radiation field (Tessier *et al.* (1993)), interpretation of satellite imagery (Gabriel *et al.* (1988)), and analysis of cloud liquid water fluctuations from aircraft measurements (Marshak *et al.* (1997)). The energy cascade in fully developed turbulence was successfully described by a multifractal model in Meneveau and Sreenivasan (1987). Fractal properties of cloud fields were explored among others by Cahalan and Joseph (1989), Cahalan *et al.* (1993). Recent theoretical studies of cloud radiation used fractal (Barker and Davies (1992)) and multifractal (Cahalan *et al.* (1994)a,b; Marshak *et al.* (1995a),b) cloud models. Marshak *et al.* (1994) explored multifractal properties, nonstationarity and intermittency of bounded cascade models used in simulation of cloud inhomogeneity.

I will employ spectral analysis and multifractal analysis in my investigation of the spatial structure of cloud optical depth and cloud droplet effective radius in chapter 7.

1.5 Previous satellite and aircraft observations of cloud optical depth and cloud droplet effective radius

The connection between macro and microphysical cloud properties means that to interpret changes in cloud radiative processes one has to monitor many cloud characteristics together. On the global scale satellite imagery provides one means by which such a task might be accomplished. Early satellite observations of cloud properties

concentrated on determination of cloud amount and cloud top temperature. Rossow (1989) and Rossow and Lacis (1990) extended the satellite measurements of cloud properties to retrievals of cloud optical depth. The inference of cloud optical depth from satellite observation relies on the dependence of cloud visible wavelength reflectivity on cloud optical depth. Extensive measurements of global cloud amount, cloud top temperature and cloud optical depth are the mandate of the International Satellite Cloud Climatology Project (ISCCP). The ISCCP analysis of satellite radiances for the inference of the cloud optical depth assumes a constant droplet size for all clouds (cloud droplet effective radius of 10 μm, where the effective radius is a parameter which characterises the distribution of cloud droplets sizes). This assumption leads to uncertainties of 15% - 25% in the retrieved optical depth for water clouds (Rossow *et al.* (1989), Nakajima *et al.* (1991)).

Inclusion of information from the near infrared and infrared spectral bands permits the inference of cloud droplet size from satellite radiance measurements. Arking and Childs (1985), Nakajima and Nakajima (1995), and Platnick and Valero (1995) utilised the visible and near infrared band radiances for simultaneous retrieval of cloud optical depth and cloud droplet effective radius from the AVHRR flown on board of a series of NOAA polar orbiting satellites. Similar techniques were employed in the retrieval of cloud droplet size and cloud optical depth form airborne remote sensing platforms (Nakajima and King (1990), Rawlins and Foot (1990), Nakajima *et al.* (1991)). Han *et al.* (1994) used the AVHRR near-infrared channel measurements to produce global retrievals of cloud droplet effective radius for the ISCCP data and revise the ISCCP retrievals of cloud optical depth. The possibility of utilising other wavelengths in cloud droplet size retrievals was explored by Lin and Coakley (1993) who used two AVHRR thermal channels to retrieve the droplet size for semi-transparent clouds. The advantage of this technique is its applicability to nighttime observations, however its accuracy is not as good as that of the methods employing the visible and near infrared channels.

To date, the AVHRR and Landsat Thematic Mapper are the only satellite instruments whose measurements allow for a simultaneous retrieval of cloud optical depth and cloud droplet effective radius. In field experiments, the First ISCCP Regional Experiment (FIRE) and the Atlantic Stratus Transition Experiment (ASTEX) aircraft observations during satellite overpasses were used to validate the AVHRR estimates of cloud optical depth and cloud droplet effective radius by comparison with the in situ aircraft measurements. These studies (Nakajima and Nakajima (1995), FIRE and ASTEX; Platnick and Valero (1995) ASTEX) found that the remotely and in situ measured cloud optical depth agreed within 3 for most part in clouds with mean optical depths between 10 and 40, although Nakajima and Nakajima (1995) reported some large excursions of ~ 10. They attribute these large differences to the satellite measurements encompassing a large field of view ($\sim 1 \times 1\ km$) compared to the in situ measurements. Remote sensing consistently retrieves larger droplet sizes than measured in situ by about 2 μm for effective radii around 10 μm (Nakajima and Nakajima (1995), Platnick and Valero (1995)). The cause of this overestimation has not been determined. However, very good spatial correlations between in situ and remotely measured τ and r_{eff} were reported in Nakajima and Nakajima (1995).

1.6 Thesis outline

In this thesis I present satellite derived observations of cloud optical depth (τ) and cloud droplet effective radius (r_{eff}) and interpret them using a simple cloud model in which the relationship between τ and r_{eff} is parametrised in terms of cloud droplet number concentration. Furthermore, I quantify the spatial variability of cloud optical depth, cloud droplet effective radius and cloud visible wavelength radiance fields within the formalism of multifractal analysis.

The thesis will address the following questions:

- Are the retrievals of cloud optical depth and cloud droplet effective radius valid? (i.e. do they agree with in situ aircraft measurements considered in chapter 5.)

- Can the observed variability in τ and r_{eff} be stratified in terms of other cloud parameters? (cloud droplet number concentration, cloud liquid water path, geographical location.) To assist in this stratification, and in the in situ validation I will introduce a simple "reference cloud model" in chapter 3, and present data sets that conform to and depart from this reference model in chapters 3 and 4.

- Is there a characteristic spatial structure in fields of τ and r_{eff}? Does it depend on factors such as cloud droplet number concentration or cloud thickness?

Chapter 2 contains a description of the cloud optical depth and effective radius retrieval technique developed of Nakajima and Nakajima (1995) which was use in this study.

Chapter 3 introduces the "reference cloud model" which leads to a power law relationship between τ and r_{eff} parameterised by cloud droplet number concentration and gives examples of cloud scenes which are representative of the simple model and examples of scenes which mark a departure form the simple behaviour.

In **Chapter 4** the relationship between cloud optical depth and cloud droplet effective radius is explored with statistical methods. Bivariate linear regression with errors in both variables is used to fit a power law to the τ and r_{eff} data for 325 cloud scenes of approximate areas of 256 km $\times$ 256 km. On this spatial scale, I find that the reference cloud model provides an accurate description of τ and r_{eff} correlations for over 55% of examined cloud scenes. I also show how a measure of cloud droplet number concentration concentration can be derive from satellite retrievals with help of the reference cloud model.

Further in **Chapter 4** I present mesoscale frequency distribution of cloud

optical depth and cloud droplet effective radius and parametrise these distributions in terms of a gamma function (Barker (1996)). I discuss the relationship between mean mesoscale τ and r_{eff}.

In **Chapter 5** I analyse satellite and aircraft observations acquired during the Southern Ocean Cloud Experiment (SOCEX). The aircraft observation provide a validation of the remote sensing retrievals of cloud optical depth and cloud droplet effective radius and confirm the relationship between τ and r_{eff} observed in the satellite data as consistent with the reference cloud model.

Chapter 6 introduces the formalism of multifractal analysis, and the concepts of nonstationarity and intermittency in geophysical data following Davis *et al.* (1994) and Marshak *et al.* (1997). **Chapter 7** presents the results of spectral and multifractal analysis of 34 AVHRR fields of cloud visible wavelength radiance, cloud optical depth and cloud droplet effective radius. The scenes come from four different data sets: 1) the FIRE 1987 data set, 2) Pacific Ocean 1994 data set, 3) Pacific Ocean 1995 data set, and 4) SOCEX 1995 data set. Also included in Chapter 7 is a practical guide to this spectral and multifractal analysis.

Chapter 8 summarise the results, discusses the implication of the thesis findings to remote sensing and the climate modelling and outlines the possibilities for future research.

Chapter 2

Retrieval of cloud parameters from AVHRR radiance measurements

The retrievals of cloud optical depth and cloud droplet effective radius in this study were obtained with the technique developed by Nakajima and Nakajima (1995). This chapter describes radiative transfer basis and some details of this technique.

Section 2.1 presents the principal idea behind the simultaneous retrieval of cloud optical depth and cloud droplet effective radius from satellite radiance measurements. Sections 2.2 and 2.3 describe the details of Nakajima and Nakajima (1995) forward model and retrieval algorithm respectively. In section 2.4 I discuss sources of errors and estimates of uncertainty in retrievals of cloud optical depth and cloud droplet effective radius from satellite measurements.

2.1 Basic concept

The retrieval technique of Nakajima and Nakajima (1995) relies on the reflectance of solar radiation by cloud droplets. Techniques based on solar reflectance use visible wavelengths which are scattered by water droplets without absorption and near-infrared wavelengths absorbed by cloud droplets for the simultaneous retrieval of cloud optical depth and cloud droplet effective radius . The visible range cloud reflectance is sensitive primarily to cloud optical depth , while the near-infrared re-

flected radiance depends mostly on cloud droplet effective radius . This wavelength dependent sensitivity is due to the different absorption of visible and infrared wavelength by water droplets.

Cloud droplets absorb strongly in infrared. As a result infrared radiation which emerges back from the cloud and reaches the satellite sensor consist mostly of photons which underwent just a few scattering events near the cloud top. These photons having scattered only a few times carry the 'memory' of the size of the droplet they interacted with. The visible wavelength radiation propagates through a cloud practically without absorption. It can penetrate deep into the cloud before it is reflected back to space in a sequence of scattering events. In the process of multiple scattering the photons lose the information about the size of cloud droplets ,but being able to sample deep into the cloud they gather information of the column extinction (cloud optical depth).

The AVHRR makes measurements in 5 channels. Table 2.1 list the spectral band width of the AVHRR channels for the instrument on board on the NOAA9 satellite (NOAA Polar Orbiter Data User's Guide
http://www2.ncdc.noaa.gov/POD/podug/index.htm).

channel	band width $[\mu m]$
1	0.58-0.68
2	0.725-1.10
3	3.55-3.93
4	10.3-11.3
5	11.5-12.5

Table 2.1: Wavelength bands of the 5 channels of the AVHRR on board of NOAA 9.

For my application the visible and near-infrared wavelength ranges correspond to AVHRR channel 1 (visible) and 3 (near-infrared) respectively.

At a given sun-satellite geometry, a layer cloud of cloud optical depth τ and cloud droplet effective radius r_{eff} reflects a specific amount of solar radiation in AVHRR channel 1 and 3. The sun-satellite geometry can be expressed in terms of solar zenith angle θ_0, the satellite zenith angle θ and the relative sun-satellite azimuth ϕ which are all shown in Figure 2.1. Figure 2.2 defines the satellite viewing angle θ_s.

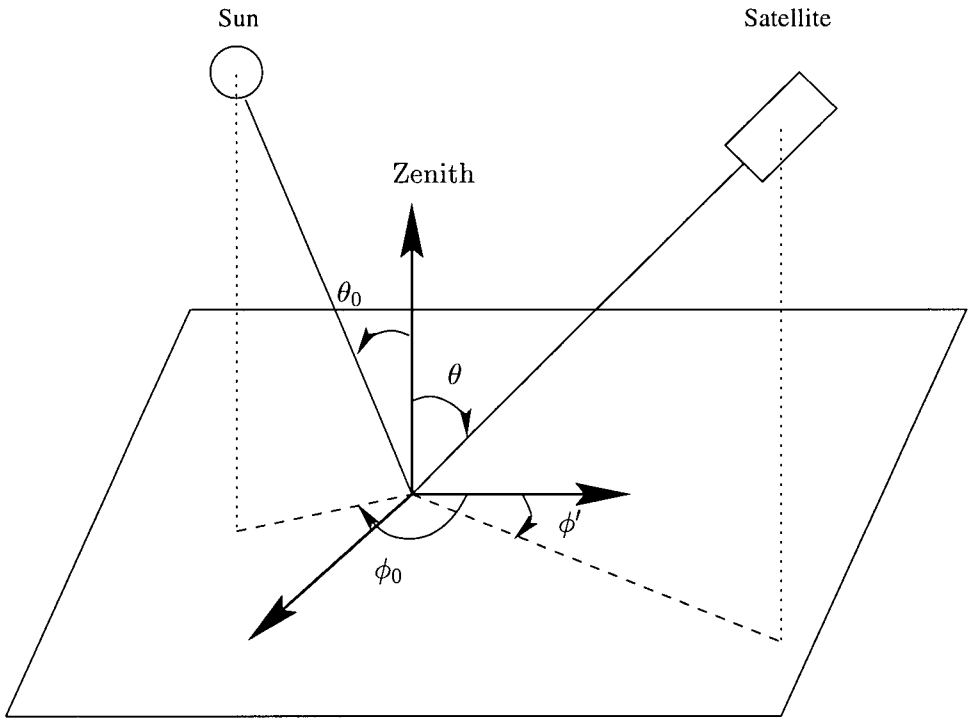

Figure 2.1: Angles defining the sun-satellite geometry: θ_0 sun zenith angle, ϕ_0 sun azimuth angle, θ satellite zenith angle, ϕ' satellite azimuth angle, relative sun-satellite azimuth $\phi = \phi_0 - \phi'$.

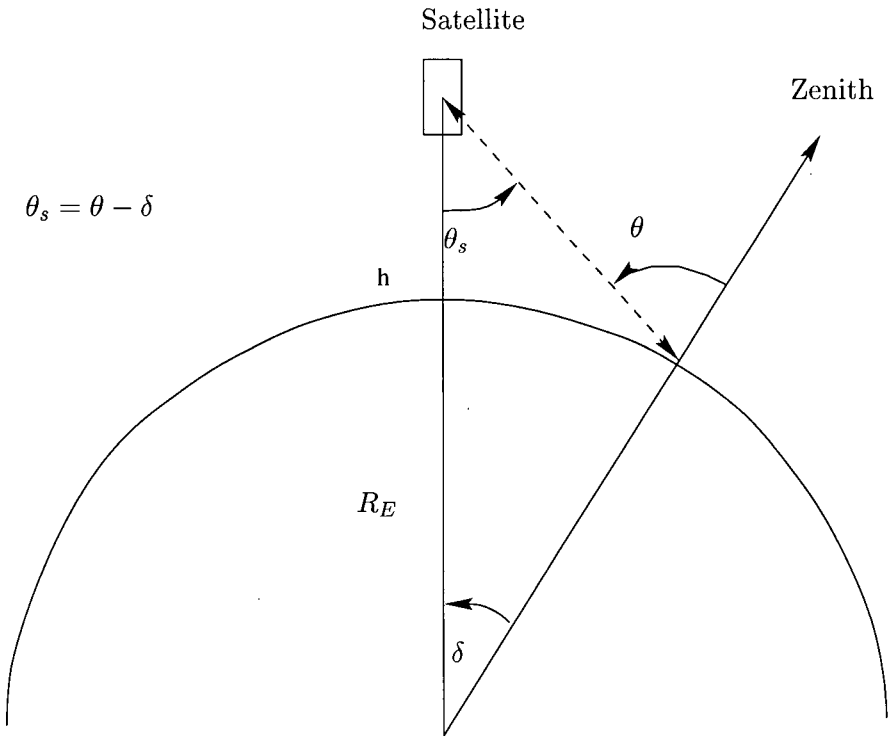

Figure 2.2: Angles defining the satellite geometry: θ satellite zenith angle, θ_s satellite viewing angle, R_E radius of the Earth, h height of the satellite above the ground.

Figure 2.3 shows a plot of modelled solar radiance reflected by cloud in AVHRR channel 3 against the radiance reflected in AVHRR channel 1 computed by the code of Nakajima and Nakajima (1995) (see section 2.2) for a particular sun-satellite geometry (expressed in terms of the solar zenith angle (θ_0=60°), satellite zenith angle (θ=40°) and the relative sun-satellite azimuth angle (ϕ=50°). The radiances were computed for a range of values of cloud optical depth (τ) and cloud droplet effective radius (r_{eff}). Solid lines are lines of constant cloud optical depth and dash lines represent constant cloud droplet effective radius .

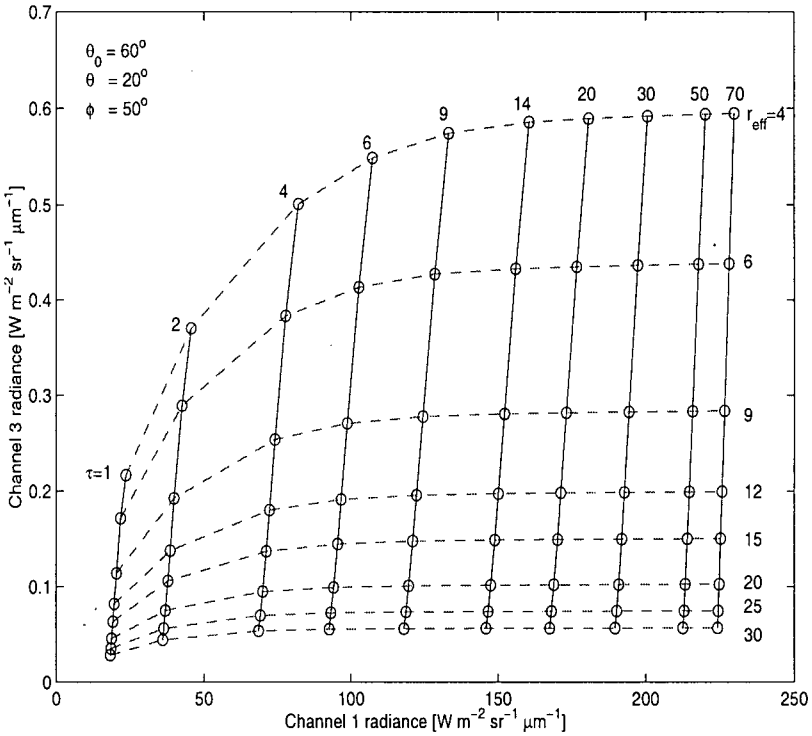

Figure 2.3: Model cloud reflected solar radiance in AVHRR channel 1 and 3 as a function of cloud optical depth and cloud droplet effective radius calculated with the code of Nakajima and Nakajima (1995) . Solid and dashed lines represent radiances at constant τ and constant r_{eff} respectively. Sun-satellite geometry is fixed at θ_0=60°, θ=40° and ϕ=50°.

Figures similar to figure 2.3 can be computed for all interesting sun-satellite geometries. Figure 2.3 illustrates the idea behind the simultaneous retrieval of cloud optical depth and cloud droplet effective radius from the visible and near-infrared radiance measurements. If the cloud reflected radiances in channels 1 and 3 are known along with the sun-satellite geometry, one can look-up the figure with the specified geometry, enter the values of channel 1 and 3 radiances and from the τ-r_{eff} grid read off the corresponding values of cloud optical depth and cloud droplet effective radius . This approach to the retrieval of τ and r_{eff} dictates a two step

procedure. First, the reflected radiances in channel 1 and 3 have to be simulated for a range of cloud optical depth and cloud droplet effective radii for all sun-satellite geometries in the problem. This step is often referred to as forward modelling. Results of the simulation are stored in tables which are used in the second phase, the actual retrieval, to look-up values of τ and r_{eff} corresponding to measure values of channel 1 and channel 3 reflected radiances at given sun-satellite geometry.

The process of the retrieval of cloud optical depth and cloud droplet effective radius from satellite measured radiances is complicated by the presence of a radiatively active atmosphere and the Earth's surface. As a result, the radiance measured by satellite is a combination of the radiance reflected from clouds (which are a function of τ and r_{eff}), radiances contributed by the surface and atmosphere below and above the cloud, and by the cloud's own emission in the near-infrared channel. The cloud reflected radiance must be decoupled from the other radiation components before one can make use of the look-up tables to retrieve the values of cloud optical depth and cloud droplet effective radius . A large percentage of the channel 3 radiance is contributed by the thermal emission from the Earth's surface and from the cloud tops (20 - 90% depending on cloud thickness).

Nakajima and Nakajima (1995) estimate the thermal emission in AVHRR channel 3 by making use of the measurements in one of the AVHRR thermal channels (channel 4). Effectively, measurements from three AVHRR channels are required to retrieve of cloud optical depth and cloud droplet effective radius with this technique.

In the following sections I describe the forward model used in Nakajima and Nakajima (1995) (2.2) and the flow of the second phase of the retrieval (2.3).

2.2 The forward model

The forward model is built on a 4 layer plane parallel atmosphere with interfaces at $z-\Delta z$, z , and 12 km and the top at 120 km, where z is the top of the cloud layer and Δz is the geometrical thickness of the cloud (see table 2.2 page29 for the grid values

of z and Δz other model parameters). A homogeneous cloud layer is assumed that consists of Mie scattering water droplets whose sizes follow a lognormal distribution

$$n(r)dr = \frac{N}{\sqrt{2\pi}\sigma r} exp[-\frac{(lnr - lnr_0)^2}{2\sigma^2}]dr \tag{2.1}$$

where r is the droplet radius, $n(r)dr$ is the number of droplets with radii between $[r, r+dr]$ per unit volume, N is the total number of droplets per unit volume, r_0 is the mode radius which is related to the effective radius by $r_{eff} = r_0 e^{3.5\sigma^2}$, and σ is the log standard deviation of the droplet size distribution. For the marine stratocumulus the model assumes σ=0.35. The effect of assuming vertical homogeneity in the cloud droplet distribution is discussed in section 2.4.

The underlying surface is assumed to be a Lambertian reflector. After Nakajima and Nakajima (1995) I assume a ground albedo A_g of 0.05 for the ocean surface. The LOWTRAN-7 midlatitude summer atmosphere (MLS) (Kneizys *et al.* (1988)) is assumed in our version of the model as representative of the climatic regions considered in this study. The profiles of atmospheric gases which include 7 principal gases and 21 trace gases come from LOWTRAN-7 atmospheric absorption and transmission package (Kneizys *et al.* (1988)).

The radiative transfer theory for plane parallel layers with an underlying Lambertian surface leads to the following equations for the the satellite received radiance in the visible (AVHRR channel 1) and near-infrared (AVHRR channel 3) spectral range

1. visible wavelengths

$$L_{obs}(\tau, r_{eff}; \mu, \mu_0, \phi) = L(\tau, r_{eff}; \mu, \mu_0, \phi)$$
$$+t(\tau, r_{eff}; \mu)\frac{A_g}{1 - r_s(\tau, r_{eff})A_g} t(\tau, r_{eff}; \mu_0)\frac{\mu_0 F_0}{\pi} \tag{2.2}$$

2. near infrared wavelengths

$$
\begin{aligned}
L_{obs}(\tau, r_{eff}; \mu, \mu_0, \phi) &= L(\tau, r_{eff}; \mu, \mu_0, \phi) \\
&+ t(\tau_u, \mu)[1 - t(\tau_c, r_{eff}; \mu) - r(\tau_c, r_{eff}; \mu)]B(T_c) \\
&+ t(\tau, r_{eff}; \mu)\frac{1 - A_g}{1 - r_s(\tau, r_{eff})A_g}B(T_g) \\
&+ t(\tau, r_{eff}; \mu)\frac{A_g}{1 - r_s(\tau, r_{eff})A_g}t(\tau, r_{eff}; \mu_0)\frac{\mu_0 F_0}{\pi}
\end{aligned} \tag{2.3}
$$

where $L(\tau, r_{eff}; \mu, \mu_0, \phi)$ is the cloud reflected radiance, $L_{obs}(\tau, r_{eff}; \mu, \mu_0, \phi)$ is the satellite received radiance, μ and μ_0 are cosines of the satellite zenith angle θ, and the solar zenith angle θ_0 respectively, F_0 is extraterrestrial solar flux, and A_g is the ground albedo. τ, τ_c, and τ_u are the total optical depth of the atmosphere, cloud optical depth and optical depth of the atmosphere above the cloud. $B(T)$ is the Planck function, T_g is the ground temperature and T_c is the cloud top temperature. The variables t, r and r_s are respectively the transmissivity, plane albedo and spherical albedo of the cloud layer defined as

$$
t(\tau, r_{eff}; \mu_0) = \frac{1}{\pi}\int_0^{2\pi}\int_0^1 T(\tau, r_{eff}; \mu, \mu_0, \phi)\mu d\mu d\phi + exp(-\frac{\tau}{\mu_0}) \tag{2.4}
$$

$$
r(\tau_c, r_{eff}; \mu) = \frac{1}{\pi}\int_0^{2\pi}\int_0^1 R(\tau, r_{eff}; \mu', \mu, \phi)\mu' d\mu' d\phi \tag{2.5}
$$

and

$$
r_s(\tau_c, r_{eff}) = 2\int_0^1 r(\tau, r_{eff}; \mu)\mu d\mu \tag{2.6}
$$

where $T(\tau, r_{eff}; \mu, \mu_0, \phi)$ and $R(\tau, r_{eff}; \mu', \mu, \phi)$ are bidirectional transmission and reflection functions

$$
T(\tau, r_{eff}; \mu, \mu_0, \phi) = L(\tau, r_{eff}; -\mu, \mu_0, \phi)/F_0 \tag{2.7}
$$

$$R(\tau, r_{eff}; \mu', \mu, \phi) = L(\tau, r_{eff}; \mu', \mu, \phi)/F_0. \tag{2.8}$$

In (2.2) the second term on the RHS and in (2.3) and in the fourth term on the RHS represent the ground-reflected radiance in channels 1 and 3 respectively. The second term on the RHS of equation (2.3) is the ground emitted thermal radiation and the third term the cloud top emitted thermal radiation.

To decouple the cloud refected radiance L and the satellite observed radiance L_{obs} in (2.2) and (2.3) the transmissivities t and albedos r and r_s in AVHRR channels 1, 3 and 4 are needed. These terms are computed in the forward part of the retrieval. The forward model calculates the cloud top reflected radiance components of the AVHRR signal in channel 1 and 3 $L(\tau, r_{eff}; \mu, \mu_0, \phi)$, and transmissivities $t(\tau, r_{eff}; \mu)$, plane albedos $r(\tau_c, r_{eff})$ and spherical albedo $r_s(\tau_c, r_{eff})$ of the cloudy model atmosphere in AVHRR channels 1, 3 and 4 using the radiative scheme of Nakajima and Tanaka (1988) based on the discrete ordinate method and extended by Nakajima and King (1992) to include thermal radiative transfer as proposed by Stamnes *et al.* (1988). The computation of atmospheric absorption and transmissivity uses the k-band method with the k distribution of absorption coefficients taken from LOWTRAN-7. The computation accounts for 41 line absorption bands and 12 continuum bands.

The radiative transfer computations are carried out for 10 sub-bands in each AVHRR channel then averaged with the channel response function according to

$$y_n = \frac{\sum_{i=1}^{N} \varphi_n(i) y_n(i)}{\sum_{i=1}^{N} \varphi_n(i)} \tag{2.9}$$

where $y_n(i)$ stands for one of the radiative transfer output fields for channel n at subchannel wavelength i and φ_n is the channel n response at wavelength i.

The forward model produces four look-up tables: I) AVHRR channel 1 cloud reflected radiance; II) AVHRR channel 3 cloud reflected radiance; III) transmissivities and reflectivities in channels 1 and 3; and IV) transmissivity in channel 4. The

look-up tables have up to 7 dimensions: the cloud top height z, cloud geometrical thickness Δz, angles determining sun-satellite geometry θ_0, θ and ϕ, cloud optical depth τ, and cloud droplet effective radius r_{eff}. Table 2.2 shows the grid system of the look-up tables.

quantity	gridpoints
$z(km)$	1.0, 1.5, 2.0, 2.5, 3.0, 3.5, 4.0
$\Delta z(km)$	0.1, 0.2, 0.5, 1.0, 2.0
$\theta_0(°)$	0, 5, 10, 20, 30, 35, 40, 45, 50, 55, 60, 65, 70
$\theta(°)$	0, 5, 10, 20, 30, 35, 40, 45, 50, 55, 60
$\phi(°)$	0 - 180 (every 10°)
τ	1, 2, 4, 6, 8, 10, 12, 14, 16, 18, 20, 22, 24, 26, 28, 30, 32, 34, 50, 70
$r_{eff}(\mu m)$	4, 6, 8, 10, 12, 14, 16, 18, 20, 22, 24, 30

Table 2.2: The grid system of the look-up tables.

2.3 The retrieval

The retrieval routine employs (2.2) and (2.3), and the look-up tables from the forward model to isolate the cloud reflected radiance in AVHRR channel 1 and 3 from other radiance contributions then looks up in the tables values of τ and r_{eff} which correspond to the recovered values of channel 1 and 3 cloud reflected radiance.

The ground (T_g) and cloud top (T_c) emitting temperature needed to solve equations (2.2) and (2.3) are obtained from the brightness temperature of clear and cloudy pixels measured in channel 4 of the AVHRR through the following relations

1. ground temperature

$$T_g = B^{-1}(\frac{L_{obs,clear}}{1 - A_g}) \tag{2.10}$$

2. cloud top temperature

$$T_c = B^{-1}\left(\frac{L_{obs,cloudy} - t_c(1 - A_g)B(T_g)}{1 - t_c}\right) \tag{2.11}$$

where t_c is the transmissivity of the cloud layer in channel 4 and B^{-1} represents the inverse of the Planck function at channel 4 wavelength. The retrieval process is an iteration on τ and r_{eff}. Figure 2.4 shows the flow chart of this iteration.

The iteration process starts with an initial guess for $\tau_c = 35$, $r_{eff} = 10\ \mu m$ and $z = 2\ km$. The cloud geometrical thickness Δz is calculated from the relation

$$\Delta z = \frac{lwp}{lwc} \tag{2.12}$$

where *lwc* is the cloud liquid water content, and *lwp* cloud liquid water path calculated as

$$lwp = \frac{3\tau_c r_{eff}}{2\rho} \tag{2.13}$$

For stratocumulus, $lwc = 1.28\ gm^{-3}$ is assumed following the cloud classification proposed by Liou (1976). With the known values of τ_c, r_{eff}, z and Δz the transmissivity of the cloud layer in channel 4 t_c, is retrieved from table IV and used in (2.11) which is also supplied with channel 4 pixel radiance $L_{obs,4}$ and the pixel ground temperature T_g. T_g is obtained from (2.10) and channel 4 radiance of clear pixels $L_{obs,4}^{clear}$. Equation (2.11) returns the cloud top temperature T_c. The value of z (cloud top height) is updated based on the relation

$$z = \frac{T_g - T_c}{\gamma} \tag{2.14}$$

where γ is the lapse rate, assumed constant at 6.5 Kkm^{-1}. Knowing τ_c, r_{eff}, z and Δz, and the geometry θ_0, θ and ϕ, I find the values of the cloud reflected radiances in channel 1 and 3 from Tables I and II respectively. In Table III I find

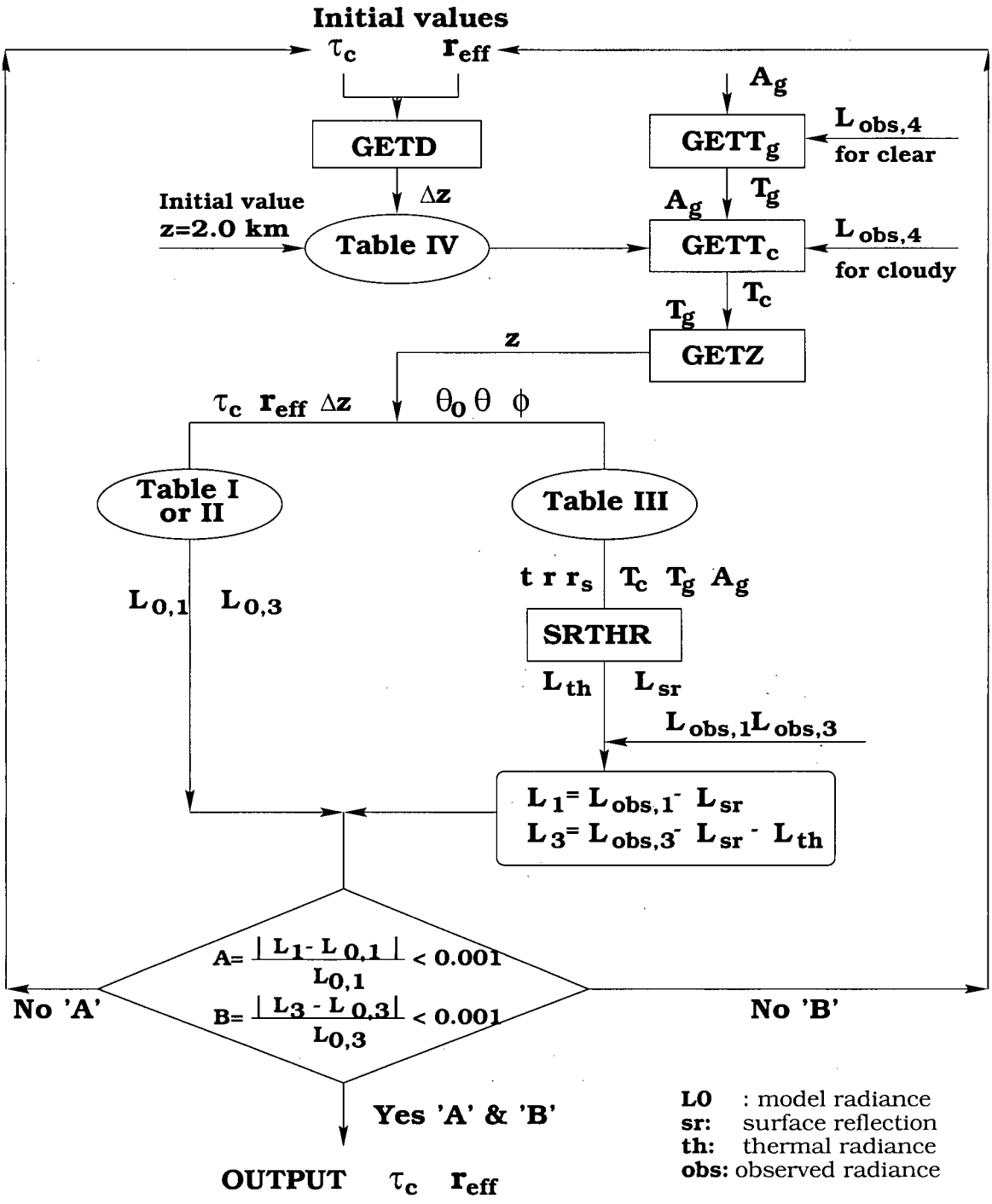

Figure 2.4: Flow chart of the iteration in the retrieval process.

the transmissivity $t(\tau, r_{eff}; \mu)$, plane albedo $r(\tau_c, r_{eff})$, and the spherical albedo $r_s(\tau_c, r_{eff})$ and with, T_c, T_g and A_g, compute the surface reflected radiance L_{sr} in channels 1 and 3 (terms 2 and 4 in equations (2.2) and (2.3) respectively), and the ground and cloud top thermal emission in channel 3, L_{th} (terms 2 and 3 in (2.3)).

The next step is to remove the undesirable radiance components (L_{sr} and L_{th}) from the satellite observed radiances in channels 1 and 3 ($L_{obs,1}$ and $L_{obs,3}$) in order to recover the measured cloud reflected radiance L_1 and L_3. Channel 1 model and measured values of cloud-top reflected radiance are compared. The value of τ_c is varied until the difference between model and measured values is less than 0.1%. That value of τ_c is fixed and r_{eff} is varied till the difference between channel 3 measured and model values is less than 0.1%. The iteration proceeds interchangeably in both variables until channel 1 and channel 3 differences are both less than 0.1% or a maximum number of 10 iterative loops is reached. Typically convergence is achieved after about 4 iteration loops. When the routine does not converge τ_c and r_{eff} are assigned default values of 1 and 4 μm which mark bad retrievals. The lack of convergence occurs typically for optically thin clouds when the removed radiation significantly dominates over the signal.

2.4 Theoretical estimates of errors

2.4.1 Errors due to approximations in the retrieval method

Nakajima and Nakajima (1995) estimate that the largest error of this retrieval technique arises from neglecting the thermal radiation of the atmosphere. Compared to this error, the error introduced by averaging over the channel response function is small. Nakajima and Nakajima (1995) find that the approximations of equation (2.2) and (2.3) introduce an error of 1% or less to the retrieved cloud optical depth. Error introduced by the approximations of the radiative transfer equations (2.2 and (2.3) to the retrieved cloud droplet effective radius can be large if τ_c is small and

r_{eff} is small, especially at low solar angles and high ground reflectivity (error can reach up to 60%). This error decreases quickly with increasing optical depth and decreasing cloud droplet effective radius and for typical clouds ($\tau_c > 5$, $r_{eff} \sim 10$ μm) in most realistic conditions ($\theta_0 < 50$ °, $A_g < 0.3$), the error is usually less than 10%.

2.4.2 Errors due to model assumptions

Model assumptions refer to: 1) the cloud layer, and 2) the atmosphere in which the cloud layer is embedded (profiles of the atmospheric gases specifically).

1) Cloud Model. Nakajima and King (1990) considered the effect of vertical inhomogeneity in cloud droplet effective radius and cloud liquid water path on the retrieval of τ and r_{eff} with measurements in 0.75 μm, 2.16 μm and 3.70 μm channels. They found that approximating "real clouds" (vertical profiles of lwc and r_{eff} observation based) by clouds that are vertically homogeneous leads to overestimation of the retrieved τ by no more than 3% for effective radii at the cloud top greater than about 6 μ. At 3.70 μm the retrieved cloud droplet effective radius was found to be within 90% of the r_{eff} at the top of the inhomogeneous cloud for $\tau \geq 5$.

2) Atmospheric Model. Pincus *et al.* (1995) estimated uncertainty in cloud optical depth retrievals due to 15% perturbations in the atmospheric profiles of ozone amount and aerosol optical depth at less than 5% for most solar zenith angles and cloud optical depths. Rossow *et al.* (1989) also reported less than 5% error in cloud optical depth estimates due to atmospheric effects.

The atmospheric model neglects absorption by in cloud water vapour. This was once thought to be responsible for the systematic overestimate (approximately 2 μm) of remotely measured cloud droplet effective radius with respect to in situ values. However, Platnick and Valero (1995) showed that the bias in cloud droplet effective radius due to in cloud water vapour absorption is only $\sim +3\%$ for a typical

cloud ($\tau > 6$, $r_{eff} \sim 10$). On the other hand, uncertainties in size distribution can amount to an error of ($\sim \pm$ 10%).

2.4.3 Errors due to measurement uncertainty

The errors reported above are due to the approximation of the retrieval method only. Retrieval errors arising from uncertainty of measurements are a separate issue. Nakajima and King (1990) assumed 5% error in the measured visible (0.75 μm) and near infrared (2.16 μm) radiance and estimated retrieval errors in τ and r_{eff}. They found the error in cloud optical depth increasing with τ from about 6% for small τ to about 30% for $\tau \sim 30$ and error in cloud droplet effective radius about 30% for small radii ($\sim 6\mu m$) and decreasing to about 7% for $r_{eff} \sim 30$ and large optical depths.

Han *et al.* (1994) tested the sensitivity of the retrieved cloud droplet effective radius to the uncertainty in the thermal emission contribution to channel 3 radiance and found that for clouds with $r_{eff} < 20$ μm a 10% variation (which roughly corresponds to 4 K uncertainty in the channel 4 brightness temperature) leads to changes in the retrieved value of $r_{eff} < 0.7$ μm. They also find that a 5% variation in surface reflectance alters the retrieved values of r_{eff} by less than 0.3 μm for $\tau \sim 1$. This effect becomes completely negligible for $\tau > 3$.

Pincus *et al.* (1995) investigated the uncertainties of the cloud optical depth retrievals due to instrument calibration and discretization error and uncertainties of the atmospheric profiles used in the forward modelling stage of the retrieval. They found the uncertainty of τ to be dominated by the uncertainties in the calibration of the radiometers for both AVHRR and the Vertical Atmospheric Sounder (VAS) of the GOES satellites. Their estimate of the uncertainty in τ due to calibration error is about 10% for $\tau < 10$ and small solar angles. This uncertainty increases with both τ and the solar angle to reach about 30% for $\tau \sim 30$ and solar angle of $\sim 60°$.

Platnick and Valero (1995) modelled errors in the retrieved values of τ and r_{eff} assuming uncertainties in AVHRR channel 1 surface albedo, and channel 1 and channel 3 reflected radiance. The uncertainty in surface albedo introduces large error in the retrieved value of τ for thin clouds. This error decreases rapidly as τ increases above 3. Error in cloud optical depth due the uncertainty in channel 1 reflected radiance also decreases sharply as τ goes from 1 to 3 but increases steadily with τ with after that. Errors in cloud droplet effective radius are large for small r_{eff} and decrease with increasing r_{eff} until it reaches about 8 μm. For cloud droplet effective radius greater than about 8 μm the retrieval error becomes independent of r_{eff}.

2.4.4 Errors introduced by the independent pixel approximation

Another type of error is introduced by the assumption of the independent pixel approximation (IPA). The independent pixel approximation introduces a bias in retrievals of τ. This bias is due to the neglect of the horizontal radiative transfer between neighbouring pixels. Chambers *et al.* (1997a) estimate that this bias for the retrieval of τ can range between 6-45% depending on geometry and cloud fraction. The effect of the IPA on the retrieval of r_{eff} has not yet been investigated.

In case of the AVHRR stratocumulus field the IPA is considered well justified on the ground that the AVHRR pixel size (1.1 $\times$ 1.1 km) is greater than the photon mean free path in a stratocumulus cloud, thus horizontal transfer between AVHRR pixels is small. In fact, Marshak *et al.* (1995a) and Marshak *et al.* (1995b) demonstrated that the IPA performs well for pixels sizes greater than 100 m but recommend using only channels with strong absorption for pixel sizes less than 100 m. Cahalan *et al.* (1994) showed that tha IPA are accurate to within 1% when power spectra of τ behave like k^{-s}, where k is frequency and $s \geq$ approximately 1.5 . This is indeed the case for the marine stratocumulus (Barker and Davies (1992), Barker (1996), this thesis chapter 7).

Summarising, for most realistic clouds I can anticipate retrieval errors in the range of 10 - 30% for the cloud optical depth and cloud droplet effective radius inferred form AVHRR radiance measurements.

Validation of the satellite retrievals by in situ measurements will be discussed in chapter 5.

Chapter 3

The relationship between cloud optical depth and cloud droplet effective radius

I begin this chapter with a presentation of a conceptual model of a layer cloud with a particularly simple relationship between cloud optical depth and cloud droplet effective radius (section 3.1). In section 3.2 I review previous simultaneous measurements of cloud droplet effective radius and cloud optical depth or cloud liquid water path (*lwp*). In section 3.3 I present observations of τ and r_{eff} for which the relationship between the two parameters corresponds to the one derived from the simple model. Departures from the model are discussed in section 3.3.2. A more detailed treatment of the statistical relationship between τ and r_{eff} follows in chapter 4.

In this thesis I am primarily concern with variability of τ and r_{eff} on spatial scales of 256 $km \times$ 256 km. I delay the justification of focusing of these scales to the summary of this chapter (section 3.3.5) as it will refer to the results presented here. The analysis will be restricted to fully cloudy pixels only. The identification of fully cloudy pixels was based on the spatial coherence analysis Coakley and Bretherton (1982) and is described in more detail in section 3.3.

3.1 A simple model of boundary layer cloud

I sketch a diagram of an idealised layer cloud in Figure 3.1 on page 38. This simple model assumes that the cloud liquid water content increases linearly with height, as indicated by the heavy dashed lines in Figure 3.1, either adiabatically or at some fraction of the adiabatic. All droplets are activated (begin growth) at cloud base, and entrainment and precipitation act to reduce the cloud droplet number concentration uniformly throughout the depth of the layer.

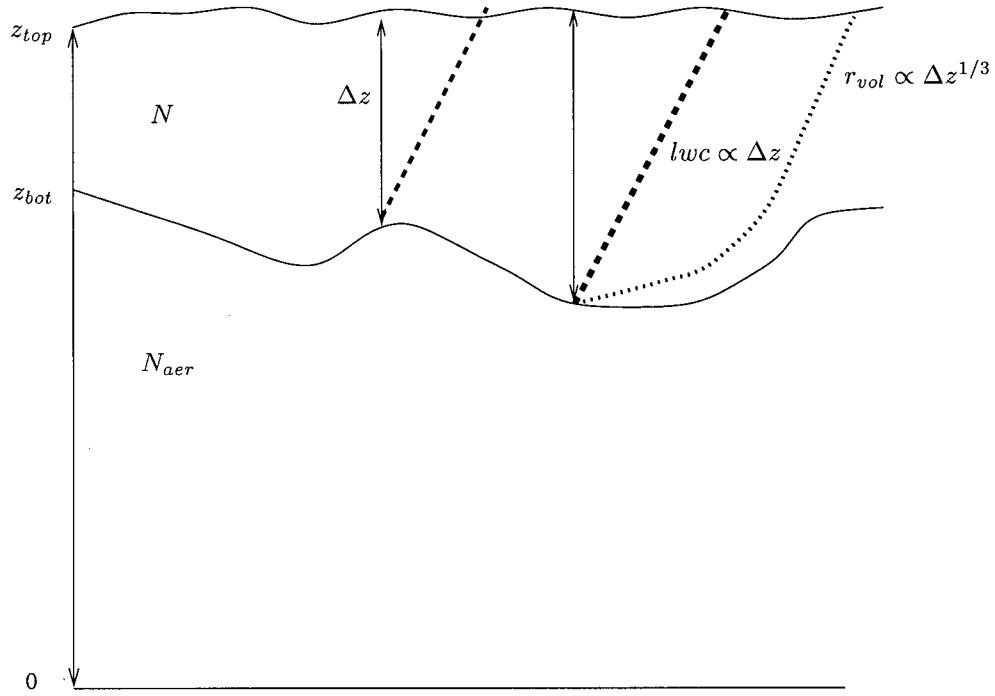

Figure 3.1: Sketch of a cloud layer: z_{top} cloud top height, z_{bot} cloud base height, Δz cloud geometrical thickness, r_{vol} cloud droplet volume radius, N cloud droplet number concentration , N_{aer} sub-cloud aerosol concetration which detrmines N. Heavy dashed lines show lwc profile with identical slope $\beta = dlwc/dz$. Light dashed line is the profile of cloud droplet radius.

Under these conditions the size of cloud droplets increases with height within

the cloud as

$$r_{eff} \propto r_{vol} \propto z^{1/3} \tag{3.1}$$

where r_{vol} the cloud droplet volume radius is proportional to r_{eff} (see Appendix A for a detailed discussion). In Figure 3.1 the light dashed line represents the vertical profile of cloud droplet radius given by (3.1).

Aircraft observations (Paluch and Lenschow (1991), Austin *et al.* (1995)) show that in FIRE and ASTEX, cloud variability in geometrical thickness on horizontal scales of 10-100 km is due primarily to variations in cloud base as depicted in figure 3.1. Horizontal variations in cloud thickness will produce fluctuations in τ, lwp and r_{eff} at cloud top that can be observed by either aircraft or satellite sensors. In Appendix A, I show that, for the simple model described above, r_{eff} is given by

$$r_{eff} = a_0 \beta^{\frac{1}{5}} N^{-\frac{2}{5}} \tau^{\frac{1}{5}} \tag{3.2}$$

Alternatively, τ can be written as a function of lwp ($\propto \Delta z^2$) (defined in (1.3))

$$\tau = a_1 lwp \; r_{eff}^{-1}. \tag{3.3}$$

In the simplest case, with only Δz varying while both β and N are held constant, we expect to see $r_{eff} \propto \tau^{1/5}$ in scatter plots of r_{eff} vs. τ.

Figure 3.2 shows the model relationship for τ and r_{eff} for two values of cloud subadiabaticity $\beta = 0.5$ and 1.0 and several values of cloud droplet number concentration N. For fixed β and N, τ and r_{eff} are distributed along a curve $r_{eff} \propto \tau^{1/5}$.

In the following sections I examine measurements of cloud optical depth, cloud droplet effective radius and cloud liquid water path made in previous work, and my own satellite data for evidence that (3.2) and (3.3) describe real cloud layers.

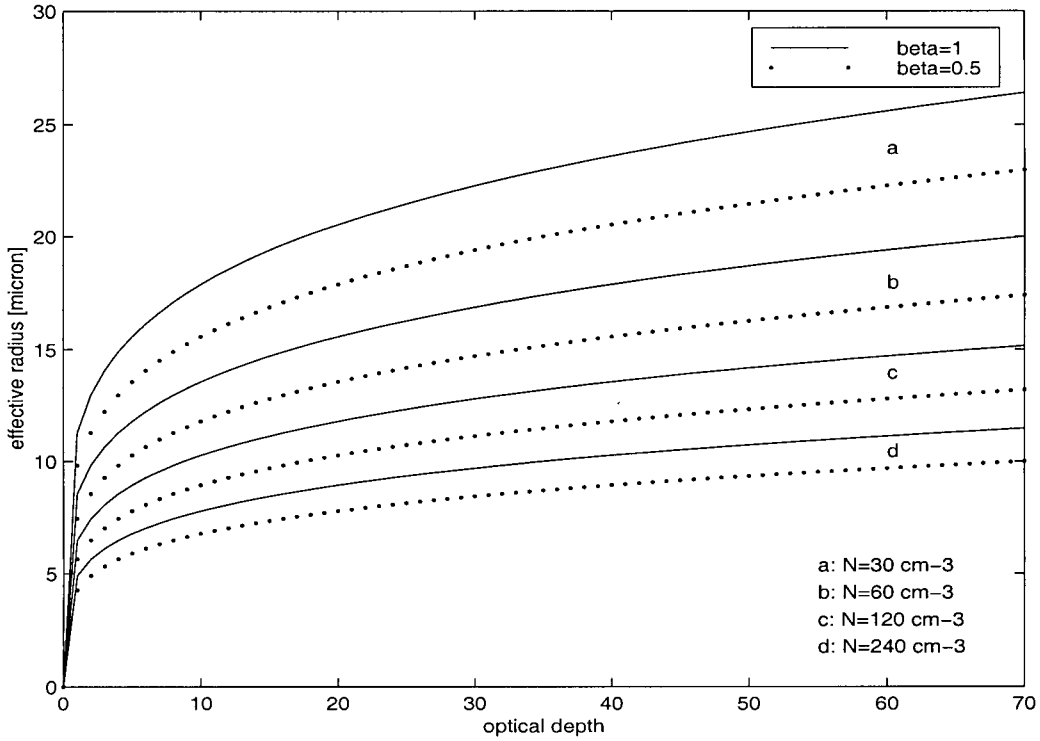

Figure 3.2: Lines of constant cloud droplet concentration in parameterisation according to (3.2). For each indicated cloud droplet concentration ($a - d$) solid and dotted lines are drawn for an adiabatic $\beta = 1.0$, and sub-adiabatic cloud of $\beta = 0.5$ respectively. Constant concentration lines are plotted for cloud droplet concentrations of: a) 30 cm^{-3}, b) 60 cm^{-3}, c) 120 cm^{-3}, d) 240 cm^{-3}.

3.2 Previous observations of r_{eff} and τ or r_{eff} and lwp

Stephens (1978) and Stephens *et al.* (1978) compiled a summary of regional aircraft observations and suggested that cloud optical properties (albedo, emissivity and absorption) could be modelled in terms of integrated cloud liquid water content without further information about cloud microphysics. Stephens (1978) proposed parametrisation of τ as function of lwp for the conservative (non-absorbing) and non-

conservative (absorbing) wavelengths respectively. This parametrisation is based on assumption that r_{eff} is a function of lwp but neglects the dependence of r_{eff} on cloud droplet number concentration .

Stephens (1978) model was extended by Curry and Herman (1985) who compared aircraft observations of cloud microphysics and infrared radiances to the results of radiative models and argued that single parameter representations of cloud optical properties using variables such as the liquid water path did not work, due to the variability of cloud particle size. They proposed a parametrisation of the cloud absorption coefficient in terms of cloud liquid water content and cloud droplet effective radius. Platt (1989) also argued that cloud particle size changes could offset the radiative effects of cloud liquid water path variations.

Satellite multi-channel observations allow for simultaneous monitoring of τ and r_{eff} (see chapter 2) and thus can provide a means of investigating and developing the parametrisation of the dependence between cloud microphysical τ and microphysical r_{eff}. Arking and Childs (1985) and Nakajima and King (1990) developed techniques for simultaneous retrieval of cloud optical depth and cloud droplet effective radius from multi-spectral reflected solar radiance measurements. This technique was applied by Nakajima *et al.* (1991) to measurements of cloud reflected solar radiance obtained by the Multi-spectral Cloud radiometer (MCR) flown on the NASA ER-2 aircraft during the marine stratocumulus intensive field observation (IFO) phase of the First ISCCP Regional Experiment (FIRE) (Albrecht *et al.* (1988)). The authors analysed four days of data. They plotted values of τ and r_{eff} retrieved for 35 km $\times$ 140 km cloudy scenes and observed a positive correlation between the retrieved cloud optical depth (and liquid water path) and the retrieved cloud droplet effective radius on optically thin (mean optical depth) days (July 7 and 13). In contrast, they observed weak negative correlation on optically thick days (July 10 and 16). These results were confirmed by effective radii and liquid water path measurements obtained from simultaneous in flight observations made within

cloud by the University of Washington C-131A aircraft. Good agreement was found between the in situ and remotely sensed cloud optical depth . The remotely measured cloud droplet effective radius was consistently greater the the in situ values by 3-5 μm.

Using a different MCR (with different spectral channels) Rawlins and Foot (1990) retrieved optical depth and effective radius on five FIRE days and observed that larger effective radii were associated with greater optical thickness.

Nakajima and Nakajima (1995) (see also chapter 2) extended the method of Nakajima and King (1990) to infer cloud optical depth and cloud droplet radius from the radiance measurements in three channels of the Advanced Very High Resolution Radiometer (AVHRR) flown on board of the NOAA polar orbiting satellites. They applied the technique to retrieve optical depth and effective radius for one FIRE scene and one Atlantic Stratocumulus Transition Experiment (ASTEX) scene. I show their τ and r_{eff} scatter plots in Figures 3.3 (FIRE region) and 3.4 (ASTEX region) (Figures 17 and 18 in Nakajima and Nakajima (1995)). Each panel represents an area of 100 km $\times$ 100 km.

We note the similarity between (3.2) as plotted in Figure 3.2 and the lower boundary of the τ-r_{eff} clusters in Figure 3.3 $C4$, $D2$ and $D3$ and almost all boxes of Figure 3.4. Lines similar to (3.2) delineate also the upper boundary of the clusters in Figure 3.3 $C3$, $C4$, $D2$ and $D3$ and 3.4 $B1$, $C2$. I discuss these envelopes in my own aircraft and satellite data in the next chapter. Figures 3.3 and 3.4 also show that mean effective radius may actually decrease with increasing optical depth in some clouds (Figures 3.3 $B3$, $C2$ for example).

Nakajima and Nakajima (1995) postulated that such a strong negative correlation between τ and r_{eff} is an indicator of a transition in the microphysical state of a cloud induced by cloud-aerosol interaction (decrease of cloud droplet effective radius due to increased aerosol concentration). An example of such transition in cloud microphysical state would be large scale modifications due to intrusion of aerosol

rich continental air into the clean marine environment. On smaller scales, cloud microphysical properties can be modified by aerosol from ship stacks emission.

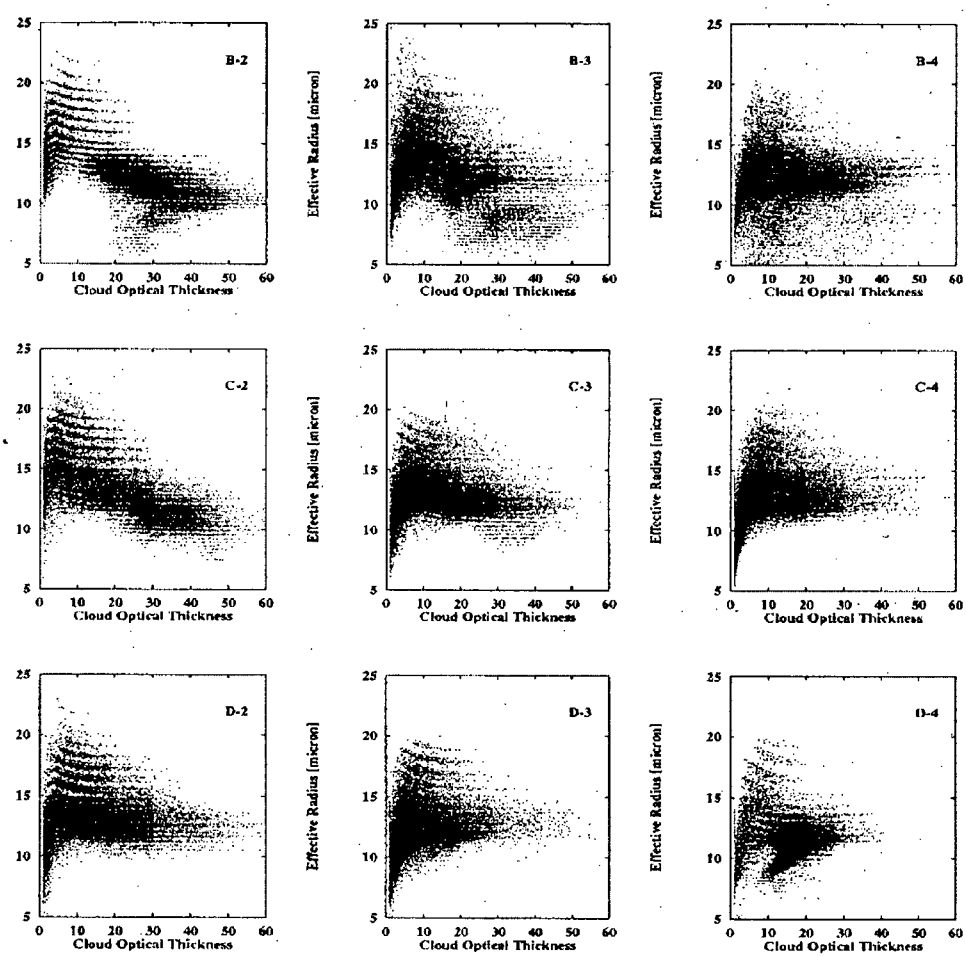

Figure 3.3: Scatter plots of r_{eff} and τ from FIRE scene for July 10 1987 after Nakajima and Nakajima (1995)

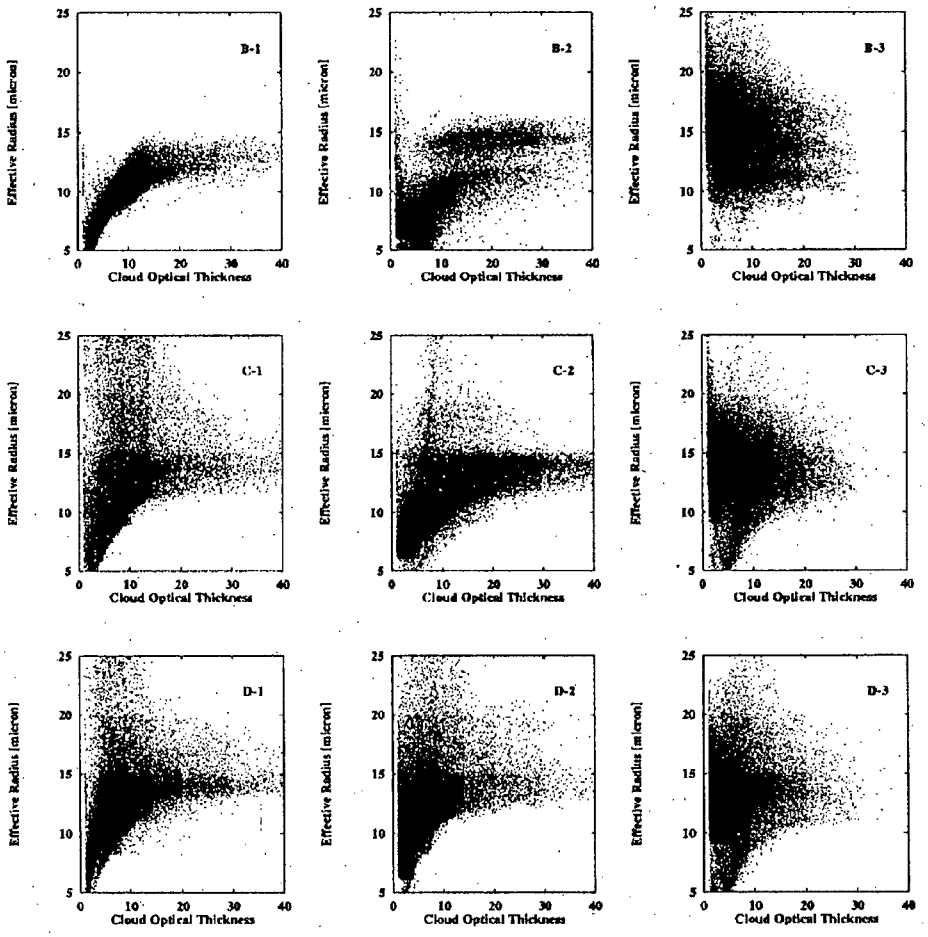

Figure 3.4: Scatter plots of r_{eff} and τ from ASTEX scene for June 13 1992 after Nakajima and Nakajima (1995)

In other work, Zuidema and Hartmann (1995) used the Special Sensor Microwave/Imager (SSMI) on board of the F-8 satellite of the Defense Meteorological Satellite Program to infer cloud liquid water path together with the Earth Radiation Budget Experiment (ERBE) albedo data set to study microphysical of stratus clouds. They derived cloud droplet effective radius from the LWP and cloud albedo measurements using the plane-parallel cloud albedo model of Slingo (1989). At their pixels size of 70x24 km for SSMI and 37x28 km for ERBE, they find no correlation

between cloud effective radius and cloud liquid water path.

Han *et al.* (1994) carried out large scale retrievals of cloud droplet effective radius based on AVHRR data sampled to a spacing of about 30 km and inferred correlation between τ and r_{eff} on global spatial and annual time scales. They found positive correlations between τ and r_{eff} at small optical depths and negative at large optical depth, both over land and ocean confirming the observations of Nakajima *et al.* (1991). The relationship between monthly means of cloud optical depth and cloud liquid water path seemed to follow the parametrisation of Stephens (1978) in some instances for midlatitude continental and subtropical marine clouds but more generally the relationship varied within the range suggested by Curry and Herman (1985). They attributed the variability of the relationship between τ and lwp to the fact that cloud droplet effective radius and τ vary "somewhat independently". This thesis will argue that the "independent" aspect of the variability of τ and r_{eff} stems mostly from the variability of cloud droplet number concentration through (3.2).

3.3 Observations of τ and r_{eff}

I used the retrieval technique of Nakajima and Nakajima (1995) described in chapter 2 to infer cloud optical depth and cloud droplet effective radius from AVHRR radiance measurements. The observational basis of this study are about 600 cloudy sectors 256 km $\times$ 256 km in size extracted from a total of 50 days of AVHRR imagery of Northern Pacific Ocean (three different years: 1987, 1994 and 1995) and the Indian Ocean (1995). The AVHRR data is described in detail in Appendix B which also identifies scenes used in this chapter as examples. For each scene overcast pixels were identified with the spatial coherence analysis technique of Coakley and Bretherton (1982). I limited my retrievals to the "cold foot" of the [mean(ch4), standard deviation (ch4)] scatter plot, where ch4 denotes the AVHRR channel 4 temperature. The mean and standard deviation where computed for 2 $\times$ 2 pixel subregions.

I will begin by showing τ-r_{eff} scatter plots for 14 cloud scenes listed in Table B.1. I focus on a qualitative interpretation of the data in this chapter and return to it in more detail in chapter 4.

3.3.1 Examples of power law dependence between τ and r_{eff}

Equation (3.2) gives us a relationship between cloud optical depth and cloud droplet effective radius in a simple cloud. I now ask: is it possible to find horizontally extensive cloud regimes in which (3.2) provides an accurate description of the observed correlations between τ and r_{eff}?

Figure 3.5 (page 47) shows, as an example, six (out of 325) such regimes found in clouds over Pacific Ocean. The image scale is between 128 km $\times$ 256 km and 256 km $\times$ 256 km. The figures are labeled with values of N_{sat}

$$N_{sat} = \frac{N}{\sqrt{\beta}}. \tag{3.4}$$

which slightly simplifies (3.2). N_{sat} has units of number concentration $[cm^{-3}]$ and can serve as a scaled measure of cloud droplet number concentration . For adiabatic clouds $N_{sat} = N$.

N_{sat} can be inferred from satellite observations (see chapter 4). If we can find estimates of β, from simultaneous in situ measurements or climatology for example, then the "absolute" cloud droplet number concentration N can be found from (3.4). I do this in chapter 5 where I discuss simultaneous satellite and in situ aircraft measurements.

In the examples presented in figure 3.5 the N_{sat} lines, which were fit to the data as a general power law (this will be discussed in detail in chapter 4), appear to accurately represent the relationship between τ and r_{eff}. If cloud subadiabaticity does not vary significantly over the sample area then the width of the scatter plot corresponds to the range of cloud droplet number concentration in the background air.

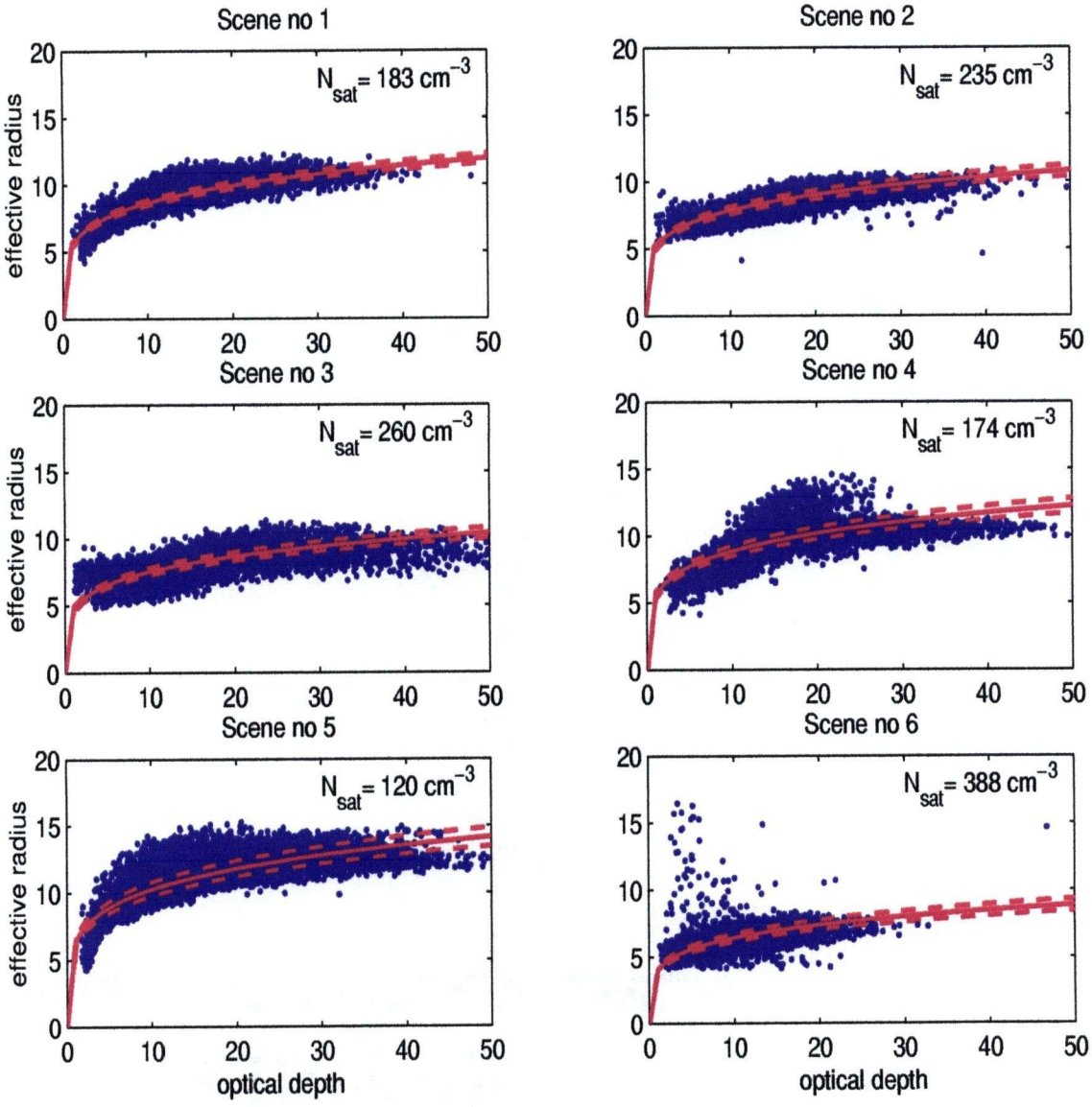

Figure 3.5: Scatter plots of r_{eff} and τ from 6 cloudy scenes of approximate areas ranging from 128x256 to 256x256 km. Solid lines are constant N_{sat} lines of (3.2) fitted to the data. Dashed lines represent one standard deviation departure from the best fit value of N_{sat} for the sample.

3.3.2 Departures from a power law behaviour

Figure 3.6 (page 49) shows examples of scatter plots for scenes 7-10 of Table B.1 where the distribution of τ and r_{eff} does not follow the simple model relationship but rather the cluster of data is encompassed by two lines corresponding to (3.2) with different N_{sat} (solid lines) and a dashed line corresponding to constant geometrical cloud thickness or equivalently cloud liquid water path . These scatter plots are comparable to the observations of Nakajima and Nakajima (1995) (see Figures 3.3 and 3.4 (pp 43 and 44)).

In the model (3.2), for a given amount of available cloud liquid water the attained cloud optical depth and cloud droplet effective radius depend on the cloud droplet number concentration, which is determined by the CCN concentration of the subcloud air and diabatic processes such as precipitation and entrainment. If as before I assume a linear increase of liquid water content with height then for a given cloud liquid water path (lwp) the cloud optical depth dependence on cloud droplet number concentration can be shown to follow (see Appendix A for the details of the derivation)

$$\tau \propto \beta^{-\frac{1}{6}} lwp^{\frac{5}{6}} N^{\frac{1}{3}} = lwp^{\frac{5}{6}} N_{sat}^{\frac{1}{3}} \tag{3.5}$$

The cloud droplet effective radius of a cloud with cloud liquid water path lwp and cloud droplet number concentration N is given by

$$r_{eff} \propto \beta^{\frac{1}{6}} lwp^{\frac{1}{6}} N^{-\frac{1}{3}} = lwp^{\frac{1}{6}} N_{sat}^{-\frac{1}{3}} \tag{3.6}$$

I also find the relationship between cloud optical depth and cloud droplet effective radius under the condition of constant cloud liquid water path (conservation of cloud liquid water) which is given by (3.3).

According to (3.2) clouds that are homogeneous with respect to cloud droplet number concentration and cloud subadiabaticity form clusters in (τ, r_{eff}) space along a line of constant N_{sat} corresponding to that of the cloud.

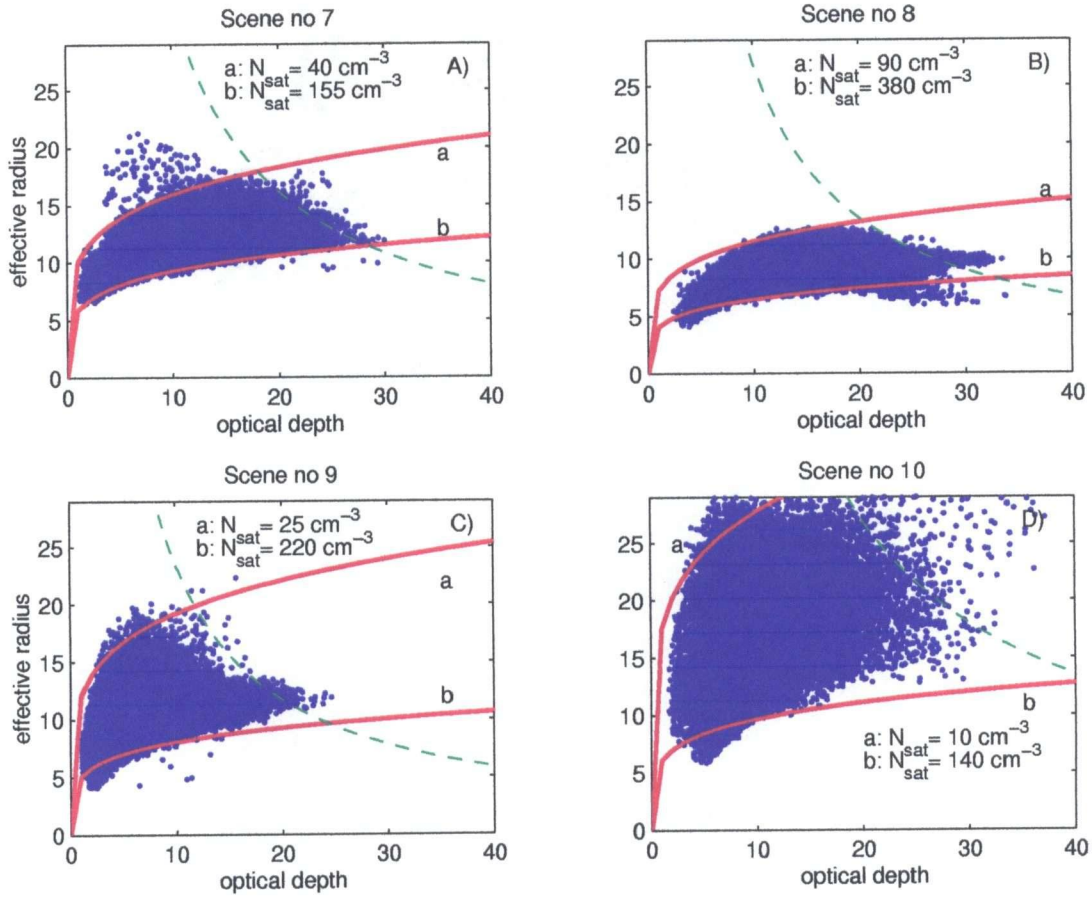

Figure 3.6: Scatter plots of r_{eff} and τ from 4 cloudy scenes of approximate areas of 256×256 km. Solid lines are constant N_{sat} lines of (3.2) which envelope the range of data. Dashed lines represent the envelopes of constant cloud liquid water path A) 180 $[g\ m^{-2}]$, B) 160 $[g\ m^{-2}]$ C) 130 $[g\ m^{-2}]$, and D) 300 $[g\ m^{-2}]$. A)-D) correspond to scenes 7-10 in Table B.1 Appendix B.

In Figure 3.7 I plot constant N_{sat} lines of two distributions of (τ, r_{eff}) (thick lines) one with low N_{sat} at 42 [cm^{-3}], and one with high N_{sat} at 340 [cm^{-3}]).

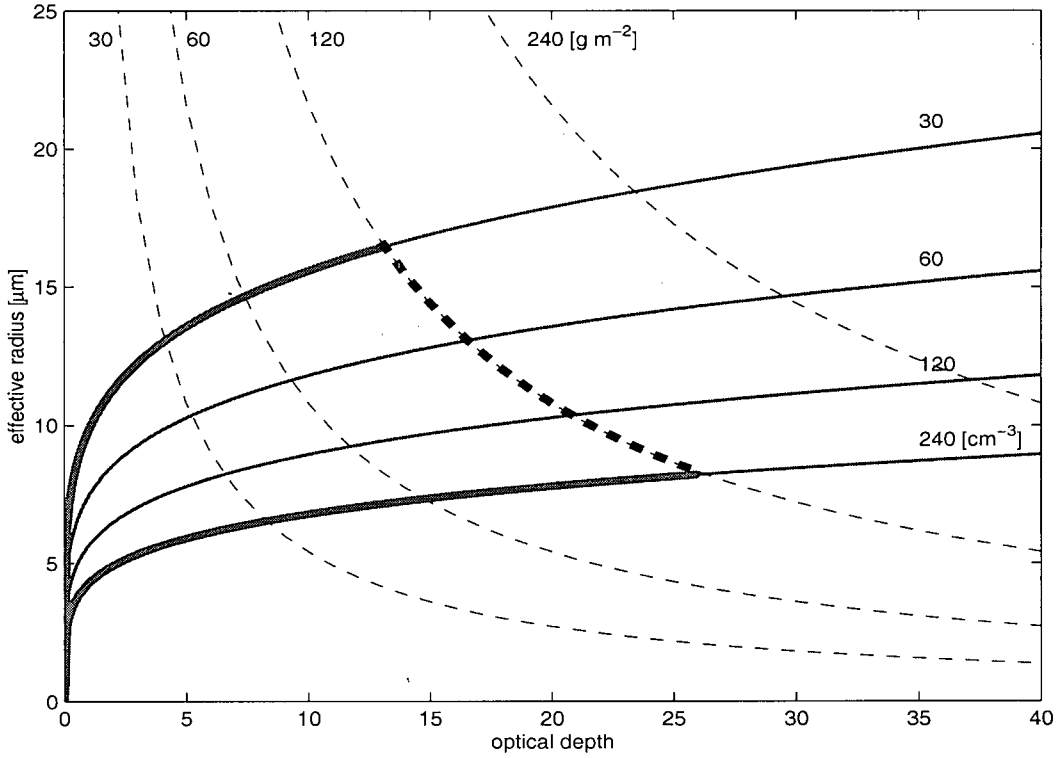

Figure 3.7: Lines of constant cloud droplet concentration 30, 60, 120 and 240 cm^{-3} in parameterisation according to (3.2) at cloud subadiabaticity β =0.5 (solid lines) and lines of constant cloud liquid water path 30, 60, 120 and 240 $g\ cm^{-2}$ according to (3.3) (dash lines). Thick lines follow trajectories in the (τ, r_{eff}) space of two clouds, low cloud droplet number concentration of 30 cm^{-3} and high cloud droplet number concentration of 240 cm^{-3} to the intersection with the cloud liquid water path line of 120 $g\ cm^{-2}$.

In the figure, I assume that both clouds are in the same thermodynamic state (cloud subadiabaticity β=0.5) but have different cloud droplet number concentra-

tion (low N cloud at 30 $[cm^{-3}]$, high N cloud 240 $[cm^{-3}]$). The dashed lines are the isolines of constant cloud liquid water path according to (3.3). If cloud subadiabaticity β is constant, then constant lwp is equivalent to constant cloud geometrical thickness. The isolines of lwp (Δz) (labeled with lwp in $[g\ m^{-2}]$ show possible combinations of τ and r_{eff} for the given cloud lwp (Δz). Intersections of these contours with lines of constant cloud droplet number concentration indicate what maximum cloud optical depth and cloud droplet effective radius is attainable for given cloud lwp and given cloud droplet number concentration . Figure 3.7 shows, that for the same cloud lwp, clouds with low cloud droplet number concentration attain smaller maximum optical depth and larger maximum effective radius than cloud with high cloud droplet number concentration.

It can be deduced from Figure 3.7 that a cloud with variable N and Δz will produce a distribution of τ and r_{eff} similar to those shown in Figure 3.6 enveloped by (3.2) for maximum and minimum N_{sat} (solid lines) and maximum attainable τ and r_{eff} at each N_{sat} for given maximum cloud liquid water path (or cloud geometrical thickness Δz equivalently).

The excursion from a constant lwp envelope will indicate different maximum lwp at different N. In Figure 3.6 lines of constant lwp represents the trend of the maxima of τ and r_{eff} quite well. There are, however, some excursions from constant lwp envelopes especially in Figure 3.6 B and D.

In Figure 3.8 I show contours of the joint probability distributions of τ and r_{eff} corresponding to the scatter plots of Figure 3.6. The multiple N_{sat} structure of the cloud field is clearly visible in the Figure 3.8. All probability distributions have multiple maxima (at least two) which represent clouds of the low and high and sometimes intermediate N_{sat} .

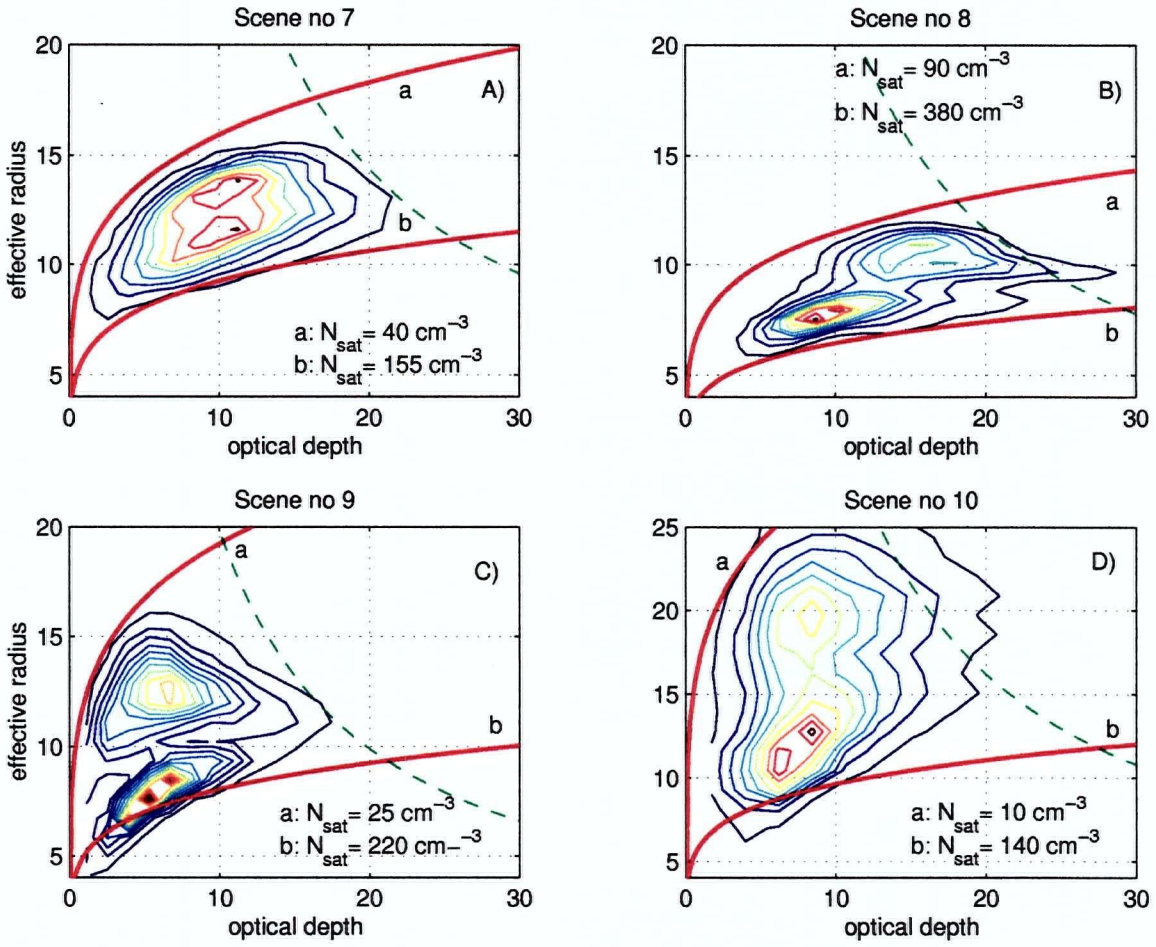

Figure 3.8: Contours of a joint probability distribution of τ and r_{eff} corresponding to the scatter plots of figure 3.6. The contour plot is enclosed by the constant N_{sat} lines. The values of N_{sat} on the constant N_{sat} lines are indicated in the figure. Dashed lines represent the envelopes of constant cloud liquid water path A) 160 $[g\ m^{-2}]$, B) 130 $[g\ m^{-2}]$ C) 110 $[g\ m^{-2}]$, and D) 180 $[g\ m^{-2}]$.

Later in chapter 4 I will argue that the multiple modes of N_{sat} represent clouds with different cloud number concentrations (in other words variability in β is not large enough to explain the occurrence of multiple N_{sat} modes if N is assumed

constant). We can expect to encounter highly varying N_{sat} (cloud droplet number concentration) in two regimes:

1. in frontal zones between two air masses of distinctly different aerosol properties (CCN concentration) each air mass producing cloud with different cloud droplet number concentration . Cloud modification due to CCN concentration changes occurs on a large scale when clouds which were formed in a clean marine air approach land and encounter an increasing CCN concentration of the continental air. On a smaller scale and example of cloud droplet number concentration modification due to increase in aerosol concentration is the 'ship track' phenomena (Coakley *et al.* (1987), Radke *et al.* (1989), Platnick *et al.* (1997)).

2. when cloud processes lead to a change in cloud droplet number concentration . For example, precipitation and cloud droplet growth by collection can reduce cloud droplet number concentration .

3.3.3 Special case: thick clouds

Figure 3.9 shows contours of the joint probability distribution of cloud optical depth and cloud droplet effective radius in thick clouds ($\tau > 10$). I found scenes of thick clouds that exhibit either uni-modal (Figure 3.9A and C) or bi-modal (Figure 3.9B and D) distributions of τ and r_{eff} similarly as for the moderately thick clouds I discussed before. However, in thick clouds the mode where r_{eff} increases with τ is typically not observed. Thick clouds ($\tau > 10$) have a wide range of optical depths with similar values of r_{eff}. This is a consequence of the asymptotic behaviour of (3.2) at large τ, and in case of τ retrieved from radiance measurements the consequence of the saturation of cloud visible reflectance with cloud optical depth for τ greater than about 30.

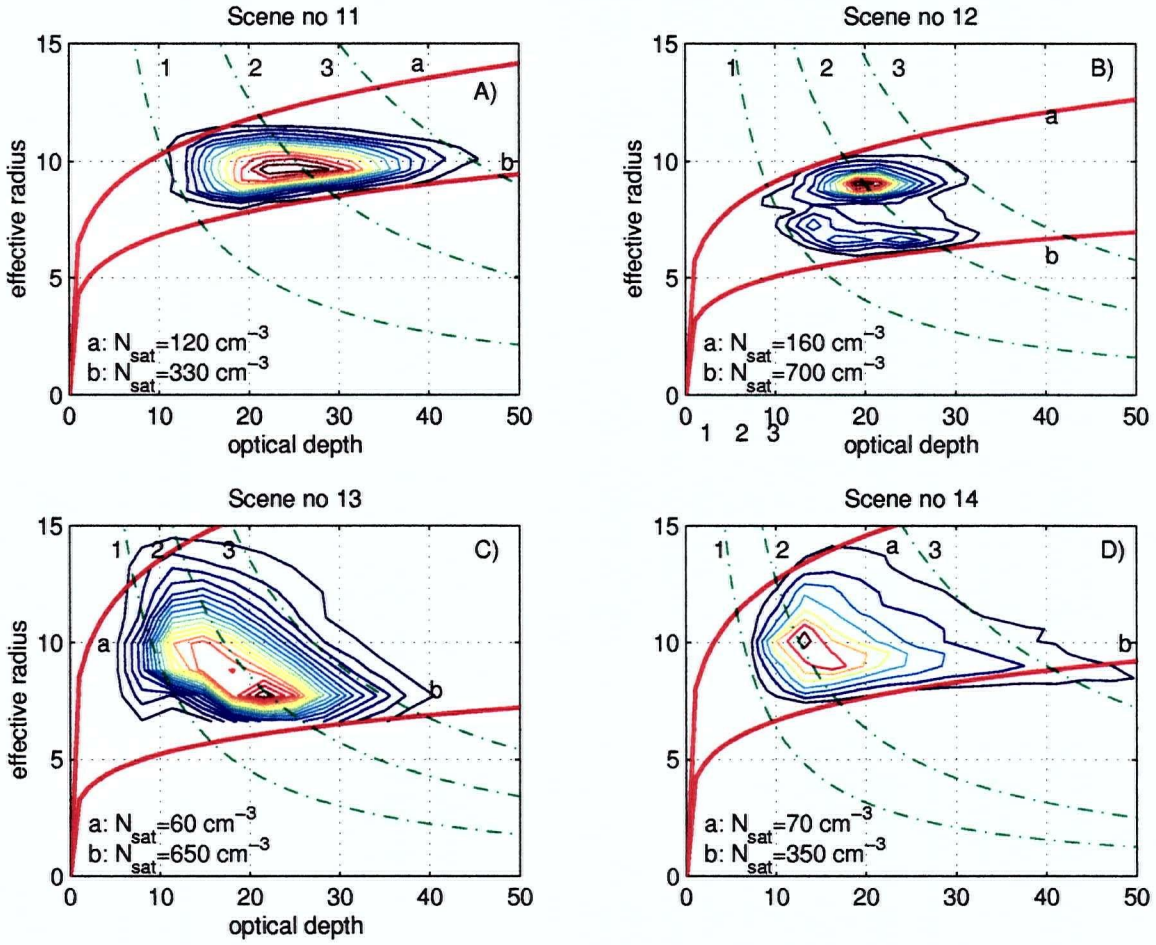

Figure 3.9: Contours of a joint probability distribution of τ and r_{eff} for thick clouds. The contour are enclosed by the constant N_{sat} lines (solid lines). The values of N_{sat} on the constant N_{sat} lines are indicated in the figure. Also drawn are lines of the constant cloud liquid water path (dash lines). The values of *lwp* labels are: 1-3, a) 45, 65 and 100 $[g\ m^{-2}]$; b) 50, 95 and 150 $[g\ m^{-2}]$; c) 10, 70, 110 $[g\ m^{-2}]$; and d) 35, 70 and 200 $[g\ m^{-2}]$; Each plot represents data from an area of approximately 200 $\times$ 300 km. A)-D) correspond to scenes 11-14 in Table B.1 Appendix B.

Although the range of the detected N_{sat} values is often large (max N_{sat} - min

$N_{sat} \sim 600\ cm^{-}3$) some of the distributions of τ and r_{eff} in the cases presented in Figure 3.9 lack a strong bi-modal character representative of distinct cloud populations with different N_{sat} . Instead, the elongated maxima of the joint probability distribution appear to closely follow the lines of constant cloud liquid water path (see Figure 3.9C for example). This behaviour may indicate a modification to cloud droplet number concentration which is followed by changes in cloud optical depth and cloud droplet effective radius .

3.3.4 Bi-modal joint probability distributions of τ and r_{eff}

In this section I focus on cases where the joint probability distribution of τ and r_{eff} exhibits two-maxima. In terms of (3.2), the two maxima structure in (τ,r_{eff}) space (bi-modal distribution) can be interpreted as evidence of two cloud regimes with distinct N_{sat} existing next to each other. If this interpretation is correct then I expect that distinct clusters (branches) in scatter plots of τ and r_{eff} correspond to distinct regions in the physical space defined by the two cloud regimes of different N_{sat} . I examine two bi-modal cases labeled scene 7 and 8 in Table B.1 of Appendix B.

Figures 3.10a and 3.10b page 56 show the separation of the branches in scatter plots of the cloud optical depth an cloud droplet effective radius in scenes 7 and 8 respectively. Figures 3.10c and 3.10d show the spatial location of the two branches in the scene.

I used the '1/5' power curve (3.2) to separate the clusters in the scatter plots of τ and r_{eff}. There is no need for great precision in this operation as it serves mostly an illustrative purpose. It is only important that the two maxima of the joint probability distribution of τ and r_{eff} lay on the opposite side of the separating line (in Figures 3.10a and b).

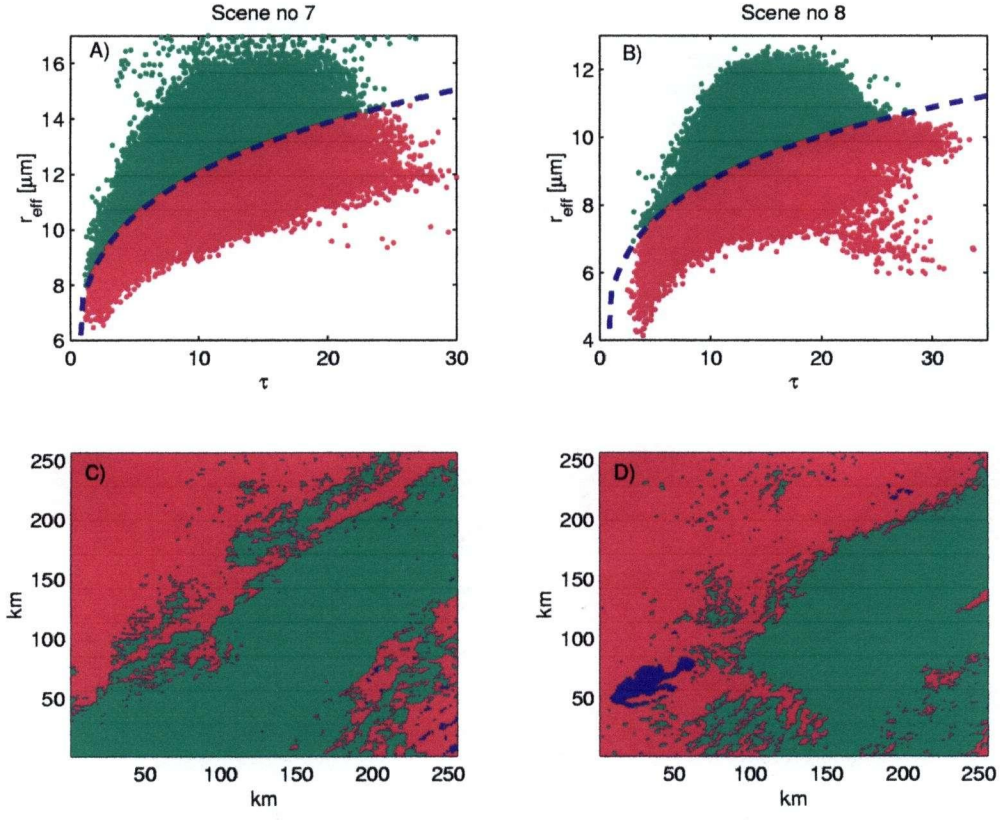

Figure 3.10: A) separation of the two clusters in the scatter plot of cloud optical depth and cloud droplet effective radius in scene 7; B) separation of the two clusters in the scatter plot of cloud optical depth and cloud droplet effective radius in scene 8; C) spatial location of the two clusters in the image for scene 7; D) spatial location of the two clusters in the image for scene 8. Blue colour indicates bad retrieval (usually clear pixels).

In Figures 3.10C and 3.10D pixels belonging to the same branch are the same colour. One can see that clusters of the τ and r_{eff} scatter plots (branches) are spatially separated (come from distinct regions in the scene). This supports my interpretation of the different clusters in τ and r_{eff} scatter plots representing cloud fields of different properties (different cloud droplet number concentration).

The distinct modes of the bi-modal distributions of τ and r_{eff} presented in Figure 3.8 separate spatially in a similar way. In contrast, attempts to separate pixels in uni-modal scenes along a "1/5" curve drawn through the center of a cluster resulted in green and red patches uniformly distributed over the scene.

The spatial separation of N_{sat} modes offers a physical explanation for the departure of maximum τ and r_{eff} envelopes from constant lwp lines for bi-modal clouds (section 3.3.2). In section 3.3.2 I noted that the excursion from a constant lwp envelope indicates different maximum lwp at different N. In this last section I found that different Ns are spatially separated. It is reasonable to expect that different spatial regions of a cloud will have different maximum lwp. The difference in maximum lwp between regions may be due to: 1) different range of geometrical cloud thickness, 2) different cloud subadiabaticity β in different parts of the cloud field.

3.3.5 Summary

In a simple cloud model whose variability in τ and r_{eff} is governed by fluctuations in the height of cloud base, cloud optical depth and cloud droplet effective radius are related by a "1/5" power law. I found that many clouds exhibit a power law relationship between τ and r_{eff} on scales of 256 km $\times$ 256 km.

Departures from the simple power law behaviour indicate additional variability in cloud droplet number concentration N or cloud subadiabaticity β (or N_{sat}). In a sense, the adherence of the τ and r_{eff} relationship to the "1/5" power law as scene size increases establishes the scale of variability of N_{sat} . Scenes larger than the typical 256 km $\times$ 256 km are usually too inhomogeneous in N_{sat} to show the power law behaviour attributed to simple clouds. This explains the focus on this work on scales of 256 km $\times$ 256 km (besides of it being a typical scale of GCM grids). The exact size of 256 km (power of 2) was chosen in anticipation of Fourier analysis of the scenes (to follow in chapter (7)).

I showed that a limiting envelope at large cloud optical depth in scatter plots of τ and r_{eff} ("negative correlation" of Nakajima and Nakajima (1995)) emerges as a result of variable N_{sat} and different maximum attainable cloud optical depth and cloud droplet effective radius depending on N_{sat} .

I distinguished between thin and thick clouds noted that clouds thicker than about 10 frequently lack the mode of r_{eff} increasing with τ due to the asymptotic behaviour of (3.2) at large optical depths.

Chapter 4

Quantitative treatment of the relationship between cloud optical depth and cloud droplet effective radius

In chapter 3 I showed that on scales of 256 km $\times$ 256 km distributions of cloud optical depth and cloud droplet effective radius conform frequently to the simple cloud model of (3.2). I now extend this analysis by:

1. showing that in uni-modal clouds τ and r_{eff} are correlated and the correlation is statistically significant,

2. showing that the statistical analysis confirms the model $r_{eff}(\tau)$ relationship proposed in Chapter 3 section 3.3 by finding parameters of a general power law fit to τ and r_{eff} in uni-modal clouds using bivariate regression,

3. presenting frequency distributions of τ and r_{eff}, with fits to gamma distributions along with a summary of mean τ and r_{eff},

4. estimating the value and the confidence limits of N_{sat} (and N) from the measurements of cloud optical depth and cloud droplet effective radius .

As examples I reexamine the scenes discussed previously in chapter 3 (see Table B.1 in Appendix B).

4.1 General power law fit to the observations of τ and r_{eff}

4.1.1 Scene selection for the general power law fit

The example scatter plots of τ and r_{eff} presented in chapter 3 (see Figure 3.5) suggest a power law dependence between cloud optical depth and cloud droplet effective radius . Theoretical consideration presented in section 3.3 led to a model of this relationship in the form of (3.2), a power law with the exponent "1/5".

In this chapter I seek an independent confirmation of that power law by letting the power law exponent be a free parameter and fitting a general power law in form of

$$\tau = \alpha \, r_{eff}^{b} \tag{4.1}$$

to τ and r_{eff} from 256 km $\times$ 256 km scenes, rather than forcing the $b = 1/5$ relationship. Obtaining $b = 1/5$ from the general power law fit will be considered a strong argument in favour of the model (3.2).

For the analysis I select cloudy scenes 256 km $\times$ 256 km in size. For each approximately 1km $\times$ 1km pixel in the satellite scene I have a simultaneous measurement of τ and r_{eff}.

The scatter of data points around the fitted curve can come several sources: random measurements errors, vertical inhomogeneity, nonlinear lwc profiles, or variations due to the range of values of N_{sat} (N and β) present in the measurement area which leads to scatter in α. For the purpose of fitting a curve to the data points I assume that the scatter of data is due to the random measurement errors only. Of course, if the variability in α in a sample is large, due to variability in N or β then we cannot expect to obtain a meaningful fit. Therefore, I imposed the following requirements (or guidelines) on the distributions of τ and r_{eff} in the scene which have to be satisfied for the scene to be considered suitable for fitting:

(I) Single maximum in the joint probability distribution of τ and r_{eff} (this requirement restricts the variability in N_{sat}).

(II) Pearson's linear correlation coefficient between $log(\tau)$ and $log(r_{eff})$ greater than at least 0.60 . This value has been determined experimentally to select scenes with a broad enough range of τ and r_{eff}, and a narrow distribution of α.

The first (I) requirement tests for scene homogeneity in N_{sat} . I require that all scatter in N_{sat} comes from a fluctuation around one value. The second (II) requirement establishes that the variables are indeed correlated and effectively limits the fluctuations around mean N_{sat} so the scatter remains low. Both requirements together select scatter plots of τ and r_{eff} in form of a single narrow elongated cluster. At the same time I will require that the data have a broad range of variability in τ and r_{eff}. This is necessary to assure that the fit parameters are meaningful. Figure 4.1 illustrates how a limited range in either of the variables can result in the power law fit returning erroneous parameters.

There is a power law relationship between the variables x and y in Figure 4.1. Clearly, if all observations available are confined to one of the rectangles 1 or 2 the power law fit based on those values will not reflect the true character of the relationship between x and y. We need the full range of values to obtain a meaningful fit. Scenes with scatter plots corresponding to the situation of rectangle 2 fail to satisfy the requirement II (correlation coefficient in rectangle 2 is ~ 0) and are easily eliminated. Scatter plots corresponding to rectangle 1 have high correlation coefficients and are not eliminated by II. To eliminate such cases I imposed additional constrain: if $\bar{\tau} < 10$ I reject cases with large variance in r_{eff} ($\sigma_{r_{eff}} \sim 1$).

Summarising, to obtain meaningful estimates of the power law parameters I require the data to cover a wide range the τ values, and constitute a set homogeneous in α (N_{sat}). For scatter plots of τ and r_{eff} it means that the sample data should

form a single, narrow cluster which spans a range of τ from 1-4 to at least 25-30.

Other data scenes might well have the '1/5' power law dependence (in fact, I think they do) but we might not be able to detect it by fitting a general power law. In the next several paragraphs I outline the strategy for the power law test taking into consideration the problems listed above.

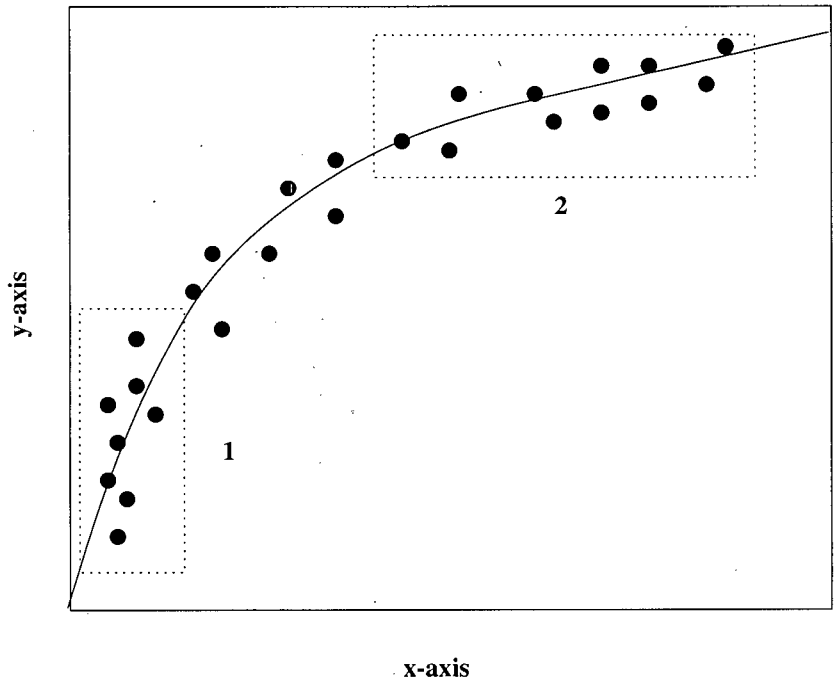

Figure 4.1: Pitfalls of fitting a power law curve to data points from a narrow range.

As an example I selected a sample of ten cloud scenes (256 km $\times$ 256 km) in size. Six of these scenes (1-6) contain sectors at least (150 km $\times$ 150 km) which satisfy the requirements for a meaningful fit (wide range of τ, homogeneous α i.e. low scatter of r_{eff} values around long line of τ). Two scenes (7-8) exhibit a bi-modal structure. I will show that each mode separately is described by the '1/5' power law and obtain estimates the cloud droplet number concentration for each cluster. I also show two examples of cloud scenes corresponding to the situations of rectangles 1 (scene 15) and 2 (scene 11) in figure 4.1 where the conditions of the corresponding

to meaningful fit are not satisfied. Scenes 1-6, 7-8 and 11 are familiar to the reader form chapter 3 Figures 3.5 (uni-modal scenes), 3.6 (bi-modal scenes) and 3.9 (thick clouds) respectively, where they bear the same numbers.

It is important to establish that regression variables are indeed correlated and that the correlation is significant. For uni-modal scenes (1-6) which satisfied the requirements of a meaningful fit I found Pearson's correlation coefficients between 0.63 and 0.80 for the log-transformed variables and Spearman's rank correlation coefficient between 0.63 and 0.81. The bi-modal distributions (7-8) also have high correlation coefficients (0.57 and 0.65) and so does scene 15 (0.71). Correlation coefficients are discussed in details in Appendix D.

Figure 4.2 (page 64) shows scatter plots of τ and r_{eff} for four of the test scenes. The scatter plot in figure 4.2a (scene 2) is a single relatively narrow cluster which extents over a broad range of τ values. The Spearman rank correlation coefficient between τ and r_{eff} (see Appendix D) is high (0.81). This is an example of a scene for which it makes sense to fit a model to the data as we can expect to obtain meaningful regression parameters. Figure 4.2b (scene 8) is a bi-modal case. The lower cluster appears to be suitable for fitting with correlation coefficient of 0.65. The upper cluster clearly is not suitable for fitting. The correlation coefficient is practically zero. This corresponds to the situation of the rectangle 2 in figure 4.1. Figure 4.2c (scene 11) is another example of the case of rectangle 2 of figure 4.1. The correlation between the variables is only 0.09. There are no data points below τ of around 15. Again, fit of a power curve to this data will not yield meaningful results. In figure 4.2d I show an example of the rectangle 1 case of figure 4.1. Although the correlation between variables appears to be strong (r_s=0.71) a narrow range of τ ($\bar{\tau}$=9.7 $\pm$ 3.9) and $\sigma_{r_{eff}} = 0.9$ indicate that fit to this data might be biased towards large slopes.

4.1.2 Transformation of variables

The power law nature of the modelled relationship dictates the logarithmic transformation of the variables to a linear model. I introduce new variables $t = log(\tau)$, $r = log(r_{eff})$. The general power law model of (4.1) transforms to

$$t = log(\alpha) + b\ r = a + b\ r. \tag{4.2}$$

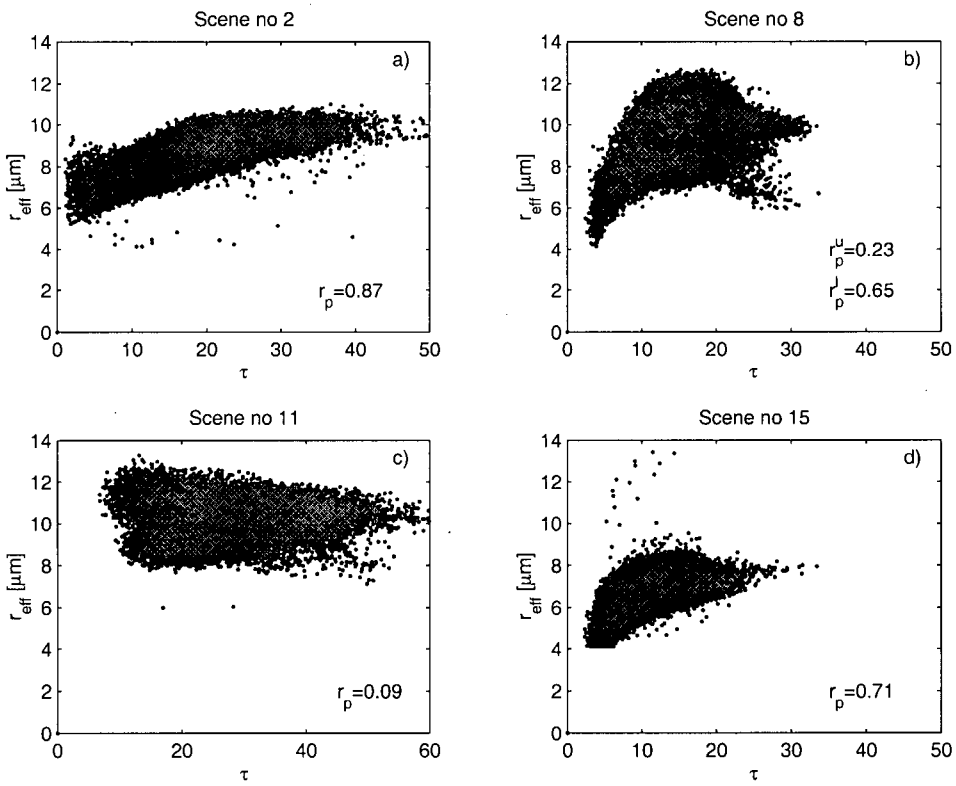

Figure 4.2: Scatter plots of cloud optical depth and cloud droplet effective radius for 4 test scenes; a) scene 2: single maximum, $r_p = 0.87$, scene suitable for a fitting; b) scene 8: two maxima in the joint probability distribution of τ and r_{eff}, the entire scene is not suitable for fitting but the lower cluster is ($r_p = 0.65$); c) scene 11: $r_p = 0.09$, scene not suitable for fitting; d) scene 15: $r_p = 0.71$ but $\bar{\tau} < 10$ and large variance in r_{eff} will bias the fit towards large values of the slope parameter b.

Linear least squares regression on log-transformed variables is considered a standard approach for a power law fitting and is used frequently in many areas of science. However, caution should be exercised when using this technique.

Generally, a least squares regression of log-transformed data is not the same as a least squares regression of the non-transformed data (original model). The best fit regression is based on the assumption of normal distribution of the regression residuals around the line of the best fit. Solution to the regression problem in the log-transformed variables results in log-normally distributed residual when the model is detransformed. Thus the best fit, in a least squares sense, to the log-transformed data is not necessarily the best fit to the original data. The consequences of this disagreement to the estimates of the parameters of the original model can be twofold (Jansson (1985)):

1. The estimate of the intercept (a) can be biased towards low values.

2. The estimate of the slope (b) can be too small.

Miller (1984) proposed a correction factor to reduce the transformation bias in the intercept that arises when regressions of natural logarithms are detransformed. With Miller's correction

$$\alpha = e^{a} e^{\frac{\sigma_e^2}{2}} \tag{4.3}$$

where σ_e^2 is the variance of the regression residuals of the log-transformed variables.

Jansson (1985) notes that the effect of the transformation on the estimate of the slope is significant if the number of low t values is large in comparison with the number of high t values . Moreover, if the scatter of the independent variable is low and there are few low t values the biases in the intercept and slope are low.

The conditions of minimal bias could, in principle, impose further restrictions on the scene selection for fitting the power law.

I computed the Miller's correction factor for the regression on the data from scene 2 (figure 4.2a) and found it be less 0.2% . Several other scenes which I classified as suitable for fitting showed similarly small bias. This leads us to the conclusion that the requirements I impose on scenes to be eligible for fitting already select scenes with small transformation biases.

4.1.3 Bivariate linear regression with errors in both variables

The classical linear regression problem assumes that all of the deviation from the regression line is due to the error in the predicted variable whereas the predictor variable is error free. If, as it is a case in many experimental designs, both variables are subject to error then the results of classical linear regression depend on the choice of the independent (predictor) variable. Methods of structural regression (major axis and reduced major axis) have been designed to work in cases when errors in both variables are unknown.

If we know or can estimate the uncertainties of each variable then it is most advantageous to use the method of linear regression with known errors in both variables. The merit function for fitting $y(x) = a + bx$ is in this case given by

$$\chi^2(a,b) = \sum_{i=1}^{N} \frac{(y_i - a - bx_i)^2}{\sigma_{y_i}^2 + b^2\sigma_{x_i}^2} \tag{4.4}$$

where x_i and y_i represent measurements, σ_{x_i} and σ_{y_i} are the standard deviation of x and y for point i, and N is number of measurement points.

This method is capable of achieving much greater precision of the estimates of regression coefficients than the classical or the structural linear regression. The greater precision comes at the cost of a more complicated computational problem. The complication arise due to a nonlinearity in the equation for the maximum likehood estimator for the slope b of the linear model.

The cloud optical depth and cloud droplet effective radius measured from satellites are both subject to the retrieval errors. I estimate the retrieval uncertain-

ties for τ and r_{eff} and employ the method of linear regression with known errors in both variables (approach of Press *et al.* (1992)) to find the maximum likehood estimators and their uncertainties for the slope (b) and intercept a of the model (4.2).

Estimation of the uncertainties in τ and r_{eff}

In estimating the uncertainty of the retrieved values of cloud optical depth and cloud droplet effective radius I considered three source of errors:

1. the approximation error - error introduced by the approximation to the radiative transfer model. This error is estimated Nakajima *et al.* (1991)) to be $\approx$ 1% for τ, and $\approx$ 10% for r_{eff} for most typical values of τ and r_{eff}.

2. the independent pixel approximation (IPA) error is introduced by neglecting the horizontal radiative transfer between pixels. Chambers *et al.* (1997a) estimate that this error for the retrieval of τ can range between 6-45% . For the range of values the solar angle and cloud fraction in our data sets the 6% error appears to be appropriate. However, this is not a random error. The independent pixel approximation introduces a bias in retrievals of τ. The effect of IPA on r_{eff} is unknown. Since I am mostly concerned with comparing pixel values in the same scene it appears that all pixels will be affected by using the IPA in the same way and the bias will not change the relationship between pixel values.

3. the measurement (retrieval) error is dominated by the uncertainty of sensor calibration and digitisation, estimated for τ at about 15% for our range of τ and solar angle values (Pincus *et al.* (1995).

4. for a typical cloud ($\tau > 6$, $r_{eff} \sim 10$) Platnick and Valero (1995) estimated the worst net uncertainty in AVHRR retrieved r_{eff} at -20% to 25% accounting for: measurement error of channel 3 radiance (assumed at 15%) ($\sim \pm$ 13%), in cloud water vapour absorption ($\sim +$ 3%), size distribution uncertainties ($\sim \pm$

10%).

5. I assume average values of the errors listed above and estimate the total pixel error at 15% for τ and 20% for r_{eff} (root of sum of squares).

This estimates of the uncertainties in τ and r_{eff} propagate to uncertainties of the transformed variables t and r. Typical values of the transformed variables uncertainties are 5% for t and 8% for r.

Results of the linear regression for the test scenes

I performed linear regression on the transformed variables t and r with uncertainties of 5% in t and 8% in r for the eleven test scenes introduced in 4.1.1 For each scene the linear regression model parameters were obtained for each of the 100 realisation of the sampling procedure and the realisation average was computed. Table 4.1 summarising the results of the general power law fit for the eleven test scenes. It shows the values of the regression coefficients a and b for each scene and their uncertainties σ_a and σ_b together with scene characteristics (solar and view angles, description of the scene texture).

The goodness of fit is 1 in all cases presented in table 4.1. This number might seem suspiciously high. It is possible that our estimates of the τ and r_{eff} uncertainties are too high for the cases I consider. On the other hand, we know from Appendix D that τ and r_{eff} are highly correlated (see table D.1) so we can expect highly significant statistical results of the linear regression. Another factor which helps in achieving highly statistical results significant is the large number of data points I use in our analysis (typically over 300 data point per scene after sub-sampling). The standard deviation of the estimates of the regression parameters a and b is between 3-5% for a and between 10-20% for b.

In table 4.1 scenes 1-6 which satisfy the meaningful fit requirements all yield the power law exponent within the error bars of 0.2 . For the bi-modal cases 7 and 8, the separate clusters which conform to the meaningful fit requirements also yield b = 0.2. In three cases, scene 11, 15 and the upper cluster in scene 8), b is significantly

different than 0.2. These are the cases where requirements for the meaningful fit are not satisfied. Refer again to figure 4.1. Cases 8 and 11 correspond to the situation of rectangle 2, and case 15 corresponds the situation of rectangle 1.

scene no.	solar angle	view angle	texture	a	σ_a	b	σ_b
1	55	0-10	long cells (10x20)	1.58	0.03	0.19	0.01
2	57	12-28	long cells (10x50)	1.60	0.04	0.19	0.01
3	55	0-15	small and larger cells	1.56	0.04	0.19	0.01
4	55	13-30	dense close cells	1.72	0.04	0.19	0.02
5	52	7-22	very large cells	1.87	0.05	0.20	0.02
6	65	16-33	open cells	1.40	0.05	0.20	0.02
7	50	7-22					
1st cluster			medium, elongated cells	2.17	0.09	0.20	0.04
2nd cluster			large, elongated cells	1.88	0.06	0.21	0.02
8	54	7-22					
1st cluster			thick, dense elongated small cells	-	-	0.11	0.07
2nd cluster			small cells less dense	1.65	0.07	0.18	0.03
11	57	0-14	very thick, dense	-	-	0.09	0.01
15	60	4-20	small open cells	-	-	0.31	0.01
			small cells, 100% cloud fraction				

Table 4.1: Parameters intercept a and slope b and their uncertainties from the linear regression for 10 test scenes (see Table B.1).

Figure 4.3 shows the general power law fit to single realisations of the sampling procedure for four test scenes (1,2,3 and 5 of table 4.1) in log-log space of τ and r_{eff}. For each scene the model is fitted to 100 sample realisations and the average values of the regression parameters are obtained. These are the values of a, b given in the figure. The Pearson's linear correlation coefficient r_p is also the average for 100 realisations of the sampling procedure.

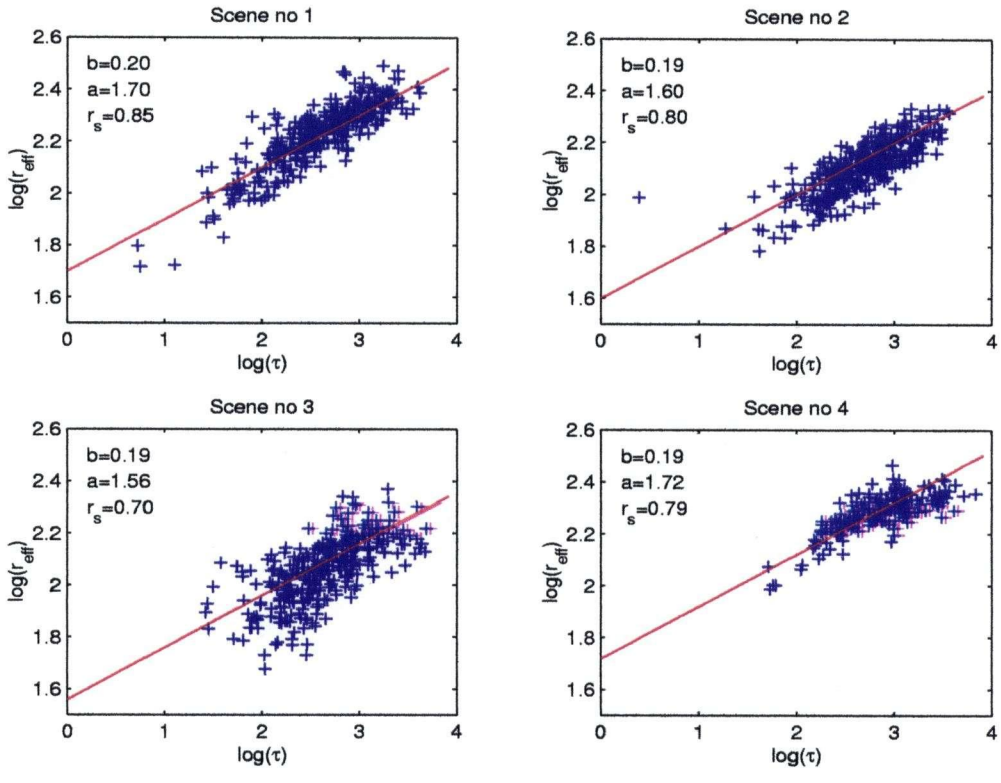

Figure 4.3: Scatter plots of cloud optical depth and cloud droplet effective radius (in the log-log scale) for a single realisation of the sampling procedure and the line of linear regression for 4 test scenes: a) scene 1; b) scene 2; c) scene 3; and d) scene 4. Also given are values of the linear regression parameters of intercept a, and slope b, and the Pearson's linear correlation coefficient r_p. All four data sets satisfied the requirements for a meaningful fit.

I have analysed 325 cloud scenes of approximate areas of 256km $\times$ 256km which exhibited a single cluster structure of τ and r_{eff} scatter plot and presented the potential of obtaining a meaningful fit. For 55% of those scenes I obtained a power law exponent of 0.2 within error bars. For another 25% of scenes b=0.2 was contained in the range between $b \pm \sigma_b$ but the estimated errors σ_b, were greater than 0.06 (30%) or $b \pm \sigma_b$ was less than 0.02 away from b =0.2 with errors less than 30%.

within error bars. was $b \pm \sigma_b$ less than 0.02 away b =0.2 or within the error bars of b which were however greater than 0.06 (30%). Of the remaining 20% of the scenes the majority returned b between 0.1 and 0.3.

Collectively, the results of this section provide a strong argument in favour of the '1/5' power law relationship between the cloud optical depth and the cloud droplet effective radius in low layer clouds and validation of the model of the (3.2).

4.2 Mesoscale frequency distributions of τ and r_{eff}

Mesoscale mean cloud albedo can be approximated by computing (Barker (1996))

$$\overline{r}(\mu_0) = \int_0^\infty p(\tau) r_{pp}(\tau, \mu_0) d\tau \tag{4.5}$$

where r_{pp} is an albedo of a subregion (pixel) computed with the assumption of plane parallel homogenoeus cloud over the area of the pixel, and $p(\tau)$ is the mesoscale distribution of τ.

In an effort to quantify the variability of cloud optical depth and cloud droplet effective radius on scales of approximately 256 km $\times$ 256 km we computed frequency distributions of τ and r_{eff} for scenes 1) representative of the model (3.2), and 2) exhibiting bi-modal joint distribution of τ and r_{eff}, 3) thick clouds ($\tau > 10$).

Once again I reexamine the 15 scenes (uni-modal, bi-modal and thick clouds) previously discussed in chapter 3 and section 4.1.3 of this chapter (see also Table B.1 in Appendix B). In addition, I expand the set of uni-modal scenes by 10 scenes

drawn randomly from our data base of 170 uni-modal cloud scenes. The random scenes are listed in Table B.2 in Appendix B.

Figure 4.4 shows the geographical location of the sample 25 scenes. The sample densely covers the North Pacific stratus region and appears representative of the area.

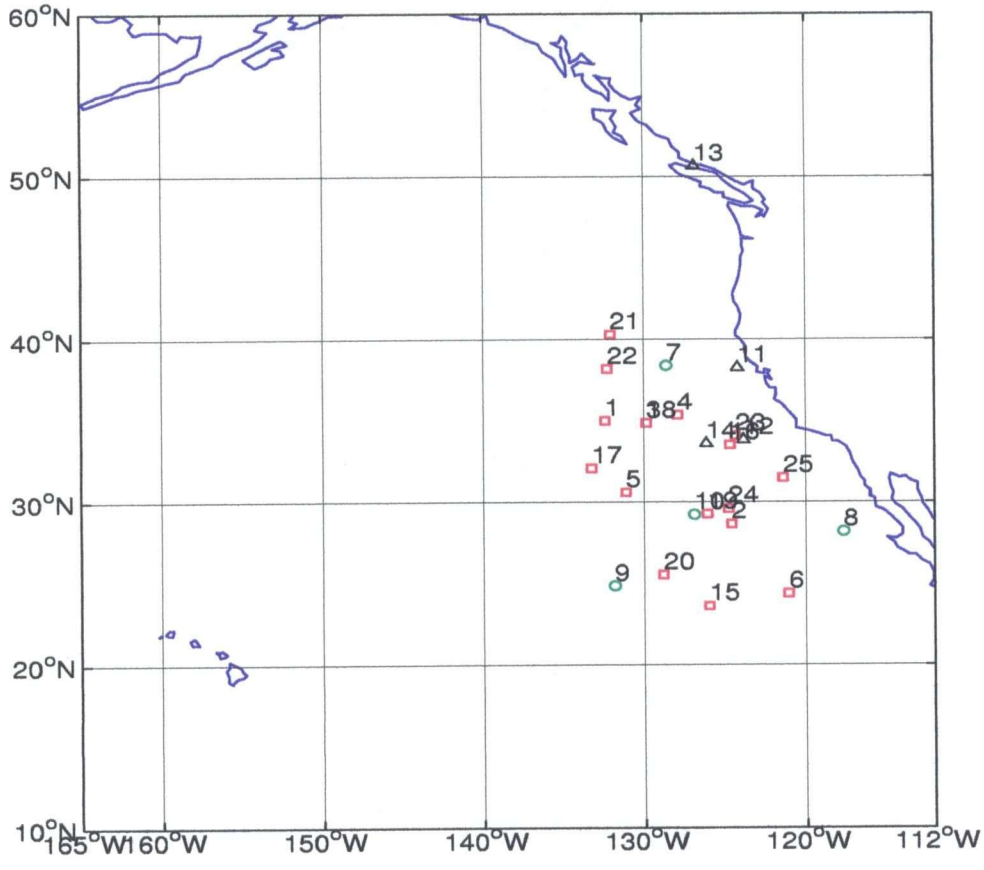

Figure 4.4: The geographical location of the scenes listed in Tables B.1 and B.2, and discussed in chapters 3 and 4: 1) uni-modal scenes 1-6, 15 and 16-25 (random) (□); 2) bi-modal scenes 7-10 (○); 3) thick clouds 10-14 (△).

Barker (1996) has shown that if $p(\tau)$ follows a gamma distribution then (4.5) can be integrated analytically for r_{pp} given by a two stream approximation (Meador and Weaver (1980)).

I find the parametrisation of the distributions of τ and r_{eff} in terms of gamma distribution given below

$$p(\tau) = \frac{1}{\Gamma(\nu)}(\frac{\nu}{\bar{\tau}})^{\nu}\tau^{\nu-1}e^{-\nu\tau/\bar{\tau}}, \qquad \tau > 0, \nu > 0, \tag{4.6}$$

where $\nu = (\bar{\tau}/\sigma)^2$ in which $\bar{\tau}$ and σ are mean and standard deviation of τ. $\Gamma(\nu)$ is the gamma function. The gamma distribution was fitted to the observations using the maximum likehood method (MLE) as described in Barker *et al.* (1996).

Barker *et al.* (1996) succeeded in showing that the gamma distribution is a good fit to the frequency distribution of cloud optical depth on 58 km $\times$ 58 km scales retrieved from Landsat measurements at resolution of 57 m . I confirm this for τ retrieved with 1 km resolution from 256 km $\times$ 256 km AVHRR scenes with uni-modal and bi-modal joint distributions of τ and r_{eff} and extend the analysis to cloud droplet effective radius .

4.2.1 Clouds with power law relationship between τ and r_{eff}

Figures 4.5 and 4.6 show the frequency distributions of τ and r_{eff} for the uni-modal scenes 1-6 of Table B.1 (and Figure 3.5$a-f$) and three of the randomly selected uni-modal scenes 16-18 Table B.2 (Figure 3.5$g-i$). I discussed scenes 1-6 previously in chapter 3 and section 4.1.3 of this chapter and showed that the distributions of τ and r_{eff} in these scenes are related by a power law with an exponent b=1/5. In Figures 4.5 and 4.6 solid lines represent the data and dashed lines are the fit to the gamma distribution.

Mean, standard deviation and the parameter ν of the fitted gamma distribution are given for all scenes in Table 4.2 (page 80) and will be discussed later in section 4.2.4.

The gamma distribution is a very close fit for the frequency distribution of cloud optical depth on 256 km $\times$ 256 km scales with the 1 km AVHRR resolution. The gamma fit is good in case of r_{eff} if the frequency distribution of cloud droplet

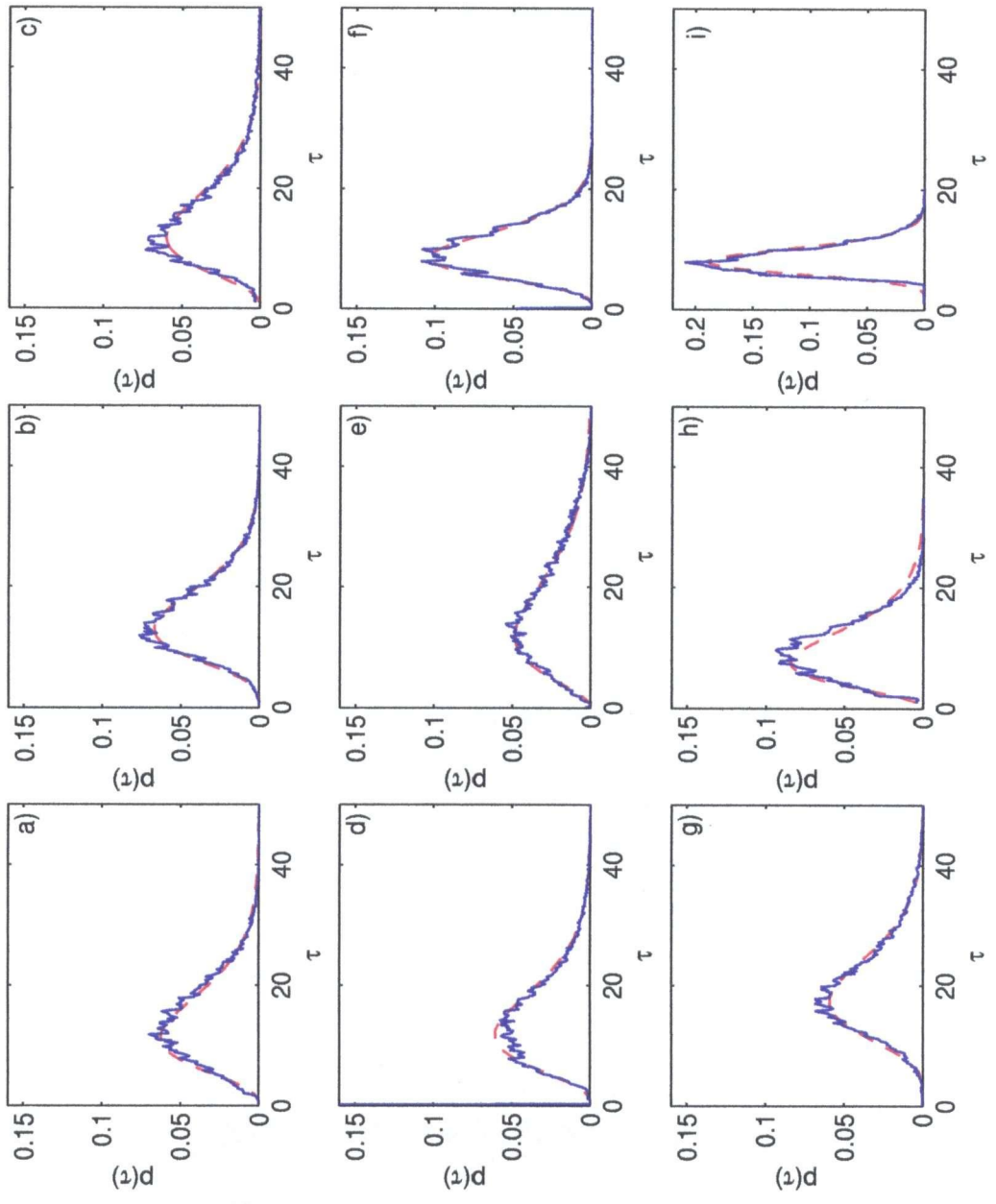

Figure 4.5: Frequency distribution of cloud optical depth for 9 uni-modal scenes (scenes 1 to 6 from Table B.1 and 1 to 3 from Table B.2). Solid and dashed lines represent data and the fitted gamma distribution respectively. The mean, standard deviation and parameter ν of the gamma distribution are listed in Table 4.2.

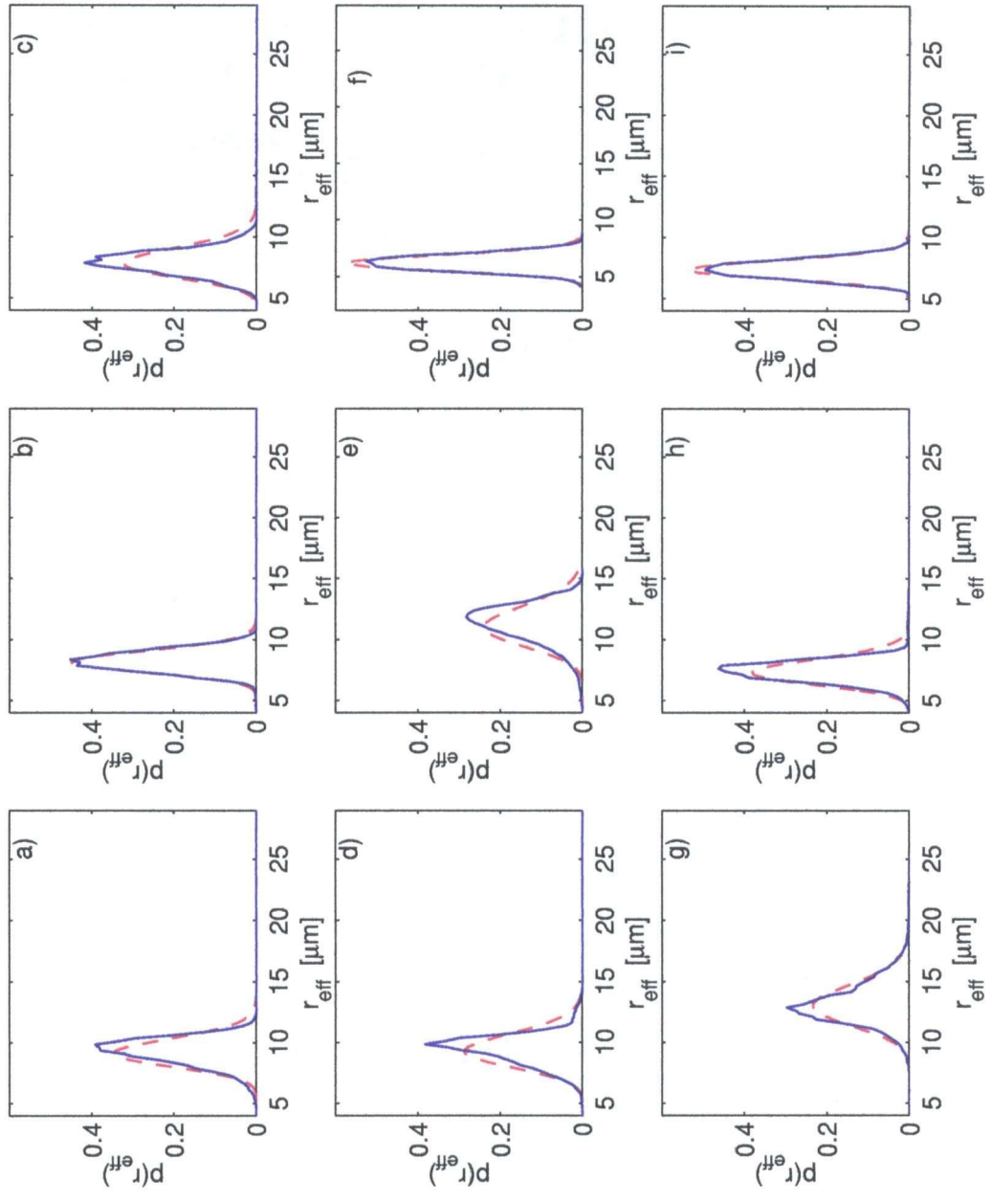

Figure 4.6: Frequency distribution of cloud droplet effective radius for 9 uni-modal scenes (scenes 1 to 6 from Table B.1 and 1 to 3 from Table B.2). Solid and dashed lines represent data and the fitted gamma distribution respectively. The mean, standard deviation and parameter ν of the gamma distribution are listed in Table 4.2.

effective radius is symmetric or positively skewed. There are however cases where the r_{eff} distribution is negatively skewed (Figure 4.6d,e) and as such cannot be well represented by gamma function.

In Figure 4.7 I plotted the mean cloud droplet effective radius ($\bar{r}_{eff}$) against the mean cloud optical depth ($\bar{\tau}$) for all uni-modal scenes scenes discussed in this chapter. The error bars in Figure 4.7 indicate the standard deviation of r_{eff}. The number near each data point is the number of the scene the data point represents.

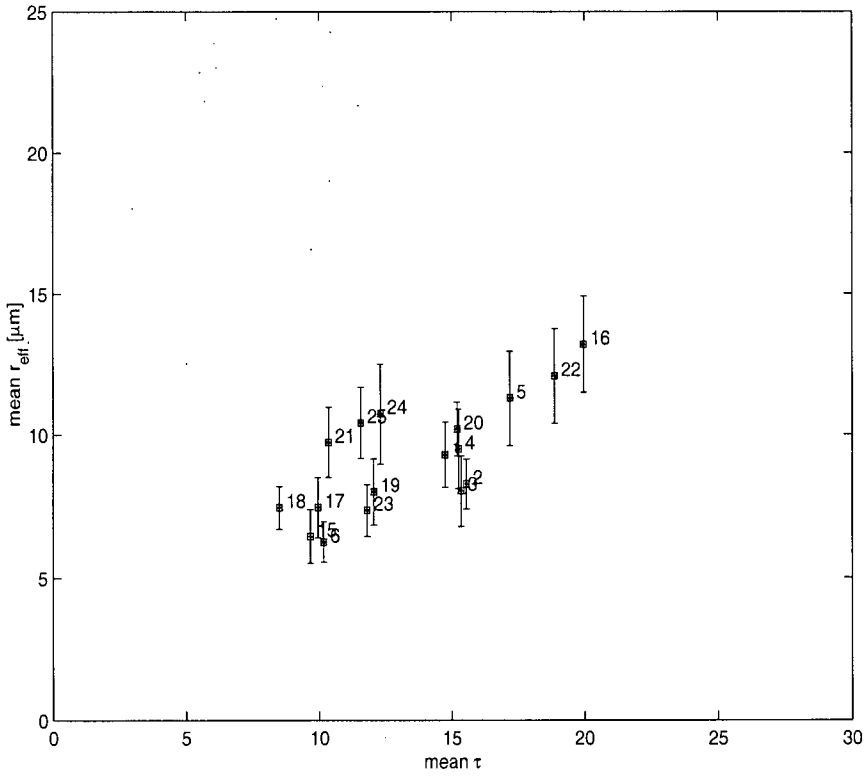

Figure 4.7: Scatter plot of mean cloud optical depth and mean cloud droplet effective radius for uni-modal scenes in Tables B.1 (1 to 6) and B.2 (16 to 25). The error bars represent the standard deviation of r_{eff}. The number near each data points denotes the number of the scene this data point represents.

Points in Figure 4.7 represent mean properties of uni-modal clouds. These

points form an elongated cluster describing an increase of mean r_{eff} with mean τ.

4.2.2 Clouds with a bi-modal joint distribution of τ and r_{eff}

Figure 4.8 (page 78) shows the frequency distributions of τ $(a-d)$ and r_{eff} $(e-h)$ for the bi-modal scenes 7-10 of Table B.1 (and Figure 3.8). As before, the gamma distribution provides a good fit to the frequency distribution of τ but obviously fails to reproduce the bi-modal structure of the r_{eff} distribution. In scene 7, where the separation of modes is least pronounced, the difference between the fit and the data appears small. Although, the gamma approximation cannot resolve the bimodal structure of the histograms it does provide an estimate of the width of the frequency distribution. In this sense the gamma approximation is representative of the bimodal frequency distributions.

4.2.3 Special case: thick clouds

Figure 4.9 (page 79) shows the frequency distributions of τ $(a)-d))$ and r_{eff} $(e)-h))$ for the thick cloud scenes 11-14 of Table B.1 (and Figure 3.9). The gamma distribution provides a good fit to the frequency distribution of τ in scenes a) and b). In scenes c) and d) the fit is not as good. In chapter 3 I interpreted these two cases as scenes where N_{sat} varies significantly across the scene and where τ and r_{eff} change along lines of constant cloud liquid water path . The distribution of r_{eff} is well represented by gamma function only in case e) where the distribution is symmetric.

4.2.4 Parameters of the fit gamma distribution

In table 4.2 I show the mean, standard deviation and the parameter ν of the gamma fit to the frequency distributions of cloud optical depth and cloud droplet effective radius of all uni-modal (1-6, 15, and 16-25), bi-modal (7-10) and thick cloud (11-14) scenes discussed din this chapter (and listed in Tables B.1 and B.2 in Appendix B).

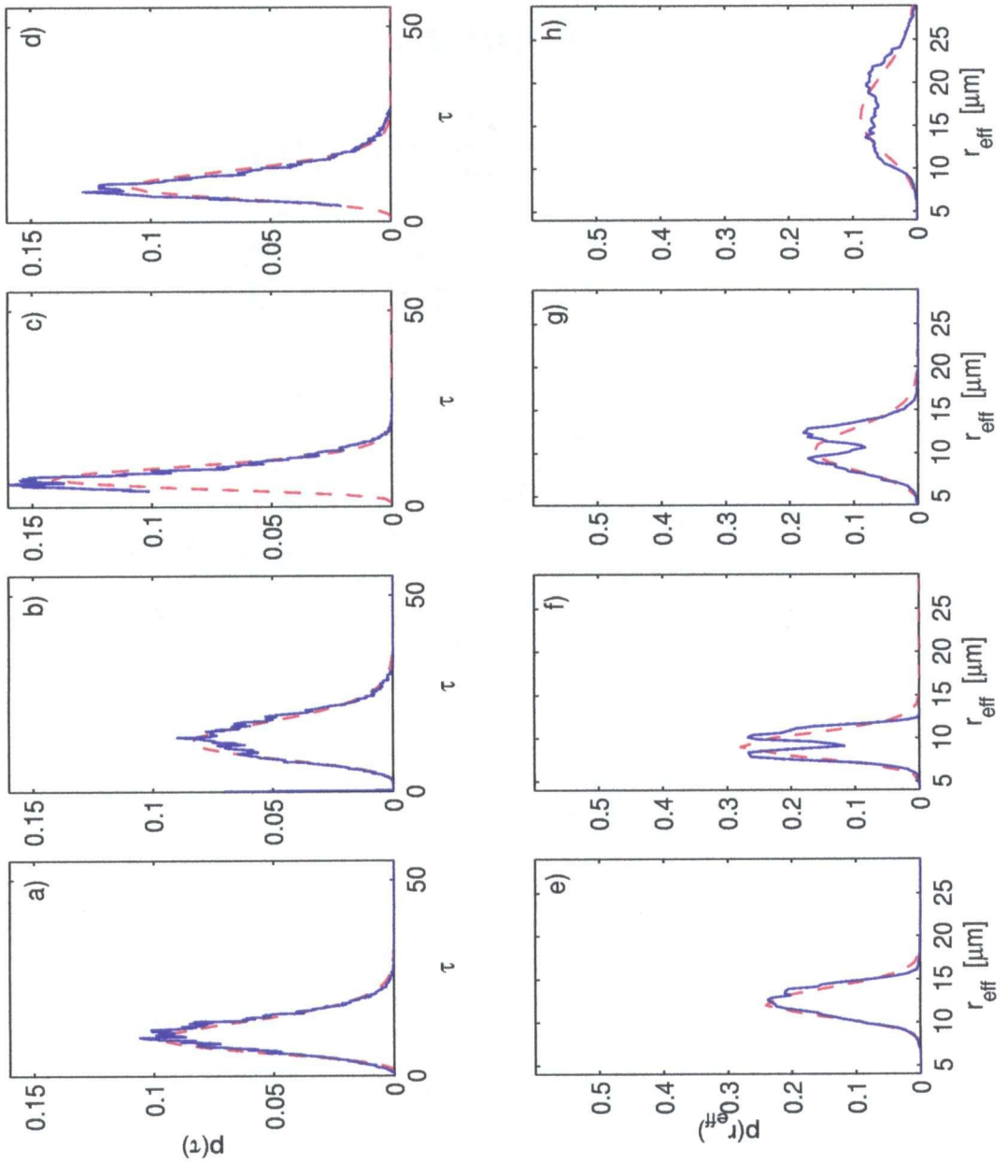

Figure 4.8: Frequency distribution of cloud optical depth $(a-d)$ and cloud droplet effective radius $(e-h)$ for bi-modal scenes 7 to 10 in Table B.1). Solid and dashed lines represent data and the fitted gamma distribution respectively. The mean, standard deviation and parameter ν of the gamma distribution are listed in table 4.2.

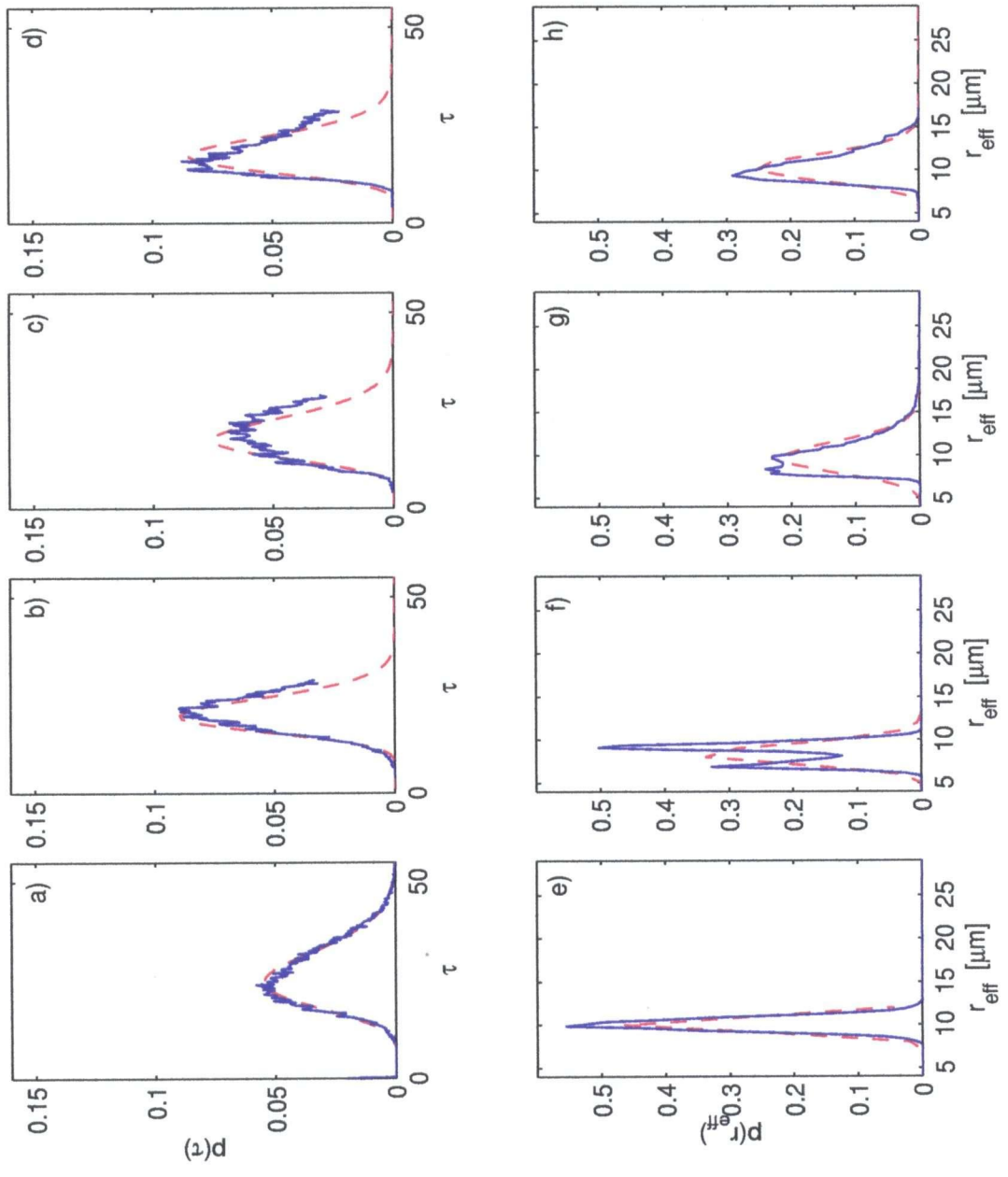

Figure 4.9: Frequency distribution of cloud optical depth $(a-d)$ and cloud droplet effective radius $(e-h)$ for thick cloud scenes 11 to 14 in Table B.1. Solid and dashed lines represent data and the fitted gamma distribution respectively. The mean, standard deviation and parameter ν of the gamma distribution are listed in table 4.2.

scene no.	$\bar{\tau}$	σ_τ	ν_τ	$\bar{r}_{eff}$ $[\mu m]$	$\sigma_{r_{eff}}$ $[\mu m]$	$\nu_{r_{eff}}$	A_c
1	14.75	7.06	4.33	9.29	1.11	64.83	0.94
2	15.55	6.42	5.87	8.26	0.89	86.40	0.98
3	15.35	7.42	4.28	8.02	1.24	41.84	0.93
4	15.25	7.27	4.40	9.49	1.40	45.79	0.99
5	17.19	9.58	3.22	11.29	1.68	45.14	0.95
6	10.17	4.14	6.02	6.25	0.69	81.18	0.92
7	11.37	4.40	6.68	12.46	1.65	57.18	1.00
8	14.53	5.02	8.37	9.32	1.44	42.02	0.98
9	8.30	3.14	7.81	10.82	2.53	18.87	0.94
10	10.67	4.10	7.48	17.36	4.63	13.48	0.99
11	26.83	7.51	12.71	10.10	0.74	187.79	1.00
12	20.76	5.27	20.84	8.44	1.14	52.71	1.00
13	21.06	7.24	7.24	10.00	1.96	28.73	1.00
14	24.67	11.99	14.73	10.46	1.59	44.74	1.00
15	9.67	3.87	6.49	6.44	0.90	49.12	0.92
16	19.96	7.11	7.88	13.21	1.72	59.01	0.99
17	10.38	5.38	3.72	7.44	1.05	50.28	0.82
18	8.50	2.17	15.27	7.43	0.75	99.66	0.83
19	12.06	6.19	3.79	7.99	1.16	47.33	0.82
20	15.20	4.86	9.36	10.19	0.94	116.23	0.98
21	10.35	3.56	8.43	9.73	1.23	62.69	1.0
22	18.87	7.10	7.20	12.08	1.72	51.45	0.99
23	11.81	4.12	8.22	7.34	0.90	66.11	0.99
24	12.31	7.39	2.78	10.74	1.77	36.61	0.61
25	11.57	4.99	5.67	10.42	1.22	69.22	0.59

Table 4.2: Parameters of gamma distribution fitted to cloud optical depth and cloud droplet effective radius frequency distributions in 256 km $\times$ 256 km AVHRR scenes of cloud fraction A_c. Scenes 1-11 were discussed in 4.1.3 (see Table 4.1).

Also included in Table 4.2 are estimates of cloud fraction (A_c). The majority of the scenes in Table 4.2 represent the class of overcast or broken stratocumulus. The range of values of $\bar{\tau}$, σ_τ, and ν_τ in Table 4.2 corresponds closely to that obtained by Barker *et al.* (1996) for τ of overcast and broken stratocumulus retrieved from Landsat imagery.

The greatest difference between the fields of cloud optical depth and cloud droplet effective radius is in the parameter ν which quantifies variance of the measured (approximated) distribution. Values of $\nu_{r_{eff}}$ are 2-10 times greater than the corresponding values of ν_τ. This is an indication of much greater mesoscale variability of τ over r_{eff}.

The weaker relative variability of r_{eff} reflects the $r_{eff} \propto \tau^{1/5}$ relationship predicted by model (3.2). We will see more evidence of this weaker variability of r_{eff} with respect to τ in chapter 7.

From (3.2) one can find variance of $log(r_{eff})$

$$var[log(r_{eff})] = var[log(\frac{\tau^{1/5}}{N_{sat}^{2/5}})] + e = 0.04\ var[log(\tau)] + 0.16\ var[log(N_{sat})] + e. \tag{4.7}$$

where e accounts for correlations between variables.

I computed $var(log(r_{eff}))$ and $var(log(\tau))$ for the uni-modal scenes 1-6 and two bi-modal scenes 7 and 8 (Table 4.2). The variability of τ accounts for approximately 70 to 80% of r_{eff} variability in uni-modal scenes and about 30% for in the bi-modal scenes. The residual variance (20 to 30% and $\sim$ 70% respectively) would be attributed to variability of N_{sat} and the correlation term e in (4.7).

The greatest r_{eff} variance was found in bi-modal scenes with large r_{eff} and small τ (scenes 9 and 10). Surprisingly, two other bi-modal scenes (8 and 9) exhibit only moderate variance in r_{eff}. Optically thick clouds or clouds with small droplets have least variance in r_{eff} (2, 6 and 11).

In figure 4.10 I plotted the mean cloud droplet effective radius ($\bar{r}_{eff}$) against

the mean cloud optical depth ($\bar{\tau}$) for all scenes in Table 4.2. In effect I added all bi-modal and thick clouds scenes to the Figure 4.7 which comprised only the uni-modal scenes. As in Figure 4.7 the error bars in Figure 4.10 indicate the standard deviation of r_{eff}. The number near each data points is the number of the scene this data point represents.

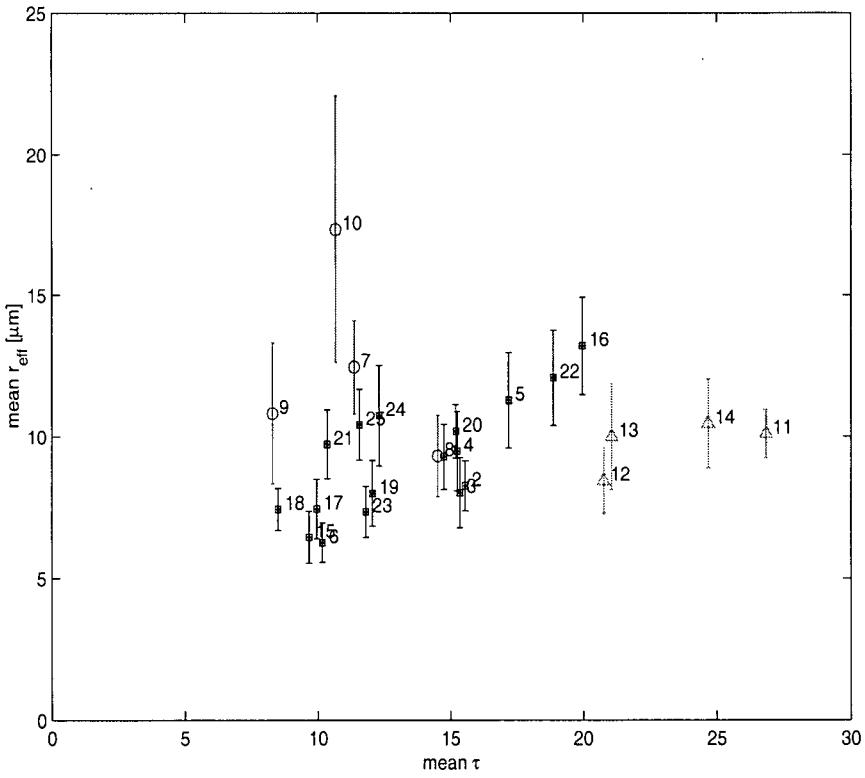

Figure 4.10: Scatter plot of mean cloud optical depth and mean cloud droplet effective radius for: 1) uni-modal scenes (1-6 and 15) in Table B.1 and (16-25) in Table B.2 (□); 2) bi-modal scenes (7-10) in Table B.1 (○); 3) thick clouds (11-14) in Table B.1 (△). The error bars represent the standard deviation of r_{eff}. The number near each data points denotes the number of the scene this data point represents.

I can now distinguish three regions in figure 4.10. Beside the central line cluster of uni-modal scenes (□) we find a region of large $\bar{r}_{eff}$ and small $\bar{\tau}$ occupied

by scenes (o) (7,9 and 10), and a region of very thick clouds with a relatively small r_{eff} ($\triangle$) (11-14).

Collectively, figure 4.10 points to different properties of very thick and very thin layer clouds. In light of the results of this and the previous chapter, this difference between thick and thin clouds can be related to respectively high and low cloud droplet number concentration in those clouds.

4.3 Inference of the N_{sat} based on the relationship between cloud optical depth and cloud droplet effective radius

In the previous sections I was primarily concerned with the slope of the linear regression b. Now I turn my attention to the intercept parameter a. The intercept of the linear regression is a physically interesting parameter since it carries information about cloud droplet number concentration .

It follows from (3.2) and (4.2) that if b in (4.2) equals 0.2 then

$$a = log(\alpha) \tag{4.8}$$

In section 4.1.3 I have shown empirically that in stratocumulus clouds the relationship between τ and r_{eff} follows a power law with the exponent b=0.2 . Thus, b in (4.2) can now for all purposes be replaced by 0.2 .

Substituting in equation (4.8) for α (see (3.2)) one can derive a formula for N_{sat}

$$N_{sat} = [\frac{a_0}{exp(\ a)}]^{5/2}. \tag{4.9}$$

I estimate the uncertainty in N given the uncertainty of the regression intercept a. I employ the method of propagation of errors (Bevington and Robinson

(1992)) to evaluate the uncertainty of N_{sat} due to the error of the estimate of a. I assume small changes in variables and retain only the linear terms of the propagation expansion. The uncertainty of N_{sat} , ΔN_{sat} is given by

$$\Delta N_{sat} = \frac{dN_{sat}}{da}\sigma_a = \frac{5}{2}N_{sat}\sigma_a. \tag{4.10}$$

From table 4.1 a typical value of σ_a is about 0.06. If N_{sat}=100 cm^{-3} then according to the (4.10) the uncertainty interval around N_{sat} is $100 \pm 15cm^{-3}$ that is $\pm$15%.

In the case of a bi-modal scatter plots one would like to know if the two clusters correspond to two distinctly different N_{sat} values or whether the difference between N_{sat} of the two clusters is fully explainable by the statistical uncertainty of N_{sat} .

With the $\pm$15% uncertainty of N_{sat} estimates I anticipate that a positive distinction between clusters in a bi-modal case can be made if the difference between the N_{sat} of the two clusters is greater then about 30% of the average N_{sat} of the two clusters.

I examine the the bi-model cases introduced in section 4.1.1, scene 7 and 8. Contour plots of the joint probability distribution of τ and r_{eff} for scene 7 and 8 were shown in Figure 3.8a,b respectively. The contour plots reveal double maxima in the distributions for both scenes.

As we saw in section 4.1.3 the two clusters of scene 7 separately satisfied the requirements of the meaningful fit and I obtained the estimates of the regression parameters a and b for each cluster. In scene 8 only one cluster was suitable for fitting. Again, I used the general power law fit to obtain the values of the parameters a and b for this cluster. I used (4.9) to invert the values of the intercept a for N_{sat}. Through the (4.10) I obtained the estimates of the uncertainty in N_{sat} due to uncertainty of the estimate of the regression parameter a. Table 4.3 on page 85 shows the estimate of N_{sat} , and N_{sat} uncertainty interval for each cluster in scenes

7 and 8.

The upper cluster of scene 8 (see figure 4.2) lacks data points at low values of τ and is not expected to yield a meaningful regression parameter. However, I am now confident that the model (3.2) correctly describes the relationship between the cloud optical depth and the cloud droplet effective radius . Thus, I expect that the upper cluster follows the '1/5' power law (3.2) even though this cannot be proved through the power law fit in this case .

scene no.	7 1st cluster	7 2nd cluster	8 1st cluster	8 2nd cluster
N_{sat} $[cm^{-3}]$	57	117	144	208
N_{sat}^{-}, N_{sat}^{+} $[cm^{-3}]$	45-72	100-136	122-172	174-247

Table 4.3: Estimates of N_{sat} and the N_{sat} uncertainty intervals for each cluster in scenes 8 and 9.

I still need an estimate of a for the upper cluster. Again, in this case one cannot relay on the general power law fit to return a meaningful estimate of a . I can however fit the specific '1/5' power law to the data points in which case I expect to obtain a valid estimate of the intercept parameter a . The specific '1/5' power law fit can be accomplished in several ways. At this point I only present one of these methods which I term 'an easy fit' due to its simplicity and quick results. I introduce the following transformation of variables

$$\tau\prime = \tau \tag{4.11}$$

$$r\prime_{eff} = \frac{r_{eff}}{\tau^{1/5}} \tag{4.12}$$

If the model (3.2) holds then $r\prime_{eff}$ is independent of τ and moreover

$$r\prime_{eff} = \alpha \tag{4.13}$$

The scatter in τ and r_{eff} is now reflected in the new variable $r\prime_{eff}$. I compute the mean value of $r\prime_{eff}$ to obtain an estimate of α for the data set (or cluster), and invert α for N_{sat} .

For the upper cluster of scene 8 the above procedure yields $N_{sat} = 208\ cm^{-3}$. I compute the uncertainty of this estimate of N_{sat} using the formula (4.10) and assuming σ_a of the lower cluster (see the results in table 4.3).

Examination of the results given in table 4.3 reveals that the uncertainty in N_{sat} increases with cloud droplet number concentration and two clusters with high N_{sat} will be more difficult to detect than two clusters with lower N_{sat} . Scene 7 corresponds to a situation where two clusters are both at a relatively low N_{sat} (57 and 117). Scene 8 represents cloud field with two clusters are a relatively high N_{sat} (144 and 208). In both scenes the two clusters are distinct, their standard error uncertainty intervals do not overlap. I can attempt to generalise that in the case of low N_{sat} (57 to 117 cm^{-3}) one can distinguish between cloud areas which differ in N_{sat} by about 30 cm^{-3} and more. At higher N_{sat} the threshold for detection of different N_{sat} areas increases to $\approx$ 60 cm^{-3} at the range of 144 to 208 cm^{-3}. Notice, that should both scenes 7 and 8 occupy tangent regions in space and be captured in satellite image the combine scene would exhibit three distinguishable clusters! In the more robust scenario the combination of the two lower clusters of both images 57(45,72) cm^{-3} and 144(122,172) cm^{-3} is clearly separated and so is the combination of the two upper clusters of the two scenes 117(100,136) cm^{-3} and 208(174,247) cm^{-3}.

The question I ask now is: what contributor to the N_{sat} variability generates the bi-modal structure of the τ-r_{eff} scatter plots? In other words, how is the variability of N_{sat} partitioned between the variability of cloud subadiabaticity β

and the cloud droplet number concentration N? In particular, I ask if the range of observed cloud subadiabaticity β is large enough to generate the bi-modal structure observed in scenes 7 and 8.

Applying the propagation of errors (Bevington and Robinson (1992)) to (3.4) and keeping the first order terms only gives

$$\Delta N_{sat}^2 = [(\frac{\partial N_{sat}}{\partial \beta})^2 \Delta\beta^2 + (\frac{\partial N_{sat}}{\partial N})^2 \Delta N^2] \tag{4.14}$$

where ΔN and $\Delta\beta$ are the range of variability of N and β respectively. ΔN_{sat} represents the range of N_{sat} . I define r_β the percentage of N_{sat} variability explained by the variability of β as the ratio of the first term of RHS of (4.14) to the LHS of (4.14). Similarly, r_N the percentage of N_{sat} variability explained by the cloud droplet number concentration N is defined as the ratio of the second term of RHS of (4.14) to the LHS. In final form

$$r_\beta = 100\ (\frac{\Delta\beta}{2\beta}\frac{N_{sat}}{\Delta N_{sat}})^2 \tag{4.15}$$

$$r_N = 100 - r_\beta. \tag{4.16}$$

I take ΔN_{sat} to be difference of N_{sat} between the two clusters of the scatter plot. Observations show a range of β between 0.6-1.0 in North Pacific stratocumulus (see discussion in chapter 3 section 3.3), the cloud regime in scenes 7 and 8. If β varies in this range in scenes 7 and 8 it explains only about 10% of the difference in N_{sat} between the two clusters in scene 7 and 47% in scene 8. This result suggests that multiple clusters in the scatter plots of τ and r_{eff} are manifestation of cloud droplet number concentration varying throughout the cloud field.

From the point of view of satellite retrievals of N_{sat} and the construction of climatology of cloud subadiabaticity β it is instructive to examine the dependencies between β, N_{sat} and N. Figure 4.11 shows contour plots of N as a function of β and N_{sat} .

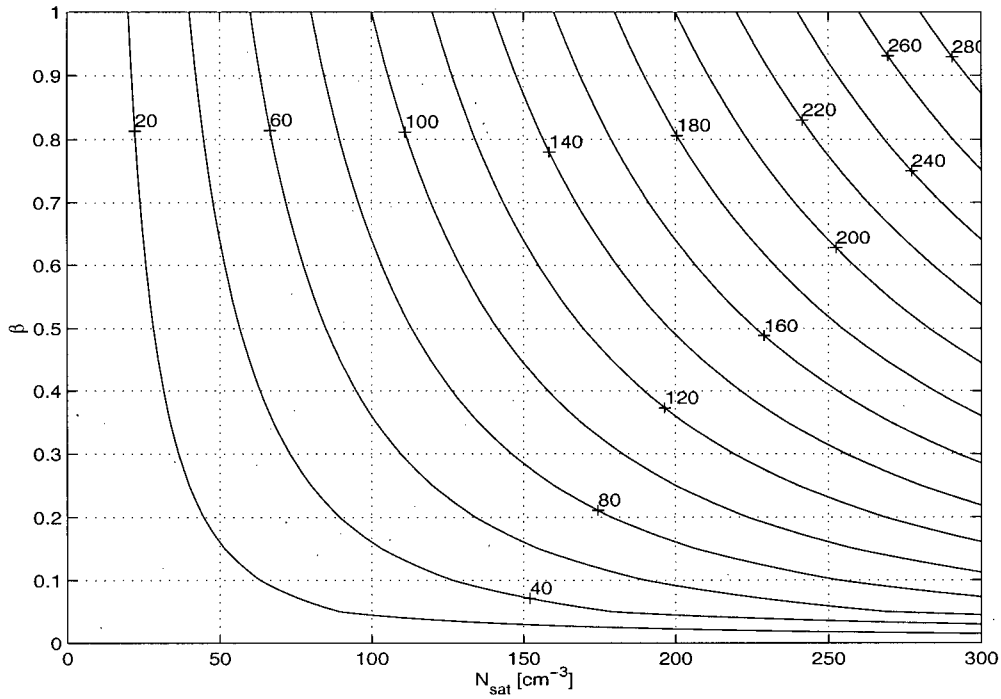

Figure 4.11: Contours of cloud droplet number concentration N labeled in $[cm^{-3}]$ as a function of N_{sat} and β.

For small N_{sat} (or N) and $\beta > 0.6$ N is almost orthogonal to β. In this regime $N_{sat} \approx N$. As N_{sat} and N increase effect of varying β becomes stronger. In chapter 5 I discuss aircraft observation which provide independent estimates of N_{sat} , N and β. In Appendix E I discuss the possible dependence of β on N. This dependence if confirmed could eliminate the ambiguity of N_{sat} with respect to β.

4.4 Summary

I showed in this chapter that scenes with a power law dependence between τ and r_{eff} can commonly be found on scales of 256 km × 256 km. This can be interpreted as an indication that on this range of scales many cloud fields fit the description of model (3.2). That is, clouds on these scales are fairly homogeneous with respect to

N_{sat} and the variability of their optical depth and effective radius is determined by the variability in cloud geometrical thickness (cloud base).

I found that the mesoscale frequency distribution of cloud optical depth can be accurately approximated by a gamma distribution in uni-modal and bi-modal scenes, and in thick clouds (with some exceptions). The gamma distribution is also a good approximation for r_{eff} distribution if this distribution is symmetric or positively skewed. However, I often find negatively skewed or bi-modal distributions of r_{eff}. The gamma distribution does not work in those cases for obvious reasons.

Mean properties of simple clouds (mean τ and r_{eff}) are well localised in the $(\bar{\tau},\bar{r}_{eff})$ space where they form a cluster along a line representing an increase of $\bar{r}_{eff}$ with $\bar{\tau}$. Departures from the simple model (bi-modality of the joint distribution of τ and r_{eff}) or large cloud optical depth divert from the line established by the uni-modal scenes and occupy distinct regions of the $(\bar{\tau},\bar{r}_{eff})$ space.

In section 4.3 I showed how to retrieve N_{sat} from satellite measurements of cloud optical depth and cloud droplet effective radius . In the next chapter I decouple N and β in N_{sat} through in situ (aircraft) observations.

Chapter 5

Validation of the satellite retrievals by in situ aircraft measurements

This chapter compares satellite retrievals and aircraft in situ measurements of cloud optical depth and cloud droplet effective radius acquired during the SOCEX II experiment and validates the cloud parametrisation of equation (3.2) using aircraft data. Using the in situ aircraft data I estimate cloud subadiabaticity β, and decouple N and β in N_{sat} . In section 5.1 I discuss previous satellite-in situ comparison studies. Section 5.2 outlines the analysis plan followed in this chapter. The aircraft data sets are described in section 5.3. In section 5.4 I estimate cloud subadiabaticity β and aircraft τ using the flight data. In section 5.5 the satellite and aircraft observations are compared in the $r_{eff} - \tau$ plane and the general power law is fitted to the aircraft τ and r_{eff} . I find cloud droplet number concentration N through N_{sat} and β for aircraft and satellite observations and compare with the direct in flight measurement. I summarise the results of this chapter in section 5.6.

5.1 Previous studies comparing satellite retrievals and in situ measurements of τ and r_{eff}

Part of a development of every remote sensing measuring technique is its validation by comparison with in situ data. For the cloud optical depth and cloud droplet

effective radius retrieval techniques based on the solar reflectance method there are relatively few studies comparing remote sensing results with the in situ observations.

Validation for satellite born sensors is complicated by the necessity of spatially and temporally coordinating the in situ measurements (aircraft missions) with the satellite overpass. Two comparison protocols can be employed: along a flight track comparison, and area comparison. The choice of the specific protocol depends often on the time lapse between the satellite and the in situ measurements.

Along a flight track pixel-by-pixel comparisons are meaningful if the time difference between measurements is small. Platnick and Twomey (1994), Nakajima and Nakajima (1995) compared pixel-by-pixel aircraft and satellite measurements taken within a 1 hour time window. Large time gaps between measurements affect the accuracy of comparison twofold: 1) navigation errors increase with time separation (couple of kilometres); 2) cloud undergoes changes in time. Area comparisons involve computing and comparing mean statistic or frequency distributions of cloud properties measured in situ and by satellite over the region of operation. This is the preferred strategy in case of longer time gaps between measurements.

Three studies analysed and compared AVHRR retrievals of cloud optical depth and cloud droplet effective radius with aircraft in flight measurements (Platnick and Twomey (1994), Nakajima and Nakajima (1995), Platnick and Valero (1995)).

Platnick and Twomey (1994) compared their AVHRR retrievals of cloud droplet effective radius for two FIRE (Californian stratus 1987) days to aircraft measurements of Rawlins and Foot (1990) and Radke *et al.* (1989). On June 30 1987 the AVHRR image was acquired within an hour of the in situ measurements and on July 10 1987 20 min prior to the aircraft measurement. Along a flight track comparison made for the June 30 case found the AVHRR overestimating r_{eff} by 1 μm compared to the in situ value. The flight on July 10 intersected two ship tracks in the stratocumulus layer (Radke *et al.* (1989)). Platnick and Twomey (1994) found

the average retrieved cloud droplet effective radius to be greater by 3-6 μm than the in situ values both in and out of the ship track. They attributed the difference to larger droplet sizes near the cloud top seen by satellite than in the middle of the cloud where the aircraft measurement was taken.

Nakajima and Nakajima (1995) compared AVHRR derived cloud optical depth and cloud droplet effective radius with in situ and remote aircraft measurements for two cloud scenes, one from FIRE (California, 1987) and one from the ASTEX (Azores, 1992) experiment. On the FIRE day a two-aircraft mission was coordinated with the NOAA satellite overpass. The University of Washington C-131A aircraft made microphysical measurements within the cloud using a Particle Measuring System (PMS) (Knollenberg (1981)) to acquire cloud droplet size distribution and a Johnson-Williams (Cloud Technologies) hot wire probe to measure the cloud liquid water content. The NASA ER-2 aircraft, equipped with the Multi-Channel Radiometer (MCR) flew above the cloud at the altitude of 18 km and measured cloud reflected radiances. Channels 1 (0.75 μm) and 6 (2.16 μm) of MCR were used to retrieve cloud optical depth and cloud droplet effective radius . On the ASTEX day the in cloud measurements were made by NCAR Electra FSSP probe and the Gerber probe (Gerber (1991)) flown on the C-131A.

For the FIRE day Nakajima and Nakajima (1995) adjusted the remote sensing values of the cloud droplet effective radius to the values at cloud geometrical centre (Nakajima and King (1990)) and compared these values with the in situ measurements. The AVHRR overestimated r_{eff} by about 1 μm . The overestimation by the MCR was larger (3-5) μm. Nakajima and Nakajima (1995) attributed the better performance of AVHRR to its use of the 3.7 μm wavelength rather than the 2.2 μm channel in MCR. The light absorption coefficient of water vapour and the imaginary index of refraction of liquid water have larger values at 3.7 μm and thus can be measured more accurately at this wavelength than at 2.2 μm. Additionally, the calibration of the 3.7 μm channel uses a blackbody standard which achieves

better accuracy than the less stable lamp used to calibrate the 2.2 μm channel on MCR.

Nakajima and Nakajima (1995) reported a very good spatial correlation along the fight path between AVHRR, MCR and in situ cloud optical depth , except for sharp dips in the in situ measurement which are less pronounced in the AVHRR data. This discrepancy is attributed to the large field of view of the AVHRR instruments (1 km) as compared to MCR (120 m) and 10 Hz sampling rate of the aircraft probes.

On the ASTEX day the cloud droplet effective radius measured by FSSP at the cloud top was within 1 μm of the AVHRR estimate. There was also good agreement between averaged values of r_{eff} measured by AVHRR and the Gerber probe. In this case, the 2 hours difference between the satellite overpass and the Gerber probe flight precludes more meaningful comparisons.

Another ASTEX day was studied by Platnick and Valero (1995) who compared AVHRR retrievals of cloud optical depth and cloud droplet effective radius and the in situ measurements with the Gerber probe and the FSSP during the C-131A flight. The AVHRR estimates of τ and r_{eff} fall between the values obtained by the two in situ instruments. For the area of approximately 11 km^2 (3×3 pixels) where the in situ measurement was taken during the satellite over pass AVHRR overestimated r_{eff} by 2.4 μm and underestimated τ by 2.2 compared to FSSP and underestimated r_{eff} by 1.7 μm and overestimated τ by 1.8 when compared to the Gerber probe measurements. For a large scale region of approximately 40 $km \times 100$ km the mean AVHRR r_{eff} was greater the FSSP value by 2.5 μm and smaller than the Gerber probe measurement by 2.9 μm.

The systematic overestimation of cloud droplet effective radius by remote sensing measurements is a manifestation of anomalous cloud absorption (Twomey and Cocks (1989), Stephens and Tsay (1990)) and has not yet been explained. My comparison of satellite and in situ measurements of cloud droplet effective radius

confirms the remote sensing tendency to overestimate r_{eff} by 1-3.6 μm for single layer clouds.

In my analysis I compare the distributions of cloud optical depth and cloud droplet effective radius inferred from satellite observations over the region of aircraft operation with the aircraft measured flight average cloud properties (area comparison). This strategy was dictated by our goal of testing the model (3.2) on large scales (100 km).

5.2 Outline of the analysis

The goal of this chapter is to test the model (3.2) and compare the AVHRR retrievals of cloud optical depth , cloud droplet effective radius and N_{sat} with aircraft in situ measurements obtained during the SOCEX experiment. The test consists of the following steps:

1. I use the FSSP measured liquid water content and effective radius data to compute estimates of cloud optical depth at several levels in the cloud layer according to equation
$$\tau = \frac{3}{2\rho}\int_0^{\Delta z}\frac{lwc}{r_{eff}}dz; \tag{5.1}$$

2. I compare the aircraft derived cloud top values of τ and r_{eff} with the satellite retrievals of τ and r_{eff} for the area of aircraft operation.

3. I establish whether the relationship between τ and r_{eff} obtained from aircraft measurements follows (3.2) by fitting a general power law to the aircraft measured τ and r_{eff};

4. if (3.2) is valid, an estimate of N_{sat} can be obtained from aircraft measurements of τ and r_{eff};

5. aircraft measurements of cloud liquid water content vertical profile allow us to obtain an independent estimate of cloud subadiabaticity β and thus decouple

cloud droplet number concentration N from β in N_{sat} ;

6. I compare N inferred from N_{sat} and β with N measured directly by FSSP mounted on the aircraft;

7. I obtain estimates of N_{sat} from satellite measurements and use aircraft estimated β to decouple N_{sat} and N;

8. I compare satellite and aircraft estimates of cloud droplet number concentration N.

5.3 Aircraft cloud sampling during SOCEX

The C-130 aircraft made microphysical measurements (liquid water mixing ratio, cloud droplet number concentration , droplet size distribution), with the FSSP probe, the Gerber probe, and the King probe (King *et al.* (1981)) and the PMS 2D-C imager (Boers *et al.* (1997)). FSSP was the only instrument from which lwc, r_{eff} and N were consistently available for all flights thus the analysis presented in this chapter is based on the FSSP data. The 6 analysed SOCEX flights are listed in table 5.1 (page 96) with their date and time and the time of the closes satellite overpass.

Figure 5.1 (page 96) shows a flight path of a typical SOCEX flight mission (flight 10). The flight path is drawn over the channel 1 AVHRR image. Figure 5.1 shows a flight path of a typical SOCEX flight mission (flight 10). The flight path is drown over the channel 1 AVHRR image.

SOCEX flight missions consisted of several horizontal stacks flown at different levels within a cloud layer. Figure 5.2 (page 97) shows the vertical stratification of the horizontal stacks in flight 10. Time is in minutes from the start of the flight. The time series corresponds to 1 Hz instrument sampling rate (averaged from original 10 Hz data).

Flight No.	Day	Flight Time (local)	Satellite orbit No.	Satellite time (local)
6	February 1	09:41-14:10	NOAA 9 52266	10:07
7	February 1	15:37-19:08	NOAA 14 00462	15:49
8	February 6	15:11-18:40	NOAA 14 00532	14:55
9	February 8	09:45-13:30	NOAA 9 52365	10:17
10	February 8	15:15-19:02	NOAA 14 00561	16:14
11	February 9	10:03-13:48	NOAA 9 52379	10:04

Table 5.1: SOCEX flight missions and coordinated satellite overpasses.

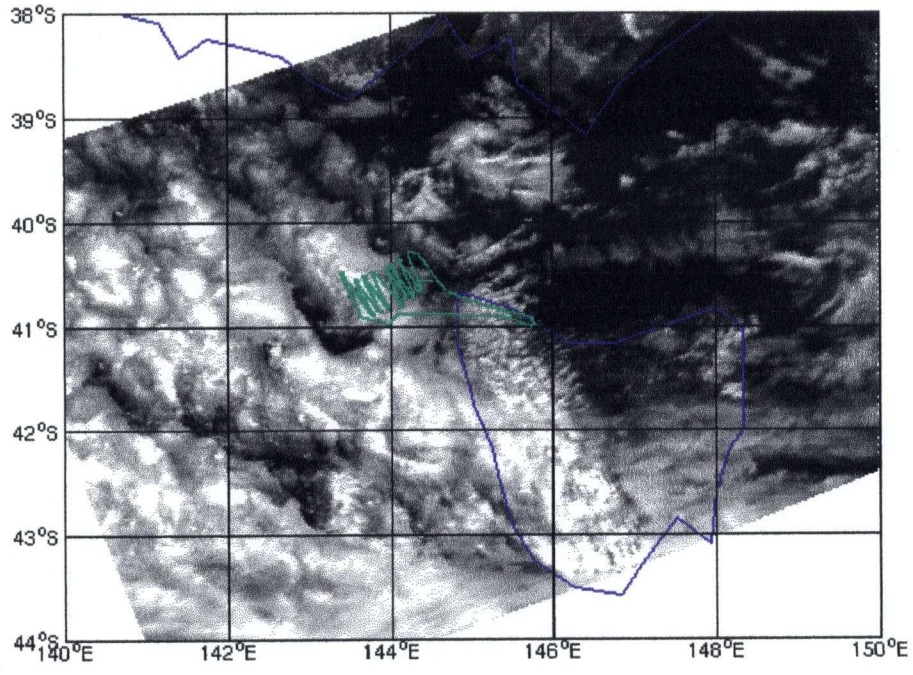

Figure 5.1: Flight path of SOCEX flight no. 10 overlayed on channel 1 AVHRR image.

The entire flight took about $3\frac{1}{2}$ hours. The horizontal in cloud sampling legs were flown for approximately 10 minutes each, corresponding to about 48 km. Similar flight patterns were executed in all flights.

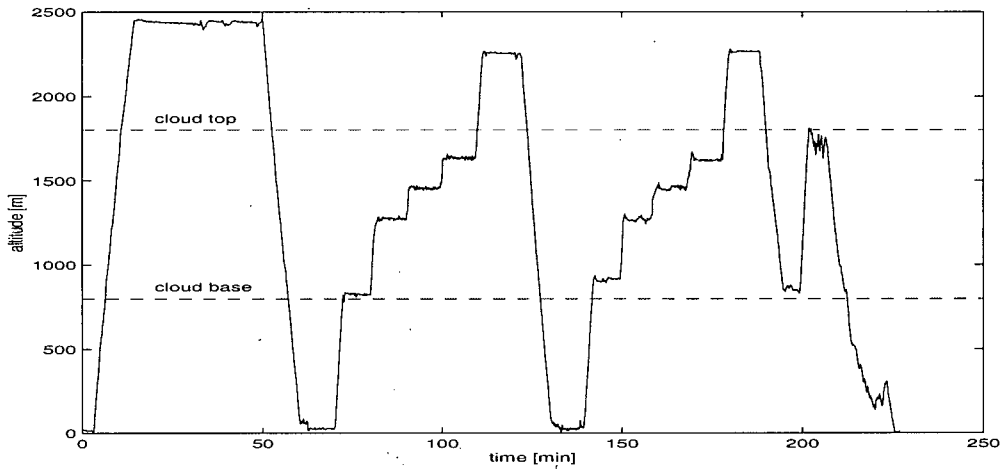

Figure 5.2: Aircraft vertical cloud sampling pattern (horizontal stacks) in SOCEX flight no. 10. Time is in minutes from the start of the flight. Flight average cloud top and cloud base are indicated by the dashed lines.

Such a sampling strategy is not ideal from the point of view of the analysis attempted in this chapter. A number of constant rate ascent/descent sounding flights, when many altitudes are sampled with the same weight, would be preferable. Since no sounding flights are available I use the stack flight data to produce an flight average sounding for each of 6 flights considered. Every flight average represents an area of approximately 50 $km \times 100$ km. This area is sampled over a time of $1\frac{1}{2}$ hours.

5.4 Flight average soundings, estimation of β and τ.

Figures 5.3a-f show the flight average FSSP liquid water content (*lwc*) soundings computed for the 6 SOCEX flights. Only the cloud sampling part of each flight was included in the average. Samples with FSSP measured $lwc < 0.005\ gkg^{-1}$ were considered noise (Paul Krummel private communication) and were excluded from the average. The data were sorted according to altitude and averaged over intervals corresponding to 2 minutes of sampling time. The dashed line in figures 5.3a-f represents the adiabatic liquid water profile starting at cloud base.

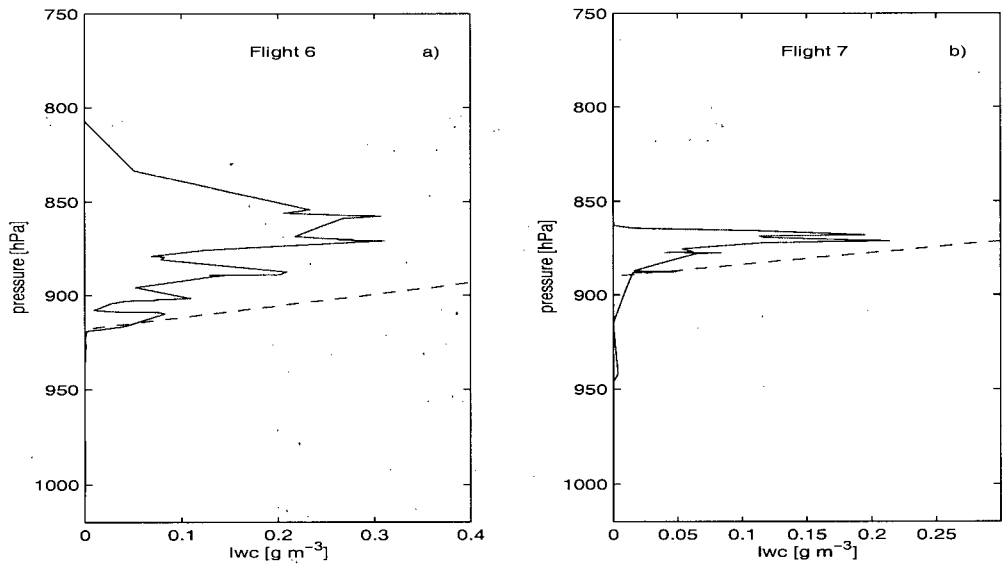

Figure 5.3: Flight average liquid water profiles. a)-f) flights 6-11 respectively. Dashed lines indicate the adiabatic liquid water profile.

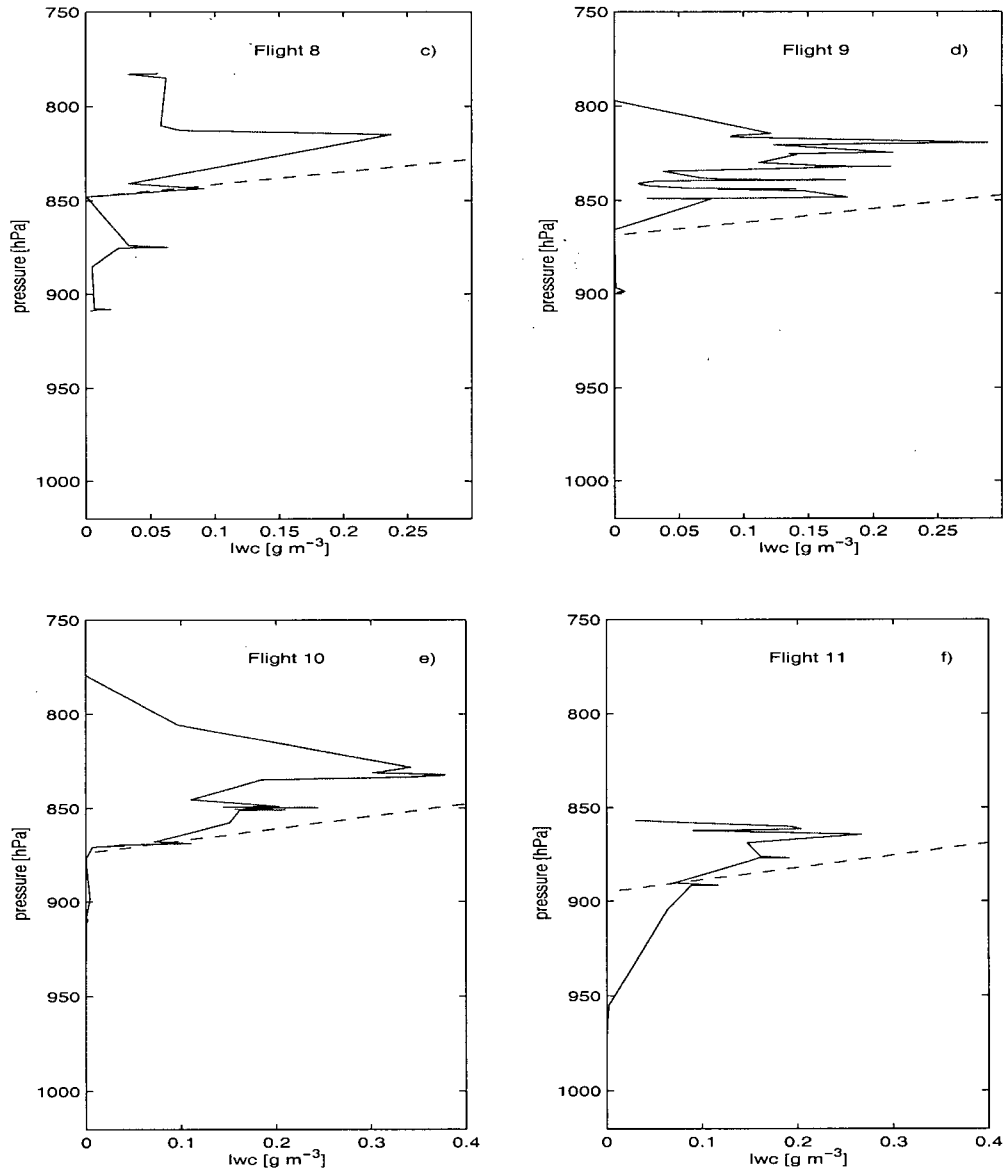

Figure 5.3 continued.

In figures 5.4a-f I show flight average profiles of cloud droplet number concentration (N) in the 6 SOCEX flights.

The flight average cloud profiles reveal a complex multilayer structure in the

sampled clouds. Flight notes (Paul Krummel private communication) describe the cloud system on all flight days as clearly decoupled stratus layer with penetrating convective turrets or convective lines. The multilayer cloud structure was most apparent in flight 8 where at least two cloud layers were separated from each other by discontinuities in thermodynamic variables. All flights with the exception of flight 7, reported drizzle. Flights 8 and 11 had the highest drizzle (rain) rates up to 160 $mm\ day^{-1}$ and 70 $mm\ day^{-1}$ respectively. The occurrence of drizzle and rain suggests the presence of strongly non-adiabatic clouds in the area of measurements. I found the lowest values of cloud subadiabaticity β for flights 8 and 11 which also reported the highest drizzle (rain) rates of the experiments.

The cloud subadiabaticity was found as the ratio of the actual and adiabatic rate of increase of the cloud liquid water content with height within the cloud layer. For each flight the adiabatic rate of increase was computed for the pressure and temperature conditions at cloud base and the actual rate of increase of the cloud liquid water content with height was found from the linear least square fit to the flight average *lwc* profile as function of altitude over the range from cloud base to the height where *lwc* begins decreasing with height. Table 5.2 contains the estimates of cloud subadiabaticity β and its uncertainty σ_β for the 6 SOCEX flights. The uncertainty σ_β in table 5.2 is the uncertainty of the parameter estimation from the least square regression of the cloud liquid water content data on height.

Higher level clouds were occasionally present. High level cirrus was reported for flight 8, satellite imagery shows streaks cirrus clouds on flights 9 and 11 although not directly over the flight area.

Aircraft sampling was usually confined to the stratus layer between 700 to 1800 m and only occasionally were the convective lines sampled. This biases the aircraft data towards smaller optical depths when compared with the satellite retrievals of cloud optical depth for the aircraft operation region. In fact, the satellite retrievals often indicate a presence of very thick clouds in the vicinity of the aircraft.

The bias will be most apparent in flight 7 which did not transect any convective elements.

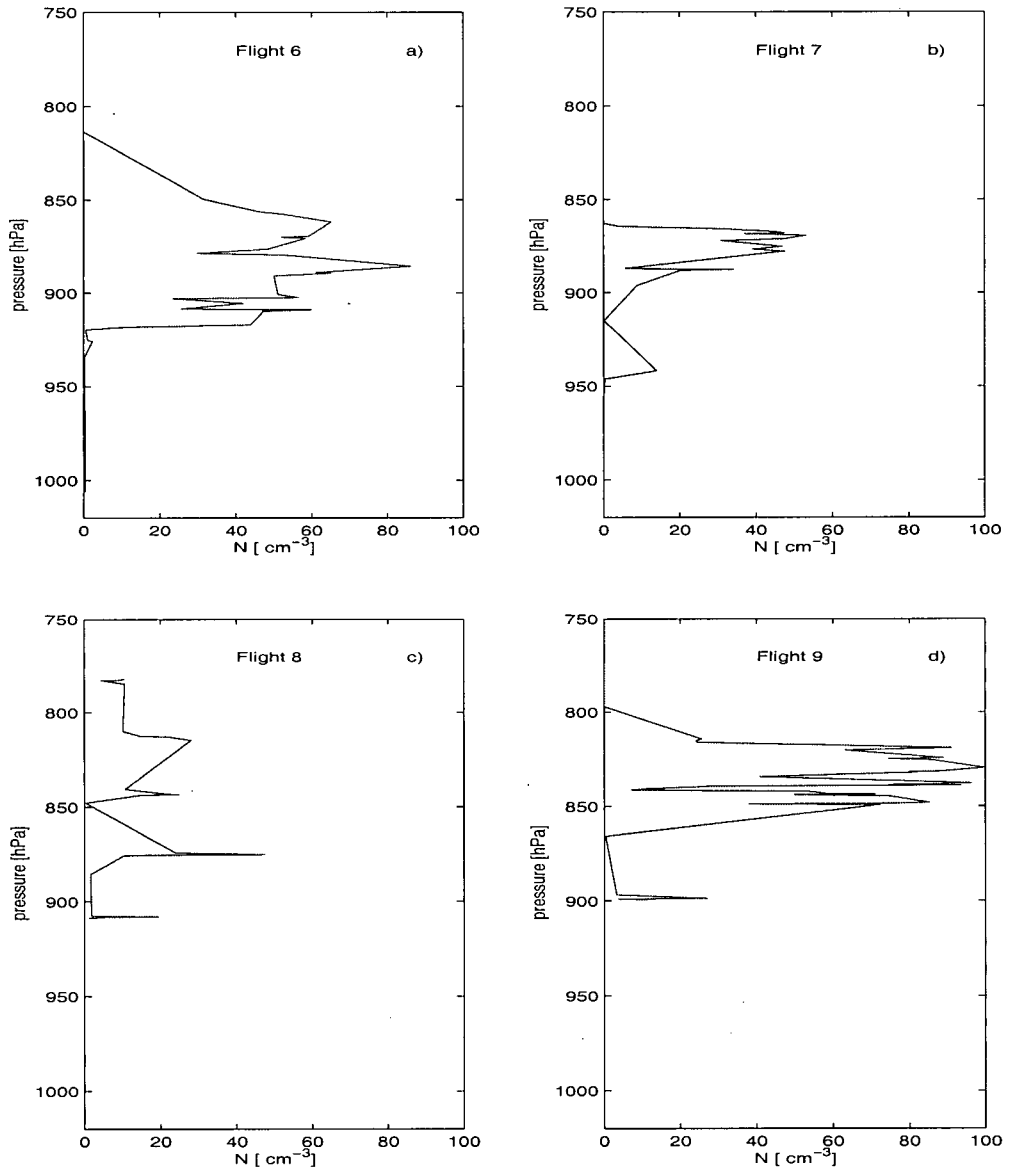

Figure 5.4: Flight average cloud droplet number concentration profiles. a)-f) flights 6-11 respectively.

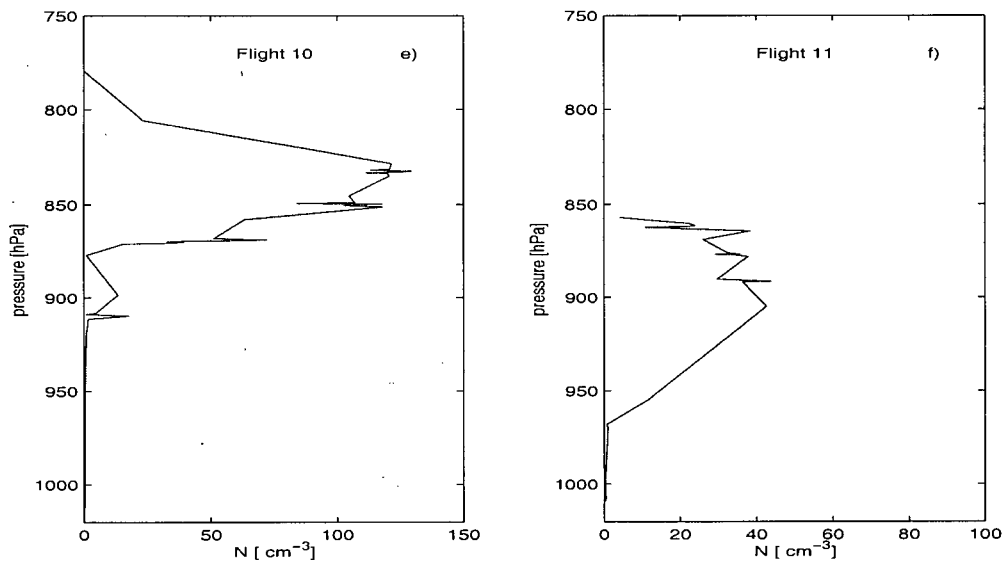

Figure 5.4 continued.

The aircraft flight average cloud optical depth profiles are shown in figure 5.5a-f. The highest observed τ was about 28 on flight 10 and the smallest one was about 5 on flight 7 which did not cross any convective turrets. In section 5.5 I compare the satellite and aircraft estimates of cloud optical depth and cloud droplet effective radius .

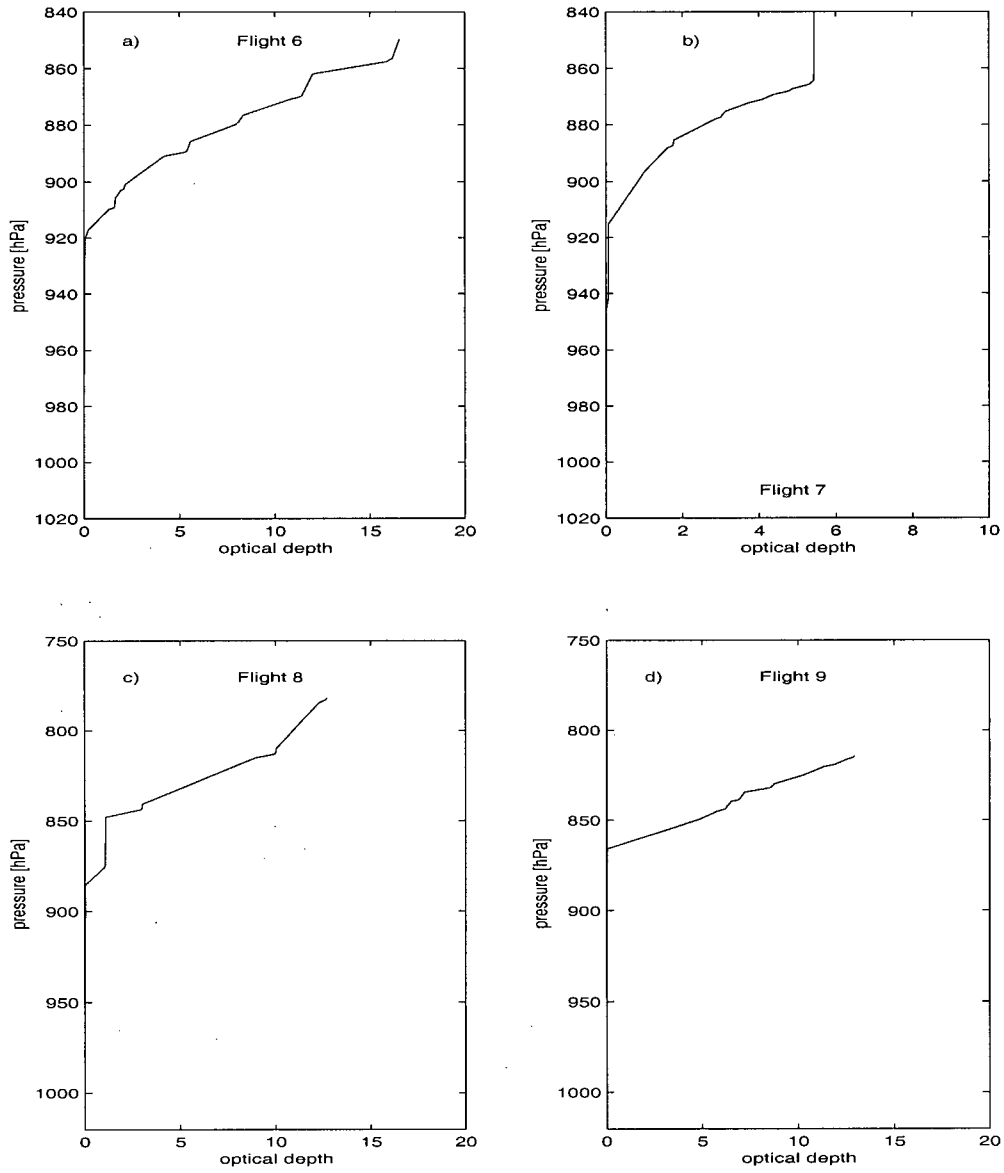

Figure 5.5: Flight average cloud optical depth profiles. a)-f) flights 6-11 respectively.

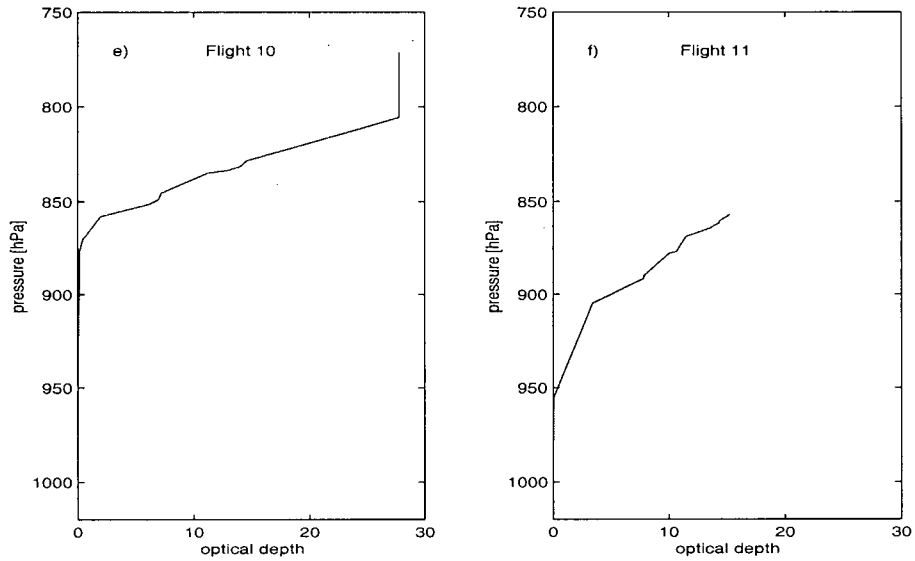

Figure 5.5 continued.

5.5 Comparison of satellite and aircraft observations in the $r_{eff} - \tau$ plane.

The comparison of the satellite and aircraft derived cloud optical depth and cloud droplet effective radius in the $r_{eff} - \tau$ plane allows for simultaneous comparison of the measurements of these two parameters and at the same time tests the cloud parametrisation 3.2.

We have seen in chapters 3 and 4 that the model (3.2) accurately describes the character of the correlation between cloud optical depth and cloud droplet effective radius in satellite data. However, since neither cloud subadiabaticity nor cloud droplet number concentration are available directly from satellite measurements, a more stringent test of the model, based solely on satellite data is not possible. Aircraft in situ cloud observation can provide measurements of cloud droplet number concentration , cloud droplet effective radius , cloud optical depth and estimates

of cloud subadiabaticity , and thus are ideal for testing the validity of (3.2) and assumptions leading to it.

In figure 5.6a-f I plotted, in the $r_{eff} - \tau$ plane, the satellite (blue points) and aircraft (red stars) measurements of cloud optical depth and cloud droplet effective radius for the 6 SOCEX days respectively. The aircraft measured τ and r_{eff} represent cloud optical depth from the mean cloud base to the altitude of the aircraft and cloud droplet effective radius at that altitude. This is what the satellite would see if the part of the cloud above the aircraft was stripped away.

The solid red line represents the "1/5" power curve of equation (3.2) with the cloud subadiabaticity β estimated form aircraft averaged cloud liquid water content sounding in section 5.4 and cloud droplet number concentration found from the general power law fit to flight average τ and r_{eff} data of each flight and the estimated value of β. These values of the cloud droplet number concentration are listed in table 5.2 together with their range $N_- - N_+$ corresponding to the uncertainty of the intercept estimated by the least square method.

The general power law fit ($\tau = \alpha\, r_{eff}^b$) to the flight average aircraft τ and r_{eff} data yield the exponent of "1/5" within 20-50% error bars estimated by the least squares method on all but one flight (flight 7). Table 5.2 contains the results of the general power law fit to the aircraft data for all flights.

Data points at the cloud base with cloud liquid water content less 0.005 $g\ cm^{-3}$ and data points at the cloud top above the level where cloud liquid water content begins to decrease with height (entrainment layer) were excluded from the fit. The log-transformed linear least square method with errors in both variables was used in fitting the power law to the data. The standard deviation of the 2 minute averages used to compute the flight average profiles of τ and r_{eff} was assumed as the errors of τ and r_{eff} (see 5.4).

In case of the very thin cloud in flight 7, retaining for the fit the very low cloud liquid water content samples near cloud base brings down the exponent b from

0.60 ($\pm$0.30) to 0.18($\pm$0.03) and changes the intercept value significantly (from 1.37 to 2.01 which corresponds to cloud droplet number concentration change from 261 to 53 cm^{-3}). The second value, N =53 cm^{-3} is used to plot the "1/5" power curve in figure 5.6b and appears to represent the data well.

The examination of Figure 5.6 reveals:

1. The aircraft data are likely biased towards the smaller cloud optical depth due to the sampling strategy.

2. Both, the satellite and the aircraft measured τ and r_{eff} appear to follow the "1/5" power law.

3. In 5.6a, d and f the cluster of satellite data lays clearly above the curve of aircraft measurements indicating an overestimation of r_{eff} by satellite retrievals.

To assess the size of the satellite overestimation of r_{eff} I plotted in Figure 5.7 the aircraft data (same as in Figure 5.6, red (*)) and satellite retrieved r_{eff} averaged over intervals of $\Delta\tau$=1 (blue line). In view of (3.2) I will compare aircraft and satellite r_{eff} only for the same τ. In Figures 5.7a, d and f the line representing satellite date is shifted by approximately 0 to 5 μm towards larger values of r_{eff} than those observed by aircraft at the same cloud optical depth. I computed the $RMSD$ (root mean square deviation) between the aircraft and satellite r_{eff} for $\tau > 1$ and indicated the values in Figure 5.7. The average $RMSD$ for all flights is 2.88 μm. The $RMSD$ is greatest in case 5.7d (flight 9) where there are sections in aircraft data where r_{eff} decreases with increasing τ. Such behaviour may be expected in multilayer clouds. The lwp profile for flight 9 was shown in Figure 5.3d on page 98. Large fluctuations of lwp with height support the argument of multilayer structure of clouds encountered on that day. For clouds with single layer structure the overestimate of r_{eff} by remote sensing is between 0 and 3.6 μm and is not a function of τ.

Strictly speaking, since the satellite sees only top of the cloud values one should compare r_{eff} at τ corresponding to the cloud optical depth measured by aircraft near the cloud top.

Unusually good agreement is observed for flight 10 (Figure 5.7*e*). For flight 7 and 8 (Figures 5.7*b*) and *c* the agreement is poor. In case of flight 7 the selective aircraft sampling (in thin cloud only) may contribute to the different picture emerging from the aircraft and satellite data. In flight 8, the satellite data seem to indicate a variable cloud droplet number concentration (r_{eff} decreasing with τ). However, this structure is not resolved by the aircraft measurement.

To make a stronger argument in favour of the model expressed by (3.2) I apply this equation to aircraft measured cloud optical depth and cloud droplet effective radius data to infer the cloud droplet number concentration according to (4.9) (see section 4.3) and compare these values with those actually measured during the aircraft mission by the FSSP probe. The values of cloud droplet number concentration N and the range of uncertainty $N_- - N_+$ inferred based on (3.2) are given in table 5.2. Comparing these values of N and $N_- - N_+$ with the actual measurements (see figure 5.4) I find that the inferred cloud droplet number concentration well represents the range of the observed N.

Values of cloud droplet number concentration inferred from AVHRR estimates of N_{sat} and estimates of cloud subadiabaticity β from corresponding in flight measurements are given in column N^* of Table 5.2. Since the satellite retrievals tend to overestimate the cloud droplet effective radius we expect that the cloud droplet number concentration inferred from satellite measured τ and r_{eff} will underestimate N with respect to the in situ value.

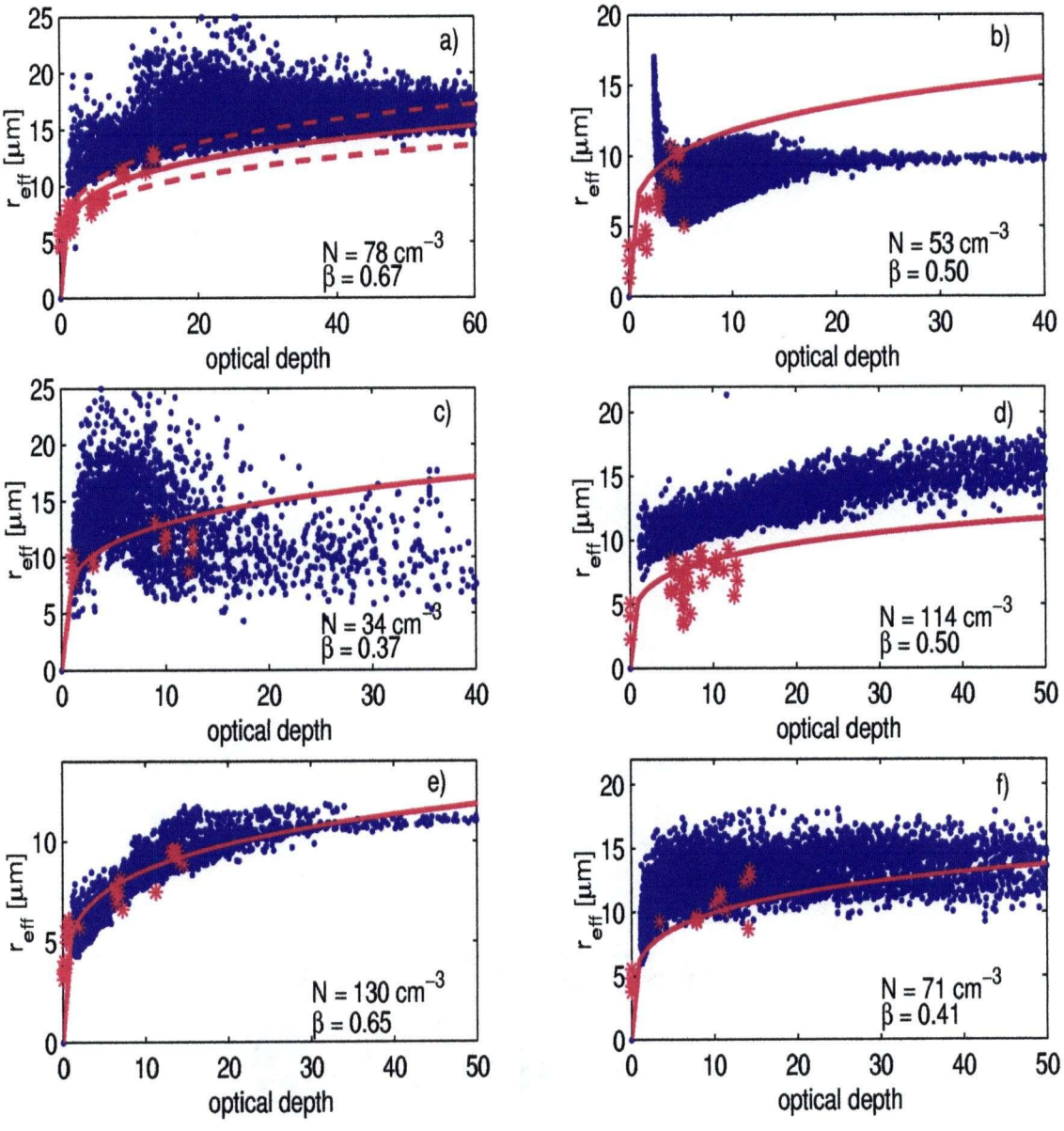

Figure 5.6: Scatter plots of satellite retrieved τ and r_{eff} (blue points) and in situ aircraft measurements (red stars) for 6 SOCEX days, a)-f) flights 6-11 respectively. Solid red lines is the "1/5" power law curve with cloud droplet number concentration (N) obtained from the least square fit to the aircraft data and cloud subadiabaticity β estimated from the flight averaged cloud liquid water profile (lwc). In figure a) the dashed lines indicate the uncertainty in N estimated by the least square method (see table 5.2).

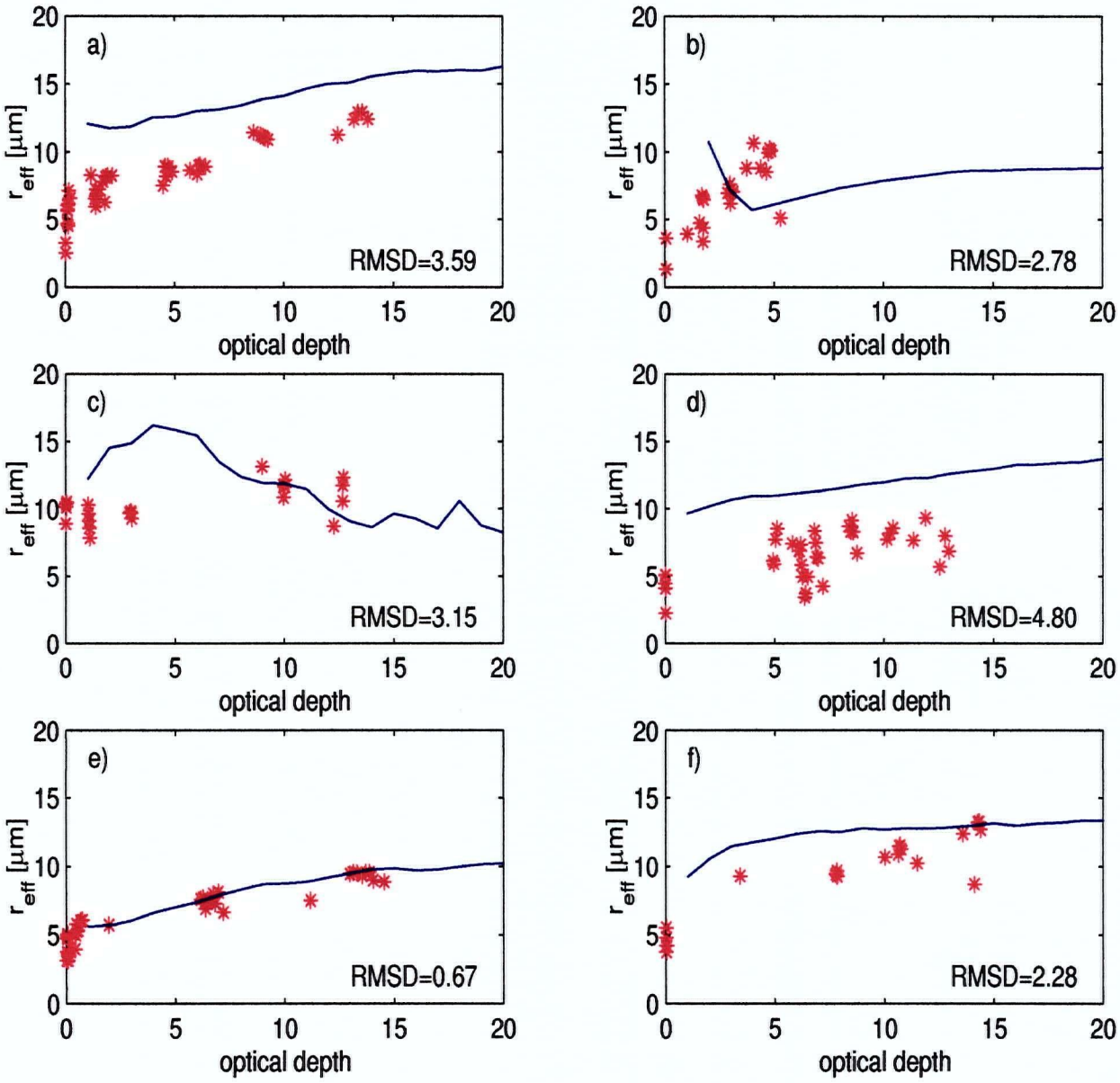

Figure 5.7: Plots of satellite retrieved τ and r_{eff} averaged over intervals $\Delta\tau$=1 (blue lines) and in situ aircraft measurements (red stars) for 6 SOCEX days, a)-f) flights 6-11 respectively.

This can be best seen in flights 6 and 9 where the cluster of satellite data lies clearly above the line fitting the aircraft data. In figure 5.6d for flight 9 the fitted line does not appear to be the best fit to the data. There are few data points clearly below the best fit line suggesting that the best fit line should lie lower than it does. However, these data points are burdened with large uncertainties and thus contribute little weight to the regression.

The satellite underestimate of N for flight 9 is almost 60 cm^{-3}. It is less severe for flight 6, only 25 cm^{-3} which is within the uncertainty of N estimates from satellites (see section 4.3). For flight 10 the agreement between satellite retrievals and aircraft in situ measurements is very good. The line fitted to aircraft measurements represents well both aircraft and satellite data. The good agreement in this case is likely due to a relatively uniform cloud layer sampled during this flight.

Flight No.	τ	a	σ_a	b	σ_b	β	σ_β	N $[cm^{-3}]$	$N_- - N_+$ $[cm^{-3}]$	N^* $[cm^{-3}]$
6	17	1.91	0.12	0.22	0.05	0.67	0.11	78	58 - 105	59
7	5	1.37	0.58	0.60	0.30	0.50	0.11			
		(2.01)	(0.05)	(0.18)	(0.03)			53	46 - 60	155
8	13	2.10	0.25	0.18	0.10	0.37	0.06	34	18 - 64	34
9	13	1.68	0.09	0.19	0.04	0.50	0.12	114	91 - 143	58
10	28	1.69	0.12	0.21	0.05	0.65	0.06	130	96 - 176	154
11	15	1.84	0.15	0.25	0.06	0.41	0.12	71	49 - 104	51

Table 5.2: Validation of the cloud parametrisation given by equation (3.2): results of the general power law fit to the SOCEX aircraft data, estimates of cloud subadiabaticity β from aircraft in situ cloud liquid water content profiles, estimates of cloud droplet number concentration N (and range of uncertainty $N_+ - N_-$ based on equation (3.2) and aircraft measurements. N^* are estimates of cloud droplet number concentration based on satellite measurement of N_{sat} and aircraft estimate of β.

5.6 Summary

During the Australian SOCEX II experiment January/February 1995 aircraft in situ cloud sampling missions were flown within 3 hours of polar orbiters overpasses. This provided an opportunity for a validation of the satellite retrievals and the cloud parametrisation based on (3.2) by comparison with the aircraft in situ data.

I have found that the occurence of very thick pixels in satellite data is not always confirmed by aircraft observations. This might be the effect of the complex multiple layer structure of sampled clouds, the sampling strategy of avoiding the convective cores, or large time lag between the aircraft and satellite observations.

Typically, both the aircraft and satellite data are well described by the parametrisation of equation (3.2). An exception is the case of flight 8 where the cloud layer was very nonuniform. This is reflected in both the aircraft soundings and in the satellite data where the scatter plot of τ and r_{eff} indicates high inhomogeneity in cloud droplet number concentration..

The cloud droplet number concentration N inferred from aircraft estimates of τ and r_{eff} and cloud subadiabaticity β agrees well with the range of N measure in situ. This constitutes a strong argument in favour of the cloud reference model (3.2).

The cloud droplet number concentration infer from satellite measurements of cloud optical depth and cloud droplet effective radius typically underestimate the actual values of N. This tendency is related directly to the satellites overestimation of r_{eff}.

Chapter 6

Spatial structure of stratocumulus clouds I: Basic concepts and definitions

In previous chapters I have been concerned almost exclusively with one point statistics. In this chapter I extend the analysis to include two point statistics and investigate the spatial structure of fields of cloud parameters. I employ a combination of spectral and multifractal analysis (section 6.4) to quantify the stationarity and intermittency of cloud fields. I state the problems I will address through this analysis in section 6.1. In section 6.2 I introduce the concepts of scale invariance, stationarity, and singularity in stochastic processes. I discuss earlier observations of the spatial structure of clouds in section 6.3 obtained with a traditional spectral analysis approach. In section 6.4 I present the formalism of multifractal analysis (as proposed by Davis *et al.* (1994)) which I employ in analysis of my data. In section 6.5 I discuss results obtained with the multifractal approach in earlier studies of cloud structure. The results of the analysis for my own data are presented in the chapter 7.

6.1 Questions

In previous chapters I have shown that

1. I can find mesoscale cloud fields with a uni-modal distribution of τ and r_{eff} obeying the reference cloud model;

2. bi-modal distributions of τ and r_{eff} occur due to spatial variability of N_{sat} on scales approaching the scene size; departures from (3.2) are caused by spatially variable N_{sat} in these scenes;

3. a two parameter gamma function accurately describes frequency distributions of τ for all types of scenes, but the frequency distribution of r_{eff} is often negatively skewed even in uni-modal scenes and cannot be well approximated by a gamma function.

In this chapter I ask: How is the variance of τ and r_{eff} distributed as a function of scale?

I will show, as others have (see section 6.3), that over a limited range of spatial scales, the variance of τ, r_{eff} and the visible wavelength cloud radiance is described by a power law. The power law dependence on scale is called scaling and the domain in which it holds is called the scaling regime.

Scaling behaviour may reflect an underlying physical mechanism that is recursive and internally generated and thus representative across a wide range of conditions. Its presence also permits a particularly simple representation of fluctuating fields in models. The scaling range determines a minimum averaging scale of the process. Therefore, it is important to understand the spatial properties of cloud parameters, especially the scaling behaviour of these fields and factors which determine the scaling regime.

In addition, from the point of view of cloud processes, it is interesting to ask whether cloud spatial and scaling properties are universal. Such universality would point to the common nature of the non-linear processes that determine cloud internal structure.

With these concerns in mind I define the terms employed in this analysis and proceed to review some recent work which has focused on spatial structure of clouds.

6.2 Stochastic processes and geophysical data sets

Multifractal analysis considers three properties of variable fields: scale invariance, statistical stationarity and stochastic continuity. This section introduces the concepts of statistical stationarity, continuity and scale invariance and explores dependencies between them in physical and Fourier space.

6.2.1 Scale invariance in stochastic processes

Let $\varphi(x)$ denote a real-valued random process defined on finite interval $(0 \leq x \leq L)$. Process $\varphi(x)$ is said to be stochastically self-similar (scale-invariant or scaling) if the probability distribution of $\varphi(x)$ satisfies the equation

$$\{\varphi(\lambda x)\} = \{\lambda^H \varphi(x)\}, \qquad \lambda > 0, H \in \mathbf{R} \tag{6.1}$$

Scaling in this distribution sense is known as *strict − sense scaling* as opposed to *wide − sense scaling* which refers to scaling in the covariance function (moments of the distribution).

The process in (6.1) represents simple scaling (monoscaling) where variability of the process is scale independent. It follows from (6.1) that the moments $E(\varphi^q)$ of the process, where q is the order of the moment, if they exist, satisfy

$$E[\varphi^q(\lambda)] = \lambda^{\zeta(q)} E[\varphi^q(1)] \tag{6.2}$$

here $E[\cdot]$ denotes the expected value and $\zeta(q) = qH$. Thus, in case of simple scaling one exponent determines the scaling of all moments of the distribution.

Another class of processes scale as (6.2) but with $\zeta(q)$ that is a nonlinear, concave function of q. Processes which exhibit such behaviour are known as wide sense multiscaling. One also finds processes that are strict sense multiscaling (see Gupta and Waymire (1990) for definition and discussion). Many geophysical fields

belong to the category of the wide sense multiscaling processes (see for example Gupta and Waymire (1990), Davis *et al.* (1994)).

6.2.2 Statistical stationarity and stochastic continuity

Statistical stationarity (statistical invariance under translation in time or space) is crucial for obtaining meaningful statistics from data sets of geophysical measurements. Yet, this issue is rarely addressed in the analysis of geophysical data sets. The automatic assumption of stationarity is a common but potentially dangerous practice as the statistical properties are usually not well defined for nonstationary processes.

In the analysis of a geophysical data sets we are interested in the statistically well-defined properties of a particular realization of some geophysical process $\varphi(x)$. To focus our attention we can imagine $\varphi(x)$ to represent a transect of cloud liquid water path field. Let $\{\varphi_i\} = \varphi(x_i)$ represent a measurement on the process $\varphi(x)$ (satellite retrieval of *lwp* for example), which produces a discrete series of data equally spaced in x at points $x_i = il(i = 1,...,N)$ where l is the sampling scale and N is the total number of points. In this example $\{x_i\}$ correspond to satellite pixels. If the process $\varphi(x)$ is stationary then all n-point statistics computed for $\varphi(x)$ (or its particular realization $\{\varphi_i\}$) are independent of position x. In particular, the autocorrelation function, a two-point statistics defined as

$$G(r,x) =< \varphi(x)\varphi(x+r) >= G(r) \tag{6.3}$$

where $< \cdot >$ denotes ensemble average, is independent of the position x depending only on the distance r between two points.

Equation (6.3) is the so-called broad sense definition of stationarity based on only two-point statistics. The narrow sense definition uses all n-point statistics.

Stochasic continuity relates to correlations between neighbouring points. If for a small separation r, $\varphi(x+r)$ and $\varphi(x)$ are highly correlated then the increment $|\varphi(x+r)-\varphi(x)|$ is usually small and the data is stochastically continuous. If this increment is large then the data is discontinuous. In short, stochastic continuity requires that (Papoulis (1965))

$$< [\varphi(x+r)-\varphi(x)]^2 > \rightarrow 0 \quad as \ |r| \rightarrow 0 \tag{6.4}$$

For stationary processes

$$< [\varphi(x+r)-\varphi(x)]^2 >= 2[G(0)-G(r)] \tag{6.5}$$

thus $\varphi(x)$ is stochastically continuous if $G(r)$ is continuous at $r = 0$. Processes which are not continuous are intermittent (or singular).

The following three processes are often presented to illustrate the concepts of (non)stationarity, (dis)continuity and scaling (scale invariance) and nonscaling (Davis *et al.* (1996)).

1. White noise. White noise is a sequence of independent random numbers. Its autocorrelation function is

$$G(r) \propto \delta(r) \tag{6.6}$$

   where $\delta(r)$ is the Dirac δ. It can be seen from (6.6) that white noise is stationary (satisfies condition of (6.3)) but discontinues process (does not satisfy condition of (6.4)).

2. Brownian motion. Brownian motion is the integral of white noise. The one-point variance of Brownian motion depends on position (is proportional to $|x|$) and the two-point autocorrelation function depends on both x and r and has the form:

$$G(x,r) \propto |x| + |x+r| - |r|. \tag{6.7}$$

It follows from (6.7) that Brownian motion is a nonstationary process. At the same time it is a stochastically continuous process since $< [\varphi(x+r)-\varphi(x)]^2 > \propto r$.

3. Ornstein-Uhlenbeck processes. Contrary to white noise and Brownian motion Ornstein-Uhlenbeck process has a nonscaling autocorrelation function

$$G(r) \propto exp(-\frac{|r|}{R}) \tag{6.8}$$

where R is the integral scale of the process. Although not scale invariant, Ornstein-Uhlenbeck processes are both stochastically stationary and continuous ($< [\varphi(x+r) - \varphi(x)]^2 > \propto [1 - exp(-\frac{|r|}{R})]$ which goes to zero with $|r| \to 0$).

6.2.3 Scale invariance and stationarity in Fourier space

Let $\tilde{\varphi}(k), -\infty < k = 1/r < \infty$ be the Fourier transform of the stochastic process $\varphi(x)$ introduced in section 6.2.1. The energy spectrum E(k) (wavenumber spectrum, power spectrum, variance spectrum and power spectral density are equivalent terms) of the process $\varphi(x)$ is defined as

$$E(k) = \frac{1}{L} < |\tilde{\varphi}(k)|^2 + |\tilde{\varphi}(-k)|^2 >, \qquad k > 0 \tag{6.9}$$

where $< \cdot >$ denotes ensemble average (average over all possible realizations of $\varphi(x)$).

The Wiener-Khinchine theorem (Monin and Yaglom (1965)) guarantees that the autocorrelation function of stationary process $G(r)$ (defined in (6.3)) and the power spectrum $E(k)$ (defined in (6.9)) are Fourier transforms of each other. The

autocorrelation function of a stationary, scale invariant process is given by a power law

$$G(r) \propto |r|^{-\mu} \tag{6.10}$$

where the exponent μ has to be positive since the autocorrelation is expected to decrease as $|r|$ increases. Notice, that the singularity at $r = 0$ implies that stationary, scale invariant processes are necessarily stochastically discontinuous.

The Fourier transform of (6.10) leads to a power spectrum $E(k)$ in form of

$$E(k) \propto k^{-\beta} \tag{6.11}$$

where

$$0 < \beta = 1 - \mu < 1 \tag{6.12}$$

Equation (6.12) states a spectral criterion for stationarity: $\beta < 1$. It is interesting to consider the limiting cases: $\beta \to 0$ and, $\beta \to 1$. When $\beta \to 0$ we approach a flat power spectrum which correspond to $G(r) \propto \delta(r)$ (white noise) not $G(r) \propto |r|^{-1} (\mu = 1)$. In the limit $\beta \to 1$ ($1/f$ noise) (6.12) does not apply neither since the autocorrelation function (6.10) obtained in this limit (β=1, $\mu = 0$) gives $G(r) =$ constant which is not a power law and its power spectrum does not have the required form (6.11). $\mu \to 0$ indicates very long range correlations (longer than any power law such as (6.10) that is still integrable).

Summarising, if in a certain range of scales $\eta \leq r \leq R$ the power spectrum of a stochastic process $\varphi(x)$ follows a power law $E(k) \propto k^{-\beta}$ then the process $\varphi(x)$ is scale invariant in the range $\eta \leq r \leq R$. If, additionally, the exponent $\beta < 1$ then the process $\varphi(x)$ is stationary and discontinuous. If $\beta > 1$, then the process $\varphi(x)$ is nonstationary but can be continuous. Generally, process $\varphi(x)$ can be stationary at some scales and nonstationary at other. Typically, in atmospheric data on scales larger than the Kolmogorov dissipation range (typically *mm* to *cm*

in the atmosphere), the integral scale R separates the regions where $\beta \approx 0$ (large scales $r > R$) and regions where $\beta > 1$ (at small scales $r < R$). Thus, the integral scale constitutes a threshold between the small scale nonstationary regime and large scale stationarity. From the continuity point of view, data are highly correlated at scales $< R$ and essentially uncorrelated at scales $> R$.

The upper bound R of the scaling range has to exist for all physical processes with $\beta > 1$. These processes have finite variance in all wavenumbers k but as $k \to 0$ arbitrary amounts on energy (variance) accumulate in the large scales. Since variance cannot be infinite, $E(k)$ has to approach a constant value as we move towards small k.

This has important implications for modellers. Parametrisations used in models should be based on inference from data which are stationary (extent over a range $r > R$). Observational averages restricted to scales $< R$ are missing important portion of the variability of the field.

6.2.4 Scale invariant nonstationary process with stationary increments

The nonstationarity of the process ($\beta > 1$) does not preclude the existence of stationary features in the data set. Mandelbrot and Ness (1968) introduced a class of scale invariant processes whose increments $\Delta\varphi$ satisfy the equation

$$\{\Delta\varphi\} = \{\varphi(x_0 + \lambda r) - \varphi(x_0)\} = \{\lambda^H[\varphi(x_0 + r) - \varphi(x_0)]\} \tag{6.13}$$

for any $x_0 \in \mathbf{R}$ and $\lambda > 0$. Equation (6.13) defines a process whose increments are scale invariant and stationary. Notice that obtaining increments of a process in physical space (taking a gradient or nearest neighbour differences) is equivalent to changing the slope of the power spectrum by 2 in the Fourier space ($\beta \to \beta - 2$). Thus, the spectral criterion for a nonstationary process with stationary increments

is $1 < \beta < 3$. Conversely, one can obtain a nonstationary process with stationary increments by an integration of a regular stationary process ($\beta < 1$).

Many geophysical fields are, over some range of scales, nonstationary with stationary increments. For example, the turbulent velocity field in the inertial subrange is nonstationary ($\beta \approx 5/3$) but the squared velocity gradients which represent energy dissipation filed are stationary although highly intermittent. In the next section I discuss observations which indicate that the spectral exponents for one dimensional transects of cloud liquid water content (lwc) fluctuation generally fall within the range β = 1.3 - 2.0. From the standpoint of the stationarity analysis lwc fluctuations constitute moderately nonstationary process with stationary increments. This moderate nonstationarity in the lwc field can be a disadvantage when gradient fields are to be considered. Processes with $\beta < 2$ yield irregular gradient fields with $\beta < 0$. The cloud optical depth and cloud radiance fields considered in this study corresponds to vertically integrated lwc. In a sense, τ is a smoothed version of lwc. With spectral exponents between 2 and 3 (see Barker and Davies (1992), section 7 of this thesis) transects of cloud optical depth (cloud radiance) should be better suited for the analysis involving gradient fields than transects of lwc.

I should mention that there are ways of circumventing the difficulties of dealing with $\beta < 0$ gradient fields (Schmitt *et al.* (1992)) by carrying out a fractional differentiation. This, of course, complicates the analysis.

6.3 Previous work: Fourier analysis approach

In the traditional approach one investigates the scaling behaviour of cloud fields by means of Fourier analysis with an objective to find the scaling range, the power law exponent (β in (6.11)) and possible scale breaks.

Scale invariance has been observed in the AVHRR fields of cloud radiance

visible and thermal channels by Barker and Davies (1992). They found two scaling regions in the AVHRR images of shallow cumuliform clouds off the east cast of North America. For the smallest scales (less than about 5 km) the wave number spectra of visible and infra-red radiances followed the -3 power law. At larger scales the spectral slope varied between scenes but was in the range of -1 to -5/3. This change in scaling (spectral slope) was similar to that observed by Cahalan and Snider (1989) in Landsat Thematic Mapper images of California stratocumulus although the scale break (-3 to -5/3) occurred at about 200 m in this case. Whereas Cahalan and Snider (1989) related the scale break at 200 m to the scale of cloud geometrical thickness, Barker and Davies (1992) relate the scale break at 5 km to the size of typical cloud cells in their images. The 200 m scale break observed by Cahalan and Snider (1989) in Landsat radiance fields was not confirmed by in situ aircraft observations of cloud *lwc* (Davis *et al.* (1996)). Recently, Davis *et al.* (1997a) have shown, using fractal cloud models and Monte Carlo radiative transfer simulations, that the 200 m scale break in Landsat cloud scenes is caused by radiative smoothing due to horizontal photon transport. The scale break which occurs at 5-20 kilometres is however seen in aircraft *lwc* measurements and (Davis *et al.* (1996), Davis *et al.* (1997a) and marks the integral scale for cloud variability.

Barker and Davies (1992) applied Monte Carlo techniques to photon transport to show the similarities between the spectral slopes of cloud vertically integrated optical depth and the corresponding reflected and emitted radiation fields. They found that a the power spectrum slope of -3 for the cloud radiance field also implies a -3 slope for cloud optical depth or the vertically integrated cloud liquid water content. This, in turn, implies that transects of *lwc* should have spectral slope close to -2 (under the assumption of isotropic variability of *lwc*). Many observations indeed find the nearly -2 (-1.3 to -2) scaling for *lwc* transects in cumulus and stratocumulus-like clouds (see King *et al.* (1981), Marshak *et al.* (1997)).

Serio and Tramutoli (1995) used infrared AVHRR imagery and combined

spectral and variogram analysis to study the scaling laws in a cloud system generated by strong baroclinic instability. They found two distinct scaling regions, one extending from 1 km to 15 km with the power slope close to -2, the other stretching from 20 km to 100 km with the slope close to -1.33.

Davis *et al.* (1996) investigated spatial fluctuations of cloud liquid water content in marine stratocumulus measured by the Gerber probe (Gerber (1991)) on board of the C-131A aircraft during the Atlantic Stratocumulus Transition Experiment (ASTEX) and the King (King *et al.* (1981)) probe on the NCAR Electra aircraft in marine stratocumulus over the Pacific Ocean off the coast of California during FIRE. They found scaling regimes of 60 m-60 km in the ASTEX data and 20 m-20 km in FIRE, and scaling exponents between -1.08 and -1.68.

Lovejoy *et al.* (1993) analysed 15 AVHRR images of cloud fields (512 km $\times$ 512 km) over the Atlantic Ocean and reported scaling in all five AVHRR channels with no breaks over the entire available range (2 to 512 km) with spectral exponents -1.67 (channels 1 and 2), -1.49 (channel 3) and -1.91 and -1.85 for channels 4 and 5 respectively. They supplemented the $\sim$ 1.1 km resolution AVHRR observations with Landsat MSS data obtained with the resolution of 160 m found that scaling continued through to scales $\approx$ 300 m.

The above studies indicate that there is no general consensus on the extent of the scaling regime in cloud fields. In particular, the occurrence of scale break between 5 to 60 km is disputed. Scaling regimes can be determined for the AVHRR imagery as it is presented in this thesis. Moreover, the range of scales resolved by the AVHRR captures the interesting scale of the transition (scale break) between nonstationary scaling region and the stationary. In chapter 7 I present results of my analysis of 34 satellite scenes where I observed transitions between stationary and nonstationary regimes occurring at distances between 3 to 20 km.

6.4 Multifractal analysis

6.4.1 Motivation

The traditional approach to the investigation of the spatial (temporal) variability of geophysical signals employs spectral analysis to determine the scale invariant regimes where the wavenumber spectra follow power laws. Spectral analysis is applicable to both stationary and nonstationary data (Davis *et al.* (1996), see Flandrin (1989) and Wornell (1990) for the extension of the power spectra formalism to nonstationary processes). In the presence of scaling, the stationary and nonstationary regimes can be empirically detected in the power spectrum of the process. This is of a critical importance since stationarity is a prerequisite to obtaining meaningful spatial statistics. Scale invariance describes the statistical symmetry of the system and is a valuable information for models of the system which should reproduce this symmetry. There are however some unresolved ambiguities which plague conventional spectral analysis. Very different stochastic processes can yield very similar wavenumber spectra. For example, Gaussian white noise and randomly positioned Dirac δ functions both have flat power spectra $S(k) \sim k^{-\beta}$ with $\beta = 0$. Pure Brownian motion and randomly positioned Heaviside functions both have power spectra with $\beta = 2$. The spectrum of fractional Brownian motion (Mandelbrot (1977)) can be made to coincide with that of the cloud liquid water content (lwc) fluctuations, although fractional Brownian motion is symmetrical while the fluctuations of lwc have a negatively skewed probability density function. This ambiguity suggests that, for the accurate modelling of the cloud liquid water distribution, more information is needed than can be obtained through spectral analysis alone. A multifractal analysis finds information about the stochastic process which provides additional constrains on the behaviour of the system. In particular, it quantifies the degrees of stationarity intermittency of the process.

Davis *et al.* (1996a) give two examples of circumstances where two signals with radically different spatial properties but identical power spectra remain unresolved: 1) in seismic signals the background noise (white) and the interesting events (Dirac δ-functions) both have flat wavenumber spectra; 2) temporal fluctuations of air temperature (Brownian motion-like) and a passage of a front (Heaviside function) both have the same power spectrum ($E(k) \propto k^{-2}$). These intermittent signals do have however unique multifractal statistics.

6.4.2 Concept of multifractals

The concept of multifractals was introduced by Parisi and Frisch (1985) to describe the scaling behaviour of the velocity field in fully developed turbulence. Their turbulent velocity example can be translated to an approximately passive scalar such as the cloud reflectivity field $R(x)$, where x denotes horizontal position. Parisi and Frisch (1985) considered scaling of qth order increments $< \Delta R(r)^q >=< (R(x+r) - R(x))^q >$ over a distance r (this relation formally defines the qth structure function). They determined that different orders of structure function obey scaling laws (6.2) with different exponents, and related this behaviour to the intermittent nature of $R(x)$ field.

The intermittent (singular) character of cloud reflectivity fluctuations is related to cloud internal structure. On scales accessible to satellites, structures (cells) as small as few kilometres in size (AVHRR) or 100s of meters (Landsat) are easily resolved in cloud fields. Aircraft observations reveal intermittent fluctuations of cloud liquid water path down to centimeter scales (Davis *et al.* (1997b)).

These intermittent fields possess singularities defined as points (x) such that $\lim_{x \to y} |R(x) - R(y)|/|x - y|^{\alpha} \neq 0$. Here, $\alpha > 0$ is the order of the singularity. In terms of a satellite image singularity describes a rapid jump in reflectivity between adjacent pixels. If $S(\alpha)$ is a set of points where the field has a singularity of order α then one can find a fractal (Hausdorff) dimension $D_H(\alpha)$ of that set (see Appendix

F for definitions concerning fractals). Parisi and Frisch (1985) postulated the set $D_H(\alpha)$ can have a nontrivial dependence on α. In the limit of $|x-y| \to 0$ the probability of having a singularity of order α in the field $R(x)$ behaves as $|x-y|^{E-D_H(\alpha)}$ where E is the Euclidean dimension of space embedding the process $R(x)$ (see Appendix F for more detailed treatment). The qth order structure function can now be written as

$$< \Delta R(r)^q > \sim \int d\mu(\alpha) r^{qh+E-D_H(\alpha))} \sim r^{\zeta_q} \tag{6.14}$$

where $d\mu(\alpha)$ is a measure on $S(\alpha)$. It follows from (6.14) that ζ_q is a function (generally nonlinear) of the order q of structure function and the order α of the singularity. This corresponds to the case of multiscaling in definition (6.2).

The numeric technique for computing the dimensions $D_H(q)$ is described in the next section.

6.4.3 Formalism of multifractal analysis

The multifractal analysis of nonstationary and intermittent geophysical fields is based on two concepts: structure functions and singular measures (Davis *et al.* (1994), Marshak *et al.* (1997)). In the frame of the multifractal analysis, structure functions quantify and qualify nonstationarity while singular measures quantify and qualify intermittency. Alternatively, in a geometrical sense, structure functions provide a measure of roughness while singular measures quantify sparseness of the field. In this section we introduce the concepts of structure functions and singular measures and their interpretation as quantifiers and qualifiers of nonstationarity and intermittency.

Since the process of interest, the cloud optical depth, cloud droplet effective radius or cloud radiance in transects of stratocumulus fields, belong to the class of scale invariant (over a limited spatial scale), nonstationary processes with stationary increments $1 < \beta < 3$, they are suited to this type of analysis.

a. Structure functions

Consider again the random process $\varphi(x)$ introduced in section 6.2.1. We will require now that the process is scale invariant over some range of scales $[\eta, \leq R]$ and nonstationary with stationary increments. Such process matches the description of the cloud liquid water path fluctuation in linear transects through a stratocumulus cloud field.

The power spectrum of scale invariant, nonstationary process $\varphi(x)$ with stationary increments is given by (6.11) with $1 < \beta < 3$. The structure function of order q of the process $\varphi(x)$ is defined as

$$g_q(r,x) =< |\Delta\varphi(r,x)|^q >, \quad q \geq 0 \tag{6.15}$$

where $< \cdot >$ is again the ensemble average and $\Delta\varphi(r,x)$ are increments of the process at points x over a distance r

$$\Delta\varphi(r,x) = \varphi(x+r) - \varphi(x) \tag{6.16}$$
$$0 \leq r \leq L, \quad 0 \leq x \leq L - r$$

Since the increments of this process are stationary their statistical properties are independent of the position x. In particular

$$g_q(r,x) =< |\Delta\varphi(r,x)|^q >=< |\Delta\varphi(r)|^q >= g_q(r) \tag{6.17}$$

Due to the scale invariance of the increments we expect (recall (6.2))

$$g_q(r) =< |\Delta\varphi(r)|^q > \propto r^{\zeta(q)}, \quad q \geq 0 \tag{6.18}$$

in the scaling regime $[\eta, \leq R]$. In (6.18) proper normalisation requires $\zeta(0) = 0$. It can also be shown that the function $\zeta(q)$ is concave (Davis *et al.* (1994), Parisi and Frisch (1985)) and nondecreasing if the increments $\Delta\varphi(r,x)$ in (6.15) are bounded

(Marshak *et al.* (1994). For a concave function $\zeta(q)$ one can define a hierarchy (a monotonic function) of the exponents

$$H(q) = \frac{\zeta(q)}{q} \tag{6.19}$$

which in this case is nonincreasing (Marshak *et al.* (1994). We have a case of monoscaling if $\zeta(q)$ is linear in q and multiscaling if $\zeta(q)$ is nonlinear (recall the discussion following equation (6.2)).

Two special cases of structure functions are usually considered:

1. q =1. The first order structure function is related to the fractal structure of the graph $g(\varphi)$ of the process $\varphi(x)$ viewed as a scale invariant geometrical object in the two dimensional Euclidean space (see for example Davis *et al.* (1994), Mandelbrot (1977)) . There exist the following relationship between the exponent $\zeta(1)$ and the fractal dimension D_g of graph $g(\varphi)$ (Hölder or roughness dimension) (see Appendix F for definitions of fractals and fractal dimensions)

$$\zeta(1) = H(1) = 2 - D_g \geq 0 \tag{6.20}$$

   In two dimensional Euclidean space the range of values attainable by D_g extends from 1 (for almost everywhere differentiable functions), to 2 (two dimensional space filling graphs).

2. q=2. The extension of the Wiener-Khinchine theorem to processes with stationary increments states that for such processes the Fourier duality exists between the second order structure function and the energy spectrum (recall that the duality is between the autocorrelation function and the energy spectrum for stationary processes). This duality leads to the following relationship between the slope of the power spectrum and $\zeta(2)$

$$\beta = \zeta(2) + 1 = 2H(2) + 1 \geq 1 \tag{6.21}$$

I now discuss how the structure function is related to (non)stationarity.

Stationary processes have stationary increments thus (6.21) applies also to stationary processes. From the spectral criterion for stationarity $\beta < 1$ for a stationary process. The limit $\beta \to 1^+$ implies $\zeta(2) \to 0^+$ in equation (6.21) thus $\zeta(q) \equiv 0$ (since $\zeta(0) = 0$ and $\zeta(q)$ is nondecreasing, concave function) and $H(q) \equiv 0$. For stationary processes $\zeta(q) \equiv 0$ we have a case of trivial scaling (the increments are scale independent). A nontrivial structure function implies a degree of nonstationarity. (In practice, due to the effects of finite spatial resolution, all measurements and even theoretical models have some small $\zeta(q) > 0$ (Marshak *et al.* (1994)).)

It can be seen from the (6.18) that the complete description of nonstationarity of a scale invariant data set is contained in the exponents $\zeta(q)$, or the hierarchy $H(q)$ equivalently. Davis *et al.* (1994) adopt the $H(1)$ $(0 < H(1) < 1)$ to quantify to first order the degree of nonstationarity of the data. Yet, the entire $H(q)$ function is required to qualify the nonstationarity i.e. determine the type of scaling (mono or multiscaling).

If the increments of a process are narrowly (Gaussian-like) distributed then in (6.18) $< |\Delta\varphi(r)|^q > \approx < |\Delta\varphi(r)| >^q$ which immediately implies $\zeta(q) = q\zeta(1) = qH(1)$, or equivalently $H(q) =$ constant. Thus processes with narrowly distributed increments (also known as 'short-tailed' processes (Waymire and Gupta (1981)) are monoscaling. The τ and r_{eff} reported in chapter 4 like typical passive tracer distributions in turbulent flows, have large tails. The extreme located in these tails may produce multiscaling behaviour as we will see below.

For a process with stationary increments the autocorrelation function can be computed for the increments of the process (the increments field is stationary so the autocorrelation function is well defined). In can be shown that the correlation coefficient between two successive r increments is

$$\frac{<\Delta\varphi(r,x+r)\Delta\varphi(r,x)>}{\Delta\varphi(r,x)^2} = 2^{\zeta(2)-1} - 1 \tag{6.22}$$

Equation (6.22) yields positive correlations for $(1 < \zeta(2) \leq 2)$ or equivalently $(1/2 < H(2) \leq 1)$ or $(2 < \beta \leq 3)$ and negative correlations for $(0 \leq \zeta(2) < 1)$ or $(0 \leq H(2) < 1/2)$ or $(1 \leq \beta < 2)$. Processes with positively (negatively) correlated increments are sometimes termed as persistent (antipersistent) (Waymire and Gupta (1981)). For pure Brownian motion $\zeta(2) = 1$, which means uncorrelated increments (i.e. the right hand side of (6.22) vanishes).

For q=1, it follows from (6.18) that as long as $\zeta(1) > 0$ the process is stochastically continuous (compare equation (6.4)). Thus only stationary processes ($\zeta(1) = 0$) can be stochastically discontinuous.

b. Singular measures

Given the nonstationary random process $\varphi(x)$ $(0 \leq x \leq L)$ with stationary increments $(\beta < 3)$ which is scale invariant over the range of scales $[\eta, \leq R]$ we can derive a scale invariant, nonnegative stationary process by taking an absolute value of small scale (i.e. η) differences in the field $\varphi(x)$

$$|\Delta\varphi(\eta,x)| = |\varphi(x+\eta) - \varphi(x)|, \quad 0 \leq x \leq L - \eta. \tag{6.23}$$

Equation (6.23) takes the following form for the nearest neighbour differences of a discrete series of measurements

$$|\Delta\varphi(1,x_i)| = |\varphi(x_{i+1}) - \varphi(x)| = \varphi_{i+1} - \varphi_i, \quad 0 \leq i \leq L-1. \tag{6.24}$$

One can define a nonnegative measure of the η scale gradient field as

$$\epsilon(\eta,x) = \frac{|\Delta\varphi(\eta,x)|}{<|\Delta\varphi(\eta,x)|>} \tag{6.25}$$

where $< |\Delta\varphi(\eta, x)| >$ is the mean of the nonnegative gradient field. In the discrete measurement representation

$$< |\Delta\varphi(1, x)| >= \frac{1}{L} \sum_{i=0}^{L-1} |\Delta\varphi(1, x_i)|. \tag{6.26}$$

The $\epsilon(\eta, x)$ defined by (6.25) are called singular measures.

Davis *et al.* (1994) cite other procedures for deriving a stationary nonnegative field. These methods include taking fractional derivatives (Schmitt *et al.* (1992), second derivatives Tessier *et al.* (1993), squares rather than absolute values (Meneveau and Sreenivasan (1987)). However, work of Lavallée *et al.* (1993) indicates the details of the procedure do not influence the final results of the singularity analysis.

In our discrete measurement representation I make an implicit assumption that the smallest scale of interest (η) coincides with the resolution of the measurement. This is not necessarily true. If the resolution of the instrument is better than η the transition to the scaling regime will be observed in the power spectrum and in the physical space in structure functions. In this case one should take the η scale gradients. If the spatial sampling l is insufficient to resolve this transition ($l > \eta$) one can take the nearest neighbour differences.

After the nonnegative measures $\epsilon(\eta, x)$ of the gradient field have been defined, the next step in the singularity analysis is to determine the spatial behaviour of these measures. The scale dependence of the measures $\epsilon(\eta, x)$ is explored through their spatial averages over increasing scales r (the spatial degradation or coarse graining of the measures). The spatially degraded version of the measures at scale r is obtained by computing the average measure on the interval $[x, x + r]$

$$\epsilon(r, x) = \frac{1}{r} \sum_{x' \in [x, x+r-1]} \epsilon(1, x'), \quad 0 \leq x \leq L - r \tag{6.27}$$

The multiscaling properties of the measures are accessed through the moments $< \epsilon(r, x)^q >$ of the spatially degraded measures with respect to the scale r. Since we

are dealing with a stationary field of measures taking spatial averages of $\epsilon(r,x)$ is well defined.

In the scaling range (if it exists) we can write (recall equation (6.2))

$$< \epsilon(r,x)^q > \propto r^{-K(q)}, \quad q \geq 0, \quad 0 \leq x \leq L - r \tag{6.28}$$

From the normalisation requirement on the probability density distribution of measures $\epsilon(r,x)$ we immediately have $K(0) = 0$. It follows from the definition of measures given in (6.25) that $< \epsilon(r,x) > \equiv 1$ thus $K(1) = 0$. By analogy to (6.18) ($K(q)$ corresponds to -$\zeta(q)$) $K(q)$ has to be a convex function. From the above, it can be inferred that $K(q) \leq 0$ for $0 \leq q \leq 1$ and $K(q) \geq 0$ elsewhere. Furthermore $K'(1) \geq 0$ where the prime denotes the first derivative.

Similarly as for the structure function one can define a hierarchy $C(q)$ of the exponents $K(q)$

$$C(q) = \frac{K(q)}{q-1} \tag{6.29}$$

For $q \to 1$ equation (6.29) and the l'Hospital's rule yield

$$C(1) = K'(1) \tag{6.30}$$

This time the hierarchy $C(q)$ is nondecreasing for $q > 1$. $C(q)$ is related to the nonincreasing hierarchy of 'generalised dimensions' $D(q)$ (Appendix F)

$$D(q) = 1 - C(q) = 1 - \frac{K(q)}{q-1} \tag{6.31}$$

introduced by Grassberger (1983) and Hentschel and Procaccia (1983) in an investigation of strange attractors. As before $D(q) \equiv$ constant corresponds to a monoscaling measure while $D(q)$ which varies with q corresponds to a multiscaling measure. $D(1)$ is related to the mean of $\epsilon(r,x)$ distribution and is known as the information dimension. Events which contribute most to the mean of $\epsilon(r,x)$ (singularities) occur on a set with fractal dimension $D(1)$.

Intermittency plays the same role for singular measures as nonstationarity does for structure functions. $C(1)$ is again designated as a quantifier of the intermittency whereas the entire function $C(q)$ is required to qualify it (mono- or multiscaling). In terms of $C(1)$, if $C(1)$ =0 the data is nonintermittent whereas any $C(1) > 0$ implies some degree of intermittency.

It is instructive to consider two examples of intermittency:

1. Weakly intermittent data. In case of weakly variable fields $< |\epsilon(r,x)|^q > \approx < |\epsilon(r,x)| >^q$. It follows from (6.28) and (6.29) that in this case $K(q) = qK(1) \equiv 0$ thus $D(q) \equiv 1$ and monoscaling prevails in its 'trivial' form. If $D(q) < 1$ for $q \geq 0$ the distribution of measures is singular (skewed). At small scales the most frequent values are small but occasionally spikes with high values occur.

2. Extreme intermittency. An example of an extreme case of intermittency is a delta function randomly positioned in the interval $0 \leq x \leq L$. Let x_c denote the location of the delta function in the interval $0 \leq x \leq L$. In limit $\eta \to 0^+$ we have $\epsilon(x) = lim_{\eta \to 0^+} \epsilon(\eta, x) = \delta(x - x_c)$. The spatial averaging over an interval $[x, x+r]$ yields

$$\epsilon(r,x) = \frac{1}{r}\int_x^{x+r} \epsilon(x')dx' = \begin{cases} \frac{1}{r} & \text{if } x_c \in [x, x+r] \\ 0 & \text{otherwise} \end{cases} \tag{6.32}$$

If x_c is uniformly distributed over the interval $[0\ L]$ then for the spatially averaged moments one obtains

$$< \epsilon(r,x)^q >= \frac{1}{L}\int_0^L \epsilon(r,x)^q dx_c = \frac{r}{Lr^q} \propto r^{1-q} \tag{6.33}$$

implying $K(q) = q-1$ hence $C(q) \equiv 1$ and $D(q) \equiv 0$ for $q > 0$ which indicates that all activity in concentrated in a single point.

6.5 Previous work: multifractal approach

Davis *et al.* (1994) postulated the use of two multifractal statistics, the singularity measures and qth order structure functions to describe the spatial variability and scale dependence in geophysical fields. These measures seek to quantify the degrees of nonstationarity and intermittency in a geophysical signal by comparing their statistical properties to those of known random processes.

Davis *et al.* (1994) investigated spatial fluctuations of cloud liquid water content in marine stratocumulus measured by the Gerber probe (Gerber (1991)) on board of the C-131A aircraft during the Atlantic Stratocumulus Transition Experiment (ASTEX). Their analysis yield the ensemble average $(H(1), C(1)) \approx (0.29, 0.08)$ in range of 60 m-60 km. Marshak *et al.* (1997) found 5 flights ensemble average $(H(1), C(1)) \approx (0.28, 0.10)$ over the scales 20 m-20 km for the LWC fluctuation measured by the King (King *et al.* (1981)) probe on the NCAR Electra aircraft in marine stratocumulus over the Pacific Ocean off the coast of California during FIRE. Marshak *et al.* (1997) point to the close proximity of the ASTEX and FIRE data sets in the bifractal plane and interpret this proximity as a consequence of the common nature of the nonlinear physical processes that determine the internal structure of the marine stratocumulus. The authors link the different scaling range of these two data sets (60 m-60 km for ASTEX and 20 m-20 km for FIRE) to the different boundary layer depth (1.5 km for ASTEX and 0.5 km for FIRE).

Davis *et al.* (1996a) reported $(H(1), C(1)) = (0.28, 0.09)$ and scaling range 5 m to 5 km for an ensemble of aircraft measurements of lwc (Gerber probe) obtained during SOCEX.

The location of both data sets in the bifractal plane indicates that the LWC fluctuation in marine stratocumulus are both nonstationary and intermittent and calls for hybrid stochastic models which combine both the nonstationarity and the intermittency to adequately describe the processes governing the LWC fluctuation in clouds and likely other geophysical fields.

Marshak *et al.* (1997) note a large scatter of the individual spatial averages around the ensemble averages which suggests ergodicity violation and argues in favour of non-ergodic models. They stress the need for data to test their findings.

So far, the ASTEX, FIRE and SOCEX *lwc* flight data, and one FIRE Landsat Thematic Mapper (channel 2) scene [$(H(1), C(1)) = (0.54, 0.06)$] (Davis *et al.* (1996a)) are the only data sets placed in the bifractal plane. Satellite data are much easier accessible and provide much grater spatial and temporal coverage than any aircraft data. They have the disadvantage of limited resolution towards the small scales (1 km for the AVHRR) thus necessarily shorter cascades of the scaling range.

In chapter 7 of my dissertation I find the multifractal characteristics of the AVHRR data sets of cloud radiances, cloud optical depth and cloud droplet effective radius and in particular their location in the bifractal plane. I apply the analysis to four sets of satellite data: 1) $F87$ - Pacific Ocean the FIRE 1987 data set, 2) $P94$ - Pacific Ocean 1994 data set acquired by UBC satellite Lab, 3) $P95$ - Pacific Ocean 1995 data set acquired by UBC satellite Lab and, 4) $S95$ - Southern Ocean Experiment (SOCEX) 1995 data set acquired over the Indian Ocean.

6.6 Summary

The goal of multifractal analysis is to find the scaling behaviour $\zeta(q)$ of the structure functions in (6.18) and the scaling behaviour $K(q)$ of the singular measures in (6.28). The analysis establishes the mono- or multifractal character of the scaling . The scaling exponents of the first order moments of the structure functions $H(1)$ and the singular measures $C(1)$ quantify respectively the degree of nonstationarity and intermittency in the data.

Marshak *et al.* (1997) argue that close proximity the mean multifractal parameters of $[H(1), C(1)]$ for both their data sets (FIRE and ASTEX) could be a manifestation of a universal character of the processes determining the structure of

marine stratocumulus. Arguing against such universal behaviour is the large number of physical processes that lie between the characteristic scaling behaviour of inertial range turbulence and cloud variables such as τ and r_{eff}. As the review in section 1.2 indicated, the aerosol population in particular may be injecting its own characteristic scale on τ and r_{eff} which has nothing to do with the variability of passive tracers in turbulent flow.

I have assembled a large number (34) of AVHRR images of cloud optical depth, cloud droplet effective radius and visible cloud radiance corresponding to different micro and macrophysical marine stratocumulus regimes. My scenes correspond to uni-modal, bi-modal, and optically thick clouds as discussed in chapters 3 and 4. If the universality argument holds all these regimes should yield similar values of $[H(1), C(1)]$.

In the next chapter I show that this is indeed the case. There is no clear difference in neither $H(1)$ nor $C(1)$ parameters for any of these regimes. There is however a considerable scatter between ensemble averages of $H(1)$ and $C(1)$ for the four major data sets I considered. A trivial dividing line runs between fully cloudy and broken cloud fields which have markedly larger values of $C(1)$ and are often multiscaling in $\zeta(q)$.

The $[H(1),\ C(1)]$ set constitutes a test for structural compatibility of cloud models with real clouds. When mapped into the $[H(1),\ C(1)]$ space, realistic cloud models, whether dynamic or stochastic, should lie as close as possible to the point which represents real data.

In another application, the $[H(1),\ C(1)]$ reference frame provides a test for assumptions about subpixel scale homogeneity made in retrievals of geophysical fields from a remote sensing imagery. The remotely sensed fields can be compared with the in situ measurements in the $[H(1),\ C(1)]$ plane. The agreement between the remote and in situ $[H(1),\ C(1)]$ points can serve as a validation of the assumptions of retrieval technique. Examples of the application of multifractal techniques

to evaluation of turbulent cascade models, cloud inhomogeneity models, the validity of remote sensing approximations for retrieval of cloud properties can be found in Meneveau and Sreenivasan (1987), Marshak *et al.* (1995a), Marshak *et al.* (1995b) among others.

From a satellite and image analysis perspective the parameters $H(1)$ and $C(1)$ may find another application as measures of texture, if it can be established that different cloud types (stratocumulus, cumulus, cirrus, etc.) or different surfaces (clouds, sea surface, land) are characterised by different sets of $[H(1), C(1)]$. However, I do not explore this possibility in this thesis.

Chapter 7 of this thesis presents the application of the combined spectral and multifractal analysis to AVHRR imagery fields of cloud radiance, cloud optical depth and cloud droplet effective radius .

Chapter 7

Spatial structure of stratocumulus clouds II: Results from multifractal analysis

This chapter presents the application of the multifractal analysis technique of chapter 6 to the satellite fields of cloud visible radiance, cloud optical depth and cloud droplet effective radius obtained from AVHRR measurements. In earlier chapters I have discussed observational and modelling results which pointed to complex interactions between cloud processes on scales ranging from the microscale (size of cloud droplets $[\mu m]$) to the macroscale (geometrical cloud thickness $\sim 300\ m$, cloud horizontal extent $\sim 100\ km$). My observations in chapters 3 and 4 indicate that many cloud fields can be described in terms of the reference cloud model (3.2) as uni-modal or bi-modal where bi-modality involves variability in N_{sat} on scales comparable to the size of the scenes ($256\ km \times 256\ km$). The goal of the analysis in this chapter is to investigate how (or if) these interactions affect cloud spatial structure. In particular, I will compute and compare:

1. spatial and multifractal properties (nonstationarity and intermittency) of the uni-modal, bi-modal, and thick cloud scenes described in chapters 3 and 4;

2. the ensemble averaged nonstationarity and intermittency parameters for the four data sets ($F87$, $P94$, $P95$ and $S95$) of cloud visible radiance, cloud optical depth and cloud droplet effective radius .

For the purpose of the comparison in 2) I have expanded the initial data base (15 example scenes discussed in chapter 4 and listed in Table 4.1) by an additional 20 scenes representing all four data sets: 1) $F87$, 2) $P94$, 3) $P95$, and 4) $S95$ (listed in Tables B.3-B.6 Appendix B).

I compare results of the analysis for the uni-modal, bi-modal, and thick cloud scenes described in chapters 3 and 4. In section 7.1 I discuss scene averages, ensemble averages and individual transects of the satellite scenes. Section 7.2 demonstrates the step by step flow of the analysis. The results of the analysis are presented in section 7.3. A summary of this chapter is given in section 7.4.

7.1 Transects of satellite fields and ensemble averages

The subject of the spectral and multifractal analysis are one dimensional transects of the satellite fields of cloud radiation and cloud optical depth and cloud droplet effective radius. The decision to use one dimensional transects was dictated by 1) the geometrical properties of the AVHRR images (discussed below), and 2) the desire to assure comparability with one dimensional in situ measurements (Marshak *et al.* (1997) in situ aircraft observations) and earlier studies which considered one dimensional transects of satellite fields (Barker and Davies (1992)).

The viewing geometry and the pixel size of the AVHRR instrument cause a substantial overlap of pixels in the scanning direction (i.e. direction perpendicular to satellite orbit). Near nadir, the size of the AVHRR pixel is about 1.1 $\times$ 1.1 km while pixel centres are about 0.8 km apart. As a result of the overlap, only about 70% of each pixel is unique to that pixel. In the tracking direction (parallel to the satellite orbit) there is much less overlap, especially if the satellite viewing angle is less than about 30°. (Barker and Davies (1992)). The overlapping of pixels causes an artificial smoothing of the AVHRR images in the scanning direction.

Another artifact of satellite imagery is pixel distortion in the scanning direc-

tion. As viewing angle increases the satellite footprint is stretched along the scanline direction from 1.1 km at nadir to about 6 km at the maximum AVHRR viewing angle.

These two effects related to the satellite viewing geometry lead to distorted spectral representations of the cloud field in the scanning direction. To circumvent this problem Barker and Davies (1992) advocate using only the tracking direction transects of AVHRR images in spectral analyses. Furthermore Barker and Davies (1992) introduce an ensemble averaged wavenumber spectrum for the tracking lines

$$< E(k) >_t = \frac{1}{n} \sum_{i=0}^{n-1} E_i(k)_t \tag{7.1}$$

where $E(i)_t$ is the power spectrum along the ith tracking line, n is the total number of tracking lines used and $< \cdot >$ denotes a ensemble average for the scene. To eliminate problems related to tracking lines overlapping Barker and Davies (1992) use only every other line to compute the ensemble average $< E >_t$.

I follow the approach of Barker and Davies (1992) and consider only along tracking direction transects of the satellite cloud field. I introduce one slight modification. Rather than including in the scene ensemble average every second tracking line in the image I opt for a more sparse sampling and include only every 5th line. The review of variograms for many satellite images indicates (see Appendix C) that many cloud fields are autocorrelated over distances of at least 3 to 5 km . Use of autocorrelated data in the computation of the scene ensemble average spectrum could likely lead to underestimation of the spectrum confidence interval. Autocorrelation can be eliminated from a data set through suitable subsampling (see again Appendix C and references therein). Thus the 5 line subsampling interval for the tracking lines which corresponds to approximately 5 km. With the image size of 256×256 pixels this subsampling rate contributes 51 lines to the ensemble average narrowing the 95% confidence interval of the power spectrum by approximately 60% on average.

The reduction of noise obtained in the ensemble average power spectrum has a side effect. When estimating the slope of the power spectrum with the least square fit to the log transformed equation (6.11) the greatest contribution comes from the smallest scales, whereas the contribution of the more sparsely sampled larger scales is almost negligible. To make all scales contribute equally, Davis *et al.* (1996) proposed octave averaging of $E(k)$, that is, computing averages of $E(k)$ over bins of increasing size 2^m (where $m = 0, ..., [log_2 N] - 2$ and N is the total number of measurement points, and $[\cdot]$ designates the integer part). Thus, the average power spectral density in bin m is given by

$$E_m = \frac{1}{2^m} \sum_{j=2^m}^{j=2^{m+1}-1} E(k_j) \tag{7.2}$$

and corresponds to average wavenumber

$$k_m = \frac{1}{2^m} \sum_{j=2^m}^{j=2^{m+1}-1} k_j = \frac{3}{2} 2^m - \frac{1}{2} \tag{7.3}$$

I compute the estimates of spectral slope using both the ensemble averaged power spectrum obtained according to (7.1) and the scene average octave binned power spectrum. With 256 data points along a tracking line the small scale resolution is lost in the octave averaged spectrum. If I want a closer look at the smallest scales the ensemble averaged power spectrum allows me to zoom into them. On the other hand, if I consider larger scales the octave binned spectrum provides a less biased estimation of the power spectrum slope.

Similarly, I compute the along-track scene ensemble average of the structure functions and singularity measures in the multifractal analysis and find the hierarchies $H(q)$ and $C(q)$ and including the nonstationarity and intermittency parameters $H(1)$ and $C(1)$ for the scene ensemble average. I then compute ensemble averages of $H(1)$ and $C(1)$ for each of the four data sets under consideration by taking averages of scene ensemble average $H(1)$ and $C(1)$ of the scenes in the data set.

To simplify the terminology, I will refer to the scene ensemble averages as simply the scene averages and reserve the name ensemble average for the ensemble averages of the four data sets I am investigating.

7.2 Flow of the analysis

This section is designed to serve as a practical guide to the spectral and multifractal analysis presented below. I describe the steps of the analysis and illustrate them with an analysis of an actual scene. The scene in the example is the channel 1 radiance field for scene no 1 of Table B.1 (page 218) ($F87$ data set) shown in Figure 7.1.

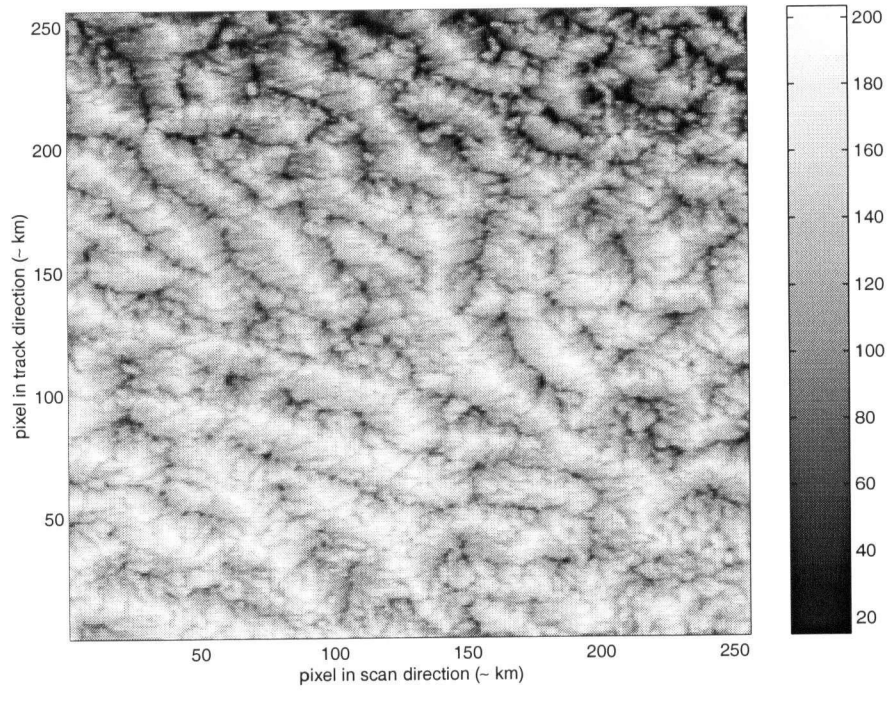

Figure 7.1: AVHRR channel 1 radiance field for scene no 1 in Table B.1 (page 218).

Flow of the analysis:

Step 1: Compute the scene average energy spectrum $E(k)$ (6.9)and the second order structure function $g_2(r)$ (6.15) in the manner outlined in 7.1. Figures 7.2 and 7.3 show the plots of $E(k)$ and $g_2(r)$ respectively. Also shown in Figure 7.2 are the 5% confidence intervals of the power spectrum estimate.

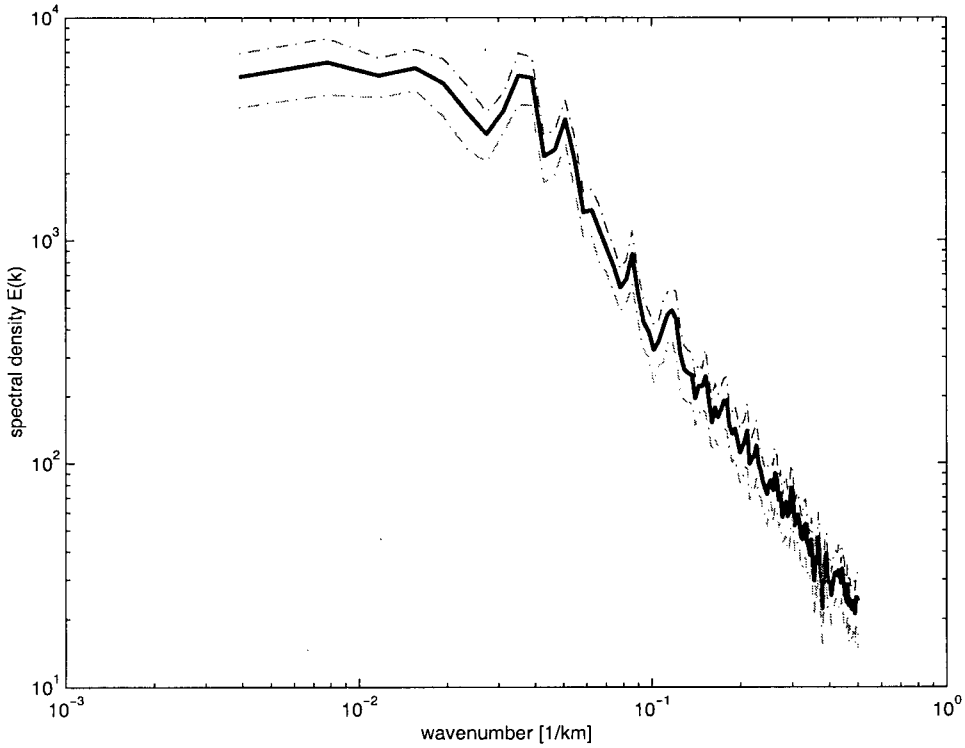

Figure 7.2: Power spectrum for channel 1 radiance field of scene no 1.(Table B.1 page 218).

Based on these two measures I estimate the scaling regimes in the data set. Both methods should yield consistent results. I expect the scaling region to originate at the smallest scale resolvable (satellite pixel size of approximately 1 $\times$ 1 km) (see Marshak *et al.* (1997)). In practice, however the smallest scale is strongly affected by the instrument resolution and may not be representative

of the fluctuation in the measured field. Also, the windowing of the Fourier transform affects the high frequency end of the spectrum and may obscure scaling at these frequencies. Thus, in establishing the extent of the scaling regime I tend to rely more on the structure function. I do however cross-check the results with the outcome of the power spectrum analysis.

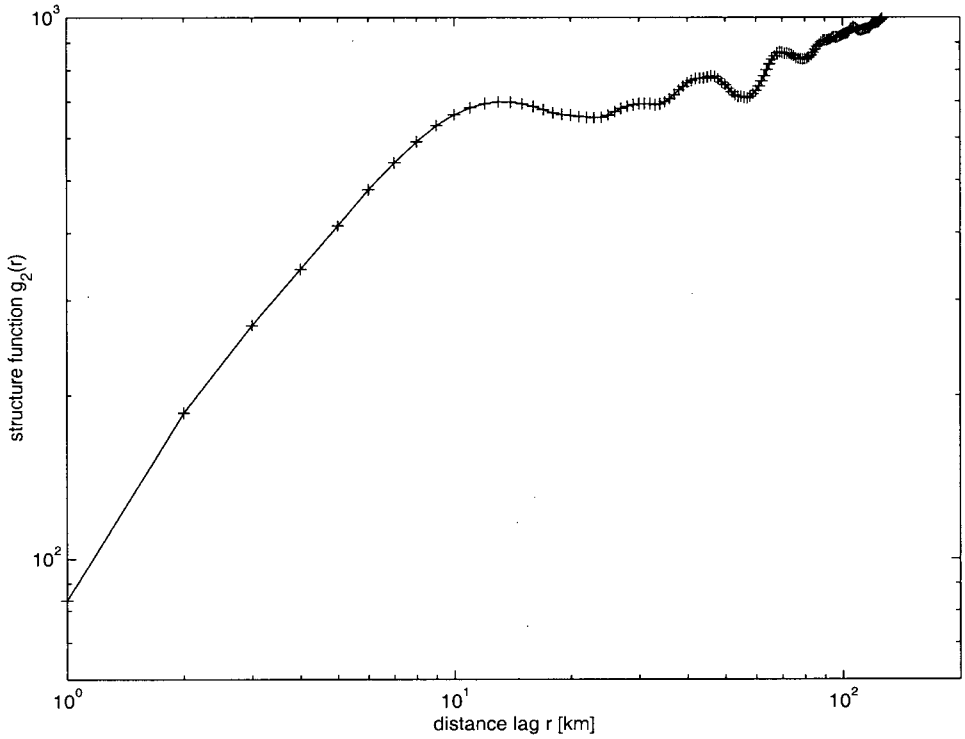

Figure 7.3: Second order structure functions for channel 1 radiance field of scene 1. (Table B.1 (page 218).

From Figure 7.3 the scaling region is found as the range of r values where the structure function is roughly linear with r in log-log coordinates. In this case, the scaling range $[\eta, R]$ is approximately between 1 and at least 8 kilometres. The structure function reveals a transition between the nonstationary scaling region and the stationary region at around 10 km. Transition at these scales

is not very well marked in the power spectrum which seems to continue along a straight line up to $\approx$ 25 km. The smaller range ([1, 8] km) is accepted as the scaling region of the radiance field in the scene of figure 7.1.

Step 2: Compute q-order scene average structure functions for $q \in$ [1,5] using (6.15). I follow Davis *et al.* (1994) in this choice of q values. Structure functions of orders 1 to 5 are plotted in Figure 7.4.

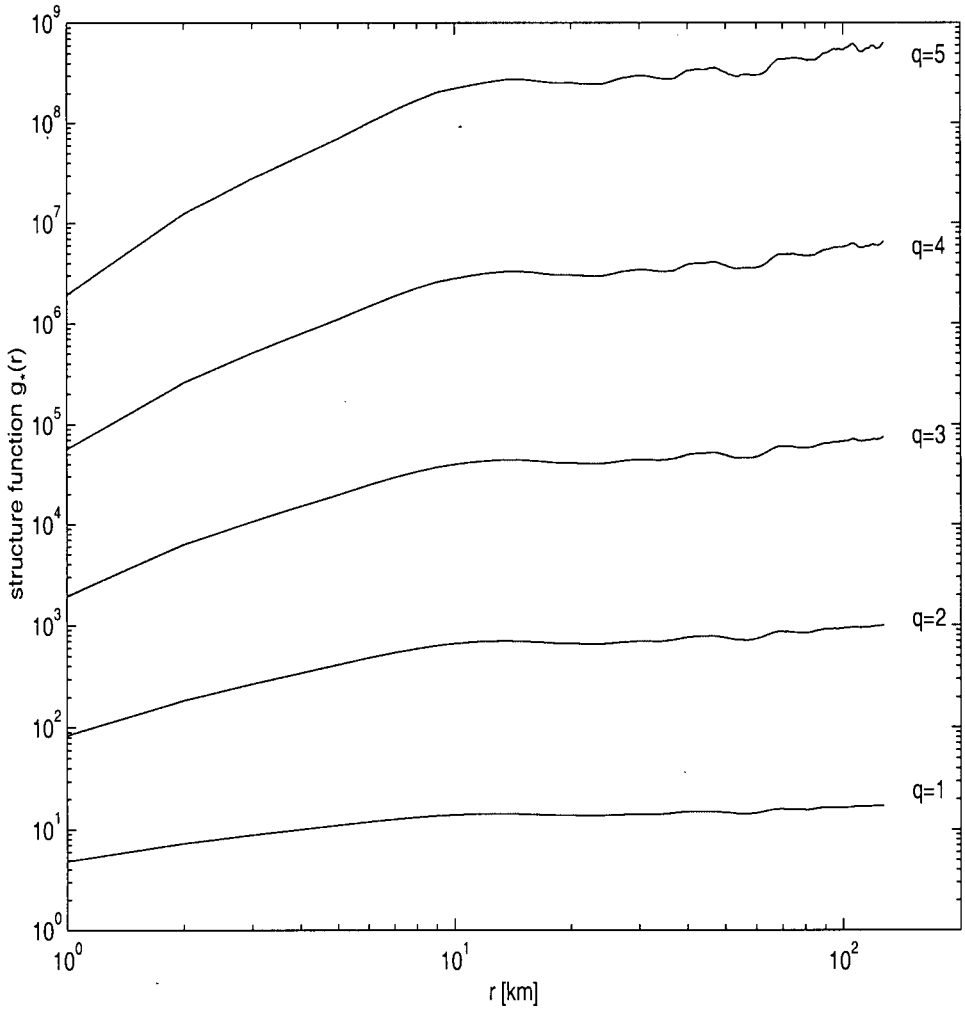

Figure 7.4: Structure functions of order 1 to 5 for channel 1 radiance field of scene 1. (Table B.1 (page 218).

The scaling region is approximately [1, 8] km consistently for all orders of the structure function considered. In the next step I consider the effect of the inaccuracy of the scaling range estimate on the values $\zeta(q)$.

Step 3: To compute the function $\zeta(q)$ I have to find the scaling region slope of the structure function $g_q(r)$ for all q. I use linear least squares to fit a straight line to the log-log representation of the q-order structure function in the scaling region. For the least square fit I assume that both the structure function $g_q(r)$ and r are known exactly. The function $\zeta(q)$ is plotted in Figure 7.5. Error bars in the plot are the uncertainties $\sigma_{\zeta(q)}$ of slope estimates from the least square fit. Table 7.1 lists the values of $\zeta(q)$ and $\sigma_{\zeta(q)}$ returned by the least squares fit for scaling range [1,8] km and $\pm$ 1 km departure from this estimate. The differences in $\zeta(q)$ for all three estimates of the scaling range lay within the uncertainties of $\zeta(q)$ from the least squares fit.

	q	1	2	3	4	5
range	$\zeta(q)$	0.48	0.94	1.36	1.75	2.11
8 km	$\sigma_{\zeta(q)}$	0.02	0.03	0.04	0.05	0.06
range	$\zeta(q)$	0.49	0.96	1.39	1.79	2.16
7 km	$\sigma_{\zeta(q)}$	0.02	0.03	0.04	0.05	0.06
range	$\zeta(q)$	0.47	0.91	1.33	1.72	2.07
9 km	$\sigma_{\zeta(q)}$	0.02	0.03	0.05	0.06	0.06

Table 7.1: Least square estimates of $\zeta(q)$ an it uncertainties $\sigma_{\zeta(q)}$ calculated for 3 different assumptions of the scaling.

In Table 7.1 I note the nonstationarity parameter $H(1) = \zeta(1) = 0.48$ and $\zeta(2) = 2H(2) = 0.94$. Through the relationship (6.21) I compute the power

spectrum scaling exponent (see (6.11) $\beta = 1.94$.

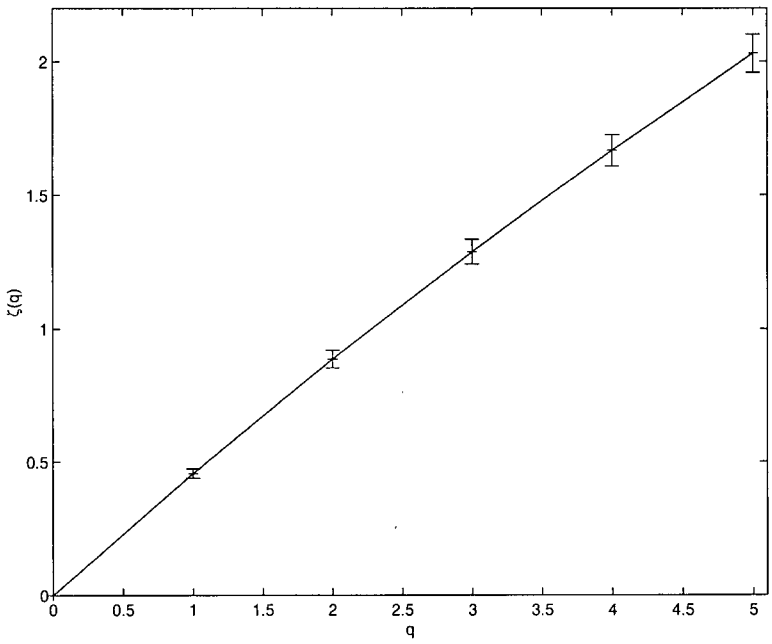

Figure 7.5: Scaling exponent $\zeta(q)$ of the moments of structure function as a function of the moment order for channel 1 radiance of scene no 1. (Table B.1 (page 218).

Step 4: From the plot of the scaling exponent function $\zeta(q)$ (Figure 7.5) I determine the type of scaling (mono- vs multiscaling). In Figure 7.5 the relationship between $\zeta(q)$ and q is linear within the error bars which suggests monoscaling or a very weak multiscaling.

Step 5: I obtain a second estimate of the power spectrum slope β directly from the linear least squares fit to the power spectrum in log-log space. For the least square fit I assume the 95% confidence interval of the power spectrum estimate as the uncertainty of the power spectrum with no error in the wavenumber k. For β from the power spectrum fit Davis *et al.* (1996) showed that the choice of a particular least squares variant (i.e with no errors in any of the variables, errors only in $E(k)$ or errors in $E(k)$ and k) does not affect the estimates of the

power spectrum slope in a significant way. I found this to be true in my cases too. I opted for the variant with errors in $E(k)$ for more realistic estimates of the uncertainty of the slope estimate. The data in this example yield $\beta = 1.90 \pm 0.06$ for the ensemble average power spectrum and 1.93 ± 0.02 for the octave binned power spectrum which are both in an excellent agreement with the value of β obtained through the structure function analysis (see **Step 3:**).

Step 6: I compute the smallest scale gradient field and scene average singular measures $< \epsilon(r,x)^q >$ of order $q \in [0,5]$ as function of the degradation scale r (see equation (6.28)).

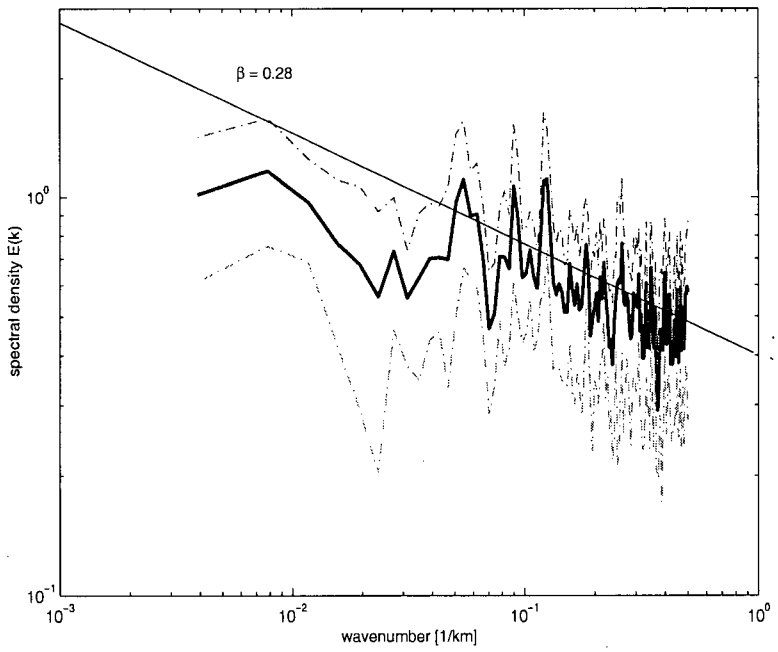

Figure 7.6: Power spectrum of the channel 1 radiance gradient field in scene no 1. (Table B.1 (page 218). $\beta < 1$ indicates a stationary process.

Figure 7.6 shows the power spectrum of the gradient field. The least square fit to the power spectrum in the scaling range returns $\beta = 0.28 \pm 0.08$, thus $\beta < 1$ and the field of increments is indeed stationary.

Step 7: In Figure 7.7 I plot $< \epsilon(r,x)^q >$ as a function of r for integer orders of $q \in [0, 5]$ in log-log coordinates . I obtain $< \epsilon(r,x) > = 1$ for all scales r and $< \epsilon(r,L)^q > = 1$ for all q which is consistent with the definition of the singular measures and their scaling properties, as discussed in section 6.4.3 (see equations (6.25) to (6.28) and the discussion thereafter). $< \epsilon(r,x) >$ is roughly linear between 2 to 16 km for all q. This range is interpreted as the scaling range for $< \epsilon(r,x) >$. In the next step I will show that the value of scaling exponents $K(q)$ is not greatly affected by the exact specification of the scaling range (Figure 7.8).

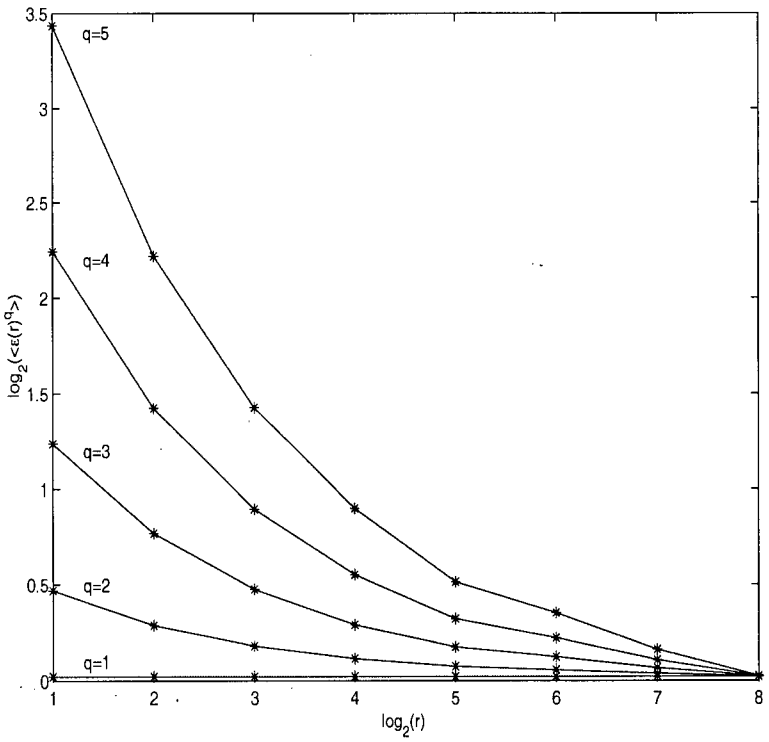

Figure 7.7: Singular measures moments plotted against the scale r for channel 1 radiance in scene no 1 (Table B.1 (page 218).

Step 8: I find the scaling exponents $K(q)$ (see (6.28)) as the slope of the linear least square fit to $< \epsilon(r)^q >$ as function of r in the log-log space. Figure 7.8 shows

the plot of $K(q)$. As in **Step 3:** I explore the effect of the uncertainties of the scaling range determination on the estimates of $K(q)$. Two curves in Figure 7.8 represent $K(q)$ computed for (1) scaling range [2, 8] km, (2) scaling range [2, 16] km. The error bars represent the uncertainty of the estimates in the least square fit. The effect of the scaling range uncertainty is negligible for $q <$ 2 and even for $q = 5$ the two lines are within error estimates of each other.

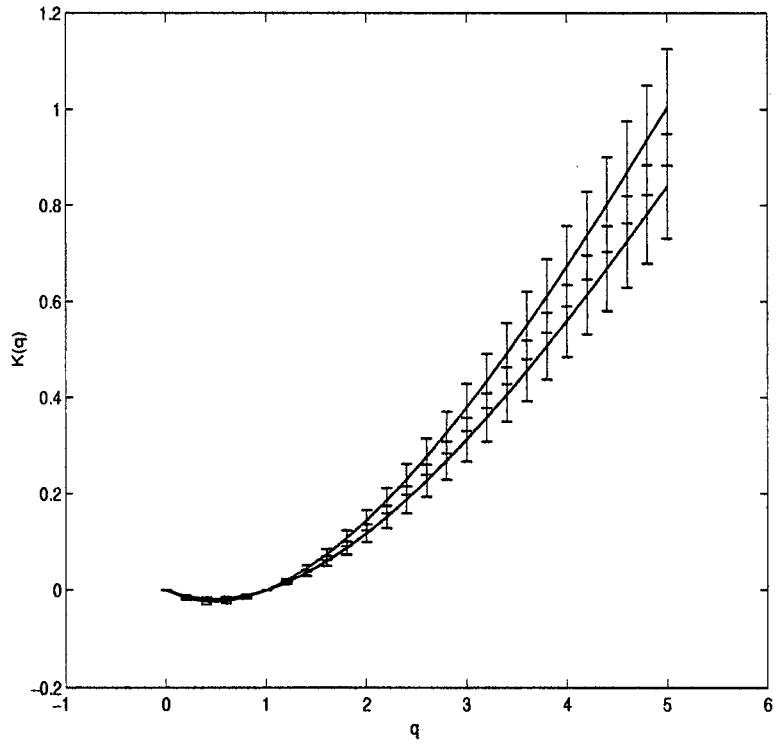

Figure 7.8: Exponent function $K(q)$ for channel 1 radiance in scene no 1 (Table B.1 (page 218). Red curve corresponds to the scaling range [2,8] km. Blue curve corresponds to the scaling range [2,16] km.

Step 9: I compute the derivative of $K(q)$ and find its value for $q = 1$ which determines the intermittency parameter $C(1)$. In this case I obtain $K'(q) = C(1) = 0.06$ $\pm$ 0.02. The estimate of uncertainty is computed according to

$$\Delta C(1) = \Delta K'(1) = \Delta(\frac{K(1^+) - K(1^-)}{\delta q}) \approx \sqrt{2}\frac{\Delta K(1)}{\delta q} \tag{7.4}$$

where $\Delta K(1)$ is the uncertainty of the $K(1)$ estimate obtained as the uncertainty of the slope estimate in the least square fit to $< \epsilon(r)^q >$ as a function of q. δq is the increment of singular measures order used in the computation of $K(q)$. There is no restriction on orders to be integers. I have used δq =0.2

.

Step 10: I compute $D(q)$ using (6.31) and plot it in Figure 7.9. $D(q) \neq const$ which reveals a multiscaling character of the singular measures as discussed in section 6.4.3.

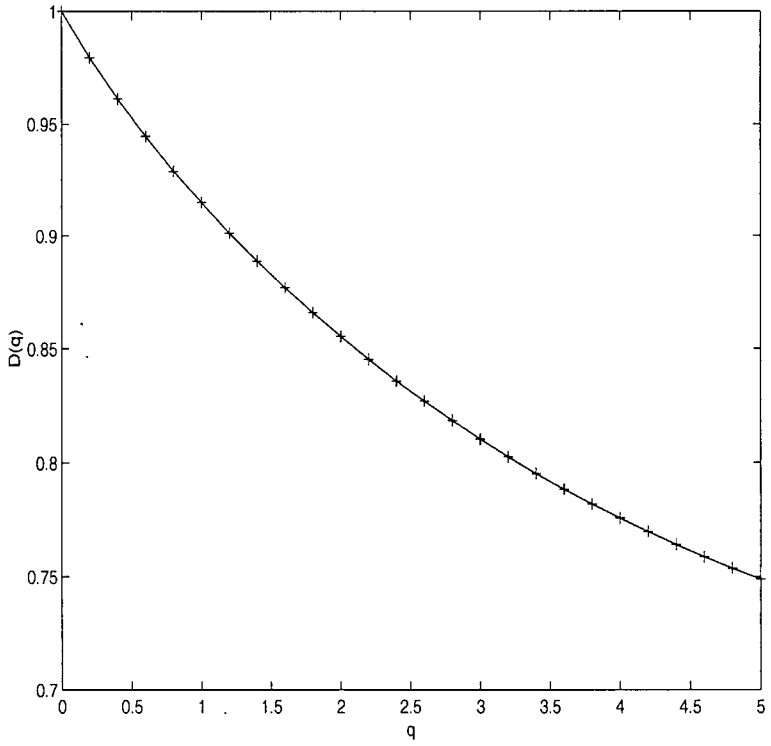

Figure 7.9: Information dimension $D(q)$ for channel 1 radiance in scene no 1

The analysis outlined above is repeated for the visible channel radiance field,

cloud optical depth field and the cloud droplet effective radius field for every scene of the four data sets in the consideration. For each observable in every data set I compute ensemble averages of $H(1)$ and $C(1)$ and find their location in the bi-fractal plane (Marshak *et al.* (1997)) for comparison with other data sets.

7.3 Analysis results

I analysed a total of 34 AVHRR cloud scenes from 4 separate data sets: 17 FIRE scenes $F87$, 8 scenes from the $P94$ data set, 5 scenes from $P95$ data set, and 4 $S95$ scenes from the SOCEX experiment covering Indian Ocean west of Tasmania. The complete list of scenes analysed in this chapter is given in Tables B.3-B.6 of Appendix B with their orbit numbers and times of overpass.

Following the steps described in section 7.2 I find the nonstationarity and intermittency parameters ($H(1)$, $C(1)$) of the cloud visible radiance field, cloud optical depth and cloud droplet effective radius for each scene and ensemble averages of the multifractal parameters for each data set. I present the results of the spectral and multifractal analysis of these scenes in the following order:

1. In tables G.1-G.3 (Appendix G) I show the estimates of the nonstationarity and intermittency parameters for cloud visible radiance field, cloud optical depth and cloud droplet effective radius for the uni-modal, bi-modal and thick cloud scenes discussed in chapters 3 and 4 (Figures 3.5 page 47, 3.8 page 52 and 3.9 page 54). The mean cloud optical depth and cloud droplet effective radius for these scenes were listed in Table 4.2 on page 80 and shown in Figure 4.10 on page 82. I examine the consistency of the spectral and multifractal approach to the estimation of the slope of the power spectrum.

2. I plot the second order structure functions $g_2(r)$, the exponent function $\zeta(q)$ (structure function scaling) and the information dimension $D(q)$ (singular measures scaling) as a function of moment order q for the uni-modal, bi-modal

and thick cloud scenes. I examine the behaviour of the structure functions and the type of scaling in the analysed fields (mono vs multiscaling).

3. In tables Tables G.4-G.13 of Appendix G I show the estimates of the nonstationarity and intermittency parameters for cloud visible radiance field, cloud optical depth and cloud droplet effective radius for all scenes of the extended data base (34 scenes). The mean cloud optical depth in the analysed scenes ranged approximately between 8 to 32 and the mean cloud droplet effective radius between 6 and 17 μm.

4. For the largest data set ($F87$) I show the location of all scenes in the bifractal plane for cloud visible radiance, cloud optical depth and cloud droplet effective radius separately.

5. For each data set ($F87$, $P94$, $P95$, and $S95$) I compute ensemble averaged nonstationarity and intermittency parameters for cloud visible radiance, cloud optical depth and cloud droplet effective radius and plot their location in the bifractal plane.

6. I summarise and discuss the results of this chapter.

7.3.1 Nonstationarity and intermittency parameters.

In tables G.1-G.3 in Appendix G) I present the estimates of the nonstationarity $H(1)$ and intermittency $C(1)$ parameters and spectral slope estimates obtained through the structure function analysis $\zeta(2) + 1 = 2H(2) + 1$, estimated from the least squares fit to the ensemble averaged power spectrum β and, estimated from the least squares fit to the octave binned power spectrum β_8 for the fields of cloud visible radiance, cloud optical depth and cloud droplet effective radius for scenes 1 to 6 (uni-modal), 7 to 10 (bi-modal), and 11 to 14 (thick clouds) (see Table B.1).

Scene 10 is missing from this analysis since the view angle for this scene exceeds 40°.

The scaling range for each scene and field is given in the tables as is the scene cloud fraction estimated using the spatial coherence method of Coakley and Bretherton (1982). The values in brackets $(\cdot)$ are the uncertainties of the estimates from the least squares fit. The uncertainties of the singular measures estimates were computed using 7.4 and found to be between 0.01 to 0.02 in all cases.

Examination of the results assembled in tables G.4-G.13 reveals the following.

1) Transition between nonstationarity and stationarity, available scaling range

Tables G.1-G.3 indicate the range of scales over which the multifractal parameter of cloud fields were estimated. With the spatial resolution of the AVHRR approximately 1 $km \times$ 1 km I can access only a upper region of the scaling range. It is known from the high spatial resolution ground based, aircraft and satellite measurements (see for example King *et al.* (1981), Cahalan and Snider (1989), Davis *et al.* (1996)) that the scaling range of cloud liquid water path extends over several decades from about 10 m to tens of kilometres. The AVHRR instrument makes measurements over the last decade of the scaling range. This is however the most interesting part of the spectrum since it is near 10 km where the transition between nonstationarity and stationarity takes place. In many scenes I observe the transition at 3 or 4 km. This limits the number of points used in the analysis to just 3 or 4. In other cases the scaling range extends to 10 or even 20 km. I expect better precision and likely better accuracy of the estimates of multifractal parameters in these cases.

2) The consistency between the three methods of the spectral slope estimation

The estimates of the spectral slope based on the structure function analysis ($2H(2)+1$) are generally consistent (within typical error bars of 3 to 5%) with the slope estimated directly from the power spectrum whether it is the ensemble average

spectrum (β) or the octave binned spectrum (β_8). There are few exceptions when the three slope estimates are further apart than the indicated error bars (the cloud visible radiance in scene no 5 for example (Table G.1, page 242) has $2H(2)+1 = 1.84$ (± 0.03), $\beta = 2.18$ (± 0.04), and $\beta_8 = 2.07$ (± 0.10)) however my estimates of errors in this analysis are rather conservative, being the uncertainties of the least squares fit with no errors in the variables. There are a few cases of clear disagreement between the structure function approach and direct estimate of slope from the power spectrum (e.g. cloud visible radiance and cloud optical depth in scenes no 13 and 14). In these scenes β is close to or even greater than 3, which is indicative of processes with nonstationary increments where $\beta = 2H(2)+1$ does not necessarily hold.

When the scaling range is short (less than *5* km) the slope of the ensemble averaged spectrum is in a better agreement with the slope estimated from the structure function for cloud radiance and cloud optical depth than is the slope estimated from the octave binned spectrum. This typically reverses for longer scaling ranges when the octave binned spectrum slope and the structure function based slope are closer. This reflects the octave binned spectrum is better representation of larger scales and the loss of small scale resolution in this method of noise reduction. Conversely, the ensemble averaging provides a good representation of small scales but fails when longer scales become important.

The spectra of cloud droplet effective radius at small scales are often dominated by white noise. This leads to underestimation of the spectral slope at small scales when using the ensemble average spectrum compared to the slope of the octave binned spectrum. To illustrate this point I show in Figure 7.10 an example of spectra of cloud radiance, cloud optical depth and cloud droplet effective radius for scene no 11.

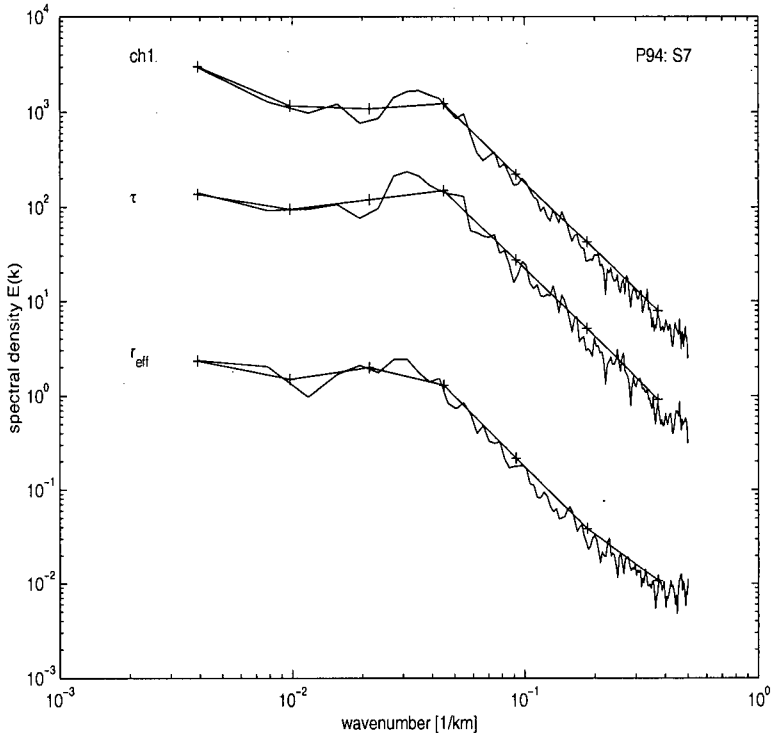

Figure 7.10: Power spectra of cloud visible radiance (*ch1*), cloud optical depth (τ) and cloud droplet effective radius r_{eff} for scene no 11. The solid lines without without symbols are the ensemble average spectra. The (+) marked lines are the octave binned power spectra. Note the noise in $E(k)$ for r_{eff} at wavenumbers > 0.3 $1/km$.

When estimating the power spectrum slope I excluded the white noise dominated region from the computations.

Typically, I found the same scaling range for all cloud parameters fields. In several scenes (8 and 12 most notably) I observed longer scaling range for r_{eff} than for either cloud radiance or τ or a second scaling region at larger scales. I discuss the similarities and dissimilarities of the multifractal properties of cloud visible radiance, τ and r_{eff} below.

3) Agreement between the spectral and multifractal parameters of cloud visible range radiance and cloud optical depth

The comparison of the multifractal parameters and the spectral slope of the cloud visible radiance and cloud optical depth fields points to very similar spatial behaviour and multifractal properties of these two fields. In Figure 7.11 (page 157) I plot the second order structure functions for fields of cloud radiance, cloud optical depth and cloud droplet effective radius for the uni-modal scenes 1 to 6. For all scenes the cloud optical depth structure function follows closely the structure function of cloud radiance field. This is not always the case with the cloud droplet effective radius in scene 3 and 5. For small scales the behaviour of all three fields of cloud parameters is similar but at larger scales cloud droplet effective radius sometimes diverges from the path established by cloud radiance or cloud optical depth and exhibits a long range correlations not present in fields of cloud radiance or τ.

These long range correlations in field of cloud droplet effective radius are more pronounced in scenes with bi-modal joint distributions of τ and r_{eff}. In Figure 7.12 (page 158) I plotted second order structure functions for fields of cloud radiance, cloud optical depth and cloud droplet effective radius for the bi-modal scenes 7 to 10. In scene 8 there is a range between 4 to 20 km where fields of cloud radiance and τ appear stationary while r_{eff} exhibits a secondary nonstationary regime. A similar case is represented by scene 10.

In Figure 7.13 (page 159) I show the second order structure functions for fields of cloud radiance, cloud optical depth end cloud droplet effective radius for thick clouds in scenes 11 to 14.

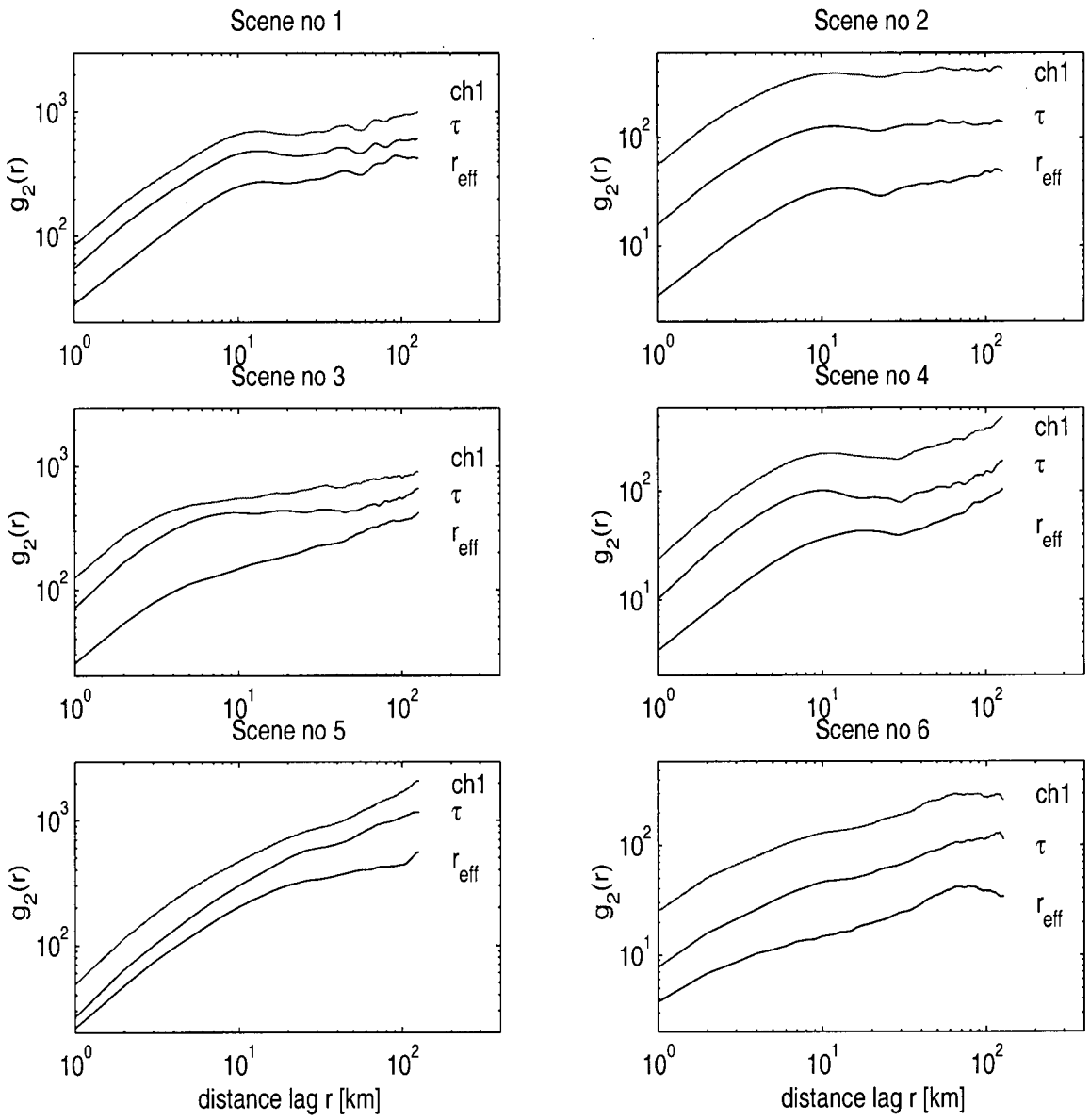

Figure 7.11: Second order structure functions of cloud visible radiance (*ch1*), cloud optical depth (τ) and cloud droplet effective radius r_{eff} for the uni-modal scenes 1 to 6 (see Figure 3.5 for scatter plots of τ and r_{eff}).

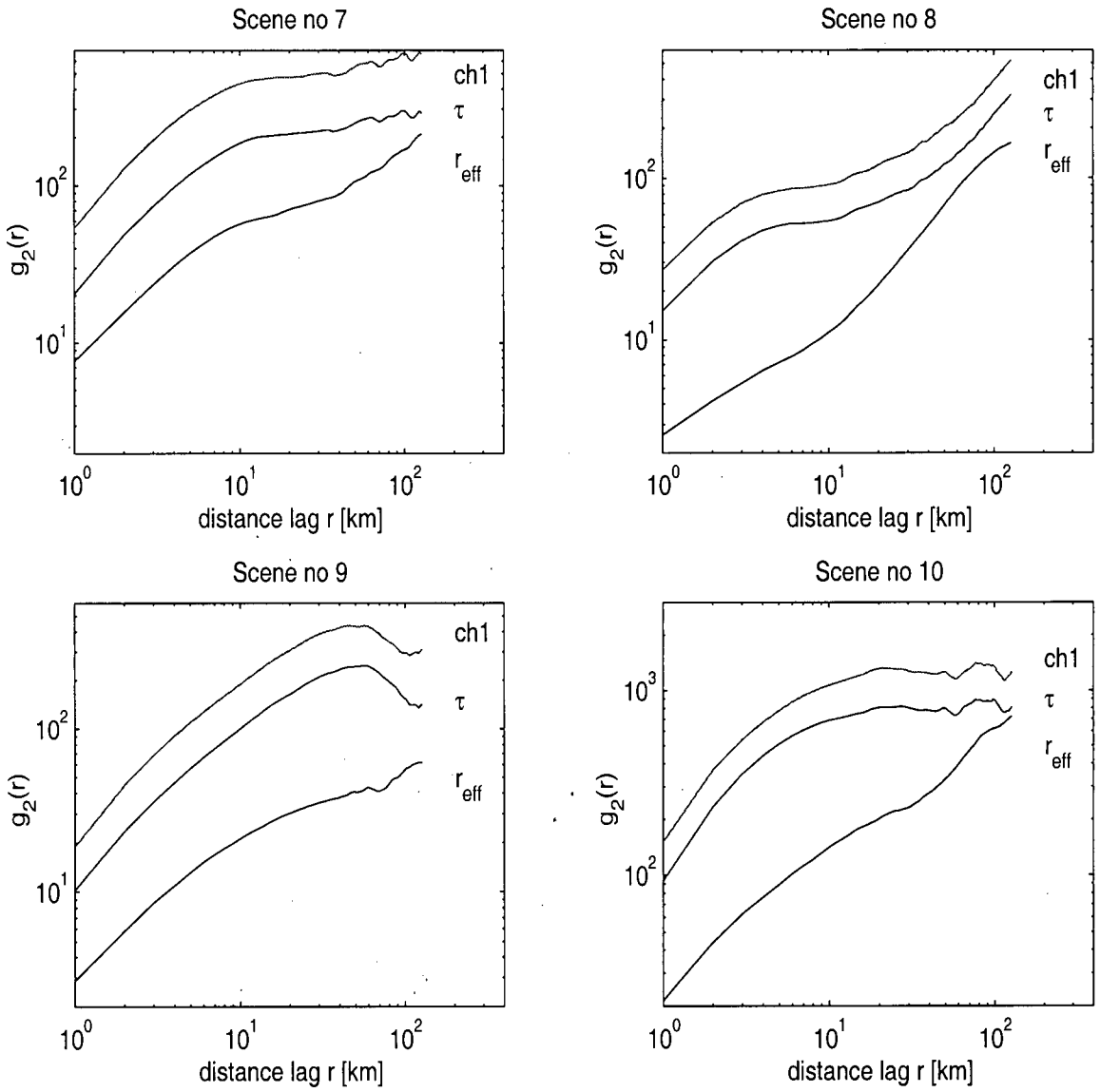

Figure 7.12: Second order structure functions of cloud visible radiance (*ch1*), cloud optical depth (τ) and cloud droplet effective radius r_{eff} for the bi-modal scenes 7 to 10 (see Figure 3.6 for scatter plots of τ and r_{eff}).

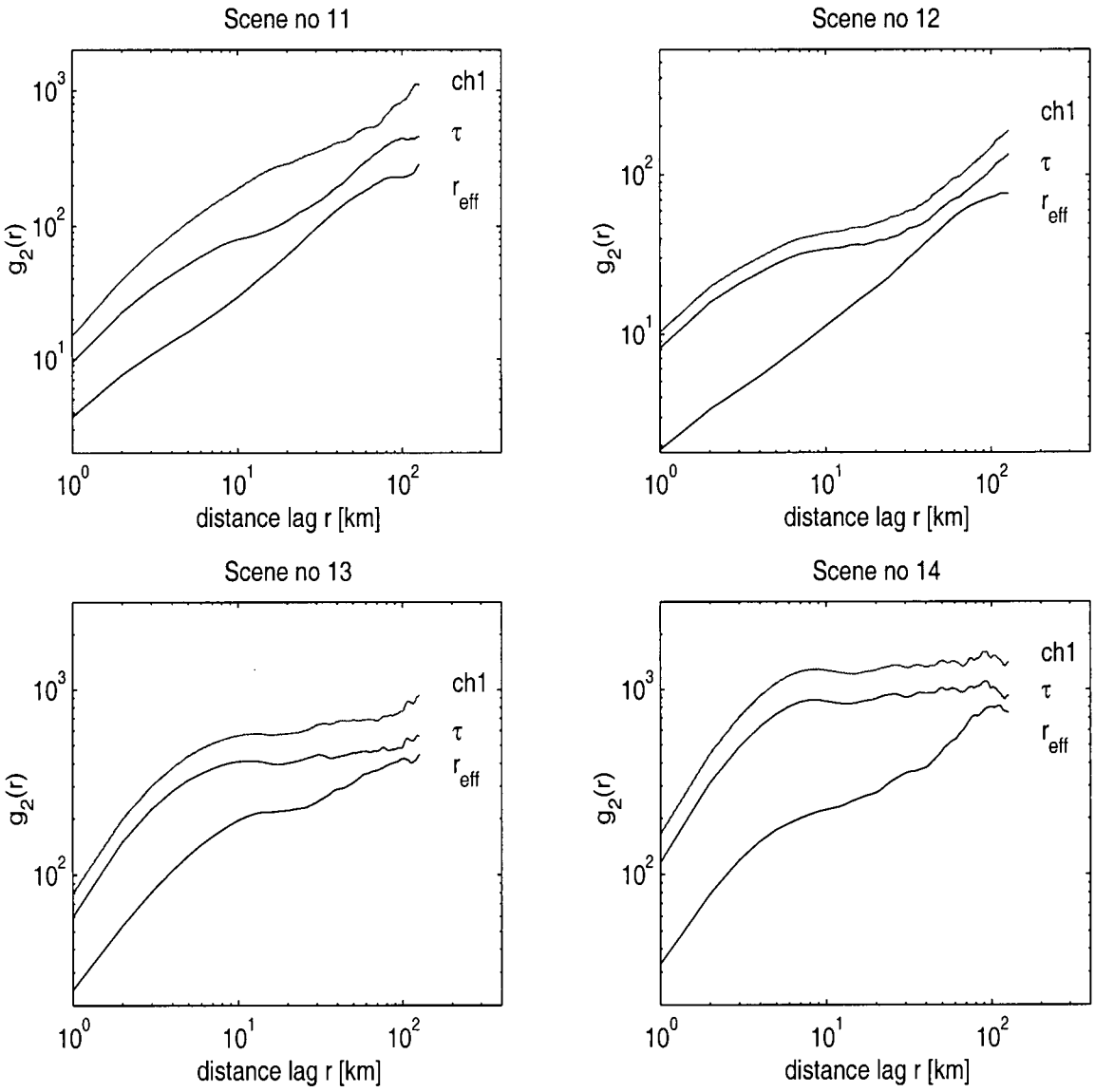

Figure 7.13: Second order structure functions of cloud visible radiance ($ch1$), cloud optical depth (τ) and cloud droplet effective radius r_{eff} for thick clouds in scenes 11 to 14 (see Figure 3.9 for contour plots of τ and r_{eff}).

In chapter 3 (Figure 3.9) I found that scene 12 had a bi-modal joint distribution of τ and r_{eff} while scenes 13 and 14 were uni-modal but exhibited a wide range of N_{sat} . The behaviour of structure functions for scene 12 indeed resembles the bi-modal cases of moderately thick clouds in Figure 7.12, scenes 8 and 10 in particular. Scenes with a wide range of N_{sat} (13 and 14) also exhibit long range correlations in r_{eff} not observed for cloud radiance or τ. Scene 11 (uni-modal) exhibits the least contrast in the behaviour of all three structure functions (τ, r_{eff} and cloud radiance) in the group of thick clouds.

The similarity between the multifractal properties of the radiance field and cloud optical depth justifies the use of the visible channel radiance as a surrogate for cloud optical thickness in studies of cloud field spatial variability when the retrievals of cloud optical depth are not available. Since cloud radiance is more readily available than cloud optical depth or cloud liquid water path, many satellite studies of spatial variability of clouds are based on fields of cloud radiance and the correspondence between the radiance and cloud optical depth is often 'silently' assumed. I make use of this result when we analyse the $S95$ data set. Clouds of that data set are very thick. Pixel values of τ frequently exceed the range of the lookup table used in the retrieval of cloud optical depth and cloud droplet effective radius , which leads to convergence gaps in the retrieved fields of τ and r_{eff}. Such fields are not suitable for spatial analysis. My analysis of the SOCEX data will thus be limited to the cloud radiance field, but in view of the correspondence between the cloud radiance field and the cloud optical depth field seen section 7.3.1, I consider the multifractal parameters of the radiance field to be representative of the cloud optical depth field as well.

4) Long range (> 10 km) variability of cloud droplet effective radius

In chapter 3 I related the occurrence of two clusters in the scatter plots of r_{eff} and τ to coherent regions with markedly different N_{sat} in the cloud scenes. The reader is

referred to Figure 3.10c and 3.10d of chapter 4 which show the spatial separation of the two branches in the image. I postulate that the variability in N_{sat} which leads to the two-branch structure of $\tau - r_{eff}$ scatter plots is also linked to the long range variability of cloud droplet effective radius in these cases. I consider scene 8 as an example.

Figure 7.14 shows the false colour image of the cloud droplet effective radius for a subscene of scene 8 (the fully cloudy part of the scene has been selected).

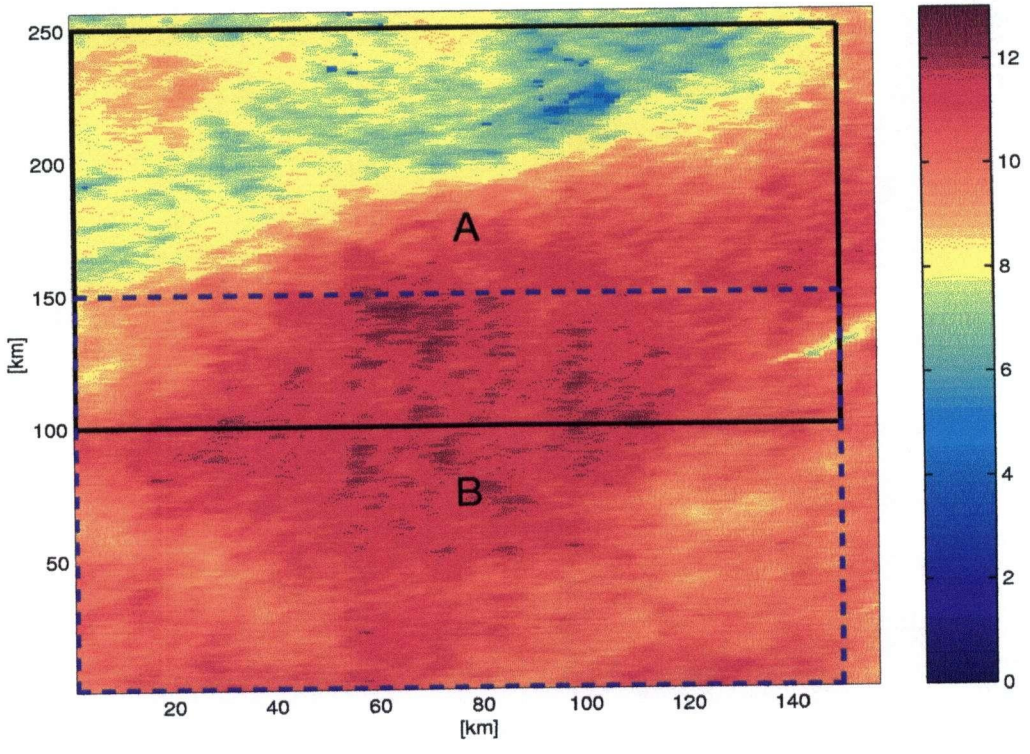

Figure 7.14: False colour image of cloud droplet effective radius [μm] in scene 8.

There is a marked difference, with a maximum of 9 μm, in r_{eff} between the lower and upper parts of the image. I compute the second order structure function for a subimage ("A") of scene 8 which intentionally contains the transition between

the two r_{eff} regimes i.e. two modes of the scatter plot of τ and r_{eff} and one for a subimage ("B") intentionally entirely within one regime (mode). As the subimage "A" I designated the rectangle between [100,250] in vertical and [1,150] in horizontal (encompassed by black solid lines). As the subimage "B" I designated the rectangle between [1,150] in vertical and [1,150] in horizontal (encompassed by blue dashed lines). Figure 7.15 shows the structure function for regions "A" and "B".

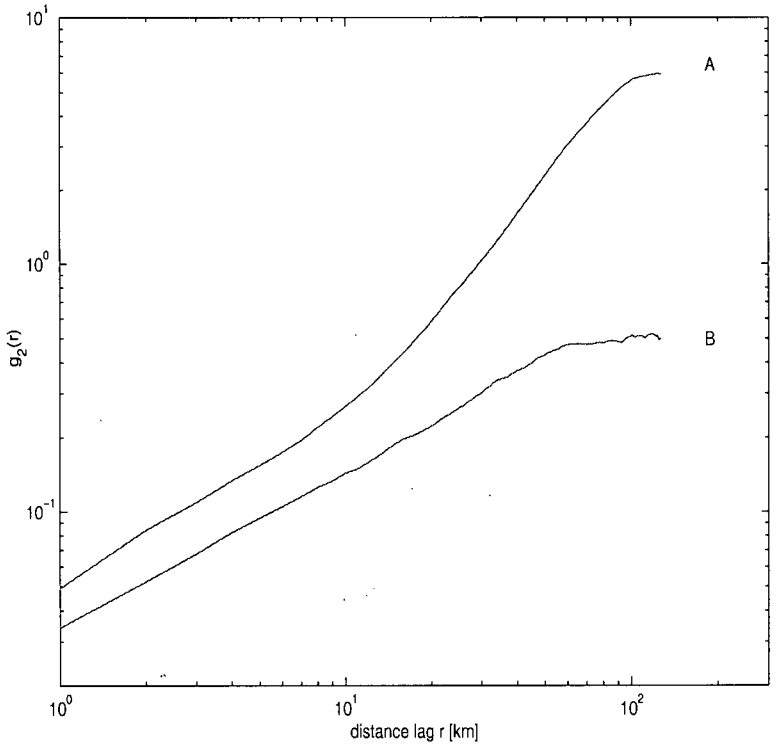

Figure 7.15: Second order structure functions for regions "A" [100:250,1:150] and "B" [1:150,1:150] of cloud droplet effective radius in scene 8.

Figure 7.15 demonstrates the emergence of the second nonstationary scaling region at larger scales in response to the transition between two r_{eff} regimes. The scaling is very similar for at small scales.

7.3.2 Type of scaling.

1) Scaling of the structure function

To examine the type of scaling of the cloud field properties I plot the exponent function $\zeta(q)$ and the information dimension $D(q)$ as functions of the order q. In Figure 7.16 (page 164) I show the exponent function $\zeta(q)$ for the cloud visible radiance, cloud optical depth and cloud droplet effective radius for uni-modal scenes 1 to 6. Figure 7.17 (page 165) shows $\zeta(q)$ for cloud radiance, τ and r_{eff} for the bi-modal scenes 7 to 9 and and Figure 7.18 (page 166) shows $\zeta(q)$ for the same fields for the thick cloud scenes 11 to 12. I excluded scenes 13 and 14 from further analysis due to the disagreement between $(2H(2)+1)$ and β (see Tables G.1-G.3).

The cloud visible radiance field exhibits predominantly monofractal behaviour (i.e. linear dependence of the exponent function $\zeta(q)$ on q) for all types of scenes. Only 3 (nos 2, 5 and 9) scenes in all the data sets show multifractal scaling in cloud visible radiance although in two of these cases the multifractality is weak. Scaling of the cloud optical depth corresponds closely to that of the cloud radiance. In contrast, multiscaling is frequent in the cloud droplet effective radius retrievals.

I find multiscaling to be primarily associated with broken cloudiness. All scenes with cloud fraction less than 1.0 exhibit (1, 5, 6 and 7) exhibit multiscaling in cloud droplet effective radius but not always in cloud optical depth or cloud radiance field. Scaling of cloud droplet effective radius appears to be most sensitive to breaks in cloud cover. Lower cloud fraction is usually associated with stronger multiscaling and can more readily cause multiscaling in cloud optical depth and cloud radiance.

In Table G.3 (and G.6 and G.9) I marked with a "*" partly cloudy scenes for which only fully cloudy sectors were used in the computation of the exponent function $\zeta(q)$. All these sectors exhibit monoscaling in all parameters, cloud radiance, τ, and r_{eff} whereas the entire scene have multiscaling structure functions at least in r_{eff}.

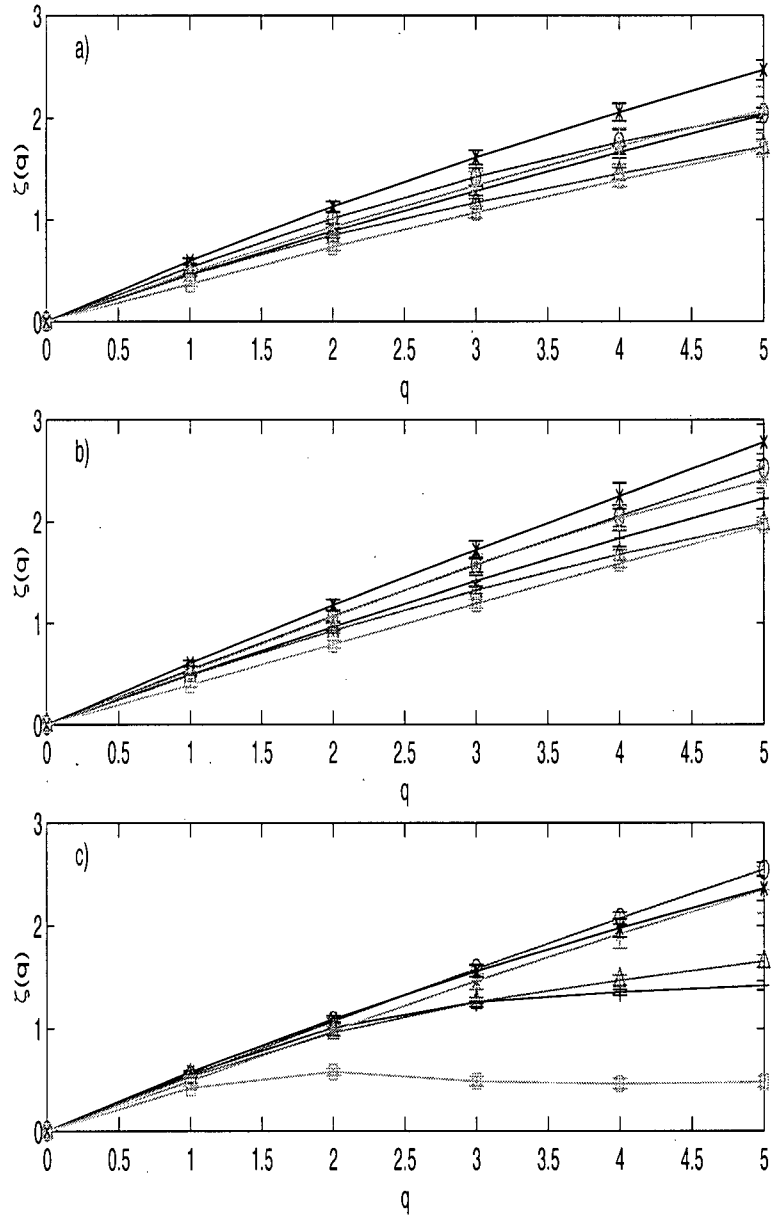

Figure 7.16: Exponent function $\zeta(q)$ of a) cloud visible radiance field, b) cloud optical depth , and c) cloud droplet effective radius for uni-modal scenes 1 to 6 of Table B.1: 1 (+), 2 (∘), 3(∗), 4(×), 5(△), 6(□).

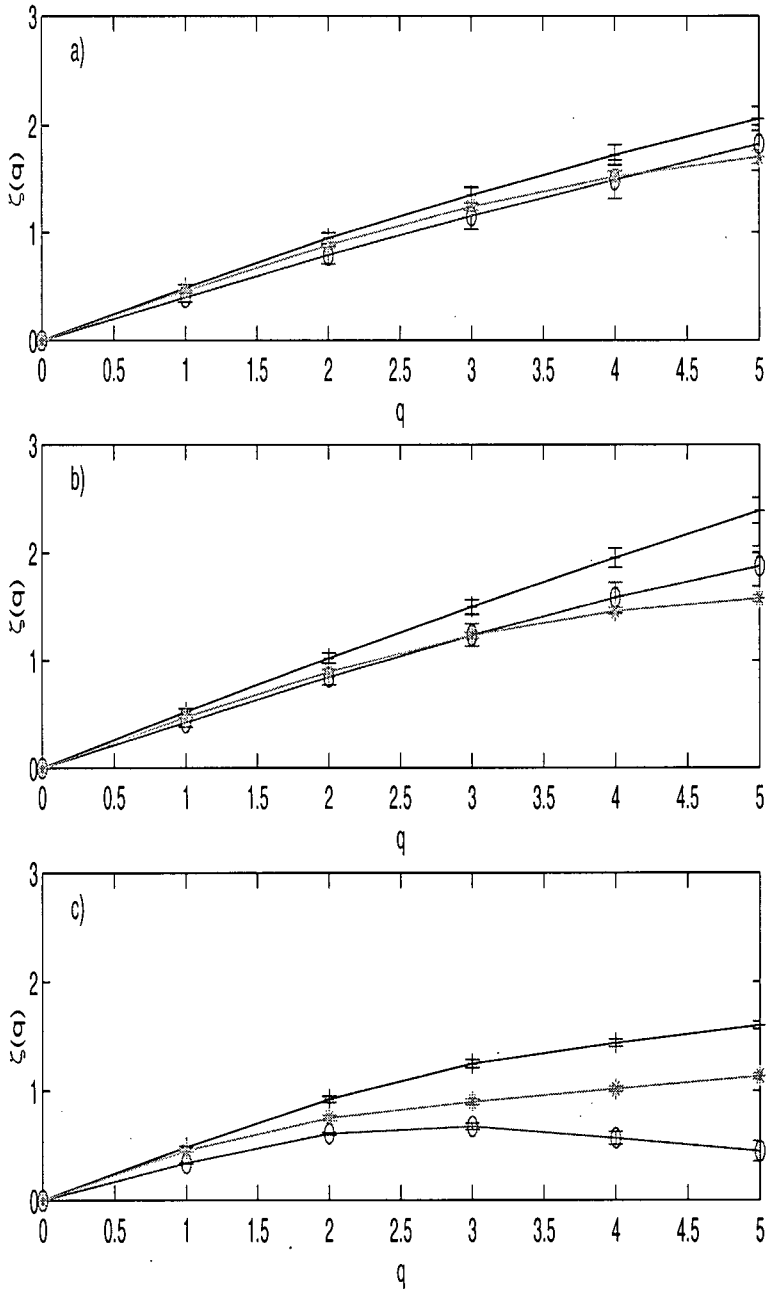

Figure 7.17: Exponent function $\zeta(q)$ of a) cloud visible radiance field, b) cloud optical depth , and c) cloud droplet effective radius for bi-modal scenes 7 to 9 of Table B.1: 7 (+), 8 (∘), 9(∗).

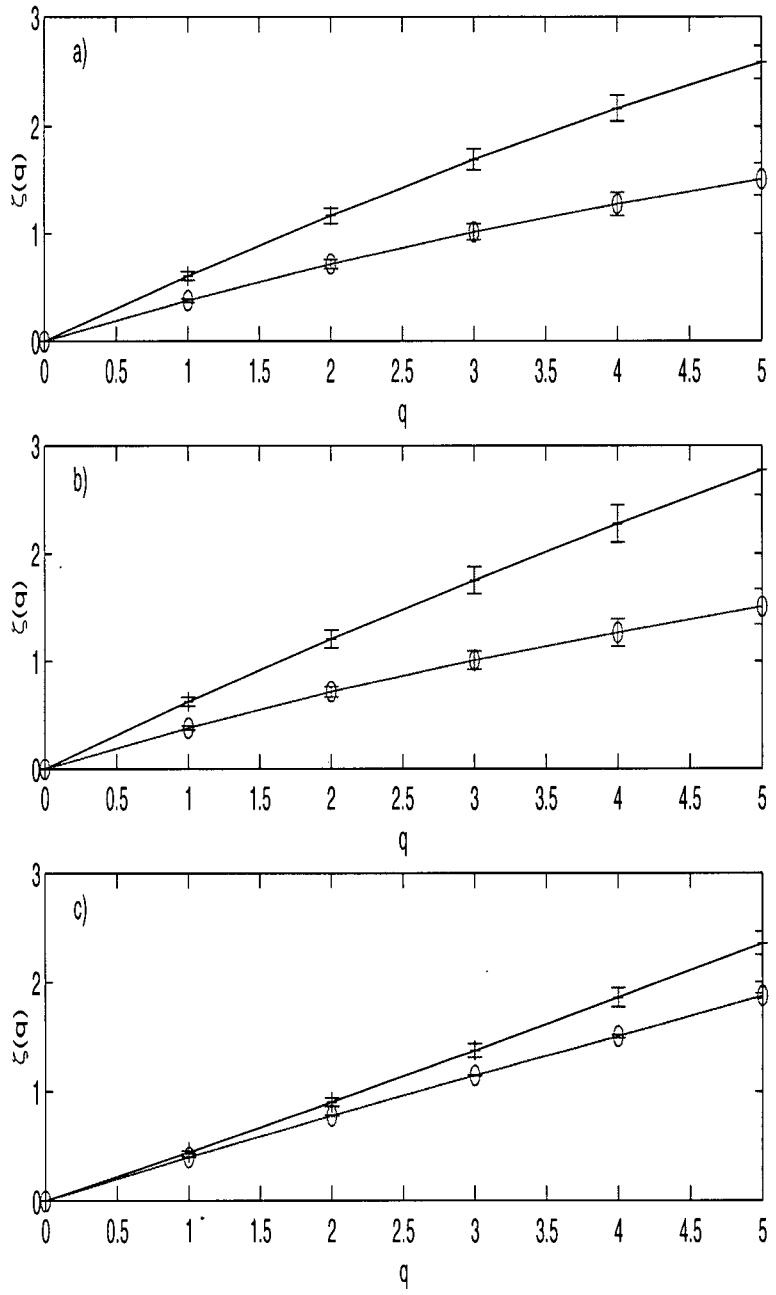

Figure 7.18: Exponent function $\zeta(q)$ of a) cloud visible radiance field, b) cloud optical depth , and c) cloud droplet effective radius for thick clouds, scenes 11 to 14 of Table B.1: 11 (+), 12 (∘), 13(∗), 14(×).

2) A conceptual model of multiscaling in broken cloud fields

The multiscaling character of broken clouds fields can be understood in terms of a simple conceptual model where a transition between cloudy and no-cloudy pixels is modelled by a Heaviside step function. Let the fully cloudy sector of the field be variable and monoscaling (resembling the scaling in fully cloudy scenes). By superimposing a step function with a variable monoscaling field one can build a nonstationary multifractal whose strength will depend on the ratio of the variability of the monoscaling field and the height of the Heaviside function.

I illustrate this with an example. I selected ordinary Brownian motion as the nonstationary monoscaling variable field ($H(q)$ =0.5 for all q, $\zeta(q) = qH(1)$). The exponent function $\zeta(q)$ for Heaviside function equals 1 for all $q > 0$. Figure 7.19 (page 168) shows how the superposition of Heaviside function and ordinary Brownian motion leads to a multiscaling signal. In the left panel of figure 7.19 I show the signals, Heaviside function $h(x)$ (a), Brownian motion $B(x)$ (c) and the superposition of $B(x)$ on the $h(x)$=1 section of the Heaviside function (e). The right panel of Figure 7.19 shows the exponent function $\zeta(q)$ corresponding to the signals of the left panel, $\zeta_h(q)$ (b), $\zeta_B(q)$ (d), and $\zeta_B h(q)$ (f) for the superimposed signals.

Figure 7.20 (page 169) shows that by changing the relative strength of the two original signals the degree of multiscaling in the signal resulting from their superposition can be controlled. Here I increased the step of the Heaviside function by a factor of 2 (7.20a) compared to Figure 7.19 and obtained a stronger multiscaling in the resulting signal (7.20b).

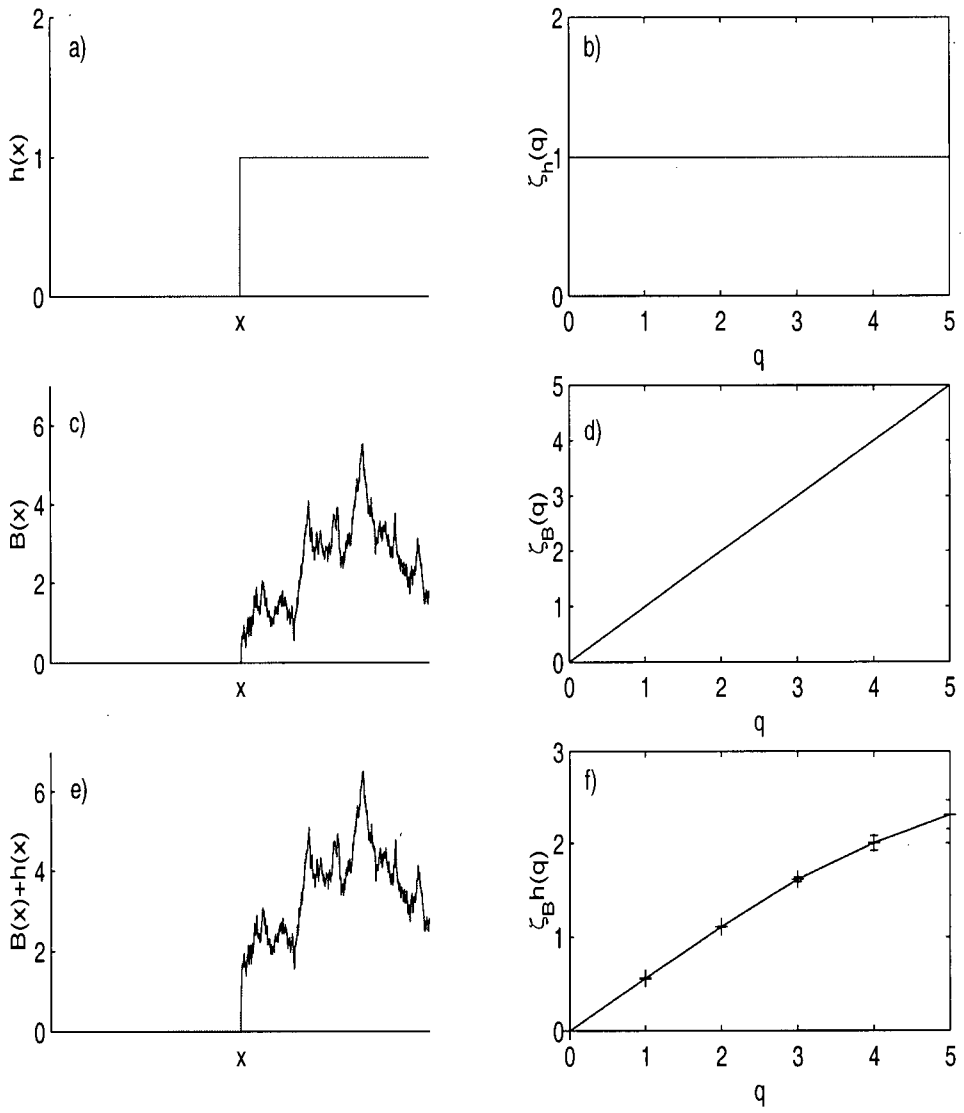

Figure 7.19: Multiscaling signal build by superimposing Heaviside function $h(x)$ and ordinary Brownian motion $B(x)$: a) Heaviside step function $h(x)$, b) $\zeta_h(q)$ the exponent function of $h(x)$, c) Brownian motion $B(x)$, d) $\zeta_B(q)$ the exponent function of $B(x)$, e) $h(x) + B(x)$ the superposition of c) and the second half of a), f) $\zeta_B h(q)$ the exponent function of $h(x) + B(x)$ given in e).

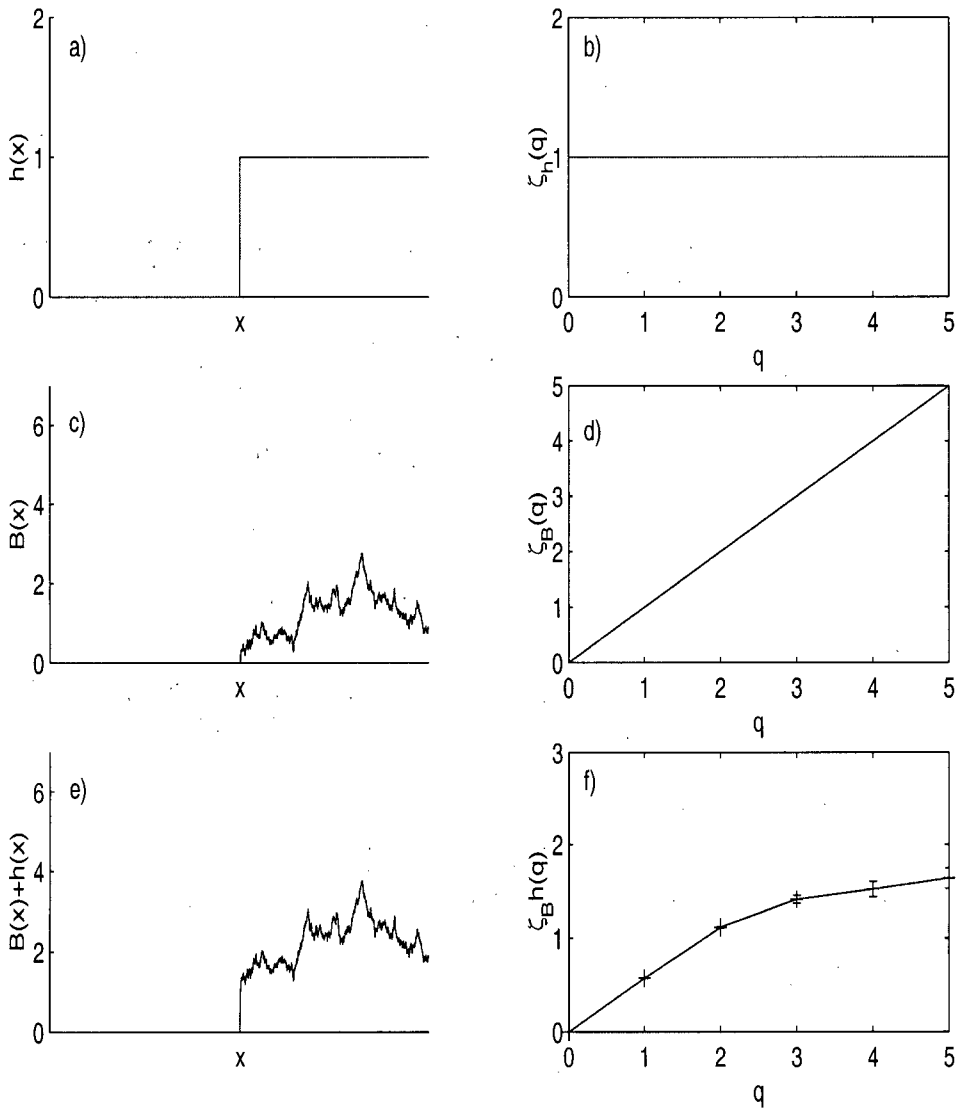

Figure 7.20: Strongly multiscaling signal build by superimposing Heaviside function $h(x)$ and ordinary Brownian motion $B(x)$. Smaller B/h ratio (larger jump in the step function) results in a stronger multiscaling signal: a) to f) as in Figure 7.19.

3) Multiscaling in cloud droplet effective radius field

I find that it is the difference between the relative strength of the variability in the fully cloudy sections of the cloud field to the height of step-like change at the transition between cloudy and non-cloudy pixels that leads to different type of scaling for fields of cloud optical depth and cloud droplet effective radius . In Figure 7.21 I show demeaned and mean normalised transects of τ and r_{eff} from scene $F_{87}16$ (see Table B.3 in Appendix B and Tables G.4-G.6 in Appendix G). This scene has cloud fraction of 0.82 (G.4) and exhibits monoscaling in cloud optical depth and multiscaling in cloud droplet effective radius .

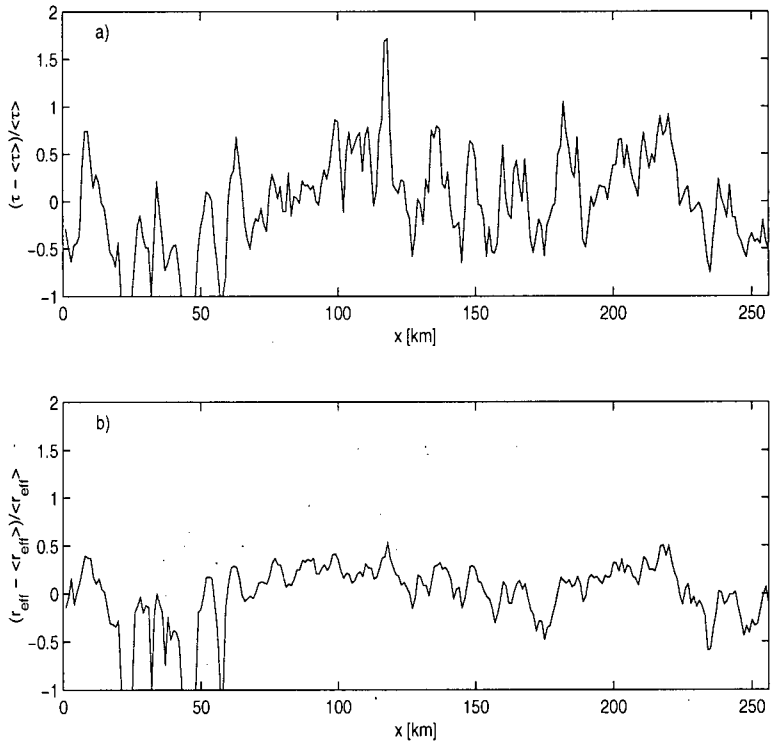

Figure 7.21: Demeaned and mean normalised transects of cloud optical depth and cloud droplet effective radius taken from scene $F_{87}16$: a) cloud optical depth , b) cloud droplet effective radius .

In Figure 7.21 the begining of the record corresponds to broken cloud (values of '-1' represent clear pixels). There is a striking difference between the τ and r_{eff} transects. For cloud optical depth the variability due to transitions between cloudy and clear pixels is of the same range or even smaller than the variability of τ in the fully cloudy sector. This case corresponds to large ratio of field variability to the step-like transitions between cloudy and clear pixels. One can expect the resulting signal to be dominated by the monoscaling variable field.

In contrast, to the cloud optical depth variability the cloud droplet effective radius field is only weakly variable in the fully cloudy sector and the step-like transition between clear and cloudy pixel is determinant to the multiscaling of the resulting signal (compare Figures 7.19e-f and figure 7.20). In Figure 7.22a-b on page 172 I show the exponent functions $\zeta_\tau(q)$ and $\zeta_{r_{eff}}(q)$ computed for the transects of τ and r_{eff} shown in Figure 7.21.

As expected, the cloud optical depth in Figure 7.22 scales as a monofractal and cloud droplet effective radius as multifractal. In the fully cloudy sector of the field the cloud droplet effective radius is monoscaling (not shown).

The lower variability of r_{eff} is consistent with the reference cloud model given by (3.2). Since

$$\sigma(bx) = b\sigma(x) \tag{7.5}$$

where σ denotes the standard variation, x is a random variable and b a numerical factor, we can expect

$$\sigma(log(r_{eff})) = \sigma(\tau^{1/5}) = 0.2\sigma(\tau) \tag{7.6}$$

or

$$\kappa = \frac{\sigma(log(r_{eff}))}{\sigma(\tau^{1/5})} = 5 \tag{7.7}$$

if N_{sat} is held constant. In practice, measurement uncertainty and the finite range of N_{sat} , even in scenes nearly homogeneous in N_{sat} , add to the variability of r_{eff}

resulting in $\kappa < 5$. For the majority of uni-modal scenes I find κ = 2-4. In other words, assuming no errors in retrievals, for a single branch case 40 to 80% of the observed variability of r_{eff} can be attributed to varying τ. The other 20 to 60% will be attributed to variable N_{sat} .

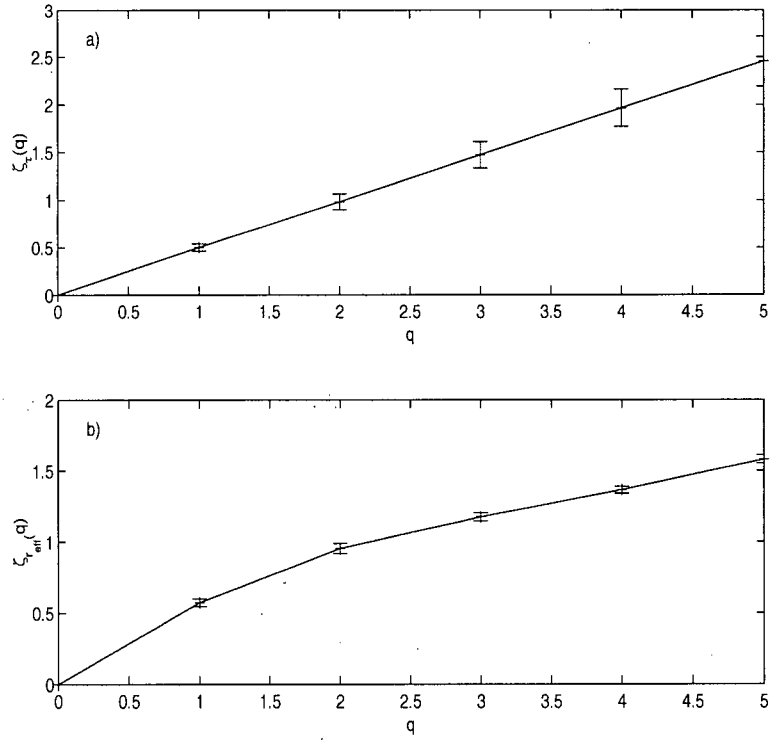

Figure 7.22: Exponent functions for the transects of cloud optical depth and cloud droplet effective radius shown figure 7.21: a) $\zeta_\tau(q)$, b) $\zeta_{r_{eff}}(q)$.

Scene 8 again deserves special attention. The scene is fully cloudy yet exhibits strong multiscaling in cloud droplet effective radius (to the point of breaking where $\zeta(q)$ begins to decrease) and monoscaling in cloud optical depth and cloud radiance. In this case it is the steep transition between two r_{eff} regimes which acts as the step function. Figure 7.23 shows transects of τ and r_{eff} across the transition line in scene 8 and Figure 7.24 (page 174) shows the exponent functions $\zeta_\tau(q)$ and $\zeta_{r_{eff}}(q)$

along these transects.

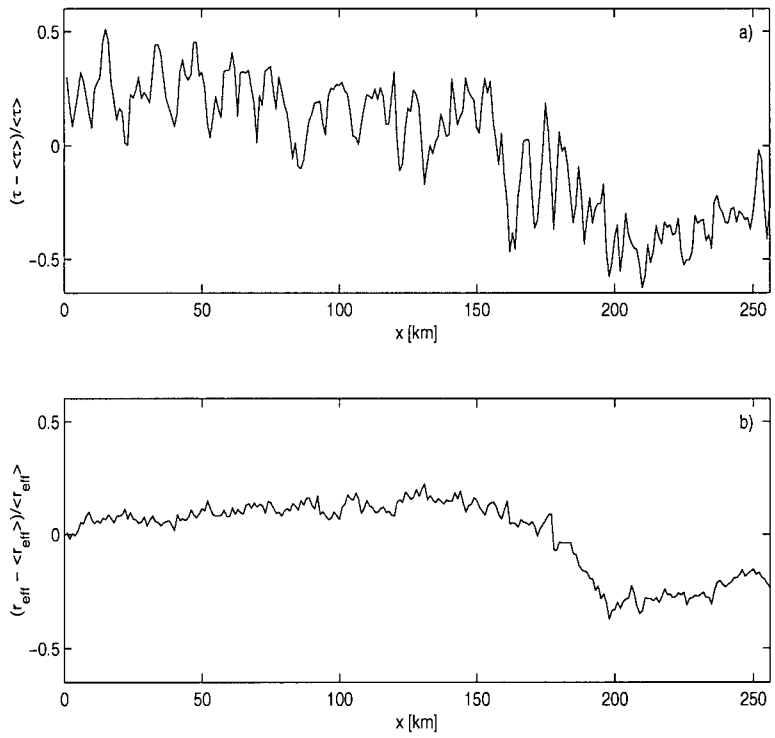

Figure 7.23: Demeaned and mean normalised transects of cloud optical depth and cloud droplet effective radius taken from scene 8: a) cloud optical depth , b) cloud droplet effective radius .

This simple example demonstrate that multiscaling occurs in signals which are composed of a weakly variable monoscaling field superimposed on a step-like transition. I found such signals in cloud parameter fields, especially cloud droplet effective radius . They are associated with

1. broken clouds

2. solid clouds in a transition zone between two very different r_{eff} regimes which in chapter 4 I linked to two air masses of distinctly different N_{sat}

This multiscaling behaviour is revealed only for $q > 1$ and does not affect the values of the nonstationarity parameter $H(1)$ (compare $\zeta(1)$ for mono and multiscaling scenes in Figures 7.16 to 7.18), and thus bears no effect on the bifractal plane location of the data.

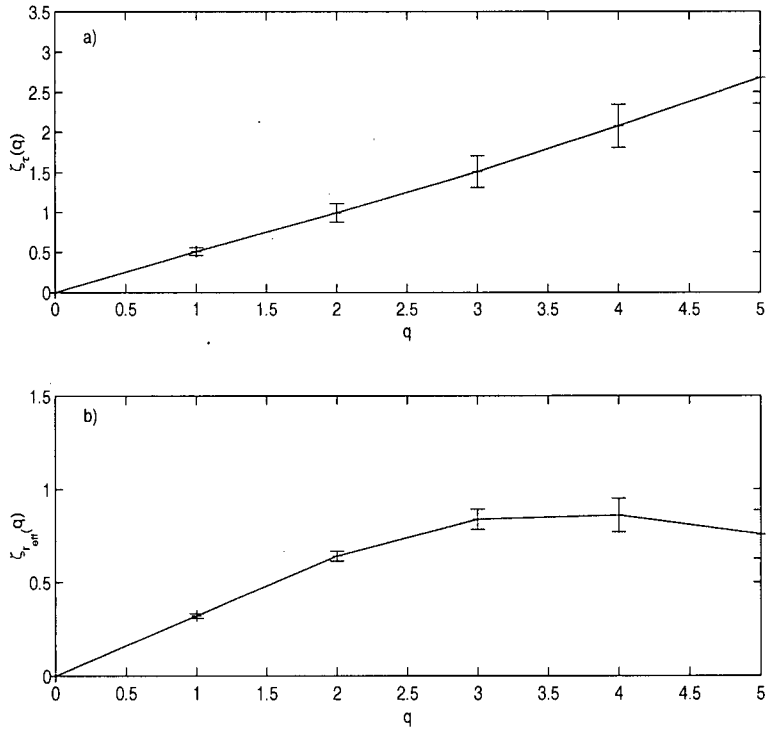

Figure 7.24: Exponent functions for the transects of cloud optical depth and cloud droplet effective radius shown Figure 7.23: a) $\zeta_\tau(q)$, b) $\zeta_{r_{eff}}(q)$.

Davis *et al.* (1996a) observed multiscaling structure functions for cloud liquid water content (*lwc*) fluctuations in aircraft measurements and Marshak *et al.* (1997) observed both multiscaling and monoscaling in aircraft measured *lwc*. Davis *et al.* (1996a) computed multifractal statistics for cloud radiance in one Landsat scene and found the structure function to be weakly multiscaling. However, 7% of the Landsat scene was saturated. Saturated pixels represent bad retrievals and as such fell into

the same category as clear pixels. As I found in my analysis 93% cloud fraction (equivalent to 7% bad pixels) was enough to generate multiscaling in structure function.

4) Scaling of singular measures

In Figure 7.25 on page 176 I show the information dimension $D(q)$ as the function of moment order q for cloud radiance, cloud optical depth and cloud droplet effective radius for uni-modal scenes 1 to 6. The multiscaling of singular measures ($D(q)$ dependent on q) is evident in all scenes and all cloud parameters.

The $D(q)$ plots for the remaining scenes of the (bi-modal and thick) are all similar to those in Figures 7.25 and are not shown here. This multiscaling of singular measures is also an intrinsic feature of fully developed turbulence. The spectrum of $D(q)$ was measured by Meneveau and Sreenivasan (1987a) for q between [-20,20]. Meneveau and Sreenivasan (1987)) found that this $D(q)$ spectrum was within the experimental accuracy identical to a spectrum generated by a simple multifractal cascade model.

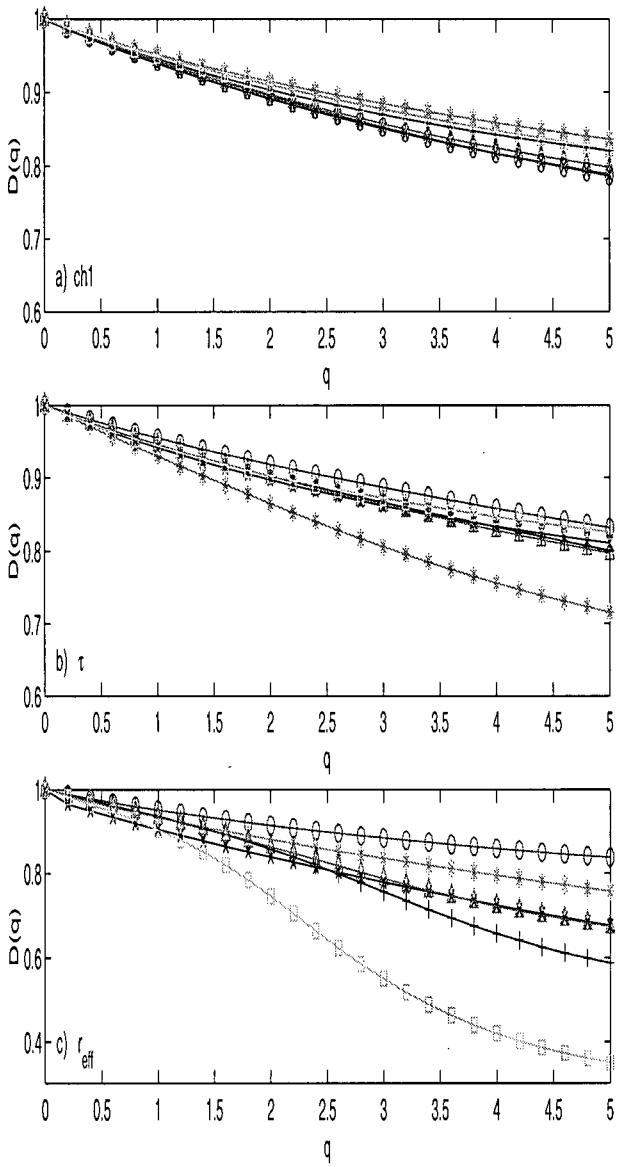

Figure 7.25: Information dimension $D(q)$ of a) cloud visible radiance field, b) cloud optical depth , and c) cloud droplet effective radius for scenes uni-modal scenes 1 to 6 of Table B.1: 1 (+), 2 (○), 3(∗), 4(×), 5(△), 6(□).

7.3.3 Nonstationarity and intermittency in the bifractal plane.

Individual scenes

In tables G.4-G.13 in Appendix G I present the nonstationarity $H(1)$ and intermittency $C(1)$ parameters and spectral slope estimates obtained through the structure function analysis $\zeta(2)+1 = 2H(2)+1$, estimated from the least squares fit to the ensemble averaged power spectrum β and, estimated from the least squares fit to the octave binned power spectrum β_8 for the fields of cloud visible radiance, cloud optical depth and cloud droplet effective radius of the analysed scenes. Scenes in Tables G.4-G.13 are labeled with the name of data set (F_{87}, P_{94}, P_{95} or S_{95}) and a scene number with the data set. Additionally, scenes which appeared before in chapters 3 and 4 (1 to 15 in Table B.1) have their original numbers indicated in brackets.

The results for the $F87$ data set are presented in Tables G.4-G.6 for cloud visible radiance, cloud optical depth and cloud droplet effective radius respectively. Tables G.7-G.9 contain the results of analysis of cloud visible radiance, τ and r_{eff} fields for the scenes of the $P94$ data set and Tables G.10-G.12 the results of analysis for the scenes of the $P95$ data set. Finally, Table G.13 contains the results of analyses of cloud visible radiance fields for scenes from the $S95$ data set.

In Figure 7.26 I show the bifractal plane location of cloud radiance ($\Diamond$) , cloud optical depth ($\triangle$) and cloud droplet effective radius ($\circ$) of the *F87* data set ensemble averages and individual scenes. For r_{eff} fields with two nonstationary regimes only the the first (starting at smallest scales) is considered. Full symbols in Figure 7.26 indicate the ensemble averages and open symbols the individual scenes. The mean τ ranges between [8,32] and the mean r_{eff} between [7 μm ,12 μm] for scenes in this plot. Scenes no $F_{87}6, 7, 9, and 12 to 15$ were taken on FIRE days when drizzle was observed during aircraft missions.

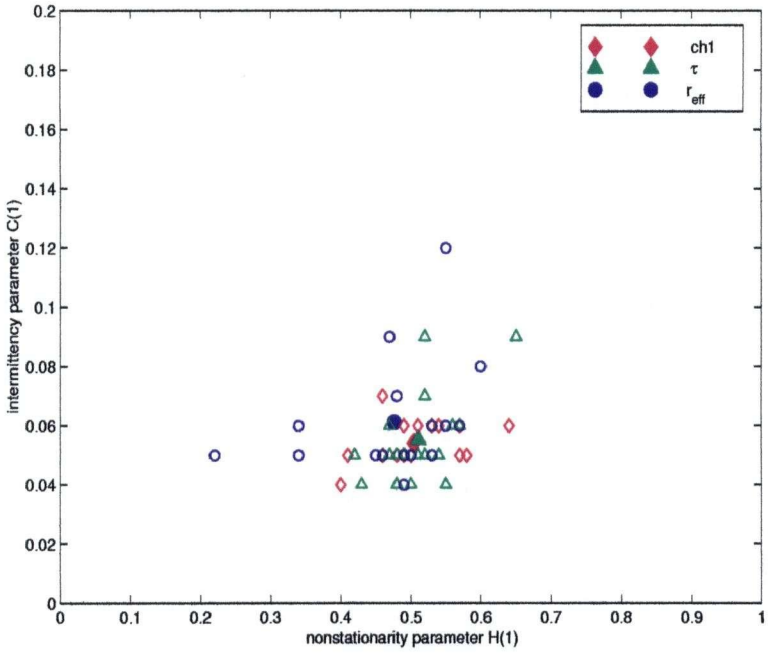

Figure 7.26: FIRE cloud field visible radiance, cloud optical depth and cloud droplet effective radius multifractal parameters in the bifractal plane. Full symbols indicate ensemble averages for the *F87* data set. Open symbols indicated individual scenes: $\Diamond$ - cloud visible radiance, $\triangle$ - cloud optical depth , and $\circ$ - cloud droplet effective radius . Individual scenes have mean τ between[8,32] and mean r_{eff} between [7 μm ,12 μm].

The bulk of data points lies between $H(1)$ of (0.4,0.6) and $C(1)$ of (0.04,0.07). The range of values of the intermittency parameter $C(1)$ (0.04,0.07) for the radiance field, (0.04,0.09) for the optical depth and (0.4,0.09) for the cloud droplet effective radius is not unlike the scatter reported by Marshak *et al.* (1997) for the intermittency parameter of LWC (0.03,0.15). The values of the nonstationarity parameter $H(1)$ are generally larger for the fields of cloud radiance, optical depth and cloud droplet effective radius than those observed by Marshak *et al.* (1997) for the LWC fluctuations. The scatter of the nonstationarity parameter is (0.40,0.64) for the

cloud radiance field, (0.42,0.65) for cloud optical depth and (0.22,0.63) for cloud droplet effective radius compared to (0.22,0.34) for the *lwc* data of Marshak *et al.* (1997). The greater range of $H(1)$ values for cloud droplet effective radius is due mainly to the one point at low value of $H(1)= 0.22$.

My observables, cloud visible wavelength radiance field, cloud optical depth and cloud droplet effective radius are not the same as in Marshak *et al.* (1997) (LWC) and I cannot make a direct comparison between our results and those of Marshak *et al.* (1997). However, if the universality of the thermo-dynamical processes shaping marine stratocumulus holds as postulated by Davis *et al.* (1996) and Marshak *et al.* (1997) one would expect each observable to cluster in the bifractal plane of nonstationarity and intermittency parameters, although not necessarily around the same point. I find this to be the case for fields of cloud radiance, cloud optical depth and cloud droplet effective radius of the $F87$ data set.

Ensemble averages

In Figure 7.27 on page 180 I show the location of $F87$, $P94$, $P95$ and $S95$ ensemble averages of the nonstationarity and intermittency parameters ($H(1)$, $C(1)$) for the fields of cloud visible radiance, optical depth and cloud droplet effective radius.

I also indicated the location of multifractal parameters of LWC data from FIRE, ASTEX and SOCEX experiments (ensemble averages) from Marshak *et al.* (1997), and results for one scene of Landsat Thematic Mapper channel 2 cloud radiance data from FIRE reported in Davis *et al.* (1996a).

The nonstationarity parameter is contained between (0.43,0.59) for all fields and all data sets which is less than the scatter between the nonstationarity parameters of the individual scenes in the $F87$ data set. All three fields of the $F87$ data set, cloud radiance, cloud optical depth and cloud droplet effective radius lie very close to each other in the bifractal plane. All fields $P94$ and $P95$ data sets are less than 0.1 apart in $H(1)$ but the cloud radiance field and τ and r_{eff} are widely separated in

the intermittency parameter. This is increased scatter is correlated with decreasing cloud fraction.

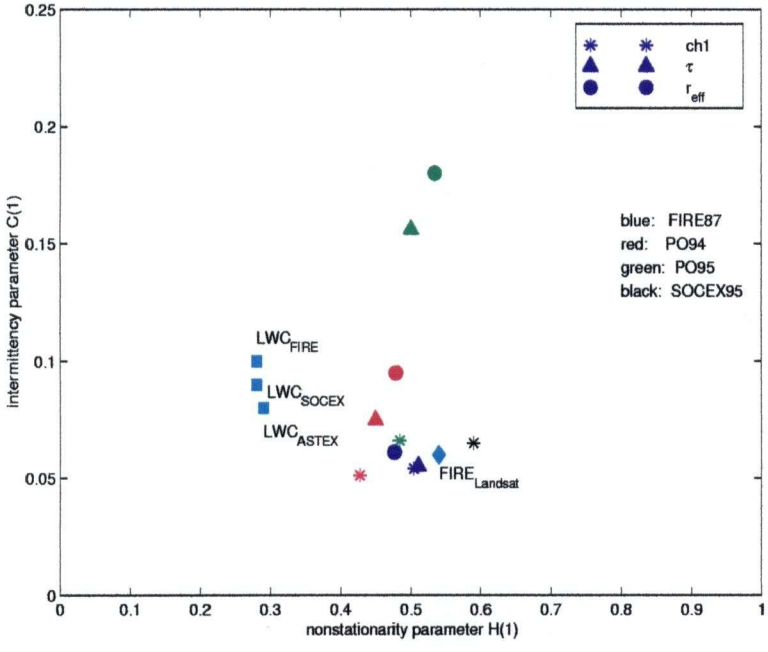

Figure 7.27: The bifractal plane location of ensemble averages of $F87$, $P94$, $P95$ and $S95$ data sets for cloud visible wavelength radiance field (*), cloud optical depth ($\triangle$) and cloud droplet effective radius ($\circ$). Also indicated is the location of the cloud liquid water content data sets from FIRE, ASTEX and SOCEX experiments ($\square$) (after Marshak *et al.* (1997)) and Landsat cloud radiance ($\Diamond$) (channel 2 of the Thematic Mapper) after Davis *et al.* (1996a).

The intermittency of the retrieved fields is necessarily greater than the intermittency of cloud radiance if clouds are broken. The fairly continuous radiance signal is overlayed with the cloud-clear mask in the retrieved field. $F87$ scenes are all almost fully cloudy and the intermittency of all fields is very close and low. $P94$ and $P95$ data sets contain scenes with low cloud fraction and this is reflected in enhanced intermittency of cloud optical depth and cloud droplet effective radius

fields as compared to the cloud radiance field in this data sets.

7.4 Summary of the results of multifractal analysis.

I used the formalism of multifractal analysis (Davis *et al.* (1994)) to quantify the spatial behaviour of marine stratocumulus cloud fields. I analysed a total of 34 AVHRR scenes of cloud visible radiance field, optical depth and cloud droplet effective radius from four different data sets: 1) the FIRE 1987 experiment, 2) Pacific Ocean 1994 data set, 3) Pacific Ocean 1995 data set and 4) the SOCEX experiment (Indian Ocean). The goal of this analysis was to quantify spatial properties of fields of cloud radiance, cloud optical depth and cloud droplet effective radius and determine spatial characteristics of uni-modal, bi-modal and thick cloud scenes.

I found:

- a similar range of nonstationarity and intermittency parameters for all type of scenes (uni-modal, bi-modal, and thick clouds) despite different structure function behaviour (i.e. observed scaling range) and sometimes different type of scaling of structure function (quality of nonstationarity) (see Table G.1 Appendix G).

- a similar behaviour of the second order structure functions of cloud radiance and cloud optical depth and distinctly different long range behaviour of cloud droplet effective radius second order structure function especially in scenes with bi-modal distribution of τ and r_{eff} or thick clouds with wide range of N_{sat} scenes. I postulated that the long range correlations in fields of r_{eff} are associated with the coexistence of spatially distinct r_{eff} (or N_{sat}) regimes within a scene.

- monoscaling in cloud radiance and cloud optical depth and cloud droplet effective radius in fully cloudy scenes with the exception of r_{eff} fields with sharp (step-like) transitions between two r_{eff} regimes (Figures 7.23 and 7.24).

- multiscaling in broken clouds, most notable in field of r_{eff}.
- bifractal plane location of important cloud parameters: cloud radiance, cloud optical depth and cloud droplet effective radius .
- no systematic dependence of $H(1)$ and $C(1)$ on cloud optical depth .

The multifractal analysis quantifies and qualifies two aspects of atmospheric processes: nonstationarity and intermittency. Values obtained in this section can be compared directly to the synthetic cloud fields begining to be generated by large eddy simulations. An alternative is to employ stochastic methods to generate nonstationary and intermittent signals with $H(1)$ and $C(1)$ taken from the data presented here. Davis *et al.* (1996a) and Marshak *et al.* (1997) found the location in the bifractal plane cloud liquid water content (lwc) fluctuations measured by aircraft in FIRE and ASTEX experiments. Additionally, Davis *et al.* (1996a) obtained $H(1)$ and $C(1)$ for aircraft measured fluctuations of lwc in SOCEX and for one scene of Landsat measured cloud visible radiance during FIRE. I have added three new parameters to the bifractal plane: 1) cloud visible wavelength radiance, 2) cloud optical depth and 3) cloud droplet effective radius, all derived from satellite observations with the AVHRR.

I found the multifractal properties of cloud visible wavelength radiance field and cloud optical depth to be very similar in the fully cloudy scenes. For the *F87* data set which consists of scenes which are all fully cloudy or almost fully cloudy the bifractal location of cloud radiance field is (0.49,0.05) whereas the cloud optical depth field has coordinates (0.50,0.05) and the cloud droplet effective radius has (0.48,0.06). The close proximity of the cloud radiance and cloud optical depth fields in the bifractal plane justifies using cloud visible radiance as surrogate of cloud optical depth field in studies of spatial distribution of cloud liquid water, when retrievals of cloud optical depth are not available. The close location of all three points is another indication that variability in τ and r_{eff} is tightly coupled in these

data sets.

Most of the cloud radiance fields and cloud optical depth fields I analysed exhibited monofractal or weakly multifractal scaling in structure function. In contrast, many of the cloud droplet effective radius fields exhibit strong multiscaling behaviour. I attribute this difference in type of scaling between cloud radiance or cloud optical depth and cloud droplet effective radius to the weak small scale variability of r_{eff} as compared to the small scale variability of τ or cloud radiance. The singular measures exhibit multiscaling behaviour in all cloud parameter fields as expected for turbulent flows.

The strong coupling between cloud optical depth, cloud droplet effective radius and cloud droplet number concentration and cloud reflectivity discussed in chapter 1 is reflected in similar spatial structure of τ, r_{eff} and cloud radiance fields. This is expected given the success of the reference model in explaining τ, r_{eff} correlations. Variability in N_{sat} on scales comparable to the size of scenes affects some characteristics of r_{eff} field. In particular, bi-modal scenes may exhibit second nonstationary scaling regime in r_{eff} and multiscaling in r_{eff} structure function. The values of $[H(1), C(1)]$ remain however unaffected by variability of N_{sat} .

Chapter 8

Conclusions

8.1 Summary

In this dissertation I investigated the mesoscale variability of cloud optical depth and cloud droplet effective radius in marine boundary layer clouds. The cloud optical depth and cloud droplet effective radius determine cloud radiative properties, and understanding their variability is important to understanding the complex interactions between clouds and climate.

The cloud optical depth and cloud droplet effective radius fields used in this study were retrieved from polar orbiting satellite AVHRR radiance measurements with the technique of Nakajima and Nakajima (1995). The data was acquired during four experimental periods: FIRE 1987 (ISCPP), Pacific Ocean 1994 (UBC), Pacific Ocean 1995 (UBC), and SOCEX 1995 (CSIRO).

For these data sets I reported the observation of a relationship between cloud optical depth and cloud droplet effective radius (chapters 3 and 4). In chapter 3 I proposed a simple "reference" cloud model (3.2) based on the assumption of a vertical profile of cloud liquid water content that is linear with height and a vertical profile of cloud droplet number concentration that is constant with height. I derived the relation $r_{eff} \propto \tau^{1/5}$ for this model, where the proportionality includes the cloud droplet number concentration N and cloud subadiabaticity β (or alternatively N_{sat}

$=N/\sqrt{\beta}$).

In the framework of this simple model I was able to provide an explanation for the observed correlation of cloud optical depth and cloud droplet effective radius as reported first by Nakajima and Nakajima (1995) and later in this work (chapters 3 and 4). I distinguished between uni-modal and bi-modal joint distributions of τ and r_{eff} and considered the special case of thick clouds ($\tau > 5$ for every pixel in the scene). The uni-modal scenes are well described by the simple "reference model" where the variability in τ and r_{eff} results primarily from the variability of cloud geometrical thickness. Bi-modal scenes mark a departure from the simple model caused by the variability of N_{sat} (e.g. due the coexistence of two distinct populations of N_{sat} in the scene). Thick clouds, treated as a special case because they do not regress to a power law (they fail to satisfy condition II for fitting suitability, see page 60), can have uni-modal or bi-modal joint distributions of τ and r_{eff}. In fact, in section 3, I observed thick clouds with one maximum in the distribution of τ and r_{eff} which extends across a wide range of N_{sat} .

In chapter 4 I used bivariate linear regression on log transformed coordinates to fit a general power law to τ and r_{eff} data for over three hundred cloud scenes classified as homogeneous with respect to cloud droplet number concentration (i.e. uni-modal) and of the approximate size of a GCM grid cell. For 55% of these scenes I found a power law dependence between τ and r_{eff} with an exponent consistent with the reference model (with error bars of less than 30%). Another 25% the scenes provided a 'marginally successful' fit (agreement with error bars greater than 30% but less than 50%).

I applied the model (3.2) to satellite data of τ and r_{eff} to infer N_{sat} , and showed that AVHRR imagery can differentiate between two N_{sat} modes if they differ by 40 cm^{-3} or more, given estimated errors of τ (15%), and r_{eff} (20%). I reported frequency distributions of τ and r_{eff} on scale of 256 $km \times 256$ km and found that the gamma distribution is a good fit to the distribution of τ which is always positively

skewed, and r_{eff} when it is both uni-modal and positively skewed or symmetric.

In chapter 5 I inferred cloud optical depth and cloud droplet effective radius from 6 in cloud aircraft flights and co-located satellite measurements acquired during SOCEX 1995, and found that both the aircraft and the satellite data were well described by the cloud model of equation 3.2. Aircraft measurements also allow for direct estimation of cloud subadiabaticity β. As a test of the reference cloud model I inferred cloud droplet number concentration from aircraft estimates of τ and r_{eff} and compared it to the in situ values. The inferred cloud droplet number concentrations, fall within the range of the cloud droplet number concentration measured in situ. I also used the aircraft estimate of β to infer N from satellite measurements of N_{sat} .

Comparing satellite and aircraft in situ measurements I found, as others have, (Nakajima and Nakajima (1995), Platnick and Valero (1995)) that the AVHRR retrievals overestimated the cloud droplet effective radius in comparison with the in situ measurements by 1 to 3.6 μm for single layer clouds. This in turn, leads to an underestimation of cloud droplet number concentration from satellite in comparison to in situ values. For a given scene this offset appears to be independent of the cloud optical depth.

Spatial variability of cloud optical depth and cloud droplet effective radius, and cloud visible wavelength reflectivity is the focus of chapters 6 and 7. I compared spatial behaviour of uni-modal, bi-modal and thick clouds and found that bi-modal scenes and thick clouds with a wide range of N_{sat} show different long range behaviour in r_{eff} than in cloud radiance or τ as evidence by the second order structure function. The behaviour of the structure function within the scaling range is similar for all parameters. In addition, all types of clouds exhibit similar values of the nonstationarity ($H(1)$ and intermittency ($C(1)$) parameters.

In 34 scenes in four data sets I observed breaks in scaling at 3 to 20 km in fields of cloud visible radiance and τ and up to 40 km in r_{eff}. I found nonstationarity

and intermittency parameters of cloud visible radiance, τ and r_{eff} for these scenes, computed ensemble averages for each field and each data set and marked their location in the bifractal plane. The nonstationarity parameter is contained between 0.43-0.59 for ensemble averages of all fields and all data sets. The scatter in $H(1)$ is greatest for the cloud radiance field due mainly to the addition of the optically thick and highly variable SOCEX data set, which contains the largest value of the nonstationarity parameter. Even excluding this data point, the scatter of $H(1)$ values is still significantly larger than that observed by Marshak *et al.* (1997) and Davis *et al.* (1996a) between three data sets of cloud liquid water content from FIRE and ASTEX and SOCEX.

All fields have very similar values of the nonstationarity and intermittency parameters in fully cloudy conditions. The intermittency parameter is typically less than 0.07 for all fields in fully cloudy scenes but rises dramatically for τ and r_{eff} if the cloud in the scene is broken.

I found structure functions for cloud visible radiance and cloud optical depth to scale predominantly as monofractals or at most weak multifractals. In contrast, multiscaling is frequent in fields of cloud droplet effective radius and is almost always associated with broken cloudiness but can also occur in the presence of a sharp transition between two cloud masses of distinctly different r_{eff}. This different type of scaling in cloud droplet effective radius field is a signature of much weaker small scale variability of this field as compared to fields of cloud optical depth or cloud radiance. Singular measures obey multiscaling for all fields in all scenes.

Thus, after exploring selected aspects of mesoscale variability of cloud optical depth and cloud droplet effective radius and cloud visible radiance, I found the variables to be strictly correlated and exhibit similar patterns of variability in scenes representative of the "reference model" (homogeneous with respect to N_{sat}). Inhomogeneity in N_{sat} can lead to quantitatively (extent of scaling range) and qualitatively (type of scaling) different spatial behaviour of cloud optical depth and cloud

droplet effective radius . However, the nonstationarity and intermittency parameters remain within the same range for all types of scenes, those which follow the simple model and those which mark departures from the reference behaviour.

8.2 Discussion

The cloud regimes I analysed in this thesis represent summer time marine stratocumulus at two geographical locations: the eastern Pacific Ocean of California, and the Southern Ocean near Tasmania, where this type of cloudiness frequently occurs. I examined cloud sectors (scenes) 256 km $\times$ 256 km in size which, with few exceptions, were fully cloudy or nearly fully cloudy (cloud fraction > 0.90). The range of observed mean cloud optical depth was approximately 8 to 32 and the observed mean cloud droplet effective radius ranged between 6 and 17 μm. In some cases (FIRE, SOCEX), aircraft measurements were made in clouds within hours of satellite overpass and both precipitating and non-precipitating clouds were encountered.

Collectively, this data set includes complicated clouds with a range of thicknesses. Both non-precipitating clouds and precipitating clouds in which microphysical processes postulated to produce important macrophysical feedbacks are represented.

8.2.1 The success of the simple "reference" cloud model

The reference cloud model (3.2) was derived with the assumptions of constant cloud droplet number concentration and constant cloud subadiabaticity β. Considering the restrictive nature of these assumptions a surprisingly large percentage (55%) of the uni-modal clouds fit relationship (3.2). This result may indicate that N_{sat} is frequently nearly homogeneous on scales 256 km $\times$ 256 km.

On the other hand, sharp transitions in N_{sat} between spatially coherent regions can be encountered in cloud scenes of this size off the California coast. Such scenes exhibit bi-modal distributions of τ and r_{eff}. Typically, to observe a bi-modal

structure in τ and r_{eff} scatter plots the difference in N_{sat} between the two modes has to be greater than 30% of the mean N_{sat} . The technique of retrieving N_{sat} has the potential to be useful in remotely detecting aerosol fronts in cloud-topped boundary layer. In this study I found sharp transitions in N_{sat} as much as 500 km off the coast. A larger, more diverse data set would permit a construction of a climatology of those aerosol fronts, as well as an investigation of how they eventually homogenise.

In the framework of the reference model the maximum attainable τ and r_{eff} at a given N_{sat} are constrained by available cloud liquid water path . This constraint is reflected in the characteristic shape of the clusters in scatter plots of τ and r_{eff} for clouds scenes with variable N_{sat} (see Figure 3.6).

Similar spatial properties of τ and r_{eff} fields for uni-modal clouds confirm the close coupling between these two cloud parameters as postulated by the reference model. Departure from the reference behaviour (bi-modality) can sometimes be detected in the difference between the spatial behaviour of τ and r_{eff}, manifested for example by different scaling ranges or different multifractal character of these two fields. The reference cloud model is also supported by in situ measurements and was found to retrieve values of N_{sat} and cloud droplet number concentration (N) (based on aircraft measurements of τ and r_{eff}) consistent with those measured directly by aircraft probes.

8.2.2 Overestimation of cloud droplet effective radius by remote sensing

I compared satellite and aircraft measurements of cloud droplet effective radius for six SOCEX flights. For these cases I found that satellite retrievals overestimated r_{eff} by approximately 0.7 to 3.6 μm for single layer clouds, which is consistent will earlier observations as discussed in section 5.1. The aircraft data in SOCEX were collected during 2 to 4 hour long flights which in their early phase coincided with

the satellite overpass . These long aircraft sampling times could affect the accuracy of the comparisons with satellite measurements.

The satellite overestimation of r_{eff} appears to be independent of τ (see Figure 5.7) for $\tau > 1$ and thus can be described as an constant offset. This is good news for the analysis of the spatial distribution of r_{eff} and lwp, meaning that the spatial structure of these fields will not be affected by this error in the retrievals but simply shifted, by a constant value, to higher effective radii and lower lwp.

From the point of view of N_{sat} retrievals, the overestimation of r_{eff} will result in underestimation of N_{sat} . The worst case r_{eff} overestimation observed in this study is an offset of 3.6 μm which resulted in approximately 32% underestimation of N_{sat} . So far there is no satisfactory explanation for this remote sensing offset overestimation of r_{eff} (recall the discussion in section 5.1). Possibly, more insight into this problem will be gained with the introduction of new satellites (NOAA K/L/M, MODIS, Landsat 7) which make available spectral bands sensitive to cloud radiation in the weakly absorbing 2 μm wavelength region, which is less affected by emission than the 3.7 μm AVHRR channel.

8.2.3 Spatial structure of cloud fields

With the 1.1 km AVHRR resolution I was able to access only the upper region of a (presumed) scaling range that extends to mm scales in turbulent cloud fields. I was, however, able to see the marked transition between nonstationary scaling regime and stationary nonscaling regime (scale break) in all scenes I analysed. I encountered scale breaks at 3 to 20 km in fields of cloud visible radiance and τ and up to 40 km in r_{eff}. These scaling ranges are consistent with the observations of Davis *et al.* (1996) who saw a scaling range of approximately 20 km for cloud liquid water content (lwc) in FIRE clouds and Davis *et al.* (1996a) who reported a scaling range of 10 km for FIRE visible cloud radiance measured by Landsat and 5 km for lwc in SOCEX. Davis *et al.* (1996) and Marshak *et al.* (1997) also reported scaling

range of 60 km for lwc fluctuations in ASTEX. Barker and Davies (1992) observed a scale break at around 5 km in AVHRR measurements of cloud visible and thermal radiances for fields of shallow cumuli. They suggested that the extent of the scaling regime might be related to the size of cloud elements (i.e. cells) and mark different scaling within and between cloud cells.

The measurements seem to disagree with the observations of Lovejoy *et al.* (1993) who analysed 15 AVHRR images of cloud fields (512 $km \times 512$ km) over the Atlantic Ocean east of Florida and reported scaling in all five AVHRR channels with no breaks over the entire available range (2 to 512 km). However, whereas my observations, and those of Davis *et al.* (1996), Davis *et al.* (1996a) and Marshak *et al.* (1997) refer to a "fairly uniform" marine stratocumulus those of Lovejoy *et al.* (1993) deal with a different cloud regime. The clouds in Lovejoy *et al.* (1993) appear much more inhomogeneous. Selecting a "meteorologically homogeneous" subregion from one of their scenes, Lovejoy *et al.* (1993) obtained a power spectrum radically different from the power spectrum for the entire scene.

I examined scenes with mean τ approximately between 8 and 32 and mean r_{eff} between 6 and 17 μm but found no stratification in the multifractal parameters $[H(1), C(1)]$ with respect to τ or r_{eff}. This result could be used as an argument of the universality of cloud processes governing the marine stratocumulus postulated in Marshak *et al.* (1997) for example, and discussed here in chapter 1. A better understanding of errors associated with estimates for these parameters combined with more measurements is clearly needed before any conclusion can be made regarding characteristic values of the stationarity and intermittency in cloud fields.

8.3 Future Considerations and new research

8.3.1 Spatial structure of marine stratocumulus

1. Accessing smaller spatial scales

In the analysis of AVHRR data fields the accessible scaling range is limited by the resolution of the instrument ($\sim 1\ km$). If the scaling range is indeed a fundamental property of boundary layer clouds fields, the estimates of $[H(1), C(1)]$ should not change with instrumental platforms or as the observation range is extended to smaller scales. In some scenes the scaling range ends at 3 or 4 km which leaves us with large uncertainties of the estimated nonstationarity parameter. It would be desirable to extend the available scaling range by using an instrument with a better resolution.

An immediate candidate is the Landsat Thematic Mapper (TM) with resolution of 28 m. However, due to radiative smoothing (Marshak *et al.* (1995a), Davis *et al.* (1997a)) probably only scales greater than about 200 m could be used in the multifractal analysis. The usefulness of the current TM is limited to measuring thin clouds due to the saturation of the visible spectral bands at higher radiances. This limitation will be alleviated with the launch of Landsat 7 equipped with the Extended TM (ETM+) where a low gain option can be set to prevent the saturation in channel 1.

The launch of the Moderate Resolution Imaging Spectroradiometer (MODIS) will put into an orbit an instrument with the resolution of 500 m. This will not results in a great extension of the scaling range compared to AVHRR but will double the number of measurement points in the available scaling range thus provide estimates of $H(1)$ with greater accuracy.

One great advantage of satellite data over aircraft measurements is their two dimensionality. I did not explore the two dimensional aspect of satellite data in this work for three reasons: 1) to assure comparability with earlier studies which consid-

ered transects of satellite fields (Barker and Davies (1992)), 2) stay within the one dimensional formalism of the multifractal analysis (Davis *et al.* (1994), 3) distortions in the AVHRR images which undermine their suitability for two dimensional analysis. Ultimately, the two dimensionality of satellite data is a valuable asset and should be explored. The distortion of images is less of a problem for Landsat data (because of smaller viewing angles) so Landsat 7 data sets should be suited to two dimensional multifractal analysis.

2. Internal structure of layer clouds : is it a universal property or not?
Marshak *et al.* (1997) note the close proximity of FIRE and ASTEX ensemble averages of the cloud liquid water content multifractal parameters and interpret this as a consequence of the common nature of the nonlinear physical processes that determine the internal structure of marine stratocumulus. In my observations, the ensemble averages of multifractal parameters of cloud visible radiance, cloud optical depth and cloud droplet effective radius for four data sets fall further apart. The high values of the intermittency parameter can be attributed to broken cloudiness. The scatter of the nonstationarity parameter is more difficult to explain.

Clearly, more data is needed to substantiate (or disprove) the proposed universality and explain the observed scatter in $H(1)$. To avoid ambiguities and additional complications introduced by broken cloudiness I would suggest to first restrict the analysis to fully cloudy scenes only.

3. Monte Carlo simulation of cloud reflectivity in channels 1 and 3
A Monte Carlo radiative transfer model can be built based on the spatial distribution of cloud optical depth and cloud droplet effective radius discussed in chapters 4 and 7 and the model relationship (3.2). Such model could be an important tool to study the effects of spatial variability of τ, r_{eff} and N_{sat} on cloud radiances at visible (channel 1) and near-infrared (channel 3) wavelengths, and to confirm the approximations in the Nakajima and Nakajima (1995) plane parallel code.

8.3.2 GCM scale cloud reflectivity and cloud droplet effective radius

It is well known (Barker (1996), Cahalan *et al.* (1993)) that in real inhomogeneous cloud a mean optical depth $\bar{\tau}$ produces a very different albedo than its plane parallel homogeneous (PPH) counterpart. The negative albedo bias (inhomogeneous minus PPH) is between 5 to 30% depending on the degree of cloud inhomogeneity.

To account for the sub-grid scale variability of cloud optical depth in GCM pixels Cahalan *et al.* (1993) proposed to use the *effective optical theckiness* (τ_{eff}) in PPH computations where $\tau_{eff} = \chi\bar{\tau}$ and χ is a reduction factor inferred from the standard deviation of cloud optical depth . Barker (1996) proposed the *gamma independent pixel approximation* (Γ IPA) where GCM albedos are computed as follows

$$r(\mu_0) = \int_0^\infty p(\tau) r_{pp}(\tau, \mu_0) d\tau \tag{8.1}$$

where $a(\mu_0)$ is the ΓIPA albedo, $a_{pp}(\tau, \mu_0)$ is the PPH albedo and $p(\tau)$ is the frequency distribution of τ in the GCM pixel approximated by the normalised gamma distribution given by (4.6). Both the above methods account for the sub-grid scale variability of cloud optical depth but neglect any sub-grid scale variability in cloud droplet effective radius, despite a potentially significant effect of r_{eff} on cloud albedo reflectivity.

Cloud properties in most GCMs, practically all of which use plane parallel homogeneous cloud models, are tuned so that the model monthly mean top of the atmosphere (TOA) broadband albedo matches the values inferred from satellite observations (Barker (1996)). Accounting for subgrid scale variability in cloud optical depth , by introducing to GCM either the *effective optical depth* approximation of Cahalan *et al.* (1993) or the Γ IPA of Barker (1996) or any other scheme would result in reduced droplet absorptance and TOA albedo at the expense of increased transmittance. The recovery of the match between the model and satellite albedos

will require an adjustment of the model mean cloud parameters (cloud liquid water path , cloud droplet effective radius). Barker (1996) showed that introducing Γ IPA to GCM to account for the subgrid scale variability will require raising the cloud liquid water path by 20-1000% to equalise the TOA albedos, depending on the parameter ν of the gamma distribution (which can be regarded as a measure of the extent of cloud inhomogeneity, see equation 4.6). The equivalent adjustment in cloud droplet effective radius while keeping cloud liquid water path constant would require 7-80% decrease in r_{eff}. Success of the reference cloud model offers a third alternative: use the cloud optical depth distribution in combination with a cloud droplet effective radius distribution given by (3.2). More work is clearly needed on the impact of the inhomogeneities in both r_{eff} and τ on cloud albedo.

8.3.3 Cloud subadiabaticity

The parametrisation of the relationship between cloud optical depth and cloud droplet effective radius given in equation 3.2 depends on cloud subadiabaticity β. We cannot infer cloud subadiabaticity from satellite measurements and have to rely on climatologies to resolve the N_{sat} and β ambiguity.

There have not been many measurements of cloud subadiabaticity . Those known to me are discussed in section 4.3 and in more detail in Appendix E. From the point of view of the parametrisation in (3.2) it would be interesting to extend my investigation of a possible dependence between β and cloud droplet number concentration as presented in Appendix E to other clouds. Couplings between β and other cloud and climatological parameters are also possible. In particular, the depth of the boundary layer comes to mind as Boers *et al.* (1991) argue that $\beta < 0.5$ (or inversely $\beta_B > 0.5$, see Appendix E) corresponds to strong decoupling between the surface and the upper part of the boundary layer, which in turn is typical for deepening boundary layers. It would be worthwhile to investigate the dependence of the depth of the boundary layer on cloud subadiabaticity .

A climatology of β could prove very useful for estimation of cloud droplet number concentration from satellite measurements and in climate modelling. Efforts are already underway to measure cloud subadiabaticity in fair weather cumulus (Bruce Albrecht 1997, private communication). I would advocate that these measurements be extended to layer clouds, both marine and continental.

Bibliography

Abdella, K. and McFarlane, N. (1997). Modelling boundary layer clouds with a statistical cloud scheme and a second order turbulence closure. *J. Atmos. Sci.*, page Submitted.

Ackerman, A., Toon, O., and Hobbs, P. (1993). Dissipation of marine stratiform clouds and collapse of the marine boundary layer due to the depletion of cloud condensation nuclei by clouds. *Science*, **262**, 226–229.

Albrecht, B. (1989). Aerosols, cloud microphysics and fractional cloudiness. *Science*, **245**, 1227–1230.

Albrecht, B., Randall, D., and Nicholls, S. (1988). Observatons of marine stratocumulus clouds durinf fire. *Bull. Amer. Meteor. Soc.*, **69**, 618–626.

Arking, A. (1991). The radiative effects of clouds and their impact on climate. *Bull. Amer. Meteor. Soc.*, **72**, 795–813.

Arking, A. and Childs, J. (1985). Retrieval of cloud cover parameters from multispectral satellite images. *J. Climate Appl. Meteor.*, **24**, 322–333.

Austin, P., Wang, Y., Pincus, R., and Kujala, V. (1995). Precipitation in stratocumulus clouds: observational and modelling results. *J. Atmos. Sci.*, **52**, 2329–2352.

Baker, B. (1992). Tyrbulent entrainment and mixing in clouds: A new observational approach. *J. Atmos. Sci.*, **49**, 387–404.

Baker, M. (1993). Variability in concentration of cloud condensation nuclei in the marine cloud-topped boundary layer. *Tellus*, **45B**, 458–472.

Barker, H. (1992). Solar radiative transfer for clouds posessing isotropic variable extinction coefficient. *Quart. J. Roy. Meteor. Soc.*, **118**, 1145–1162.

Barker, H. (1996). A parametrization for computing grid-averaged solar fluxes for inhomogenous marine boundary layer clouds. part i: Methodology and homogenous biases. *J. Atmos. Sci.*, **53**, 2289–2302.

Barker, H. and Davies, J. (1992). Cumulus cloud radiative properties and the characteristics of satellite radiance wavenumber spectra. *Remote Sens. Environ.*, **42**, 51–64.

Barker, H., Wielicki, B., and Parker, L. (1996). A parametrization for computing grid-averaged solar fluxes for inhomogenous marine boundary layer clouds. part ii: Validation using satellite data. *J. Atmos. Sci.*, **53**, 2304–2316.

Barnsley, M. F., Devaney, R. L., Mandelbrot, B. B., Peitgen, H.-O., Saupe, D., and Voss, R. F. (1989). *The science of fractal images*. Springer-Verlag.

Beck, C. and Schlögl, F. (1993). *Thermodynamics of chaotic systems*. Cambridge University Press.

Betts, A. (1982). Cloud thermodynamic models in saturation point coordinates. *J. Atmos. Sci.*, **39**, 2182–2191.

Betts, A. and Albrecht, B. (1982). Conserved variable analysis of the convective boundary layer thermodynamic structure over tropical oceans. *J. Atmos. Sci.*, **44**, 83–99.

Betts, A. and Boers, R. (1990). Cloudiness transition in marine stratocumulus. *J. Atmos. Sci.*, **48**, 1480–1497.

Bevington, P. and Robinson, D. (1992). Data reduction and error analysis for the physical scienes. *McGraw-Hill*.

Boers, R. and Betts, A. (1988). Saturation point structure of of marine stratocumulus clouds. *J. Atmos. Sci.*, **45**, 1156–1175.

Boers, R. and Mitchell, R. (1994). Absorption feedback in stratocumulus clouds. influence on cloud top albedo. *Tellus*, **46A**, 229–241.

Boers, R., Melfi, S., and Palm, S. (1991). Cold air outbreak during gale: Lidar observations and modeling of boundary layer dynamics. *Mon. Wea. Rev.*, **119**, 1132–1150.

Boers, R., Jensen, J., Krummel, P., and Gerber, H. (1996). Microphysical and shortwave radiative straycture of wintertime stratocumulus over the southern ocean. *Quart. J. Roy. Meteor. Soc.*, **122**, 1307–1341.

Boers, R., Jensen, J., and Krummel, P. (1997). A line of convection embedded in a stratocumulus-topped boundary layer. *Quart. J. Roy. Meteor. Soc.*, **123**, 207–221.

Bougeault, P. (1981). Modelling the trade-wind cumulus boundary layer. part ii: Higher order one-dimensional model. *J. Atmos. Sci.*, **38**, 2429–2439.

Cahalan, R. and Joseph, J. (1989). Fractal statistics of cloud fields. *Mon. Weather Rev.*, **117**, 261–272.

Cahalan, R. and Snider, J. (1989). Marine stratocumulus structure. *Remote Sens. Environ.*, **28**, 95–107.

Cahalan, R., Short, D., and North, G. (1982). Cloud fluctuation statistics. *Mon. Weather Rev.*, **110**, 26–43.

Cahalan, R., Ridgway, W., Wiscombe, W., Bell, T., and Snider, J. (1993). The albedo of fractal stratocumulus clouds. *J. Atmos. Sci.*, **51**, 2434–2455.

Cahalan, R., Ridgway, W., Wiscombe, W., Golmmer, S., and Harshvardhan (1994). Independent pixel and monte carlo estimates of stratocumulus albedo. *J. Atmos. Sci.*, **51**, 3776–3790.

Chambers, L., Wielicki, B., and Evans, K. (1997a). Accuracy of the independent pixel approximation for satellite estimates of oceanic boundary layer cloud optical depth. *J. Geophys. Res.*, **102**, 1779–1794.

Chambers, L., Wielicki, B., and Evans, K. (1997b). Independent pixel and two-dimensional estimates of landsat derived cloud field albedo. *J. Atmos. Sci.*, **54**, 1525–1532.

Charlson, R., Lovelock, J., Andreae, M., and Warren, S. (1987). Oceanic phytoplankton, atmospheric sulphur, cloud albedo and climate. *Nature*, **326**, 655–661.

Coakley, J. and Bretherton, F. (1982). Cloud cover from high-resolution scanner data: detecting and allowing for partially filled fields of view. *J. Geophys. Res.*, **87**, 4917–4932.

Coakley, J., Bernstein, R., and Durkee, P. (1987). Effect of ship-stack effluents on cloud reflectivity. *Science*, **237**, 1020–1022.

Curran, P. (1988). The semivariogram in remote sensing: An introduction. *Remote Sensing of Environment*, **24**, 493–507.

Curry, J. and Herman, G. (1985). Infrared radiative properties of summertime arctic stratus clouds. *J. Appl. Meteor*, **24**, 525–538.

Davies, R. (1994). Spatial autocorrelation of radiation measured by the earth radiation budget experiment: Scene inhomogeneity and reciprocity violation. *J. Geophys. Res.*, **99**, 20879–20887.

Davis, A., Gabriel, P., Lovejoy, S., Schertzer, D., and Austin, G. (1990). Discrete angle radiative transfer - part iii: Numerical results and applications. *J. Geophys. Res.*, **95**, 11729–11742.

Davis, A., Marshak, A., Wiscombe, W., and Cahalan, R. (1994). Multifractal characterization of nonstationarity and intermittency in geophysical fields: Observed, retrieved, or simulated. *J. Geophys. Res.*, **99**, 8055–8072.

Davis, A., Marshak, A., Wiscombe, W., and Cahalan, R. (1996). Scale invariance of liquid water distribution in marine stratocumulus. part i: Spectral properties and stationarity issues. *J. Atmos. Sci.*, **53**, 1538–1558.

Davis, A., Marshak, A., Wiscombe, W., and Cahalan, R. (1996a). Multifractal characterizations of intermittency in nonstationary geophysical signals and fields. a model-based perspective on ergodicity issues illustrated with cloud data. In *Current topics in nonstationary analysis*, pages 97–158. World-Scientific.

Davis, A., Marshak, A., Cahalan, R., and Wiscombe, W. (1997a). The landsat scale break in stratocumulus as a three-dimensional transfer effect: Implications for cloud remote sensing. *J. Atmos. Sci.*, **54**, 241–260.

Davis, A., Marshak, A., Gerber, H., and Wiscombe, W. (1997b). Horizontal structure of marine boundary layer clouds at 4 cm resolution: scale break at 2-5 m, non-poissonian behavior at small scales, multifractal behavior at large scales. *J. Geophys. Res.*, page submitted.

Evans, K. (1993). Two dimensional radiative transfer in cloudy atmospheres: The spherical harmomic, spatial grid method. *J. Atmos. Sci.*, **50**, 3111–3124.

Feingold, G., Boers, R., Stevens, B., and Cotton, W. (1997). A modelling study of the effect of drizzel on cloud optical depth and susceptibility. *J. Geophys. Res.*, **102**, 13527–13534.

Flandrin, P. (1989). On the spectrum of fractional brownian motion. *IEEE Trans on Information Theory*, **35**, 197–199.

Gabriel, P., Lovejoy, S., Schertzer, D., and Austin, G. (1988). Mutifractal analysis of resolution dependence in satellite imagery. *Geophys. Res. Lett.*, **15**, 1373–1376.

Gerber, H. (1991). Direct measurement of suspended particulate volume concentration and far infrared extinction coefficient with a laser-diffraction instrument. *Appl. Opt.*, **30**, 4824–4831.

Goodchild, M. (1986). Spatial autocorelation. *Concepts and Techniques in Modern Geography*.

Grassberger, P. (1983). Generalized dimensions of strange attractors. *Phys. Rev. Lett. A*, **97**, 227–330.

Gupta, V. and Waymire, E. (1990). Multiscaling properties of spatial rainfall and river flow distribution. *J. Geophys. Res.*, **95**, 1999–2009.

Gupta, V. and Waymire, E. (1993). A statistical analysis of mesoscale rainfall as a random cascade. *J. Appl. Meteor.*, **32**, 251–267.

Han, Q., Rossow, W., and Lacis, A. (1994). Near-global survey of effective droplet radii in liquid water clouds using isccp data. *J. Climate*, **7**, 465–497.

Hartmann, D., Ockert-Bell, M., and Michelsen, M. (1992). The effect of cloud type on earth's energy balance: Global analysis. *Journal of Climate*, **5**, 1281–1304.

Hentschel, H. and Procaccia, I. (1983). The infinite number of generalized dimensions of fractals and strange attractors. *Physica D*, **8**, 435–444.

Isaaks, E. and Srivastava, R. (1989). An introduction to applied geostatistics. *Oxford University Press*.

Jansson, M. (1985). A comparison of detransformed logarithmic regressions and power function regressions. *Geogr. Ann.*, **67 A**, 61–70.

Jones, A., Roberts, D., and Slingo, A. (1994). A climate model study of indirect radiative forcing by anthropogenic sulphate aerosols. *Nature*, **370**, 450–453.

Kim, Y. and Cess, R. (1993). The effect of anthropogenic sulfate aerosols om low level cloud albedo over oceans. *J. Geophys. Res.*, **98**, 14883–14885.

King, W., Maher, C., and Hepburn, G. (1981). Further performance tests on the csiro liquid water probe. *J. Appl. Meteor.*, **20**, 195–202.

Klein, S. and Hartmann, D. (1993). The seasonal cycle of low stratiform clouds. *J. Climate*, **6**, 1587–1606.

Kneizys, F., Shettle, E., Abreu, L., Jr., J. C., Anderson, S., Gallery, W., Selby, J., and Clough, S. (1988). Users guide to lowtran-7. *AFGL-TR-88-0177.*

Knollenberg, R. (1981). Techiniques for probing cloud microstructure. In *Clouds: Their Formation, Optical Properties, and Effects*, pages 15–91. P.V. Hobbs and Deepak, Eds., Academic Press.

Lavallée, D., Lovejoy, S., Schertzer, D., and Ladoy, P. (1993). Nonlinear variability, multifractal analysis and simulation of landscape topography. *Fractals in Geography, edited by L. De Cola and N. Lam, Kluwer*, pages 158–192.

Lin, X. and Coakley, J. (1993). Generalized multispectral retrieval method for semitransparent clouds. *J. Geophys. Res.*, **98**, 18501–18514.

Liou, K. (1976). On the absorption, reflection and transmision of solar radiation in cloudy atmospheres. *J. Atmos. Sci.*, **33**, 798–805.

Lovejoy, S., Schertzer, D., Silas, P., Tessier, Y., and Lavallée, D. (1993). The unified scaling model of atmospheric dynamics and systematic analysis of scale invariance in cloud radiances. *Ann. Geophysicae*, **11**, 119–127.

Mandelbrot, B. (1977). Fractals: Form, chance and dimension. *W.H. Freeman*, page 365pp.

Mandelbrot, B. and Ness, J. V. (1968). Fractional brownian motion, fractional noises and applications. *SIAM Rev.*, **10**, 422–437.

Marshak, A., Davis, A., Cahalan, R., and Wiscombe, W. (1994). Bounded cascade models as nonstationary multifractals. *Phys. Rev. E*, **49**, 55–69.

Marshak, A., Davis, A., Wiscombe, W., and Cahalan, R. (1995a). Radiative smoothing in fractal clouds. *J. Geophys. Res.*, **100**, 26247–26261.

Marshak, A., Davis, A., Wiscombe, W., and Titov, G. (1995b). Verisimilitude of the independent pixel approximation used in cloud remote sensing. *Remote Sens. Environ.*, **52**, 71–78.

Marshak, A., Davis, A., Wiscombe, W., and Cahalan, R. (1997). Scale invariance of liquid water distribution in marine stratocumulus. part ii: Multifractal properties and intermittency issues. *J. Atmos. Sci.*, **54**, 1423–1444.

Martin, G., Johnson, W., and Spice, A. (1994). The measurement and parametrization of effective radius of droplets in warm stratocumulus clouds. *J. Atmos. Sci.*, **51**, 1823–1842.

McGwire, K., Friedl, M., and Estes, J. (1993). Spatial structure, sampling design and scale in remotely-sensed imagery of a california savanna woodland. *Int. J. Remote Sensing*, **14**, 2137–2164.

Meador, W. and Weaver, W. (1980). Two-stream approximation to radiative transfer in planetary atmospheres: A unified description of existing methods and a new improvement. *J. Atmos. Sci.*, **37**, 630–643.

Meneveau, C. and Sreenivasan, K. (1987). Simple multifractal model for fully developed turbulence. *Phys. Rev. Lett.*, **59**, 1424–1427.

Meneveau, C. and Sreenivasan, K. (1987a). Physics of chaos and systems far from equilibrium. In *Chaos'87: Proceedings of the International Conference on the Physics of chaos and systems far from Equilibrium*, Monterey, CA. North Holland, Amsterdam.

Miller, D. (1984). Reducing transformation bias in curve fitting. *The American Statistician*, **38**, 124–126.

Monin, A. and Yaglom, A. (1965). *Statistical fluid mechanics: Mechanics of turbulence*. The MIT Press.

Nakajima, T. and King, M. (1990). Determination of the optical thickness and effective particle radius of clouds from reflected radiation measurements. part i: theory. *J. Atmos. Sci.*, **47**, 1878–1892.

Nakajima, T. and King, M. (1992). Asymptotic theory for optically thick layerd: Application to the discrete ordinates method. *Appl. Opt.*, **31**, 7669–7683.

Nakajima, T. and Nakajima, T. (1995). Wide-area determination of cloud microphysical properties from NOAA AVHRR measurements for FIRE and ASTEX regions. *J. Atmos. Sci.*, **52**, 4043–4059.

Nakajima, T. and Tanaka, M. (1988). Algorithms for radiative intensity calculations in moderately thick atmospheres using truncation approximation. *J. Quant Spectrosc. Radiat. Transfer*, **40**, 51–69.

Nakajima, T., King, M., Spinhirne, J., and Radke, L. (1991). Determination of the optical thickness and effective particle radius of clouds from reflected radiation measurements. part ii: Marine stratocumulus observations. *J. Atmos. Sci.*, **48**, 728–750.

Nicholls, S. (1984). The dynamics of stratocumulus: aircraft observations and comparison with a mixed layer model. *Quart. J. Roy. Meteor. Soc.*, **110**, 783–820.

Nicholls, S. and Leighton, J. (1986). An observational study of the structure of stratiform cloud sheets. part i. structure. *Quart. J. Roy. Meteor. Soc.*, **112**, 431–460.

Paluch, I. and Lenschow, D. (1991). Stratiform cloud formation in the marine boundary layer. *J. Atmos. Sci.*, **48**, 2141–2158.

Papoulis, A. (1965). Probability, random variables and stochastic processes. *McGraw-Hill*, page 583pp.

Parisi, G. and Frisch, U. (1985). A multifractal model of intermittency. In *Turbulence and Predictability in Geophysical Fluid Dynamics*, pages 84–88. ed. M. Ghil, R.Benzi, and G. Parisi, North Holland.

Pincus, R. and Baker, M. (1994). Precipitation, solar absorption, and albedo susceptibility in marine boundary layer clouds. *Nature*, **372**, 250–252.

Pincus, R., Szczodrak, M., Austin, P., and Gu, J. (1995). Precision and accuracy in satellite optical depth estimates. *J. Climate*, **8**, 1453–1462.

Pincus, R., Baker, M., and C.S., B. (1997). What controls marine boundary layer cloud radiative properties? lagrangian observation of cloud evolution. *J. Atmos. Sci.*, **submitted**.

Platnick, S. and Twomey, S. (1994). Determining the susceptibility of cloud albedo to changes in droplet concentration wit the advanced very high resolution radiometer. *J. Appl. Meteor.*, **33**, 334–347.

Platnick, S. and Valero, F. (1995). A validation of s satellite cloud retrieval during astex. *J. Atmos. Sci.*, **52**, 2985–3001.

Platnick, S., Durkee, P., Nielsen, K., Taylor, J., Tsay, S.-C., King, M., Ferek, R., and Hobbs, P. (1997). The role of background cloud microphysics in ship track formation. *J. Atmos. Sci.*, page submitted.

Platt, C. (1989). The role of cloud microphysics in high cloud feedback effects on climate change. *Nature*, **341**, 428–429.

Press, W., Teukolsky, S., Vetterling, W., and Flannery, B. (1992). Numerical recipes in fortran. *Cambridge University Press*.

Radke, L., Coakley, J., and King, M. (1989). Direct and remote sensing observations of the effects of ships clouds. *Science*, **246**, 1146–1149.

Rawlins, F. and Foot, J. (1990). Remotely sensed measurements of stratocumulus properties during fire using the c130 aircraft multichannel radiometer. *J. Atmos. Sci.*, **47**, 2488–2503.

Rossow, W. (1989). Measuring cloud properties from space: A review. *J. Climate*, **2**, 201–213.

Rossow, W. and Lacis, A. (1990). Global, seasonal cloud variations from satellite radiance measurements. part ii: Cloud properties and radiative effects. *J. Climate*, **3**, 1204–1253.

Rossow, W., Garder, L., and Lacis, A. (1989). Global, seasonal cloud variations from satellite radiance measurements. part i: Sensitivity of analysis. *J. Climate*, **2**, 419–458.

Schmitt, F., Lavallée, D., Schertzer, D., and Lovejoy, S. (1992). Empirical determination of universal multifractal exponents in turbulent velocity fields. *Phys. Rev. Lett.*, **68**, 305–308.

Serio, C. and Tramutoli, V. (1995). Scaling laws in a turbulent baroclinic instability. *Fractals*, **2**, 297–314.

Slingo, A. (1989). A gcm parametrization for the shortwave radiative properties of water clouds. *J. Atmos. Sci.*, **46**, 1419–1427.

Slingo, A. (1990). Sensitivity of the earth radiation budget to changes in low clouds. *Nature*, **343**, 49–51.

Sommeria, G. and Deardorff, J. (1977). Subgrid-scale condensation in models of nonprecipitating cloouds. *J. Atmos. Sci.*, **34**, 344–355.

Stamnes, K., Tsay, S.-C., Wiscombe, W., and Jayaweera, K. (1988). Numerically stable algorthim for discrete-ordinate-method radiative transfer in multiple scattering and emmiting layered media. *App. Opt.*, **27**, 2501–2509.

Stephens, G. (1978). Radiation profiles in extended water clouds. ii parametrization schemes. *J. Atmos. Sci.*, **35**, 2123–2132.

Stephens, G. (1988). Radiative transfer through arbitrary shaped optical media. part i: A general method of solution. *J. Atmos. Sci.*, **45**, 1818–1836.

Stephens, G. and Tsay, S.-C. (1990). On the cloud absorption anomaly. *Quart. J. Roy. Meteor. Soc.*, **116**, 671–704.

Stephens, G., Paltridge, G., and Platt, C. (1978). Radiation profiles in extended water clouds. iii observations. *J. Atmos. Sci.*, **35**, 2133–2141.

Stevens, B., Feingold, G., Walko, R., and Cotton, W. (1996). On elements of the microphysical structure of numerically simulated non-precipitating stratocumulus. *J. Atmos. Sci.*, **53**, 980–1006.

Swan, A. and Sandilands, M. (1995). Introduction to geological data analysis. *Blackwell Science*.

Tessier, Y., Lovejoy, S., and Schertzer, D. (1993). Universal multifractals: Theory and observations for rain and clouds. *J. Appl. Meteor.*, **32**, 223–250.

Twomey, S. (1977). The influence of pollution on the shortwave albedo of clouds. *J. Atmos. Sci.*, **34**, 1149–1152.

Twomey, S. and Cocks, T. (1989). Remote sensing of cloud parameters from spectral reflectance in the near-infrared. *Beitr. Phys. Atmos.*, **62**, 172–179.

Twomey, S., Piepgrass, M., and Wolfe, T. (1984). An assesment of the impact of pollution on global cloud albedo. *Tellus*, **36B**, 356–366.

Tzivion, S., Feingold, G., and Levin, Z. (1987). An efficient numerical solution to the stochastic collection equation. *J. Atmos. Sci.*, **44**, 3139–3149.

Warren, S., Hahn, C., London, J., Chervin, R., and Jenne, R. (1988). Global distribution of total cloud cover and cloud type over the ocean. *NCAR Tech. Notes*, **TN-317+STR**, 42pp.

Waymire, E. and Gupta, V. (1981). The mathemalical structure of rainfall representations. i. a review of stochastic rainfall models. *Water Resour. Res.*, **17**, 1261–1272.

Weinberger, H. (1965). *First course in partial differential equations*. Dover Publications, Inc.

Welch, R. and Wielicki, B. (1984). Stratocumulus cloud field reflected fluxes: The effect of cloud shape. *J. Atmos. Sci.*, **41**, 3085–3103.

Welch, R., Sengupa, S., and Chen, D. (1988). Cloud field classification based upon high spatial resolution textural features 1. gray level co-occurence matrix approch. *J. Geophys. Res.*, **93**, 12663–12681.

Wornell, G. (1990). A karhunen-loeve-like expansion foe 1/f processes via wavelets. *IEEE Trans on Information Theory*, **36**, 859–861.

Zuidema, P. and Hartmann, D. (1995). Satellite determination of stratus cloud microphysical properties. *J. Climate*, **8**, 1638–1657.

Appendix A

Parametrisation of the relationship between cloud optical depth and cloud droplet effective radius

For simplicity assume uniform distribution of cloud droplet radius from 0 at cloud base to r_{vol}^t at cloud top. This assumption does not affect the functional dependence between τ and r_{vol} (or r_{eff}) changing only the coefficient of proportionality. I further assume a linear increase of the adiabatic cloud liquid water content (q_{adiab}) with height within a cloud (z). Following Austin *et al.* (1995) I have

$$q_{adiab}(z) = c_{adiab} z \tag{A.1}$$

The rate c of the increase of the cloud adiabatic liquid water with height is a function of the temperature and pressure in the cloud layer. Typical values of c_q for stratocumulus conditions are range between $1.7 \times 10^{-6}[kgm^{-4}]$ for higher level cool stratocumulus to $2.3 \times 10^{-6}[kgm^{-4}]$ for low and warm clouds. For for non adiabatic clouds I modify (A.1) by introducing a coefficient β (subadiabaticity) which ranges between 0 and 1 and represents the departure from the adiabatic cloud. (A.1) becomes

$$q(z) = c_{adiab} \beta z \tag{A.2}$$

where $\beta = c/c_{adiab}$.

Following Stephens (1978) I write the cloud optical thickness in short wavelengths as

$$\tau = \int_0^{\Delta z} 2\pi [\int_0^{\infty} n(r_{vol}) r_{vol}^2 dr_{vol}] dz \tag{A.3}$$

where n(r) is the distribution of cloud droplet radii, and Δz is the cloud geometrical thickness. With the assumed uniform droplet size distribution (A.3) becomes

$$\tau = 2\pi \int_0^{\Delta z} N r_{vol}^2(z) dz \tag{A.4}$$

where N is the total number concentration of cloud droplets assumed to be independent of height within the cloud.

In (A.2) the cloud liquid water content can be written as

$$q(z) = \frac{4}{3}\pi\rho N r_{vol}^3(z) \tag{A.5}$$

From (A.2) and (A.5) follows the dependence of r_{vol} on z

$$r_{vol}(z) = \alpha_0 (\beta \frac{z}{N})^{\frac{1}{3}} \tag{A.6}$$

where the constant

$$\alpha_0^3 = \frac{c_{adiab}}{\frac{4}{3}\pi\rho} \tag{A.7}$$

$\alpha_0^3 \approx 0.41 - 0.55 \times 10^{-9} m^{-1}$ for the range of pressure and temperature encountered in stratocumulus clouds. Differentiating (A.6) yields

$$dz = \frac{3N r_{vol}^2}{\alpha_0^3 \beta} dr_{vol} \tag{A.8}$$

Substituting (A.8) to (A.4) and integrating from cloud base to cloud top one obtains

$$\tau = \frac{6\pi N^2}{5\alpha_0^3 \beta} r_{vol}^5 \tag{A.9}$$

or

$$r_{vol} = 41\beta^{\frac{1}{5}} N^{-\frac{2}{5}} \tau^{\frac{1}{5}} \tag{A.10}$$

where r_{vol} in microns is the droplet radius at the top of the cloud and N is in cm^{-3}.

Martin *et al.* (1994) showed that in marine stratocumulus clouds cloud droplet effective radius r_{eff} can be parametrise in terms of the volume radius according to

$$r_{eff} = 1.08\ r_{vol}. \tag{A.11}$$

It follows from (A.10) and (A.11) that

$$r_{efr} = 44\beta^{\frac{1}{5}} N^{-\frac{2}{5}} \tau^{\frac{1}{5}}. \tag{A.12}$$

Total cloud liquid water can be expressed in terms of liquid water path (lwp). The lwp is given by

$$lwp = \int_0^{\Delta z} q(z) dz \tag{A.13}$$

where q is liquid water content at height z in the cloud given by (A.2). From (A.8) and (A.9) one finds

$$dz = (2\pi)^{-1} N^{-1} r_{vol}^{-2} d\tau. \tag{A.14}$$

Integration of (A.13) with (A.14) yields

$$lwp = \frac{5}{9}\rho(\frac{5\alpha_0^3\beta}{6\pi})^{\frac{1}{5}} N^{-\frac{2}{5}} \tau^{\frac{6}{5}} \tag{A.15}$$

where I substituted for r_{vol} from A.9 . Equation (A.15) can be rewritten in the following way

$$\tau = (\frac{5}{9}\rho)^{-\frac{5}{6}}(\frac{5\alpha_0^3\beta}{6\pi})^{-\frac{1}{6}} lwp^{\frac{5}{6}} N^{\frac{1}{3}} \tag{A.16}$$

or in terms of r_{vol} and lwp as

$$r_{vol} = (\frac{3\alpha_0^3\beta}{2\pi\rho})^{\frac{1}{6}} lwp^{\frac{1}{6}} N^{-\frac{1}{3}}. \tag{A.17}$$

For a given supply of cloud liquid water (lwp) the maximum obtainable cloud optical thickness in proportional to the total number concentration of of cloud droplets. It follows from (A.16) and (A.10) that

$$\tau = \frac{9}{5} lwp\ r_{vol}^{-1} \tag{A.18}$$

or alternatively

$$\tau = \frac{9}{5} a_r lwp\ r_{eff}^{-1} = a_1 lwp\ r_{eff}^{-1} \tag{A.19}$$

for lwp in $[gm^{-2}]$ and r in microns and $a_r = r_{eff}/r_{vol} = 1.07$ (Martin *et al.* (1994)). (A.19) specifies what combination of optical depth and effective radius are allowed for given liquid water path.

Appendix B

Data

My investigation into the relationship between cloud optical depth and cloud droplet effective radius is based on the retrievals of cloud properties from the AVHRR radiance measurements using the method of Nakajima and Nakajima (1995). I use four sets of satellite data, three come from the Northeastern Pacific region (FIRE data set, UBC summer 1994 and UBC summer 1995 data sets) and one data set from southern Indian Ocean near Tasmania acquired during the Australian Southern Ocean Cloud Experiment II (SOCEX II). Total of 50 satellite days were retrieved from which about 600 cloudy sectors 256 km $\times$ 256 km in size were extracted for further analysis.

For the SOCEX II experiment in situ cloud data from aircraft measurements closely coordinated with the satellite overpasses are available in addition to the AVHRR satellite data. The aircraft data are used to validate the parametrisation of the relationship between cloud optical depth and the cloud droplet effective radius and asses the accuracy of the results based on satellite data. Aircraft data are also available for FIRE but they are not as closely coincident with satellite overpasses.

B.1 Synoptic conditions

The predominant feature of the summer synoptic scale circulation over Northern Pacific is the subtropical high, centred near 45° N and 140° W (see Figure B.1).

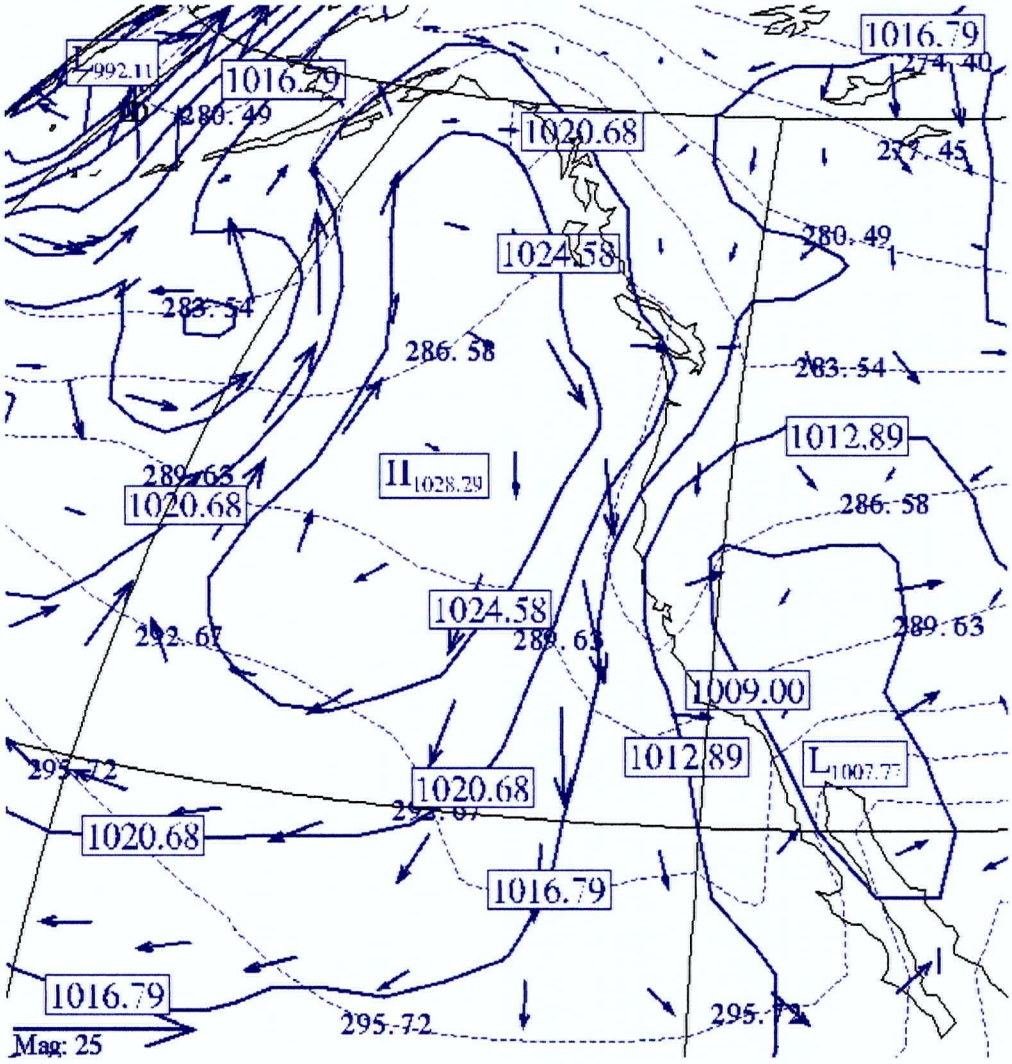

Figure B.1: North Pacific summer. Solid lines indicate pressure [mb], dashed lines are isotherms of the sea surface temperature [$^{\circ}K$], arrows represent the wind at 1000 mb level. Standard wind vector magnitude (lower left corner) is 25 $m\ s^{-1}$ (NMC analysis July 15, 1994).

Stratiform clouds frequently occur on the east side of the anticyclone and are advected towards the Equator along the coast of North America. The depth of the boundary layer in this region is about 1 km but it increases steadily as the air is advected over the warmer water. The average stratiform cloud fraction in June, July and August in this region is 60 to 70% (Klein and Hartmann (1993)). The observed monthly-averaged optical depth ranges between 5 to 14 (ISCCP Monthly Cloud Products). Typical cloud droplet effective radius for clouds of this region is about 10 μm (Han *et al.* (1994), chapter 4 of this thesis).

The summer circulation over the Indian Ocean south of Australia is more variable. Highs dominate east of Tasmania (see Figure B.2 page 217) but passages of cold fronts associated with transitory lows further south are frequent. Klein and Hartmann (1993) estimate for this region annual average stratiform cloud amount of 40%. The conditions during the SOCEX II experiment were conductive to formation of a decoupled cloud layer with strong convective elements embedded in the otherwise homogeneous cloud layer (Boers *et al.* (1997)). In the experiment area the typical observed cloud optical depth varied between 3-36 and cloud droplet effective radius between 7-14 μm.

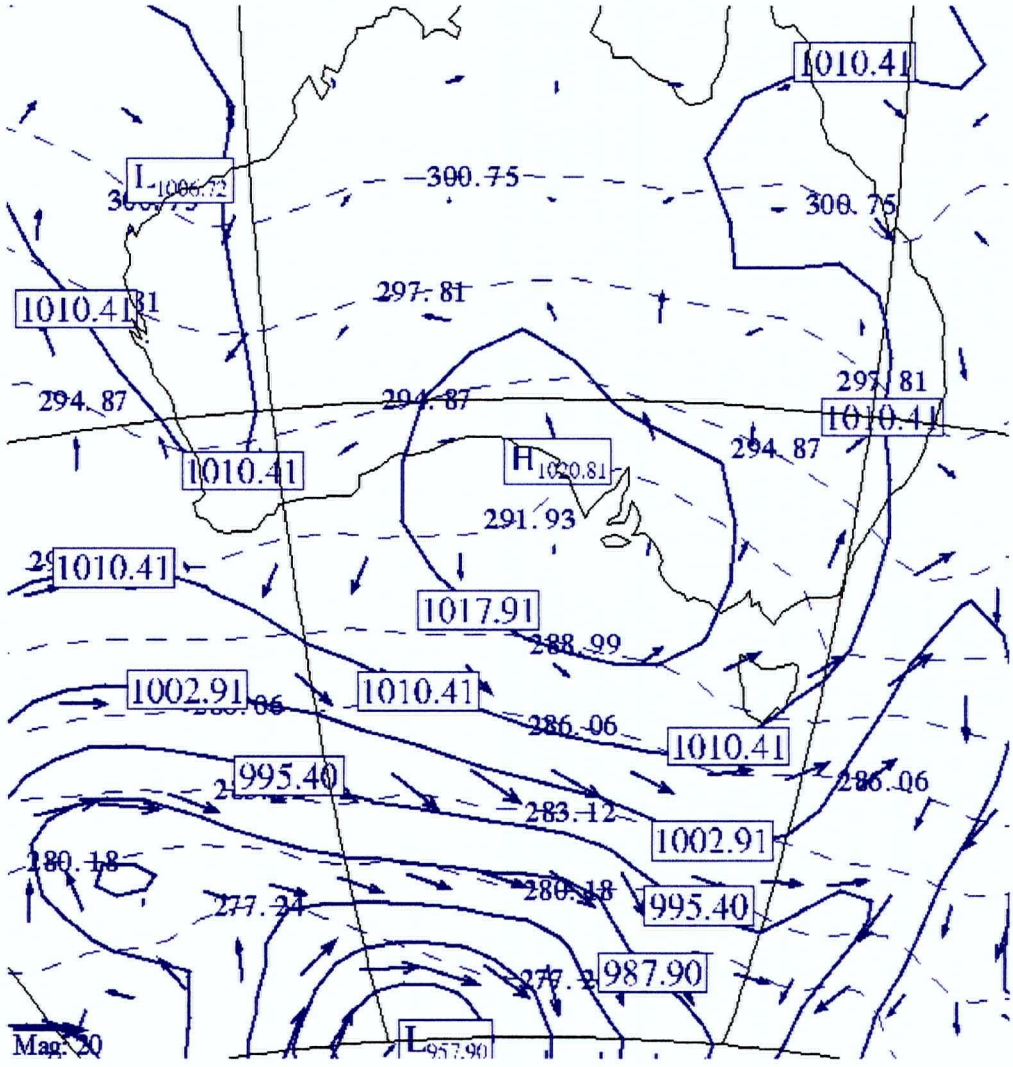

Figure B.2: Australian summer. Solid lines indicate pressure [mb], dashed lines are isotherms of the sea surface temperature [$°K$], arrows represent the wind at 1000 mb level. Standard wind vector magnitude (lower left corner) is 20 $m\ s^{-1}$ (NMC analysis January 31, 1995).

B.2 Lists of scenes analysed in the thesis

In Table B.1 I list scenes presented as examples in chapter 3 and 4. The table contains scene ID number, date, satellite and orbit number and sector coordinates. Scenes 1-6 exhibit a uni-modal distribution of τ and r_{eff}. Scenes 7-10 represent scenes with bi-modal distribution τ and r_{eff}. Scenes 11-14 represent thick clouds ($\tau > 10$). Scene 15 is an example of scene unsuitable for fitting to a power low due to an insufficient range of τ (see chapter 4 section 4.1.1).

Scene No	Date/orbit ID	lat [$^{\circ}N$]	lon [$^{\circ}W$]
1	87/07/16 N10-218.5	35.03	-132.46
2	87/07/09 N10-275.5	28.66	-124.62
3	87/07/12 N10-505.3	34.89	-129.88
4	94/07/17 N11-29943	35.38	-127.93
5	87/06/23 N10-314.2	30.61	-131.16
6	94/07/16 N11-29929	24.40	-121.11
7	87/06/23 N10-314.2	38.40	-128.62
8	87/07/14 N10-277.2	28.19	-117.65
9	95/06/15 N12-21220	24.86	-131.89
10	87/07/14 N09-277.3	29.23	-126.94
11	94/07/17 N11-29943	38.27	-124.20
12	94/07/17 N11-29943	37.93	-124.93
13	87/07/14 N09-277.3	33.84	-123.84
14	87/07/13 N09-268.4	33.60	-126.16
15	94/07/16 N11-29929	23.63	-126.02

Table B.1: List of uni-modal (1-6), bimodal (7-10) and thick cloud (11-14) scenes discussed in chapter 3 and chapter 4 Table 4.1 (1-8, 11 and 15). Scene 15 is given as an example of scene unsuitable for power law fit. Latitude and longitude are given for scene centres.

In Table B.2 I list the 10 randomly selected uni-modal scenes for which gamma distribution was fit to cloud optical depth and cloud droplet effective radius frequency distribution in chapter 4.

Scene No	Date/orbit ID	lat [$^{\circ}N$]	lon [$^{\circ}W$]
16	87/07/12 N10-505.3	33.53	-124.71
17	87/07/16 N10-218.5	32.11	-133.30
18	94/07/12 N11-29802	34.89	-129.88
19	87/07/31 N10-323.6	29.29	-126.12
20	94/06/23 N11-29802	25.54	-128.83
21	94/07/16 N11-29830	40.32	-132.12
22	94/06/23 N11-29717	38.20	-132.30
23	95/07/14 N14-20266	34.11	-124.34
24	87/07/07 N10-217.5	29.62	-124.81
25	87/07/04 N10-217.4	31.52	-121.42

Table B.2: List of 10 randomly chosen uni-modal scenes included in Table 4.2, and Figures 4.7 and 4.10 in chapter 4. Latitude and longitude are given for scene centres.

Table B.3 lists scenes of $F87$ data set used in the multifractal analysis to compute the ensemble average of nonstationarity and intermittency parameters for fields of cloud visible radiance, cloud optical depth and cloud droplet effective radius.

Scene No	Date/orbit ID	lat [$^\circ N$]	lon [$^\circ W$]	view angle
F_{87} 1(1)	87/07/16 N10-218.5	35.03	-132.46	0-10
F_{87} 2(2)	87/07/09 N10-275.5	28.66	-124.62	12-28
F_{87} 3(3)	87/07/12 N10-505.3	34.89	-129.88	0-15
F_{87} 4(5)	87/06/23 N10-314.2	30.61	-131.16	7-22
F_{87} 5(7)	87/06/23 N10-314.2	38.40	-128.62	7-22
F_{87} 6(8)	87/07/14 N10-277.2	28.19	-117.65	7 22
F_{87} 7(13)	87/07/14 N09-277.3	50.65	-126.89	0-7
F_{87} 8(14)	87/07/13 N09-268.4	33.60	-126.16	0-10
F_{87} 9	87/06/30 N10-264.1	32.79	-118.97	0-11
F_{87} 10	87/07/02 N10-217.2	34.38	-135.52	7-22
F_{87} 11	87/07/02 N10-217.2	37.42	-131.45	0-14
F_{87} 12	87/07/14 N09-277.3	33.81	-121.94	0-10
F_{87} 13	87/07/14 N09-277.3	36.16	-123.46	0-15
F_{87} 14	87/07/14 N10-277.2	29.37	-123.29	19-35
F_{87} 15	87/07/14 N10-277.2	29.57	-120.90	4-19
F_{87} 16	87/07/16 N10-218.5	32.11	-133.30	0-10
F_{87} 17	87/07/09 N10-275.5	33.39	-122.10	4-19

Table B.3: Scenes of $F87$ data set analysed in chapter 7 and included in the $F87$ ensemble average $H(1)$ and $C(1)$ for cloud visible radiance, cloud optical depth and cloud droplet effective radius. Scenes $F1-F9$ were discussed previously in chapters 3 and 4. Their numbers from Table B.1 are given in brackets.

Table B.4 lists scenes of $P94$ data set used in the multifractal analysis to compute the ensemble average of nonstationarity and intermittency parameters for fields of cloud visible radiance, cloud optical depth and cloud droplet effective radius.

Scene No	Date/orbit ID	lat [$^\circ N$]	lon [$^\circ W$]	view angle
P_{94} 1(4)	94/07/17 N11-29943	35.38	-127.93	14-29
P_{94} 2(6)	94/07/16 N11-29929	24.40	-121.11	16-33
P_{94} 3(11)	94/07/17 N11-29943	38.27	-124.20	0-10
P_{94} 4(12)	94/07/17 N11-29943	37.93	-124.93	0-10
P_{94} 5(15)	94/07/16 N11-29929	23.63	-126.02	4-20
P_{94} 6	94/06/28 N11-29675	24.07	-131.32	0-16
P_{94} 7	94/07/09 N11-29830	26.16	-119.98	4-20
P_{94} 8	94/07/18 N11-29957	36.95	-124.96	10-26

Table B.4: Scenes of $P94$ data set analysed in chapter 7 and included in the $P94$ ensemble average $H(1)$ and $C(1)$ for cloud visible radiance, cloud optical depth and cloud droplet effective radius . Scenes $P_{94}1 - P_{94}5$ were discussed previously in chapters 3 and 4. Their numbers from Table B.1 are given in brackets.

Table B.5 lists scenes of $P95$ data set used in the multifractal analysis to compute the ensemble average of nonstationarity and intermittency parameters for fields of cloud visible radiance, cloud optical depth and cloud droplet effective radius.

Scene No	Date/orbit ID	lat [$^{\circ}N$]	lon [$^{\circ}W$]	view angle
P_{95} 1(9)	95/06/15 N12-21220	24.86	-131.89	4-20
P_{95} 2	95/07/14 N14-21780	24.85	-124.83	0-14
P_{95} 3	95/07/14 N14-21780	24.03	-129.07	17-34
P_{95} 4	95/07/15 N12-21220	34.45	-130.14	10-25
P_{95} 5	95/06/24 N14-28373	27.03	-119.32	0-14

Table B.5: Scenes of $P95$ data set analysed in chapter 7 and included in the $P95$ ensemble average $H(1)$ and $C(1)$ for cloud visible radiance, cloud optical depth and cloud droplet effective radius . Scene $P_{95}1$ was discussed previously in chapters 3 and 4. Scene $P_{95}1$ number number from Table B.1 are given in brackets.

Table B.6 lists scenes of $S95$ data set used in the multifractal analysis to compute the ensemble average of nonstationarity and intermittency parameters for fields of cloud visible radiance.

Scene No	Date/orbit ID	lat [$°N$]	lon [$°W$]	view angle
S_{95} 1	95/01/31 N14-00448	-41.84	135.29	12-29
S_{95} 2	95/02/07 N09-52365	-42.03	140.63	0-16
S_{95} 3	95/02/08 N14-00561	-39.33	132.65	0-13
S_{95} 4	95/02/08 N09-52379	-40.97	141.50	1-17

Table B.6: Scenes of $S95$ data set analysed in chapter 7 and included in the $S95$ ensemble average $H(1)$ and $C(1)$ for cloud visible radiance.

Appendix C

Removing auto-correlation in spatial data

Observations find integral scales for spatial variability of cloud parameters in range of 3-60 km for fields of marine stratocumulus (Barker and Davies (1992), Marshak *et al.* (1997)). The integral scale is often interpreted as distance over which a time or space series is autocorrelated (Marshak *et al.* (1997)). Spatial patterns such as open and closed cellular structures and cloud streets are manifestation of a localised spatial dependence within cloud fields. Barker and Davies (1992) links the autocorrelation distance in cloud fields to the size of typical cloud elements (cells).

The presence of spatial autocorrelation in a variable presents a difficulty for traditional statistical methods because proximate samples may not be independent. Goodchild (1986), McGwire *et al.* (1993) state that presence of autocorrelation in data sets can affect results of regression. The clustering of samples within autocorrelated areas biases a regression line towards a precise fit of localised relationships rather than defining an accurate overall relationship.

In view of the above, I decided to address the problem of spatial autocorrelation in the τ and r_{eff} data before proceeding with the regression fit of the relationship between τ and r_{eff}. I will want to use the least square method to find the best fit to the relationship between cloud optical depth and cloud droplet effective radius in $\log(\tau)$, $\log(r_{eff})$) space. The least squares technique requires that the observations of the predictor variable are independent. This is clearly not the case

in the autocorrelated field of cloud optical depth . What are the dangers of using the least square fitting on an auto-correlated data?

An auto-correlated sample is affected by a type of implicit blocking. Consider for example a satellite scene with strong cellular structure. Values of cloud optical depth within individual cells are strongly correlated and there is little in-cell variability compared to the overall variability of the τ filed. In other words, cells form blocks in the τ space. Values of cloud droplet effective radius obtained for pixels of an individual cell (or block) will also be less variable than the overall variability of the sample and since they correspond to strongly correlated τ values they are not truly independent.

There are many replicated values of τ (from a cell), and the variation between r_{eff} at these replicated values is much smaller than the overall residual variance. This results in a too small estimate of the variance of the linear regression slope, making the test of whether the slope is 0 (and, equivalently, the test of the goodness of linear fit) anti conservative (more likely than the stated significance level to reject the null hypothesis, even when it is true).

One way of dealing with blocked samples is to replace blocks of values with single values of block averages in both variables and then perform the regression analysis with the new data set. Another approach is to sub-sample the data set so to avoid auto-correlation (Goodchild (1986), McGwire *et al.* (1993)). A possible drawback both methods is that by reducing the number of data points, the degrees of freedom associated with the residual error is reduced, thus potentially reducing the power of the test. This however should not be a problem in our case. Our number of observation is very large (256×256) and even 1% of the total number of observation (655) still constitutes a large statistical sample.

In order to avoid the auto-correlation in the sample data and satisfy the requirement of independent observation I employ a selective sampling. The idea behind this sub-sampling is to only use in the analysis those pixels which are far

enough from each other that they are unlikely to be spatially correlated (Goodchild (1986), McGwire *et al.* (1993)).

I adopt the following sub-sampling strategy:

1. find the sample range of auto-correlation l for the independent variable. I define the sample range of auto-correlation as the shortest pixel separation distance for which two pixels can be consider independent.

2. sub-sample the scene taking only pixels that are l apart (in both directions) starting from a randomly selected pixel (we call it drawing a random lattice)

3. take a random sub-sample from the lattice (the lattice sample can still have some residual spatial structure, I sub-sample the lattice to reduce the impact of that structure on the results)

4. perform the analysis on the random sample taken form the lattice

5. repeat points 2-4 for a large number of randomly selected lattices (at least 100) and compute averages of the analysis results of each lattice

The range of autocorrelation l is estimated using semivariograms (Isaaks and Srivastava (1989)). This statistics is equivalent to second order structure function and is well suited to extract spatial information from remotely sensed imagery (Curran (1988)). The semivariogram $\gamma(\mathbf{h})$ is defined as an average squared difference between pairs of values separated by lag vector $\mathbf{h}$

$$\gamma(\mathbf{h}) = \frac{1}{2\mathrm{N}(\mathbf{h})} \sum_{(\mathrm{i,j})|\mathbf{h}_{\mathrm{ij}}=\mathbf{h}} (\mathrm{v_i} - \mathrm{v_j})^2 \qquad \text{(C.1)}$$

where $(v_i, (v_j)$ are sample values at the locations i and j, $\mathbf{h}$ is the lag vector, the sum is over all pairs of data points separated by vector $\mathbf{h}$ and $N(\mathbf{h})$ is the number of all such pairs.

Generally, as the separation distance between pairs increases so does the value of the semivariogram. However, above a certain lag an increase in separation

distance no longer causes a corresponding increase in the average squared difference between pairs of values and the semivariogram reaches a plateau. Figure C.1 shows a schematic semivariogram. The lag at which the semivariogram reaches the plateau is called the range. The sill is the value of the semivariogram at the range. The fact that the semivariogram has a value greater than zero at zero distance lag is known as the nugget effect. The nugget effect can be a manifestation of a purely random variation in population density (white noise) or it may be associated with sampling errors. The range of the semivariogram can be interpreted as the distance over which the sample data are spatially correlated. Observation which are more then the range apart are considered independent.

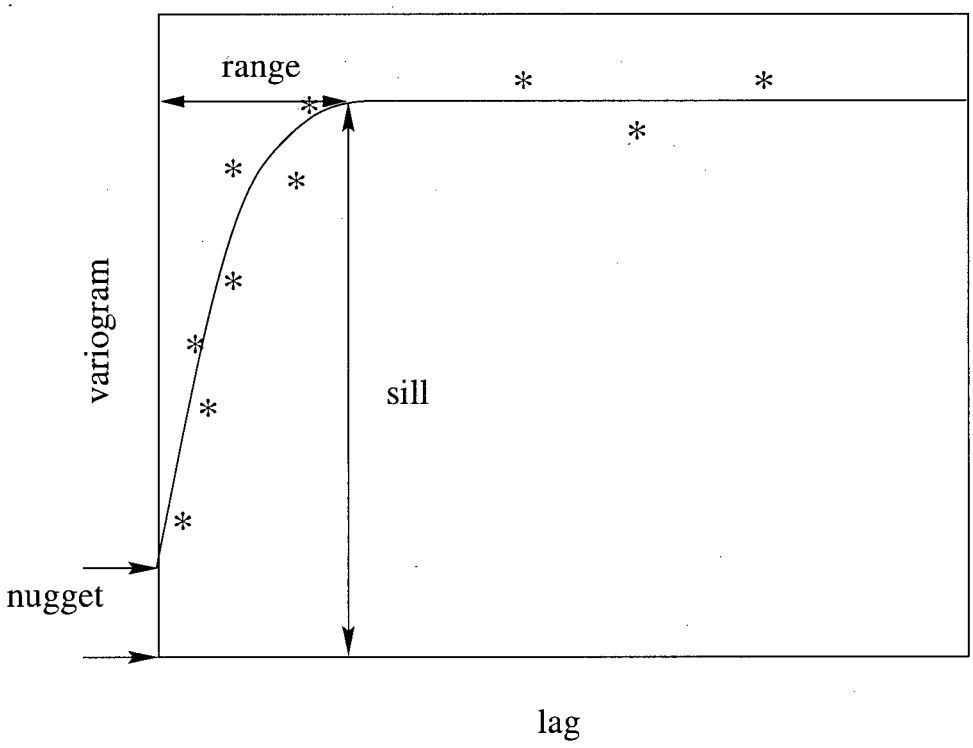

Figure C.1: Schematic semivariogram

Figure C.2 demonstrates the steps of the sampling procedure. The scatter

plot of cloud optical depth and cloud droplet effective radius for a complete sample is shown in figure C.2a. I compute semivariograms for the complete sample data in four directions (N-S, NE-SW, W-E, and NW-SE) shown in figure C.2b. The sample in this example appears to be isotropic having very similar semivariograms in all four directions. From the semivariogram I assess the range of autocorrelation, 7-10 km in this case. Our estimate of the semivariogram range does not need to be very accurate. I am limited by the pixel size (1 km) but am satisfied with 2-3 pixel accuracy opting for the overestimate rather than an underestimate of the range. Thus, I will not attempt to fit model semivariograms to the data but will relay on the visual examination of the experimental semivariogram. (As a check of the success of the sampling procedure in eliminating the autocorrelation in a sample we examine the residual of the linear regression fit, see figure C.2d). Figure C.2c shows a scatter plot of cloud optical depth and cloud droplet effective radius for one realisation of the sampling (random sample of 1000 pixels drawn from a random lattice of range=5 km).

A linear least square fit to the $\log(\tau)$, $\log(r_{eff})$ data with errors in both variables was performed for each realisation of the sampling procedure and the averaged slope and intercept were computed. (A detailed discussion of the general power law fitting to τ-r_{eff} data will follow in section 4.1.3). Figure C.2d shows the residual (observed - fitted) value of the $\log(r_{eff})$ as a function of τ. Such plots serve as an initial test of how successful the sampling procedure was in eliminating the effects of autocorrelation. If I succeeded in removing autocorrelation then the least square fit residuals should be normally distributed with zero mean and therefore, the plot of residuals versus the independent variable should show no trend nor bias. This indeed appears to be the case in this example. After this initial inspection of the performance of the sampling procedure I test the null hypothesis that the residuals are normally distributed and have mean of zero. At the 10% significance level the critical interval for the Z-test is (-1.645,1.645).

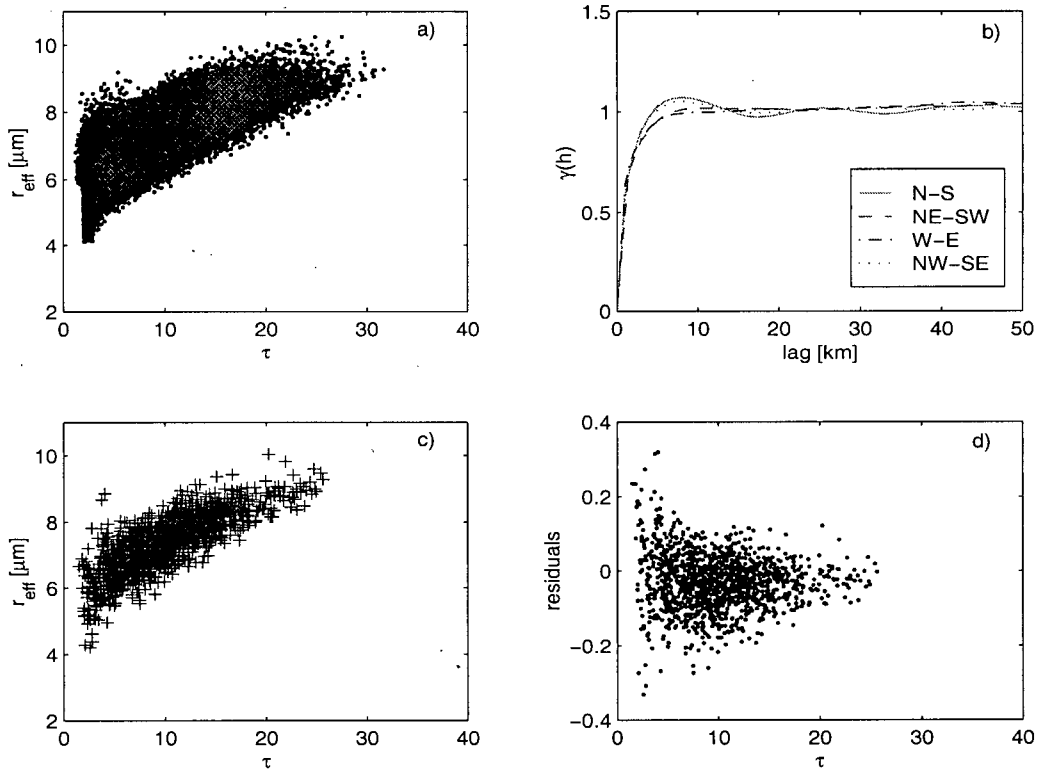

Figure C.2: The sampling procedure. a) the scatter plot of cloud optical depth and cloud droplet effective radius of the full data set; b) semivariograms of τ in four directions (N-S, NE-SW, W-E, and NW-SE) showing autocorrelation range 7-10 km; c) scatter plot of τ and r_{eff} of an autocorrelation free sample; d) plot of the residuals of the linear least square fit to $\log(r_{eff})$ and $\log(\tau)$ as a function of τ.

I performed the Z test for 500 realisations of the sampling procedure and in every case the value of the Z statistic was within the critical interval for the 10% significance level. The average mean of the 500 realisations was 0.005. The results of the Z-test indicate that at the 10% significance level null hypothesis that the residuals are normally distributed with the mean of zero should not be rejected. I accept that the sampling procedure was successful in selecting an autocorrelation free sample.

Appendix D

Correlation coefficient between τ and r_{eff}

Before proceeding with regression to establish a functional dependence between two variables one should check if the variables are indeed correlated and whether the correlation is significant. A bivariate regression will always return a set of regression parameters but these parameters are meaningless unless the correlation between the two variables is significant. Since I expect a linear dependence between $t = log(\tau)$ and $r = log(r_{eff})$ I use the Pearson's linear correlation coefficient to test the strength and significance of the correlation between the cloud optical depth and cloud droplet effective radius in the test scenes of chapter 4.

Pearson's linear correlation coefficient between two variables t and r is defined as

$$r_p = \frac{\sum_i (t_i - \bar{t})(r_i - \bar{r})}{\sqrt{\sum_i (t_i - \bar{t})^2}\sqrt{\sum_i (r_i - \bar{r})^2}} \tag{D.1}$$

where the 'bar' denotes the mean value of the variable. For the null hypothesis of no correlation between t and r ($r_p = 0$) the test statistics

$$t_p = r_p \sqrt{\frac{n-2}{1-r_p^2}} \tag{D.2}$$

has the Student-t distribution with $\nu = n - 2$ degree of freedom (n is the number of observations). The first raw of table D.1 shows the Pearson's linear correlation coefficients for the test scene. Each coefficient is an average from 100 realisations

of the sampling procedure. With the exception of scene 11 and the upper branch of scene 9 all correlation coefficients are are significant at zero level. For both scene 11 and the upper branch of scene 9 the null hypothesis cannot be rejected at approximately 40% significance level.

scene no.	r_p	r_s	scene no.	r_p	r_s
1	0.87	0.85	6	0.57(0.73)	0.67(0.73)
2	0.78	0.80	7	0.57(0.73,0.80)	0.50(0.70,0.72)
3	0.65	0.70	8	0.65(0.23,0.65)	0.60(0.26,0.61)
4	0.79(0.78)	0.79(0.70)	11	0.09	0.09
5	0.80(0.83)	0.75(0.81)	15	0.71	0.71

Table D.1: Pearson's (r_p) and Spearman's (r_s) linear correlation coefficients for 10 test scenes.

For scenes 1-7 values in brackets are the correlation coefficients in the scene sectors which satisfy the meaningful fit requirements (where no values in brackets are given the entire scene satisfies the fitting requirements). Scenes 7 and 8 are the scenes with the two branch structure. The bracket values for scenes 7 and 8 show the correlation coefficients for each branch separately. In scene 7 both branches have high values of of the correlation coefficient. I also find that each branch in scene 7 satisfies the conditions of a meaningful fit. In scene 8 only these conditions are fulfilled only by the branch with high correlation coefficient (0.66). The second branch the represents to the situation of the rectangle 2 of figure 4.1 where all data points correspond to high values of the predictor variable. Scene 11 represents a similar situation. Here again there is no observations at the low values of τ. This scene does not conform to the meaningful fit requirements and the value of correlation coefficient in this scene is low.

There appears to be a correlation between the high value of the correlation coefficient and the scene suitability for fitting. This is not surprising, I would expect two variables whose scatter plots take a form of a single, narrow and long branch to

be strongly correlated. The Pearson's correlation coefficient can be a good predictor of scene's suitability for fitting. However, caution is advised. In some cases, and scene 8 is the case in point, the correlation coefficient can be high yet the scene might not be suitable for fitting. The correlation coefficient for scene 8 is high but the scene data does not fulfilled the requirements for a meaningful fit. It represents the situation of the rectangle 1 in figure 4.1 where the available range of the predictor is very narrow and all confined to small values.

The Pearson's linear correlation coefficient does not come without warnings and limitations (Swan and Sandilands (1995)).

1. it only has a meaning for variables whose probability distribution is not too different from normal (I made the necessary assumptions about the distributions of t and r)

2. is liable to spurious high values if outliers are present

3. log-transform in two variables can raise the value of the correlation coefficient

The non-parametric statistics offers an alternative to the Pearson's measure of correlation which is much more general and robust. First of all, in the non-parametric statistics it is not necessary to make any assumption about the distribution of the variables. The non-parametric measures of correlation which relay on rank ordering are also less susceptible to outliers and are not affected by transformation of variables. To confirm the correlation results of Pearson's correlation coefficient I compute the non-parametric Spearman's rank correlation coefficient for the 11 test scenes. If T_i is the rank of t_i among other t's and R_i is the rank of r_i among other r's then the Spearman rank order correlation coefficient is defined as the linear correlation coefficient of the ranks

$$r_s = \frac{\sum_i (T_i - \bar{T})(R_i - \bar{R})}{\sqrt{\sum_i (T_i - \bar{T})^2}\sqrt{\sum_i (R_i - \bar{R})^2}} \tag{D.3}$$

where as before the 'bar' denotes the mean value of the variable. For the null hypothesis of no correlation between t and r ($rr_s = 0$) the test statistics

$$t_s = r_s \sqrt{\frac{n-2}{1-r_s^2}} \tag{D.4}$$

has the Student-t distribution with $\nu = n - 2$ degree of freedom (n is the number of observations). The values of the Spearman correlation coefficient for the 11 test scenes are given in the second row of table D.1. All correlation coefficients are significant at zero level except scene 11 and the upper branch of scene 9 where the null hypothesis of no correlation between t and r cannot be rejected even at the level of 35%. There is a very good agreement between the Pearson and the Spearman correlation coefficients. The non-parametric test validates the results of the Pearson test. This is an important result. A high rank order correlation coefficient does not by itself imply a good linear relationship between two variables. A high Pearson's correlation coefficient does imply a strong linear relationship between two variables provided it is not biased by one of it's limitations. Good agreement between the Pearson and the Spearman correlation coefficients indicate that the Pearson's coefficients are bias free.

With the good linear correlation between t and r I expect the power law fit to be good. This does not mean that we expect the power exponent to turn out "1/5" but whatever the value of the regression parameters they will be meaningful and representative of the relationship between cloud optical depth and cloud droplet effective radius in the data set.

Appendix E

Cloud subadiabaticity β

Cloud subadiabaticity β which occurs in equation 3.2 is bulk cloud property which measures the rate of increase of cloud liquid water with height with respect to the rate of increase in an adiabatic cloud and is defined in (A.2) of Appendix A). This β is related to Betts' mixing parameter (β_B) (Betts (1982)) by $\beta = 1 - \beta_B$ where $\beta_B = \delta p_* / \delta p$, p is pressure and p_* the saturation level pressure. The available observations locate β in the range between 0.4 and 1.0.

For tropical oceans Betts and Albrecht (1982) inferred β_B=0.3 from thermodynamic averages over a large number of radiosonde profiles. Betts and Boers (1990) showed a case study of a stratocumulus layer where β_B=0.3. Boers and Betts (1988) and Boers *et al.* (1991) found β_B for boundary layer clouds in the range between 0.3-0.4. Boers *et al.* (1996) observed β of 0.3-0.6 in winter time stratocumulus near Tasmania (SOCEX I). Observations of cloud liquid water content in stratus clouds (Nicholls (1984) and Nicholls and Leighton (1986)) reveal somewhat smaller values of β_B. Austin *et al.* (1995) analysed 6 FIRE fights and found β between 0.60 and 1. Our estimates of cloud subadiabaticity for the 6 SOCEX flights find β at somewhat lower values between 0.37-0.67 (β_B = 0.33-0.63). Boers *et al.* (1991) argue that $\beta_B > 0.5$ corresponds to strong decoupling between the surface and the upper part of the boundary layer. The SOCEX boundary layer was 2-3 times deeper than that during FIRE and the cloud layers were reported to be decoupled during SOCEX

flights. It would be interesting to investigate the dependence between the depth of the boundary layer and cloud subadiabaticity .

In chapter 5 I estimated β from the cloud liquid water content measurements made by aircraft in clouds over the Indian Ocean east of Tasmania during the SOCEX II experiment. In Figure E.1 I plot the cloud subadiabaticity β versus the cloud layer average cloud droplet number concentration N observed during 6 SOCEX flights (*) (see Table 5.2 on page 110). In addition I plotted the measurements for FIRE clouds reported in Austin *et al.* (1995) (o).

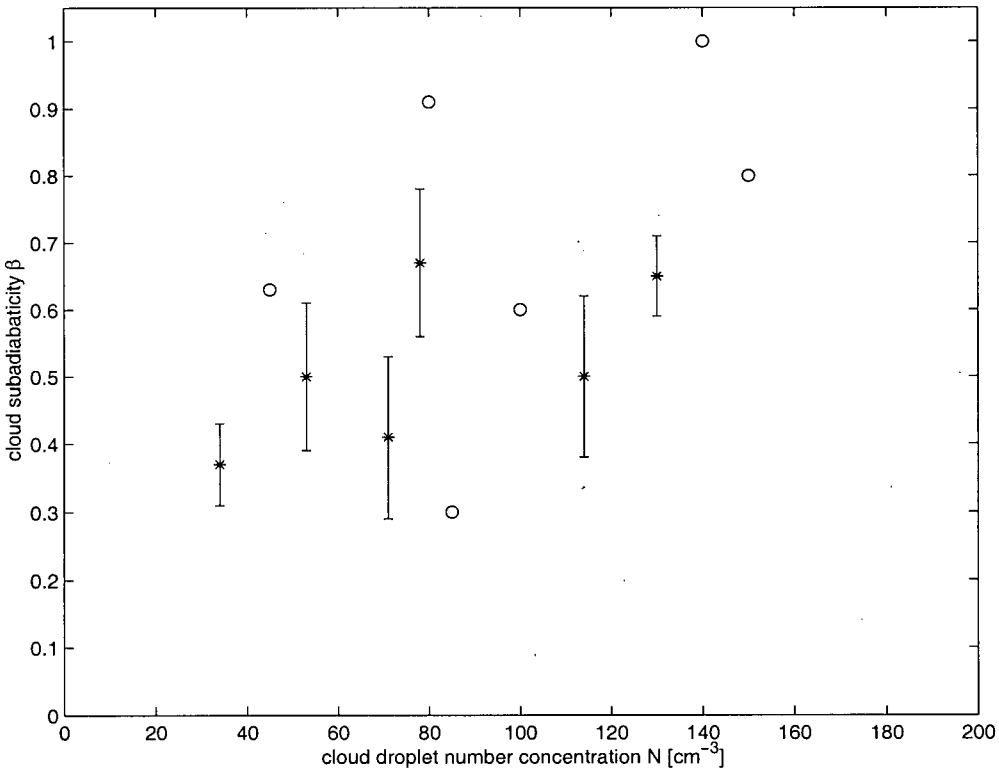

Figure E.1: Scatter plot of cloud subadiabaticity β and cloud droplet number concentration : (*) SOCEX II data (see chapter 5); (o) FIRE measurements after Austin *et al.* (1995).

There is a noticeable tendency for high β to occur with high N. However,

the observed scatter is quite large. N can be one of the factors which determine the variability of β but there probably other factors which contribute to that variability.

Nicholls and Leighton (1986) measured the deviation of the observed liquid water content from the adiabatic value (1-β) as a function of height in stratiform clouds. Their results seem to indicate that the deviation is greatest in clouds with lowest cloud droplet number concentration which qualitatively agrees with the results shown in Figure E.1.

Appendix F

Concepts related to fractal sets and fractal measures

Fractals (or fractal sets) are geometrical objects which possess nontrivial structure on arbitrary scales (Mandelbrot (1977)). A classical example of fractal is the Koch curve whose construction is illustrated in Figure F.1. In consecutive steps each linear segment of the curve is replaced by four segments as shown in Figure F.1. Each new segment is is one third the length of the previous one. After an infinitive number of steps one obtains the Koch curve.

1) Fractal dimension

To define dimensions of fractal objects one refers to the procedure known as box counting. In a d-dimensional Euclidean space (d =1, 2, 3) the number $N(r)$ of boxes of size r^d needed to to cover an object of dimension $d_0 \leq d$ is

$$N(r) \sim r^{-d_0}. \tag{F.1}$$

The dimension of an object is defined by (F.1) in the limit of $r \to 0$ (Beck and Schlögl (1993)). The same method can be applied to determine dimension of fractal objects. The *fractal dimesion*, also known as the *box* or *capacity dimension*, is defined as

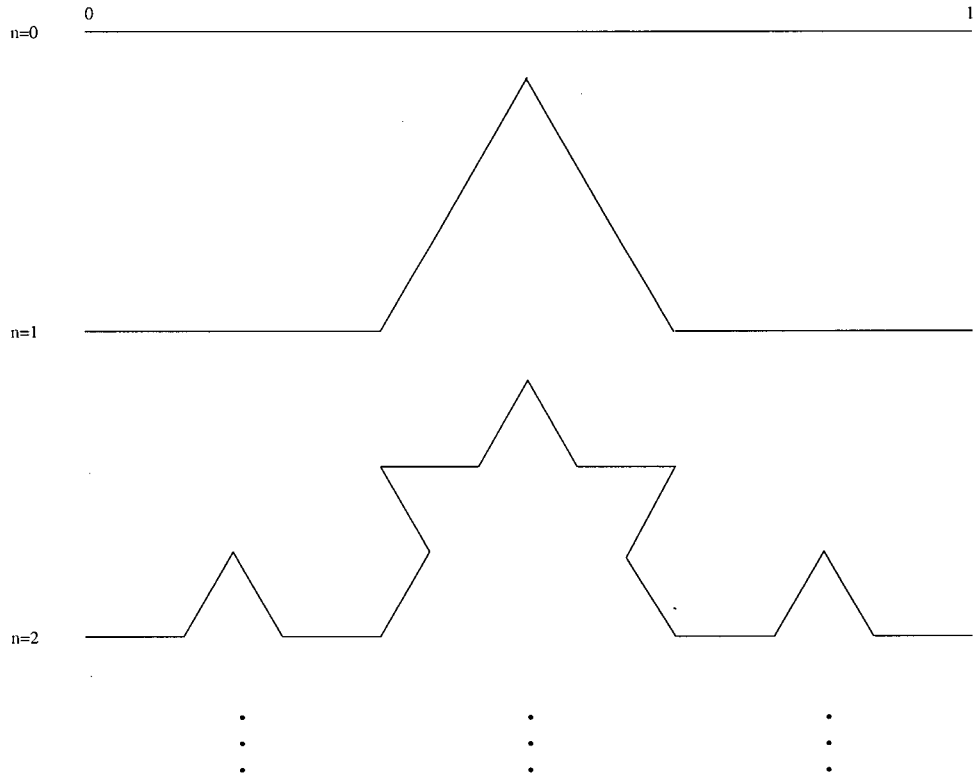

Figure F.1: Construction of the classical Koch curve.

$$D_c = -\lim_{r \to 0} \frac{logN(r)}{logr}. \tag{F.2}$$

For some simple fractals the fractal dimension can be determined by a simple theoretical arguments. For the Koch curve for example, the number of "boxes" required to cover the curve increases with each step n as 4^n while the size of the box (or yardstick in this case) decreases as 3^{-n}. Thus, from (F.2) $D_c = \frac{log4}{log3} = 1.2619....$

2) Other fractal dimensions

a) Hausdorff dimension

In definition (F.2) it is assumed that boxes which cover a fractal object A are all

the same size r^d and the dimension obtained in the limit $r \to 0$ is independent of the shape of boxes. Rigorous mathematical treatment shows that for complicated fractal objects the limit in (F.2) does not always exist. A mathematically well defined quantity is the *Hausdorff dimension* D_H whose definition utilises boxes of variable sizes (a formal definitions of Hausdorff dimension is not given here but can be found in Mandelbrot (1977) or Beck and Schlögl (1993) for example). It turns out that in all cases of practical interest $D_H = D_c$.

b) Generalised dimensions

Definition (F.2) can be generalised in the following way: if (by analogy to (F.1)) a quantity $M(r)$ attributed to a fractal object scales as

$$M(r) \sim r^D. \tag{F.3}$$

for $r \to 0$ then D can be consider a dimension of the fractal with respect to the property M.

c) Information dimension

The box counting procedure which defines capacity dimension assigns equal weights to all boxes needed to cover the object. However, the fraction of the object covered by a box can vary significantly from one box to another. In a sense, some boxes are more important (cover larger sections of the object) than others. To account for the different "importance" of the boxes Grassberger (1983) and Hentschel and Procaccia (1983) introduced a generalised dimension $D(q)$ which depends on a continuous index q,

$$D(q) = \lim_{r \to 0} \frac{log I_q(p)}{log r} \tag{F.4}$$

with

$$I_q(p) = \frac{1}{q-1} log \sum_{i=1}^{\tilde{N}(r)} p_i^q = \frac{1}{q-1} log Z(q,r) \tag{F.5}$$

where $\tilde{N}(r)$ is number of boxes of size r needed to cover the object, and p_i is the probability of finding the object in box i. $I_q(p)$ are called Rényi informations and dimensions D_q are sometimes referred to as Rényi dimensions. In (F.5) $Z(q,r)$ is a partition function of the probability distribution p.

Special cases:

1. q=0: $D(0) = -\lim_{r\to 0} \frac{logN(r)}{logr}$ which is a definition of the *capacity dimension*, thus $D(0) = D_c$.

2. q=1: in the limit of $q \to 1$ Rényi information approaches the well known in the information theory Shannon information $I(p) = \sum_{i=1}^{\tilde{N}(r)} p_i log p_i$. Correspondingly, $D(1)$ is termed information dimension.

c) Hölder (roughness) dimension

The fractal dimension is a local property which in case of a graph of a continuous function, is related to other local property, the Hölder exponent (α) of the function. Function $\varphi(x)$ is Hölder function of order α if $\varphi(x) - \varphi(x_0) \sim |x - x_0|^\alpha$ near $x = x_0$, where $0 < \alpha < 1$ (Weinberger (1965)). The number of boxes of needed to cover the graph $g(\varphi)$ of $\varphi(x)$ locally between x and $x + r$ is roughly $r^{\alpha-1}$ ((Mandelbrot (1977)). The total number of boxes needed to cover the graph is $N \sim r^{\alpha-1}/r^{-1} = r^{\alpha-2}$.

If the curve within each box is a reduced image of the whole curve (self-similarity) then from the definition of fractal dimension

$$D_g = -\frac{logN(r)}{logr} = 2 - \alpha. \tag{F.6}$$

D_g is called the Hölder (or roughness) dimension of the graph.

3) From singularity to multiscaling of structure function

Singularity of order $\alpha > 0$ in field $R(x)$ can be defined as a point where

$$\lim_{x \to y} |R(x) - R(y)|/|x - y|^{\alpha} \neq 0 \tag{F.7}$$

Let $S(\alpha)$ denote a set of points where the field has a singularity of order α and $D_H(\alpha)$ a Hausdorff dimension of that set. Denote by $f(\alpha)$ the probability of field $R(x)$ having a singularity of order α. By box counting

$$f(\alpha) \sim \frac{|x - y|^{-D_H(\alpha)}}{|x - y|^{-E}}, \; as \; |x - y| \to 0 \tag{F.8}$$

where E is the dimension of the Euclidean space. ($E - D_H$ is often called co-dimesion.)

From (F.7) it follows that

$$|R(x) - R(y)| \sim |x - y|^{\alpha} \tag{F.9}$$

Recall now the definition of q order structure function (6.15). With (F.9) the increments of the field can be replace by $|x - y|^{\alpha}$ and thus

$$< |R(x) - R(y)|^{q} > \sim < |x - y|^{\alpha q} > = \int d\mu(\alpha) r^{\alpha q + E - D_H(\alpha))} \sim r^{\zeta_q} \tag{F.10}$$

where $r = |x - y|$, $d\mu(\alpha)$ is a measure on $S(\alpha)$ and ζ_q is a function (generally nonlinear) of the order q of structure function and the order α of the singularity. Integral (F.10) integrated using the saddle point method yields (Parisi and Frisch (1985))

$$\zeta_q = min_{\alpha}[q\alpha + E - D_H(\alpha)]. \tag{F.11}$$

Appendix G

Tables of nonstationarity and intermittency parameters.

1) Scenes 1-15

Scene No	H(1)	2 H(2) + 1	β	β_8	C(1)	K(2)	range [km]	cloud fraction A_c
1	0.48 (0.02)	1.94 (0.03)	1.90 (0.06)	1.93 (0.02)	0.05	0.10	1-8	0.99
2	0.53 (0.03)	2.02 (0.05)	2.17 (0.12)	2.24 (0.07)	0.06	0.10	1-5	0.98
3	0.48 (0.04)	1.93 (0.09)	1.92 (0.16)	2.19 (0.15)	0.05	0.08	1-4	0.99
4	0.59 (0.03)	2.13 (0.05)	2.22 (0.13)	2.39 (0.01)	0.06	0.11	1-6	0.97
5	0.46 (0.01)	1.84 (0.03)	2.18 (0.04)	2.07 (0.10)	0.05	0.09	1-20	0.96
6	0.38 (0.03)	1.76 (0.05)	1.97 (0.09)	1.87 (0.08)	0.05	0.09	1-8	0.94
7	0.49 (0.03)	1.95 (0.05)	2.29 (0.08)	2.13 (0.15)	0.05	0.09	1-8	0.99
8	0.40 (0.04)	1.79 (0.08)	1.82 (0.21)	1.84 (0.15)	0.04	0.08	1-4	1.0
9	0.46 (0.01)	1.84 (0.02)	1.94 (0.05)	1.96 (0.07)	0.09	0.18	1-20	0.95
10								
11	0.60 (0.03)	2.16 (0.07)	2.10 (0.33)	2.29 (0.05)	0.05	0.08	1-3	1.0
12	0.37 (0.02)	1.71 (0.04)	1.66 (0.12)	1.69 (0.02)	0.05	0.10	1-6	1.0
13	0.57 (0.04)	2.14 (0.08)	2.77 (0.16)	2.63 (0.15)	0.05	0.08	1-4	1.0
14	0.64 (0.04)	2.26 (0.08)	3.26 (0.20)	2.91 (0.11)	0.06	0.11	1-4	1.0
15	0.39 (0.03)	1.80 (0.06)	2.05 (0.10)	1.57 (0.14)	0.05	0.09	1-6	0.92

Table G.1: Multifractal parameters of cloud visible wavelength radiance field for the 15 example scenes: (1-6, and 15) uni-modal, (7-10) bi-modal, (11-14) thick clouds.

Scene No	H(1)	2 H(2) + 1	β	β_8	C(1)	K(2)	range [km]	cloud fraction A_c
1	0.49 (0.02)	1.96 (0.04)	2.02 (0.06)	2.02 (0.01)	0.05	0.10	1-8	0.99
2	0.54 (0.03)	2.07 (0.05)	2.07 (0.05)	2.17 (0.01)	0.05	0.10	1-5	0.98
3	0.52 (0.04)	2.06 (0.07)	2.14 (0.23)	2.32 (0.18)	0.07	0.13	1-4	0.99
4	0.61 (0.03)	2.18 (0.05)	2.40 (0.17)	2.48 (0.04)	0.06	0.10	1-6	0.97
5	0.48 (0.01)	1.93 (0.03)	2.10 (0.04)	2.00 (0.11)	0.05	0.09	1-20	0.96
6	0.40 (0.03)	1.81 (0.04)	2.06 (0.10)	1.91 (0.08)	0.06	0.10	1-8	0.94
7	0.50 (0.03)	2.02 (0.05)	2.32 (0.08)	2.17 (0.11)	0.04	0.07	1-7	0.99
8	0.42 (0.04)	1.84 (0.07)	1.81 (0.21)	1.85 (0.13)	0.05	0.09	1-4	1.0
9	0.46 (0.01)	1.85 (0.01)	1.89 (0.05)	2.14 (0.11)	0.07	0.14	1-20	0.95
10								
11	0.62 (0.03)	2.20 (0.07)	2.22 (0.40)	2.34 (0.02)	0.06	0.11	1-3	1.0
12	0.38 (0.02)	1.72 (0.05)	1.75 (0.12)	1.70 (0.02)	0.05	0.09	1-6	1.0
13	0.57 (0.04)	2.13 (0.09)	2.79 (0.19)	2.68 (0.20)	0.06	0.10	1-4	1.0
14	0.65 (0.04)	2.23 (0.09)	3.20 (0.19)	2.87 (0.08)	0.09	0.16	1-4	1.0
15	0.42 (0.03)	1.81 (0.05)	1.83 (0.10)	1.60 (0.11)	0.06	0.11	1-6	0.92

Table G.2: Multifractal parameters of cloud optical depth field for the 15 example scenes: (1-6, and 15) uni-modal, (7-10) bi-modal, (11-14) thick clouds.

Scene No	H(1)	2 H(2) + 1	β	β_8	C(1)	K(2)	range [km]	cloud fraction A_c
1	0.55 (0.01)	2.01 (0.01)	1.95 (0.13)	2.00 (0.18)	0.06	0.14	1-8	0.99
2	0.53 (0.02)	2.07 (0.03)	1.90 (0.17)	1.91 (0.16)	0.05	0.09	1-7	0.98*
3	0.48 (0.03)	1.92 (0.05)	2.06 (0.25)	2.17 (0.02)	0.07	0.12	1-4	0.99*
4	0.59 (0.01)	2.13 (0.02)	1.96 (0.15)	2.14 (0.08	0.09	0.16	1-8	0.97*
5	0.53 (0.01)	1.96 (0.03)	1.84 (0.11)	1.92 (0.12)	0.05	0.11	1-10	0.96
6	0.61 (0.01)	1.83 (0.02)	1.82 (0.11)	1.77 (0.02)	0.08	0.22	1-10	0.94
7	0.49 (0.01)	1.92 (0.03)	1.84 (0.11)	1.84 (0.02)	0.05	0.10	1-8	0.99
8	0.34 (0.01)	1.61 (0.01)	1.42 (0.15)	1.26 (0.13)	0.06	0.14	1-10	1.0
8	0.63 (0.01)	2.24 (0.01)	1.85 (0.23)	2.34 (0.28)	0.06	0.14	20-80	1.0
9	0.45 (0.01)	1.75 (0.02)	1.77 (0.06)	1.89 (0.02)	0.07	0.15	1-20	0.95
10								
11	0.56 (0.02)	2.06 (0.02)	2.68 (0.82)	2.03 (0.01)	0.06	0.11	1-3	1.0
12	0.40 (0.01)	1.78 (0.01)	1.47 (0.06)	1.45 (0.02)	0.05	0.09	1-20	1.0
12	0.38 (0.01)	1.76 (0.01)	1.69 (0.13)	1.52 (0.03)	0.05	0.09	1-6	1.0
13	0.53 (0.02)	2.07 (0.03)	1.86 (0.26)	1.90 (0.06)	0.06	0.10	1-4	1.0
14	0.55 (0.03)	1.63 (0.04)	1.61 (0.33)	1.61 (0.10)	0.12	0.31	1-4	1.0
15	0.58 (0.03)	1.80 (0.03)	1.26 (0.32)	1.84 (0.01)	0.15	0.28	1-5	0.92

Table G.3: Multifractal parameters cloud droplet effective radius field for the 15 example scenes: (1-6, and 15) uni-modal, (7-10) bi-modal, (11-14) thick clouds. *) marks scenes of which only fully cloudy sectors were used in the analysis.

2) FIRE 1987 data set

Scene No	H(1)	2 H(2) + 1	β	β_8	C(1)	K(2)	range [km]	cloud fraction A_c
F_{87} 1(1)	0.48 (0.02)	1.94 (0.03)	1.90 (0.06)	1.93 (0.02)	0.05	0.10	1-8	0.99
F_{87} 2(2)	0.53 (0.03)	2.02 (0.05)	2.17 (0.12)	2.24 (0.07)	0.06	0.10	1-5	0.98
F_{87} 3(3)	0.48 (0.04)	1.93 (0.09)	1.92 (0.16)	2.19 (0.15)	0.05	0.08	1-4	0.99
F_{87} 4(5)	0.46 (0.01)	1.84 (0.03)	2.18 (0.04)	2.07 (0.10)	0.05	0.09	1-20	0.96
F_{87} 5(7)	0.49 (0.03)	1.95 (0.05)	2.29 (0.08)	2.13 (0.15)	0.05	0.09	1-8	0.99
F_{87} 6(8)	0.40 (0.04)	1.79 (0.08)	1.82 (0.21)	1.84 (0.15)	0.04	0.08	1-4	1.0
F_{87} 7(13)	0.57 (0.04)	2.14 (0.08)	2.77 (0.16)	2.63 (0.15)	0.05	0.08	1-4	1.0
F_{87} 8(14)	0.64 (0.04)	2.26 (0.08)	3.26 (0.20)	2.91 (0.11)	0.06	0.11	1-4	1.0
F_{87} 9	0.46 (0.02)	1.90 (0.04)	1.98 (0.07)	1.86 (0.15)	0.07	0.13	1-10	0.98
F_{87} 10	0.46 (0.02)	1.87 (0.06)	2.00 (0.13)	2.05 (0.09)	0.05	0.10	1-7	0.90
F_{87} 11	0.57 (0.03)	2.10 (0.07)	2.47 (0.18)	2.29 (0.05)	0.06	0.12	1-4	0.95
F_{87} 12	0.58 (0.05)	2.15 (0.10)	2.27 (0.36)	2.68 (0.29)	0.05	0.09	1-3	1.0
F_{87} 13	0.50 (0.06)	2.02 (0.12)	1.89 (0.38)	2.48 (0.30)	0.05	0.08	1-3	1.0
F_{87} 14	0.51 (0.04)	2.00 (0.08)	2.26 (0.19)	2.30 (0.09)	0.06	0.11	1-4	1.0
F_{87} 15	0.41 (0.03)	1.81 (0.06)	1.92 (0.12)	1.89 (0.01)	0.05	0.09	1-5	1.0
F_{87} 16	0.49 (0.03)	1.95 (0.06)	2.15 (0.17)	2.07 (0.01)	0.06	0.10	1-4	0.82
F_{87} 17	0.54 (0.05)	2.05 (0.10)	1.88 (0.37)	2.34 (0.14)	0.06	0.11	1-3	0.97

Table G.4: Multifractal parameters of cloud visible wavelength radiance field for $F87$ data set.

Scene No	H(1)	2 H(2) + 1	β	β_8	C(1)	K(2)	range [km]	cloud fraction A_c
F_{87} 1(1)	0.49 (0.02)	1.96 (0.04)	2.02 (0.06)	2.02 (0.01)	0.05	0.10	1-8	0.99
F_{87} 2(2)	0.54 (0.03)	2.07 (0.05)	2.07 (0.05)	2.17 (0.01)	0.05	0.10	1-5	0.98
F_{87} 3(3)	0.52 (0.04)	2.06 (0.07)	2.14 (0.23)	2.32 (0.18)	0.07	0.13	1-4	0.99
F_{87} 4(5)	0.48 (0.01)	1.93 (0.03)	2.10 (0.04)	2.00 (0.11)	0.05	0.09	1-20	0.96
F_{87} 5(7)	0.50 (0.03)	2.02 (0.05)	2.32 (0.08)	2.17 (0.11)	0.04	0.07	1-7	0.99
F_{87} 6(8)	0.42 (0.04)	1.84 (0.07)	1.81 (0.21)	1.85 (0.13)	0.05	0.09	1-4	1.0
F_{87} 7(13)	0.57 (0.04)	2.13 (0.09)	2.79 (0.19)	2.68 (0.20)	0.06	0.10	1-4	1.0
F_{87} 8(14)	0.65 (0.04)	2.23 (0.09)	3.20 (0.19)	2.87 (0.08)	0.09	0.16	1-4	1.0
F_{87} 9	0.47 (0.02)	1.91 (0.04)	2.11 (0.12)	2.12 (0.18)	0.06	0.11	1-10	0.98
F_{87} 10	0.51 (0.02)	2.00 (0.06)	2.06 (0.13)	1.96 (0.06)	0.05	0.09	1-7	0.90
F_{87} 11	0.52 (0.02)	1.98 (0.05)	2.42 (0.09)	2.34 (0.02)	0.09	0.17	1-8	0.95
F_{87} 12	0.55 (0.06)	2.09 (0.11)	3.13 (0.46)	1.93 (0.34)	0.04	0.08	1-3	1.0
F_{87} 13	0.52 (0.06)	2.06 (0.11)	1.85 (0.36)	2.61 (0.30)	0.05	0.08	1-3	1.0
F_{87} 14	0.48 (0.03)	1.96 (0.06)	2.45 (0.11)	2.34 (0.10)	0.04	0.06	1-5	1.0
F_{87} 15	0.43 (0.04)	1.88 (0.06)	2.00 (0.12)	1.98 (0.02)	0.04	0.08	1-5	1.0
F_{87} 16	0.47 (0.03)	1.96 (0.05)	2.04 (0.12)	2.08 (0.06)	0.05	0.08	1-5	0.82
F_{87} 17	0.56 (0.05)	2.07 (0.11)	2.18 (0.49)	2.42 (0.27)	0.06	0.11	1-3	0.97

Table G.5: Multifractal parameters of cloud optical depth field for the FIRE data set.

Scene No	H(1)	2 H(2) + 1	β	β_8	C(1)	K(2)	range [km]	cloud fraction A_c
F_{87} 1 (1)	0.55 (0.01)	2.01 (0.01)	1.95 (0.13)	2.00 (0.18)	0.06	0.14	1-8	0.99
F_{87} 2(2)	0.53 (0.02)	2.07 (0.03)	1.90 (0.17)	1.91 (0.16)	0.05	0.09	1-7	0.98*
F_{87} 3(3)	0.48 (0.03)	1.92 (0.05)	2.06 (0.25)	2.17 (0.02)	0.07	0.12	1-4	0.99*
F_{87} 4(5)	0.53 (0.01)	1.96 (0.03)	1.84 (0.11)	1.92 (0.12)	0.05	0.11	1-10	0.96
F_{87} 5(7)	0.49 (0.01)	1.92 (0.03)	1.84 (0.11)	1.84 (0.02)	0.05	0.10	1-8	0.99
F_{87} 6 (8)	0.34 (0.01)	1.61 (0.01)	1.42 (0.15)	1.26 (0.13)	0.06	0.14	1-10	1.0
F_{87} 6 (8)	0.63 (0.01)	2.24 (0.01)	1.85 (0.23)	2.34 (0.28)	0.06	0.14	20-80	1.0
F_{87} 7(13)	0.53 (0.02)	2.07 (0.03)	1.86 (0.26)	1.90 (0.06)	0.06	0.10	1-4	1.0
F_{87} 8(14)	0.55 (0.03)	1.63 (0.04)	1.61 (0.33)	1.61 (0.10)	0.12	0.31	1-4	1.0
F_{87} 9	0.57 (0.01)	2.13 (0.01)	2.03 (0.08)	2.24 (0.10)	0.06	0.11	1-40	0.98*
F_{87} 10	0.60 (0.01)	2.15 (0.02)	1.96 (0.20)	1.83 (0.18)	0.08	0.13	1-7	0.90*
F_{87} 11	0.50 (0.02)	1.89 (0.05)	1.95 (0.17)	2.03 (0.01)	0.05	0.10	1-7	0.95
F_{87} 12	0.49 (0.04)	1.99 (0.09)	2.22 (0.29)	2.17 (0.28)	0.04	0.08	1-3	1.0
F_{87} 13	0.45 (0.02)	1.96 (0.05)	1.67 (0.39)	2.00 (0.20)	0.05	0.09	1-3	1.0
F_{87} 13	0.19 (0.01)	1.37 (0.01)	1.44 (0.14)	1.44 (0.15)	0.05	0.09	4-20	1.0
F_{87} 14	0.46 (0.01)	1.91 (0.01)	1.65 (0.08)	1.81 (0.14)	0.05	0.10	1-30	1.0
F_{87} 15	0.34 (0.01)	1.67 (0.01)	1.00 (0.10)	1.09 (0.11)	0.05	0.10	1-10	1.0
F_{87} 15	0.41 (0.01)	1.85 (0.01)	1.60 (0.12)	1.73 (0.14)	0.05	0.10	10-50	1.0
F_{87} 16	0.47 (0.02)	1.76 (0.02)	1.75 (0.25)	1.53 (0.18)	0.09	0.18	1-6	0.82
F_{87} 17	0.22 (0.01)	1.43 (0.01)	1.33 (0.38)	1.22 (0.05)	0.05	0.09	1-9	0.97*

Table G.6: Multifractal parameters cloud droplet effective radius field for the FIRE data set. (*) marks scenes of which only fully cloudy sectors were used in the analysis.

3 Pacific summer 1994 data set

Scene No	H(1)	2 H(2) + 1	β	β_8	C(1)	K(2)	range [km]	cloud fraction A_c
P_{94} 1(4)	0.59 (0.03)	2.13 (0.05)	2.22 (0.13)	2.39 (0.01)	0.06	0.11	1-6	0.97
P_{94} 2(6)	0.38 (0.03)	1.76 (0.05)	1.97 (0.09)	1.87 (0.08)	0.05	0.09	1-8	0.94
P_{94} 3(11)	0.62 (0.04)	2.21 (0.08)	2.32 (0.19)	2.71 (0.12)	0.05	0.08	1-3	1.0
P_{94} 4(12)	0.37 (0.02)	1.71 (0.04)	1.66 (0.12)	1.69 (0.02)	0.05	0.10	1-6	1.0
P_{94} 5(15)	0.39 (0.03)	1.80 (0.06)	2.05 (0.10)	1.57 (0.14)	0.05	0.09	1-6	0.92
P_{94} 6	0.30 (0.05)	1.62 (0.12)	1.54 (0.21)	1.27 (0.35)	0.05	0.08	1-3	0.45
P_{94} 7	0.33 (0.02)	1.65 (0.04)	1.85 (0.07)	1.67 (0.03)	0.05	0.09	1-8	0.94
P_{94} 8	0.44 (0.06)	1.89 (0.12)	2.45 (0.22)	1.90 (0.34)	0.04	0.08	1-4	0.78

Table G.7: Multifractal parameters of cloud visible wavelength radiance field for the Pacific Ocean 1994 data set.

Scene No	H(1)	2 H(2) + 1	β	β_8	C(1)	K(2)	range [km]	cloud fraction A_c
P_{94} 1(4)	0.61 (0.03)	2.18 (0.05)	2.40 (0.17)	2.48 (0.04)	0.06	0.10	1-6	0.97
P_{94} 2(6)	0.40 (0.03)	1.81 (0.04)	2.06 (0.10)	1.91 (0.08)	0.06	0.10	1-8	0.94
P_{94} 3(11)	0.62 (0.04)	2.21 (0.08)	2.43 (0.17)	2.77 (0.15)	0.06	0.11	1-3	1.0
P_{94} 4(12)	0.38 (0.02)	1.72 (0.05)	1.75 (0.12)	1.70 (0.02)	0.05	0.09	1-6	1.0
P_{94} 5(15)	0.42 (0.03)	1.81 (0.05)	1.83 (0.10)	1.60 (0.11)	0.06	0.11	1-6	0.92
P_{94} 6	0.39 (0.05)	1.63 (0.08)	1.64 (0.39)	1.62 (0.16)	0.18	0.23	1-3	0.45
P_{94} 7	0.35 (0.02)	1.66 (0.03)	1.63 (0.08)	1.61 (0.01)	0.07	0.11	1-8	0.94
P_{94} 8	0.43 (0.06)	1.84 (0.11)	2.43 (0.20)	1.85 (0.34)	0.06	0.10	1-4	0.78

Table G.8: Multifractal parameters of cloud optical depth field for the Pacific Ocean 1994 data set.

Scene No	H(1)	2 H(2) + 1	β	β_8	C(1)	K(2)	range [km]	cloud fraction A_c
P_{94} 1(4)	0.59 (0.01)	2.13 (0.02)	1.96 (0.15)	2.14 (0.08	0.09	0.16	1-8	0.97*
P_{94} 2(6)	0.61 (0.01)	1.83 (0.02)	1.82 (0.11)	1.77 (0.02)	0.08	0.22	1-10	0.94
P_{94} 3(11)	0.46 (0.01)	1.93 (0.02)	1.63 (0.44)	1.71 (0.05)	0.06	0.11	1-4	1.0
P_{94} 4(12)	0.40 (0.01)	1.78 (0.01)	1.47 (0.06)	1.45 (0.02)	0.05	0.09	1-20	1.0
P_{94} 5(15)	0.38 (0.01)	1.76 (0.01)	1.69 (0.13)	1.52 (0.03)	0.05	0.09	1-6	1.0
P_{94} 6	0.58 (0.03)	1.80 (0.03)	1.26 (0.32)	1.84 (0.01)	0.15	0.28	1-5	0.92
P_{94} 7	0.39 (0.04)	1.54 (0.06)	1.29 (0.31)	1.37 (0.08)	0.21	0.28	1-3	0.45
P_{94} 8	0.42 (0.02)	1.77 (0.03)	1.67 (0.10)	1.79 (0.11)	0.07	0.13	1-8	0.94

Table G.9: Multifractal parameters of cloud droplet effective radius field for the the Pacific Ocean 1994 data set.(*) marks scenes of which only fully cloudy sectors were used in the analysis.

4) Pacific summer 1995 data set

Scene No	H(1)	2 H(2) + 1	β	β_8	C(1)	K(2)	range [km]	cloud fraction A_c
P_{95} 1(9)	0.46 (0.01)	1.84 (0.02)	1.94 (0.05)	1.96 (0.07)	0.09	0.18	1-20	0.95
P_{95} 2	0.43 (0.02)	1.86 (0.03)	1.99 (0.06)	1.89 (0.01)	0.05	0.09	1-9	0.96
P_{95} 3	0.56 (0.01)	2.05 (0.02)	2.07 (0.06)	2.05 (0.01)	0.07	0.15	1-20	0.97
P_{95} 4	0.52 (0.02)	1.97 (0.04)	2.25 (0.06)	2.12 (0.08	0.07	0.11	1-8	0.80
P_{95} 5	0.45 (0.02)	1.89 (0.05)	1.92 (0.07)	1.88 (0.05)	0.05	0.08	1-6	0.84

Table G.10: Multifractal parameters of cloud visible wavelength radiance field for the Pacific Ocean 1995 data set.

Scene No	H(1)	2 H(2) + 1	β	β_8	C(1)	K(2)	range [km]	cloud fraction A_c
P_{95} 1(9)	0.46 (0.01)	1.85 (0.01)	1.89 (0.05)	2.14 (0.11)	0.07	0.14	1-20	0.95
P_{95} 2	0.47 (0.02)	1.71 (0.02)	1.52 (0.07)	1.64 (0.11)	0.19	0.27	1-10	0.96
P_{95} 3	0.56 (0.01)	2.03 (0.02)	2.14 (0.05)	2.12 (0.05)	0.10	0.18	1-20	0.97
P_{95} 4	0.49 (0.01)	1.76 (0.02)	1.73 (0.12)	1.80 (0.14)	0.26	0.36	1-10	0.80
P_{95} 5	0.52 (0.02)	1.78 (0.03)	1.42 (0.19)	1.51 (0.11)	0.16	0.24	1-6	0.84

Table G.11: Multifractal parameters of cloud optical depth field for the Pacific Ocean 1995 data set.

Scene No	H(1)	2 H(2) + 1	β	β_8	C(1)	K(2)	range [km]	cloud fraction A_c
P_{95} 1(9)	0.45 (0.01)	1.75 (0.02)	1.77 (0.06)	1.89 (0.02)	0.07	0.15	1-20	0.95
P_{95} 2	0.58 (0.02)	2.03 (0.03)	2.23 (0.09)	2.25 (0.06)	0.15	0.20	1-10	0.96
P_{95} 3	0.59 (0.01)	1.96 (0.01)	1.87 (0.06)	1.84 (0.07)	0.11	0.23	1-25	0.97
P_{95} 4	0.47 (0.01)	1.56 (0.01)	1.29 (0.12)	1.54 (0.18)	0.37	0.47	1-15	0.80
P_{95} 5	0.58 (0.02)	1.83 (0.02)	1.44 (0.23)	1.73 (0.09)	0.20	0.30	1-6	0.84

Table G.12: Multifractal parameters of cloud droplet effective radius field for the Pacific Ocean 1995 data set.

5) Indian Ocean (SOCEX 1995) data set

Scene No	H(1)	2 H(2) + 1	β	β_8	C(1)	K(2)	range [km]	cloud fraction A_c
S_{95} 1	0.59 (0.01)	2.17 (0.03)	2.46 (0.06)	2.30 (0.12)	0.06	0.11	1-10	0.90
S_{95} 2	0.60 (0.01)	2.13 (0.03)	2.47 (0.08)	2.20 (0.08)	0.06	0.11	1-15	0.83
S_{95} 3	0.53 (0.02)	2.00 (0.03)	2.43 (0.05)	2.08 (0.11)	0.06	0.12	1-15	0.95
S_{95} 4	0.64 (0.02)	2.12 (0.04)	2.56 (0.07)	2.18 (0.08)	0.08	0.14	1-10	0.84

Table G.13: Multifractal parameters of cloud visible wavelength radiance field for the SOCEX 1995 data set.